OBSERVATIONS OF A TROPICAL INSTABILITY VORTEX

A DISSERTATION SUBMITTED TO THE GRADUATE DIVISION OF THE UNIVERSITY OF HAWAII IN PARTIAL FULFILLMENT OF THE REQUIREMENTS FOR THE DEGREE OF

DOCTOR OF PHILOSOPHY

IN

OCEANOGRAPHY

MAY 1997

By

Sean Christopher Kennan

Dissertation Committee:

Pierre Flament, Chairperson

Eric Firing

Fei-Fei Jin

Doug Luther

Bo Qiu

We certify that we have read this dissertation and that, in our opinion, it is satisfactory in scope and quality as a dissertation for the degree of Doctor of Philosophy in Oceanography.

DISSERTATION COMMITTEE

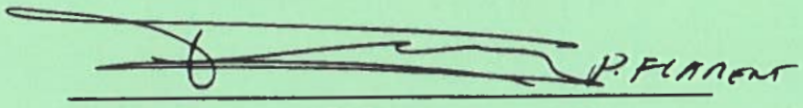

Chairperson

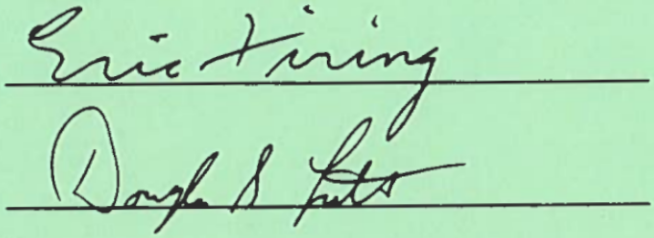

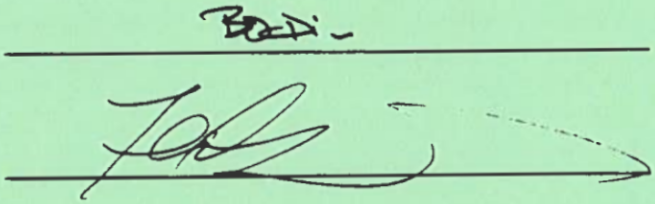

ii

I dedicate this to my family and friends.

Acknowledgements

I wish to acknowledge the hard work and support of the members of my advisory committee: Pierre Flament, Eric Firing, Fei-Fei Jin, Doug Luther, and Bo Qiu. They have worked beyond the call of duty in helping me to refine this research and manuscript.

I cannot express enough gratitude to Pierre Flament for his intellectual, emotional, and monetary support. I feel fortunate to have had the opportunity to work closely with him. He has been a mentor, colleague, friend, and inspiration.

My friends have helped me deal with difficult times through their patient listening and understanding. They may never know how crucial they have been in helping me to complete this dissertation.

The people working in the Satellite Oceanography Laboratory have collected the data, processed it, and helped with analyses. Michael Sawyer in particular offered assistance with programming techniques and data analysis on many occasions.

The Dept. of Oceanography provided monetary support and intellectual stimulation via teaching assistantships. I wish to extend special thanks to the students of Ocean 620 (Fall 1995) for their enthusiasm, challenging questions, and friendship.

I am grateful to the ARCS Foundation for monetary support and academic recognition.

This work was supported by the National Oceanographic and Atmospheric Administration through Cooperative Agreement NA37RJ0199 and the National Science Foundation through grants OCE-8918604 and OCE-9200001.

OBSERVATIONS OF A TROPICAL INSTABILITY VORTEX

by: Sean Christopher Kennan

adviser: Dr. Pierre Flament, Assistant Professor of Oceanography

Observations of an upper ocean vortex associated with tropical instabilities in the tropical Pacific were made in the vicinity of the South Equatorial Current and North Equatorial Counter Current (SEC-NECC) shear at 140°W during November-December of 1990. The dynamic and thermohaline structure of the observed vortex is mapped in three dimensions using a suite of measurements from shipboard, hydrographic, and satellite sensors and drifting buoys. Evidence that the sampled flow field is steady in a frame of reference moving with the disturbance is used to study the underlying dynamical balances and the effects on heat, fresh water, and eddy energy fluxes in the region.

The vortex translated westward at 30 cm/s (0.24°/day), less than half the speed of westward propagating meridional oscillations of the Equatorial Undercurrent (EUC) and SEC system. The associated flow deformed the North Equatorial Front through northward advection of cold equatorial water and southward entrainment of warmer tropical water, giving the surface temperature field the cusp-like pattern which is commonly associated with tropical instabilities.

A dipole of convergence and divergence had magnitudes comparable to the local inertial frequency and confirms predictions by various numerical models. Relative vorticity advection balanced convergence at the front, allowing northward moving cold water to subduct beneath the warmer tropical water. The growth of the vortex appears to have

been limited by the inertial frequency via a vortex instability mechanism. The same features are present in shear vortices in a general circulation model.

The vortex transported heat and fresh water equatorward at rates of about 0.2 MW/m^2 and 5 $g/(m^2s)$, respectively. The heat flux agrees with previous estimates from observations and models. The region from 2-5°N gained heat and fresh water at 2-5 W/m^3 and 0.1 $\mu g/(m^3s)$.

Eddy kinetic energy increased via barotropic instability at a rate of 0.15 mW/m^3 and via baroclinic conversion at 0.05 mW/m^3. The mean to eddy conversion took place in between the frontal convergence and central upwelling in the mixed layer and was coincident with a critical layer, consistent with a wave overreflection interpretation of barotropic shear instability.

TABLE OF CONTENTS

List of Tables

List of Figures

List of Abbreviations

- ADCP Acoustic Doppler Current Profiler
- AGC automatic gain control
- APE available potential energy
- AVHRR Advanced Very High Resolution Radiometer
- CTD Conductivity, Temperature, and Depth profiler
- DOF degrees of freedom
- EAPE eddy available potential energy
- EKE eddy kinetic energy
- EUC Equatorial Undercurrent
- GPS Global Positioning System
- IES Inverted Echo Sounder
- ITCZ Intertropical Convergence Zone
- KE kinetic energy
- MCSST Multi-Channel Sea Surface Temperature
- NECC North Equatorial Countercurrent
- NEF North Equatorial Front

- NOAA National Oceanic and Atmospheric Administration
- PCM Profiling Current Meter
- PMEL Pacific Marine Environmental Laboratory
- POCM Parallel Ocean Climate Model
- PVG potential vorticity gradient
- SEC South Equatorial Current
- SRL Shuttle Radar Laboratory
- SST sea surface temperature
- TAO Tropical Atmosphere and Oceans
- TIWE Tropical Instability Wave Experiment
- TIVs Tropical Instability Vortices
- TIWs Tropical Instability Waves
- UTC Universal Time Code
- WOCE World Ocean Circulation Experiment

Chapter 1

The Tropical Instability Wave Experiment

The reader is introduced to the subject of this study - an analysis of observations made during the Tropical Instability Wave Experiment (TIWE) - after which an historical background concerning tropical instabilities is presented, and the design of TIWE is described.

1.1 Introduction

Seasonal oscillations of the zonal equatorial currents are known to result from hydrodynamic instability of the mean circulation, and are believed to transport significant amounts of heat, momentum, and energy meridionally. Yet, their genesis and relationship to the mean conditions is not well understood. The present paradigm for eddy fluxes in the tropical Pacific and Atlantic oceans is a melange of equatorial long waves, meanders, and barotropic, baroclinic, and frontal instabilities. Indeed, the current state of knowledge is such that ocean models provide much of the details about the character of tropical instabilities.

Meanderings of the Equatorial Undercurrent (EUC) and South Equatorial Current (SEC), meridional deformations of the North Equatorial Front (NEF), and anticyclonic vortices and sea level highs in the SEC-NECC (North Equatorial Counter Current) have all been observed to occur when the equatorial current system is strongest and most likely to be unstable. Observed and inferred wavelengths and periods range from 500-1500 km and 15-35 days. The long wavelengths and appearance of antisymmetric oscillations of the fronts in infrared satellite images have lead to the term "equatorial

long waves," while subsequent stability analyses of the mean currents prompted the name "tropical instability waves."

While it appears clear that equatorial long wave and instability wave phenomena result from hydrodynamic instability of the mean circulation, the relationships between various observations and specific dynamics have not been established. Analyses from current meter moorings at the equator in the Atlantic and Pacific oceans have indicated that the EUC-SEC system experiences barotropic instability [Weisberg and Weingartner, 1988; Qiao and Weisberg, 1997], while observations which span most of the latitude range of the central tropical Pacific showed several eddy energy generation regions [Luther and Johnson, 1990]. Various other measurements have provided different results. Thus, there may be more than one simultaneous instability mechanism operating in the Pacific equatorial current system.

This study addresses the processes governing an SEC-NECC shear vortex by presenting its fully three-dimensional dynamic and thermohaline structure as well as detailed heat, freshwater, and eddy energy flux calculations. Features commonly associated with meanders of the EUC-SEC system - westward propagating SST cusps and sea level highs - are shown to be manifestations of a horizontal shear instability in the anticyclonic SEC-NECC shear region. Anticyclonic vortices, or sea level highs which deform the North Equatorial Front, are found to be kinematically distinct from the wave-like disturbances at the equator. Therefore, in this study, equatorial long waves and shear vortices in the central Pacific are distinguished from one another. In anticipation of the results, "tropical instability vortices" (TIVs) will be used to refer to the SEC-NECC shear vortices, while the terms "equatorial disturbances" and "equatorial long waves" will be reserved for oscillations of the EUC-SEC system. The phrase "tropical instability waves" (TIWs)

will be used only sparingly to refer to both processes as they have been discussed in the literature.

Because of the saturated finite amplitude that tropical instability vortices regularly attain, as observed from satellite AVHRR and altimeters and in numerical models, the results from this study are believed to apply in a general way to all SEC-NECC shear vortices. This proposition is continually supported throughout the manuscript by direct comparisons with simultaneous calculations on a vortex from the WOCE Parallel Ocean Climate Model (POCM). While this study makes no attempt to validate the POCM or to provide statistics on the behavior of TIWs in the model, the similarities between the observed and modeled vortices greatly strengthens the present work, limited by design to one event.

The manuscript is divided into four main sections which deal in turn with the kinematics, structure, dynamics, and energetics of an instability vortex observed during TIWE-2. The main thrust of each chapter is briefly summarized below, after which the remainder of this chapter is devoted to providing an historical background and description of the observational program.

1.1.1 kinematics - chapter 2

A cold water cusp - the canonical trait of TIWs - is directly correlated with the velocity field of an anticyclonic vortex. Tropical instability vortices and equatorial disturbances (long waves) are found to be kinematically distinct.

The vortex observed during TIWE-2 is analyzed in a reference frame that moves westward with it, rendering the flow field relatively steady. The translation speed of the vortex is determined from drifting buoys and confirmed with the aid of ADCP data and a comparison between Lagrangian and Eulerian periods. The process of transforming

all the data into the moving frame is described and a method for estimating the error of the resulting objective maps is presented. The depth and meridional range which can be studied using the moving reference frame is also addressed.

1.1.2 structure - chapter 3

Convergence exceeding the local inertial frequency (f) occurs along the leading edge of the deformed North Equatorial Front, while divergence approaching f occurs near the center of the vortex in a dipole pattern with the frontal convergence. Anticyclonic vorticity barely exceeds f in a region overlapping the strong divergence. The anticyclonic flow, high geopotential (sea level), and northward cold water advection are found to be manifestations of the same phenomenon.

Divergence and vorticity is calculated from the gridded velocity maps, revealing patterns in agreement with the POCM. The three-dimensional structure of the vortex flow field is mapped out revealing that cold, saline water from the south and warmer, fresh water from the Intertropical Convergence Zone (ITCZ) are entrained by the flow above the thermocline. A wind event during the experiment is examined - the likely result is that temporal changes in the thermohaline and kinematic fields were aliased into spatial gradients in the moving reference frame over a limited region.

1.1.3 dynamics - chapter 4

Frontal convergence is a vortex stretching response to relative vorticity advection and torques exerted by subgrid scale and turbulent stresses. The vortex has Rossby number ≥ 1 - nonlinear terms play an important role in the dynamics, especially near the front where they are related to the relative vorticity and cold water advection. Evidence that

the vortex may be inertially unstable provides an explanation for the strong divergence near the center and the regular structure of most TIVs.

The observations from Chapters 2 and 3 are used to scale the momentum and vorticity equations. All terms in the equations are then calculated directly from the gridded data and compared with a vortex from the POCM. Advection is found to play an important role for the vortex flow, especially near the NEF. Evidence is found that the vortex flow is unstable, which could explain the regular finite amplitude of such eddies as seen in AVHRR and numerical models - the long wave character. Possible relationships between the vortex and the marine ecosystem are also briefly investigated.

1.1.4 eddy fluxes - chapter 5

Eddy fluxes of heat, salt, and energy are computed by separating the flow into zonal mean and fluctuating parts. Eddy heat and freshwater fluxes in the region 2-5°N are found to be equatorward above the thermocline at 0.2 MW/m^2 and 5 g/(m^{2}s). The flux divergences imply net heating and freshening for the region.

Barotropic conversion via $-\rho_o \overline{u'v'}\overline{u}_y$ is a significant source of eddy growth for the vortex, with values 0.15 mW/m^3, comparable to previous estimates for mean to eddy energy conversion in the same region and at the equator. The eddy energy production near the front is tied to a critical layer there, where the instability remains stationary relative to the mean flow. The concept of wave overreflection is applied to reveal the likely existence of the necessary and sufficient conditions for barotropic instability near 4°N.

1.1.5 summary - chapter 6

The findings are summarized in the last chapter. An appendix is included, where the eddy energy equations are derived.

1.2 Background

Swift, zonal jets characterize the lowest order circulation of the tropical Pacific ocean surface waters, while the change in sign of Coriolis force across the equator and the large-scale meridional gradients of the easterly trade winds cause secondary circulation patterns in the meridional/vertical plane. Associated regions of upwelling and downwelling intensify along one or more fronts, usually found between 2-5°N.

However, each late summer to fall this pattern is deformed by the passage of equatorial long waves. As the Intertropical Convergence Zone (ITCZ) migrates northward, the southeast trades accelerate the South Equatorial Current (SEC), the zonal current system becomes unstable and meanderings with periods of 15-35 days occur in the EUC (Equatorial Undercurrent), SEC, and North Equatorial Counter Current (NECC). These "waves", often termed tropical instability waves (TIWs), are often visible from space, in the infrared as well as visible bands [Legeckis, 1977; Yoder *et al.*, 1994], where they manifest themselves as cusp-like, westward propagating deformations of the North Equatorial Front.

Instabilities of the equatorial currents were first detected in the Atlantic ocean in current meter records: meanderings of the SEC were found to have a period of about 14-21 days [Düing *et al.*, 1975]. Soon after they were detected in satellite infrared images of the large-scale equatorial SST front in the Pacific. Cusp-like deformations of the front

that separates cold equatorial water from warmer tropical water were observed to have wavelengths of 500-1500 km [Legeckis, 1977].

Subsequently, meridional oscillations of the zonal currents in the tropical Pacific have been observed using drifting buoys [Hansen and Paul, 1984; Chew and Bushnell, 1990; Baturin and Niiler, 1997], current meter arrays [Düing *et al.*, 1975; Lukas, 1987; Halpern *et al.*, 1988; Bryden and Brady, 1989; Qiao and Weisberg, 1995], velocity profilers [Leetmaa and Molinari, 1984; Wilson and Leetmaa, 1988; Luther and Johnson, 1990], inverted echo sounders [Miller *et al.*, 1985], moored thermistors [McPhaden, 1996], satellite infrared sensors [Legeckis, 1977; Legeckis *et al.*, 1983; Legeckis, 1986b; Pullen *et al.*, 1987], satellite altimeters [Perigaud, 1990; Busalacchi *et al.*, 1994], as well as visually from the space shuttle [Yoder *et al.*, 1994]. The stability of the equatorial current system has been investigated using idealized mean currents [Philander, 1976; Philander, 1978; Proehl, 1996] and numerical models of ocean circulation [Cox, 1980; Semter and Holland, 1980; Philander *et al.*, 1986; Philander *et al.*, 1987; McCreary and Yu, 1992; Yu *et al.*, 1995; Donohue, 1995]. Meanwhile, oscillations with periods and wavelengths that lie within the wide range of observed values are reproduced by most global scale circulation models.

Observations, in both the Atlantic and Pacific oceans, have indicated that barotropic instability within the cyclonic EUC-SEC shear is a possible generation mechanism for the waves [Weisberg, 1984; Hansen and Paul, 1984; Lukas, 1987; Weisberg and Weingartner, 1988; Luther and Johnson, 1990; Qiao and Weisberg, 1995; Qiao and Weisberg, 1997; Baturin and Niiler, 1997]. Yet, some modeling efforts have indicated the anticyclonic shear of the SEC and NECC as the more likely mechanism [Philander, 1976; Philander, 1978; Cox, 1980; Philander *et al.*, 1986], although a recent investigation by

Proehl [1996] indicates that the instability arises in the cyclonic shear region of the SEC in the Pacific. Baroclinic instability has also been suggested [Cox, 1980; Semter and Holland, 1980; Hansen and Paul, 1984; Luther and Johnson, 1990], and it has even been hypothesized that potential energy of the equatorial front is the primary source [McCreary and Yu, 1992; Yu *et al.*, 1995].

Some of the first estimates of the direct effects of TIWs in the Pacific ocean came from Hansen and Paul [1984], who followed 20 satellite-tracked drifting buoys from June through October 1979, discovering westward propagating anticyclonic eddies in the SEC-NECC shear. A few drifters in particular indicated that the northward velocity associated with these eddies was related to the cusp-like deformations to SST (sea surface temperature) along the equatorial front. Estimates of eddy momentum and heat transfers in the region 0-7°N were comparable to the fluxes associated with the annual mean circulation. Subsequent models of the circulation confirmed these results [Philander *et al.*, 1986; Philander *et al.*, 1987].

While Hansen and Paul [1984] found the largest source of eddy energy at the equator, the vortices they observed were located in the anticyclonic shear of the SEC and NECC. Similar vortices with westward moving SST cusps have been indicated by observations of dynamic topography. Miller *et al.* [1985] observed vortices near 5°N, 110°W using an IES (inverted echo sounder) array. Meanwhile, Perigaud [1990] used Geosat altimeter measurements from 1987 and 1988 to describe a train of sea level highs in the central and eastern Pacific centered at 5°N, translating westward at 40 cm/s. Busalacchi *et al.* [1994] also observed westward propagating sea level highs, using the TOPEX altimeter during 1993 to estimate the overall phase speed at 45 cm/s.

Qiao and Weisberg [1995; 1997] have confirmed that meanderings of the SEC-EUC system extract energy from the mean flow via barotropic instability, or eddy advection of vorticity associated with the mean cyclonic shear of the SEC. In contrast, Baturin and Niiler [1997] have shown that eddy energy production is largest in the SEC-NECC shear region, although they also find significant production in the SEC-EUC shear and even detect the presence of baroclinic instability. Luther and Johnson [1990] had previously found evidence for three distinct regions of eddy energy production: in the EUC-SEC shear from July-November, and in the NECC thermocline and to a lesser extent the SEC-NECC shear from December-March.

This study posits that the phenomena commonly called "tropical instability waves" are in fact two distinct processes, which we shall refer to as SEC-NECC shear vortices, or tropical instability vortices, and equatorial disturbances, or long waves. We find that cold water cusps, sea level highs, and anticyclonic vortices are all directly related to barotropic instability of the anticyclonic SEC-NECC shear, and are kinematically unrelated to equatorial long waves. The structure, dynamics, and eddy fluxes of a shear vortex are examined using data from TIWE-2 and the POCM.

1.3 Experiment design

The Tropical Instability Wave Experiment (TIWE) was designed to address the proposed theories of tropical instability generation. The most widely accepted paradigm for TIWs at the time described them as long wave disturbances to the equatorial current system resulting from shear instability. While observations in the Atlantic Ocean indicated that TIWs there resulted from cyclonic shear instability of the SEC-EUC currents, modeling of the tropical Pacific suggested that the anticyclonic shear of the

SEC-NECC system could be the cause there. TIWE aimed to provide a general description of the kinematics and energetics of TIWs in the Pacific with the hope of determining the validity of the various theories, such as cyclonic (EUC-SEC) versus anticyclonic (SEC-NECC) shear generation.

The design of the experiment called for two hydrographic cruises and two mooring arrays to be deployed in the central tropical Pacific along 140°W. An array of five subsurface ADCP (Acoustic Doppler Current Profiler) current meter moorings was deployed at 1° spacing in a diamond shape centered on the equator by Weisberg *et al.*[1991]. Data from the moorings, which were in the region from May 1990 to June 1991, have lead Qiao and Weisberg [1995; 1997] to conclude that the cyclonic shear of the SEC near 0.5°N is indeed a source for instability wave energy from late summer to fall.

The seagoing component of TIWE involved two cruises to the region; the first two (TIWE-1, TIWE-2) sampled the dynamic and thermohaline structure of the SEC-NECC shear region during the height of the 1990 instability wave season (August-December). During TIWE-1 (August 1990), the detailed structure of the equatorial front was sampled using shipboard ADCP, repeated CTD casts and a towed SeaSoar platform [Sawyer, 1996].

The second seagoing phase of TIWE (TIWE-2) took place aboard the R/V Moana Wave during November to December, 1990. The study region is shown in 1.1 - the boxed area 2-5°N, 140°W was surveyed by the ship 6 times over a 20 day period. Shipboard ADCP (Acoustic Doppler Current Profiler) and CTD casts measured the velocity and thermohaline structure of the upper 300 m of the ocean, while meteorological sensors measured wind speed, humidity, and radiative fluxes. The ADCP and hydrographic

data are described in three data reports [Trefois *et al.*, 1993; Firing *et al.*, 1994; Sawyer *et al.*, 1994].

The ship also carried a satellite dish for receiving infrared AVHRR (Advanced Very High Resolution Radar) images from the NOAA polar orbiting satellites. The images provided real-time information on the location of the equatorial front; 1.1 shows the SST of the study region, derived from AVHRR from NOAA-11 for 16 November, as the ship arrived at the survey area. A northward cusp of cold water, commonly associated with tropical instabilities, is visible at 3°N, 140°W.

Drifting buoys were deployed at the corners of the survey area and a cluster of 7 drifters was seeded in the SST cusp. Most of the drifters moved westward in cycloidal trajectories, as previously observed by Hansen and Paul [1984] and Chew [1990]. Additional simultaneous measurements during the November to December time period were available from the equatorial array of moored current meters and the moored thermistors and current meters along 140°W from the equator to 9°N (Figure 1.2).

The drifting buoys deployed during TIWE were of the holey sock drogue type, equipped with temperature sensors. They consisted of a 6 m drogue attached to a 9 m cable with two buoys. A primary buoy floats at the surface while a secondary one decouples motion at the surface from the rest of the drifter. Details and flow characteristics of these type of drifters are given by Niiler *et al.*[1987]. The nominal depth of velocity determinations from the drifters is assumed to be 15 m at all times. Strong vertical shear would decrease this depth, but except for the EUC, the equatorial currents are fairly constant within the surface layer.

The positions of the drifters were fixed during passes of the NOAA polar orbiting satellites, 5-8 times a day. These fixes were then interpolated onto a regular time grid

of 3-hour spacing using a least squares smoothing routing which allows determination of instantaneous velocity [Hansen and Herman, 1989].

All available data during the experiment are depicted in Figure 1.2. The TIWE data were augmented by the TAO array of moored thermistors and current meters along 140°W from 2°S-9°N, and the equatorial array of current meter mooring moorings [Weisberg *et al.*, 1991]. A current meter array centered at 2N, 140W (triangles) provided sporadic measurements (C. Eriksen, personal communication).

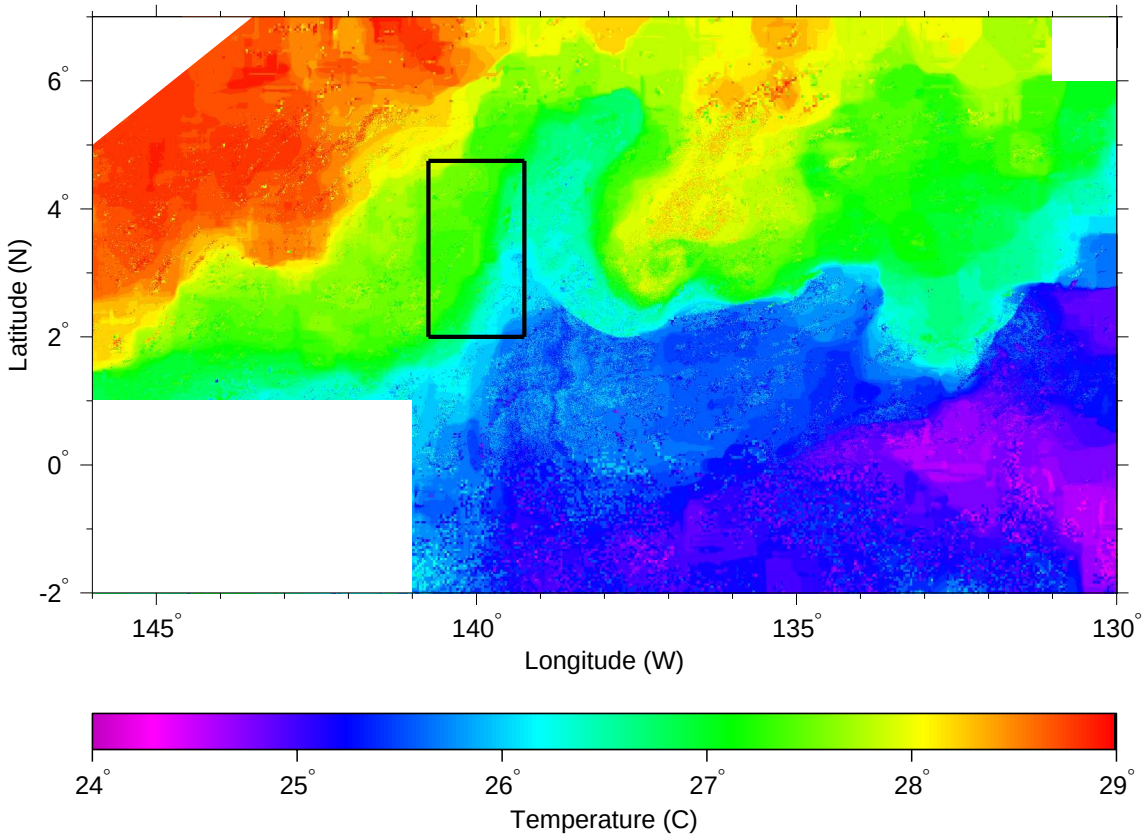

Figure 1.1: SST for the region 146-130°W, 2°S-7°N on 16 November 1990 (23:19 GMT) estimated from

The boxed region at 140°W, 2-5°N is the study area of TIWE-2.

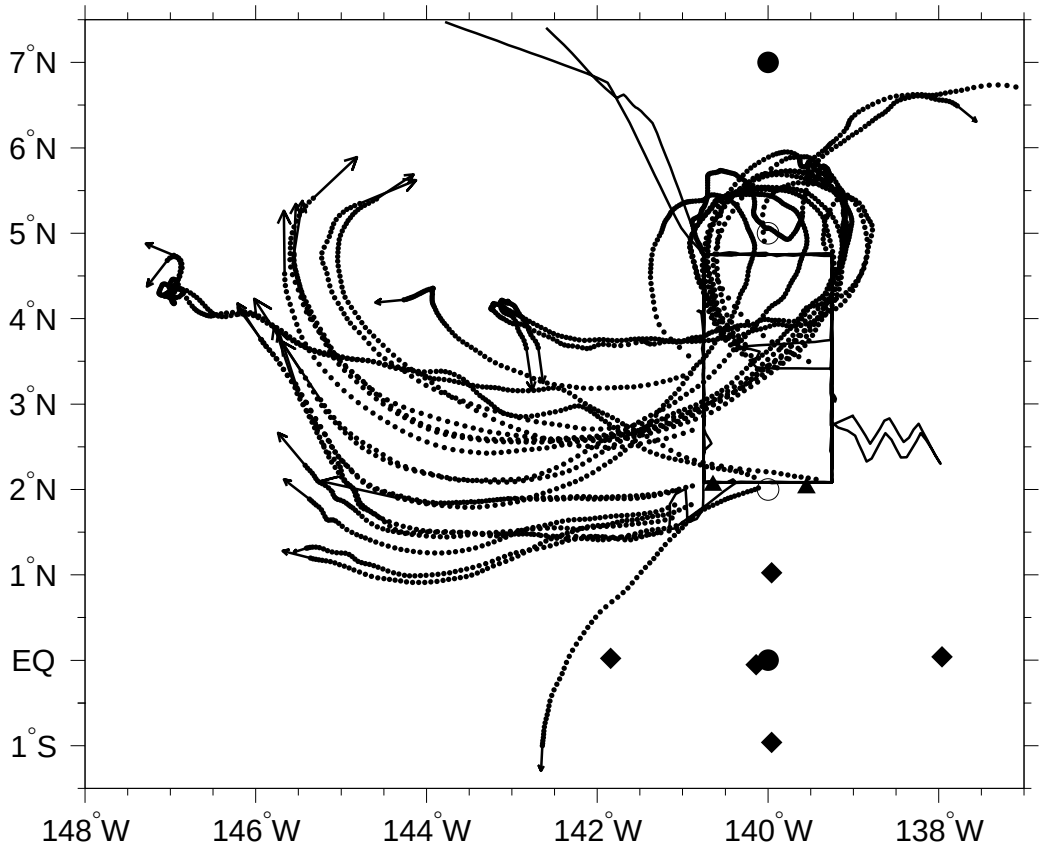

Figure 1.2: Available data for TIWE-2 are shown for the time period 11 November through 11 December, 1990 (Julian days 315-345). Legend: drifter trajectories (dotted lines), ship tracks (solid lines), and mooring locations (circles - TAO thermistors, filled - with current meters; diamonds - upward looking ADCP current meters; triangles - profiling current meters.)

Chapter 2

Mapping a Translating Vortex

In which the displacement speed of looping drifters is shown to correspond to the translation speed of a vortex, and is used to transform velocity measurements into a reference frame where the flow is approximately steady.

2.1 Sampling the flow field

Sampling of the flow field associated with a tropical instability was achieved during TIWE-2 using drifting buoys and shipboard ADCP. Drifters deployed in the cold cusp of the instability allow robust determination of its translation speed and subsequent transformation of all data into a moving reference frame, while the ADCP measurements provide wide coverage in that frame of the flow field throughout the upper 300 m.

2.1.1 drifting buoys

In all, 25 of the drifters deployed during TIWE-2 returned good data. Two clusters of drifters were deployed: 7 near 140°W, 3.25°N on 19 November (Julian day 323: three days after the AVHRR image of Figure 1.1), and 8 near 141°W, 1.8°N on 2 December (day 336). The rest were deployed at various points around the sampling box traversed by the ship, between 2-5°N and 139-141°W.

The first drifter was deployed at 140°W, 3.5°N (day 322). It followed a looping motion rapidly northward and then southward in an anticyclonic sense while drifting westward with the SEC (Figure 2.1a). This movement is similar to the eddying associated with TIW cusps described by Hansen and Paul [1984]. The next two drifters were

deployed near 2°N on day 322; they moved slowly northward at about 18 cm/s while moving 59 cm/s westward with the SEC until reaching 4.5°N where they were entrained by the NECC on day 345 (Figure 2.1b). Once in the NECC they meandered eastward.

On 19 November (day 323), 7 buoys were deployed in a cluster centered around 140.3°W, 3.7°N with a mean separation of about 10 km. The buoys were deployed as a cluster so as to directly measure convergence across the SST front through changes in the cluster area (discussed in Chapter 3). All 7 proceeded rapidly northward as did the first drifter of the previous day. Upon reaching 6°N, one was entrained by the NECC, moving eastward and out of the experiment area, while the remaining 6 followed the canonical cycloidal motion (Figure 2.1c). Of the remaining drifters, 3 others followed loop-like trajectories. Many others showed signs of looping motion but spent most of the time entrained in either the SEC or NECC (Figure 2.1d). A second cluster, of 8 buoys, was deployed in the SEC, drifting to the west and moving northward before the end of the experiment (Figure 2.1e). Of all those deployed, only one drifter crossed the equator, doing so at 60 cm/s between 1°N-1°S (day 340-345) (not shown).

Close inspection of all trajectories, and the 6 looping drifters deployed on day 323 in particular, reveals an abrupt change in behavior during the days 345-350 - in almost all 25 trajectories, signs of looping disappear. This time period corresponds to the end of the instability season as observed by the equatorial array of current meters deployed during TIWE [Qiao and Weisberg, 1995] (Figure 1.2). Figure 2.2 shows the meridional velocity at 140°W on the equator; the last strong pulse of northward flow dies out after 16 December (day 350). Thus, the drifters appear to have sampled primarily the meridional flow between the SEC and NECC during the passage of possibly the last instability, and the state of the currents after the equatorial disturbances had died out.

2.1.2 shipboard ADCP

As the drifters were looping to the west, a shipboard ADCP measured velocity of the top 300 m along the ship track depicted in Figure 1.2. The survey box was repeated every three to five days, in a counterclockwise sense. The velocity near 22 dbar is shown in Figure 2.3 for each of the five circuits of the study region. At the beginning of the experiment there was little to no flow at 5°N, while the SEC intensified to over 1 m/s by the time the ship headed northward along 139.25°W. Northward flow of about 1 m/s was found along 5°N (Figure 2.3a).

For each of the ensuing ship circuits shown in Figure 2.3 the flow is dominated by the westward SEC, but a change from strong northward flow north of 3°N early in the experiment, to southward flow can be seen in Figures 2.3b-d.

The drifting buoys and ADCP both indicate that a disturbance propagated westward through the SEC-NECC shear region. The looping drifters in particular were trapped in a vortical flow.

2.2 Vortex translation

The drifters which were seeded directly into the eddying motion of the cold water cusp followed cycloidal trajectories, suggesting that they were entrained in a translating vortex. In this section we show this to be the case: the translation speed is determined directly from the looping drifters and is confirmed as a unique solution using independent measurements from the shipboard ADCP.

2.2.1 Lagrangian estimates

Denoting a drifter's position as a function of time by $\mathbf{x}(t) = [x(t), y(t)]$, a cycloid trajectory may be modeled as:

$$x(t) = A_x sin(2\pi t/T_L) + B_x cos(2\pi t/T_L) + C_x t + D_x$$

$$y(t) = A_y sin(2\pi t/T_L) + B_y cos(2\pi t/T_L) + C_y t + D_y \tag{2.1}$$

where T_L is the Lagrangian period - the period of the harmonic being fit, or the time to complete one loop - and the coefficients A_x, etc. are to be determined. The coefficients of sine and cosine may be combined to give the amplitude and phase, while C_x and C_y correspond to constant translations in the zonal and meridional directions. If the period T_L is assumed known, then this model can be fit to the data using a least squares multiple linear regression. For the buoy tracks which displayed clear looping (Figure 2.1a,c,e), the errors of the fits were found to be minimum at periods ranging from 20-21 days.

An example of a fit of (2.1) to a buoy track is shown in Figure 2.4. The top panel gives the total fit, while the bottom panel shows the result with the constant translation removed. The latter case, in which the drifter track closes on itself, is equivalent to viewing the buoy motion in a frame of reference moving at the translation velocity [C_x,C_y]. The translation speeds which resulted from the fits to all 8 looping buoys are shown in Figure 2.5; results ranged from 26.6 to 31.6 cm/s to the west with a median of 30 cm/s. There were some significant meridional movements to the north, but the mode was only 1 cm/s. All of the fits explained more than 99% of the variance of the trajectories.

2.2.2 Eulerian estimates

Although it seems apparent that the looping drifters were entrained in a translating vortex, one could postulate that other processes influenced their motion. In that case the -30 cm/s displacement speed obtained above would not be the translation speed of a vortex and could not be used to transform the observations from TIWE-2 into a reference frame where the flow becomes approximately steady (the goal of this chapter).

The periodic looping of a drifter could be caused by either circulation around a translating vortex or motion within a periodically varying flow field induced by a train of vortices or large amplitude waves. In the latter case a drifter would not move on average with the disturbances, while in the former situation it would reside on a closed streamline moving with the vortex. To distinguish these two situations requires an independent estimate of the translation speed via at least two simultaneous Eulerian measurements separated in longitude.

Unfortunately, the TAO moorings do not provide phase information on the relevant longitude scale and the current meter array deployed at 2°N (Figure 1.2) largely failed. Consequently, we appeal to the shipboard ADCP measurements. Although the shipboard ADCP does not directly provide an Eulerian time series, gappy records for limited areas can be constructed by extracting meridional velocity data from the repeated tracks.

The western and eastern legs of the repeated ship track (along 140.75°W and 139.25°W respectively) (refer to Figure 2.3) are each separated into 1/4° latitude bins giving 11 pseudo-moorings (from 2-4.75°N) for the two longitudes. Subsequently, for each latitude bin, the phasing between the eastern and western legs combined with knowledge of the 1.5° separation provides the needed Eulerian estimate.

An example of such a time series construction for 4-4.25°N is shown in Figure 2.6a. While the time series is gappy and provides only a rough estimate of the local changes in velocity, a time lag between the two records is evident. This lag was extracted for sections of the time series where the meridional velocity was decreasing. For each latitude bin the median time lag was taken as the best estimate. The method failed for two latitude ranges (2.5-2.75 and 2.75-3°N) leaving 9 different lags. These were then converted to phase speeds using the 1.5° separation. The results are shown as a histogram in Figure 2.6b. The range of obtained phase speeds is roughly -35 to -70 cm/s with a median of -41±14 cm/s.

2.2.3 Lagrangian versus Eulerian periods

The results from the ADCP pseudo-moorings do not provide a very tight constraint on the translation speed of the disturbance which moved through the TIWE-2 region. However, it can be shown, through a series of simple arguments regarding Lagrangian and Eulerian periods, that they nevertheless invalidate the hypothesis that the drifters did not reside on closed streamlines in the moving frame. A more detailed discussion of the various relationships between Lagrangian trajectories and Eulerian measurements in unsteady flow fields is given by Flierl [1981].

Denoting the average displacement speed of a parcel by c_d (equivalent to the speed C_x in Equation (2.1)) and the true translation speed of the disturbance by c_t:

$$c_d = \frac{d}{T_L} \qquad c_t = \frac{\lambda}{T_E} \tag{2.2}$$

where d is the net displacement of the parcel over one Lagrangian period T_L, T_E is the Eulerian period, and λ is the wavelength, or extent, of the disturbance.

The displacement and translation speeds may be related to each other by considering one Lagrangian period in the reference frame moving at the phase speed [Flierl, 1981]. In time T_L there are two possibilities for the parcel in the moving frame: either it resides on a closed streamline resulting in no net displacement, or it resides on an open streamline, in which case it is displaced one wavelength in either direction. The easiest way to see this is that in the reference frame moving at the phase speed the flow is steady, and the parcel can therefore be assumed to only repeat its motion after traversing an integral number of wavelengths, which happens in an integral number of Lagrangian periods. Thus,

$$d = \begin{cases} c_p T_L & \text{closed streamline,} \\ c_p T_L \pm \lambda & \text{open streamline.} \end{cases}$$

which can be manipulated into expressions for the translation speed by substituting $d = c_d T_L$ and $\lambda = c_t T_E$:

$$c_t = \begin{cases} c_d & \text{closed streamline,} \\ c_d T_L / (T_L \pm T_E) & \text{open streamline.} \end{cases} \tag{2.3}$$

so that we need only obtain an independent measure of the Eulerian period T_E to determine the integral relationships between the displacement and translation speeds for drifters residing on open streamlines.

The Eulerian period can be roughly determined using thermistor time series from the 5°N, 140°W TAO mooring (Figure 2.7). The period is estimated from the elapsed time between subsequent minimum temperatures at the 180 m depth thermistor, which lies

within the thermocline, rendering it sensitive to the pressure fluctuations associated with eddies along the SEC-NECC ridge. Minima are chosen since they should encompass the central high pressure associated with a deepening of the thermocline, or local warming. The minima occur near 6 November and 6 December, 1990 (days 310 and 340) giving a 30±5 day period, in good agreement with the typically monthly period oscillations at 5-7°N [McPhaden, 1996].

In summary, we have $T_L = 20$ days, $T_E = 30 \pm 5$ days, and $c_d = -30$ cm/s. From Equation (2.3), then, the only possible open streamline translation speeds capable of producing the observed drifter cycloids are -12 and +60 cm/s (using 25 and 35 days as lower and upper bounds for T_E gives ranges of -11 to -13 and +40 to +120 cm/s, respectively). These values are all much slower to the west or eastward which is inconsistent with the ADCP measurements: -35 to -70 cm/s. Hence, the only possible solution to the problem is that $c_d = c_t$ - the drifters were entrained in a vortex translating to the west at -30 cm/s.

2.2.4 moving reference frame

Based on the relatively regular shape of TIWs as observed from satellite AVHRR and altimeter, as well as in numerical models, it seems likely that the flow field moving with one should be approximately steady. In that case the observations along 140°W could be used to map out the structure of the vortex as it translated through the region by transforming them into the moving frame. This is accomplished by the linear transformation:

$$x' = x - ct, \qquad y' = y, \qquad t' = t \tag{2.4}$$

where c is the translation speed of the disturbance and t is the elapsed time since an arbitrary start. The primes denote variables in the moving frame. All scalar dependent variables are unchanged by the transformation, while from Equation (2.4) it follows that:

$$u' = u - c \quad , \qquad v' = v \tag{2.5}$$

$$\frac{\partial}{\partial t} = \frac{\partial}{\partial t'} - c\frac{\partial}{\partial x'} \quad , \qquad \frac{\partial}{\partial x} = \frac{\partial}{\partial x'} \quad , \qquad \frac{\partial}{\partial y} = \frac{\partial}{\partial y'} \tag{2.6}$$

so that the spatial gradients are unchanged. The material derivative (D/Dt) is also unaltered by definition. Furthermore, if the flow in the translating reference frame is steady, the material derivative becomes equivalent to advection only:

$$\frac{\partial}{\partial t'} = 0 \quad \rightarrow \quad \frac{D}{Dt} = \frac{D'}{Dt'} = \mathbf{u}' \cdot \nabla' \tag{2.7}$$

Consequently, this transformation has the potential to greatly simplify the analysis of data widely separated in space and time in the fixed Earth frame. To the extent that the vortex was steady, or unchanging as it moved through the TIWE-2 region, transformed data may provide a snapshot picture of the vortex.

2.3 Mapping the surface flow

With the propagation speed of the vortex in hand, it is straightforward to transform all of the observed data into the moving reference frame using Equations (2.4) and (2.5). The choice of reference time and longitude for the transformation have been taken to correspond with the passage of the central high pressure of the eddy past the 5°N

TAO mooring (see Figure 2.7) - 25 November (Julian day 329) at 140°W. The resulting transformed velocity field is shown in Figure 2.8. The longitude axis corresponds to the position of the vortex on 25 November.

2.3.1 steady flow field

In the moving frame the drifter loops close on themselves while the ship tracks and mooring positions progress towards the east with time; the SEC appears weaker and the NECC stronger by the amount of the translation speed. The most striking features, however, are that velocities which were observed at varying time and space points in the fixed frame, but are collocated in the moving frame, agree remarkably well north of about 1.5°N. In other words, parcel trajectories and streamlines are identical in the moving frame and the flow is relatively steady.

Collocated vectors from the various moorings near the equator are in complete disagreement, indicating that velocity fluctuations there translated at a different speed than the vortex to the north. From Figure 2.9a, during the same observation time, the fluctuation period at the equator was about 17-20 days. The translation speed of this event was determined by examining the lag between events at the three moorings on the equator, yielding about -80 cm/s, more than twice as fast as the vortex to the north. Consequently, the transformation into the -30 cm/s moving frame is only valid over a limited region, presumably associated with the extent of the vortex. From Figure 2.8 the southern extent of the eddy is approximately 1.5°N.

Meanwhile, when the mooring data are transformed into a reference frame moving at -80 cm/s, the three moorings on the equator agree well (Figure 2.9b). Perhaps more interesting is the lack of any clearly defined vortex pattern - the disturbance looks like a meandering of the SEC, an observation which agrees with some previous descriptions of

the perturbations to the SEC and EUC in the Pacific and Atlantic [Düing *et al.*, 1975; Halpern *et al.*, 1988].

2.3.2 objective mapping

In anticipation of subsequent analyses of the flow field we proceed to objectively map the transformed data onto a regular grid which will facilitate calculations of gradients and dynamical quantities. The observed velocity data, an array of values $\tilde{\mathbf{u}}^l = [\tilde{u}^l, \tilde{v}^l]$ with positions in the moving frame $\underset{\sim}{\tilde{x}}^l = [\tilde{x}^l, \tilde{y}^l]$, are to be mapped onto a regular grid with a spacing of 1/4° (corresponding to (111.11 km)/4 in the meridional and cos(latitude)*(111.11 km)/4 in the zonal directions). The scheme chosen is a median filter of radius 75 km centered on each grid point:

$$u^{i,j} = med\left[\tilde{u}^l\right] \qquad \text{and} \qquad v^{i,j} = med\left[\tilde{v}^l\right]$$

$$\forall\ l\ \in\ \sqrt{(\tilde{x}^l - x^{i,j})^2 + (\tilde{y}^l - y^{i,j})^2}\ \leq\ 75\ km \tag{2.8}$$

where the indices i and j denote discrete latitudes (rows) and longitudes (columns) of the grid, respectively. A median filter was chosen because of its insensitivity to outliers while preserving sharp gradients.

Before blindly gridding the data, however, we ensure that the relative weighting of the various data types is unbiased. The drifter data are provided at 3 hour intervals, the ADCP at 5 minutes, the PMEL moorings at once per day, and the PCM at 4 hours. Meanwhile the average speed of the ship is approximately 10 knots, the drifters move at about 20-60 cm/s and the speed of the moorings in the moving frame is 30 cm/s. From these values the horizontal resolution of each data type can be estimated; the results are

Table 2.1: Data resolution in the moving frame

data type:	ADCP	drifters	PMEL	PCM
original sampling interval:	5 min.	3 hr.	1 day	4 hr.
effective sensor speed:	10 kts.	20-60 cm/s	30 cm/s	30 cm/s
moving frame resolution:	1.5 km	2-6.5 km	26 km	4.3 km
desired resolution:	4.5 km	2-6.5 km	4 km	4.3 km
final sampling interval:	15 min.	3 hr.	4 hr.	4 hr.

summarized in Table 2.3.2. The spacing of the drifter fixes and PCM mooring values are comparable at 4-5 km, while the ADCP is much less (1.5 km) and the PMEL moorings much coarser (26 km).

Consequently, the ADCP data were decimated by 1/3 to 15 minutes and the PMEL mooring data interpolated onto the same time grid as the PCM moorings. The final data spacing in the moving frame is shown in Figure 2.10 (decimated by 1/3 to allow visibility). (When gridding hydrographic data in the next chapter, the daily mooring data were used when combined with the CTD stations).

The data were subsequently mapped onto a grid using Equation (2.8). The results are shown in Figure 2.11, superimposed on an AVHRR SST image from 16 November (see Figure 1.1). The AVHRR image has been heavily smeared to eliminate clouds, but the equatorial front is evident with the cusp-like pattern typical of instability waves. The velocity map reveals an anticyclonic vortex with speeds approaching 1 m/s. Meanwhile,

comparison with the SST image indicates that the cold water cusp is related to the northward flow along the leading edge of the eddy. Although the AVHRR image is a true snapshot, in contrast to the smoothed picture of the gridded velocity, the association of the cold cusp with the vortex is apparent.

In the northeastern region of the map northward flow is visible, mainly sampled by a single drifter (see Figure 2.8) but also measured by the last ADCP track. This may indicate the presence of the next vortex in the instability train.

2.3.3 error analysis

In subsequent chapters structure, dynamics, and energetics of the vortex will be analyzed using the velocity and thermohaline fields gridded into three dimensional maps. Hence, it will be important to have reliable estimates of the errors of all quantities. To this end, the determination of standard errors is now discussed.

The error in the gridded fields is directly related to the variance of collocated data in the moving frame, since ideally, a perfectly sampled steady vortex would yield exact agreement among collocated data points. Additionally, the error at a grid point depends on the degrees of freedom (DOF) entering into the estimate for that point. To estimate the DOF, the decorrelation time scale of each data type (ADCP, drifting buoys, and moorings) was determined for each variable (zonal and meridional velocity, and temperature) from the first zero crossing of the relevant autocorrelation functions (Figure 2.12).

Based on the time scales from Figure 2.12, each data record was divided into segments with length equal to their respective decorrelation time scales. The unique number of records entering each grid point calculation was then taken as the DOF. As our estimate of the standard error we take the square root of the variance divided by the

DOF, which is like a standard error of the mean, each independent measurement giving a different estimate of the grid point value. Thus, standard errors and covariances for the velocity at each grid point were calculated according to the formulas:

$$(\sigma_u^{i,j})^2 = \frac{\sum(\tilde{u}^l - u^{i,j})^2}{DOF(N-1)} \quad , \quad (\sigma_v^{i,j})^2 = \frac{\sum(\tilde{v}^l - v^{i,j})^2}{DOF(N-1)}$$

$$(\sigma_{uv}^{i,j})^2 = \frac{\sum(\tilde{u}^l - u^{i,j})(\tilde{v}^l - v^{i,j})}{DOF(N-1)}$$

$$\forall\ l\ \in\ \sqrt{(\tilde{x}^l - x^{i,j})^2 + (\tilde{y}^l - y^{i,j})^2}\ \leq\ 75\ km \tag{2.9}$$

Standard error ellipses obtained in this way for the velocity field are depicted in Figure 2.13. A circle would indicate that the error is isotropic while the semi-major axis of an ellipse gives the direction in which the error is largest. Most of the eddy flow field is known to nearly ±5 cm/s. However, there are isolated regions of larger uncertainty near 138°W and especially north of 5°N. These larger errors probably result from temporal changes in the flow field which were not resolved by enough independent measures (compare with Figure 2.8). Nevertheless, the vortex flow field was steady to lowest order - errors of less than 5 cm/s over much of the region indicate that deviations from steady flow were less than 10%.

Since many of the analyses to follow involve the depth dependence of the flow and consequently rely solely on the ADCP data, the gridded surface velocity and standard error ellipses for that case are shown in Figure 2.14. The flow at the front is now known with much less precision. Comparison with Figure 2.8 reveals that the drifters passing through the front helped to minimize the error which is now large because of the sparseness of ship sampling.

2.3.4 extent of the moving frame

The relative success of the mapping can be determined by calculating the rms error over the vortex, which should be a minimum in the reference frame which moves with the vortex. In other moving frames the flow is not steady, and the mapping error should be larger.

Translation speeds ranging from 0 to -1 m/s were used to transform the velocity data and obtain gridded fields. For each of these cases, the rms error was calculated as a function of latitude, with the results depicted as a map of the rms error as a function of translation speed and latitude in Figure 2.15. The region north of 1.5°N is a minimum for speeds between -40 to -20 cm/s, while to the south the minimum is centered near -70 to -80 cm.s. The separation between kinematics at the equator and the SEC-NECC shear region is quite distinct, with no indication of a gradual change. The vortex moved at 30 cm/s to the west, while the disturbance on the equator moved at -80 cm/s.

It remains to explore how deep the propagation speed for the vortex holds. For an anticyclonic eddy viewed in its steady reference frame, we can expect that there will be a negative correlation between meridional velocity and longitude: northward velocity occurs along the western side, gradually decreasing toward the center and becoming southward to the east. The correlation should be best for the correct moving frame. Figure 2.16a (solid line) shows the correlation between meridional velocity and longitude as a function of translation speed calculated using only the 8 drifters which looped. The best correlation, near -25 cm/s, is not necessarily at the correct speed because the relationship between velocity and longitude is only approximately linear.

Unfortunately, the sampling of the other drifters and the shipboard ADCP is such that it is difficult to distinguish between correlations for varying speeds. This occurs

because in moving reference frames the ship tracks do not overlap - the data become increasingly spread out in the moving frame as the translation speed becomes more negative. Subsequently, the correlation curves for these data (Figure 2.16a) asymptote at large negative translation speeds.

Nevertheless, the correlation between meridional velocity and longitude is consistently negative for the vortex, so that this relationship can be investigated as a function of depth. Figure 2.16b shows results for data above the thermocline (approximately 120 m at the shallowest - see Chapter 3), where the correlation is significantly negative for translation speeds below -10 cm/s, and for data below the thermocline, where it is significantly positive.

We conclude that below the thermocline the moving reference frame cannot be applied with confidence. While kinematics below the thermocline could be in phase with the vortex, there is no evidence here to support the idea. In Chapter 3 it will be seen that the velocity field throughout the upper layer is remarkably coherent with depth. Furthermore, the relatively sharp and shallow tropical thermocline, in comparison to midlatitudes, would suggest that the primary dynamics be trapped to the upper layer.

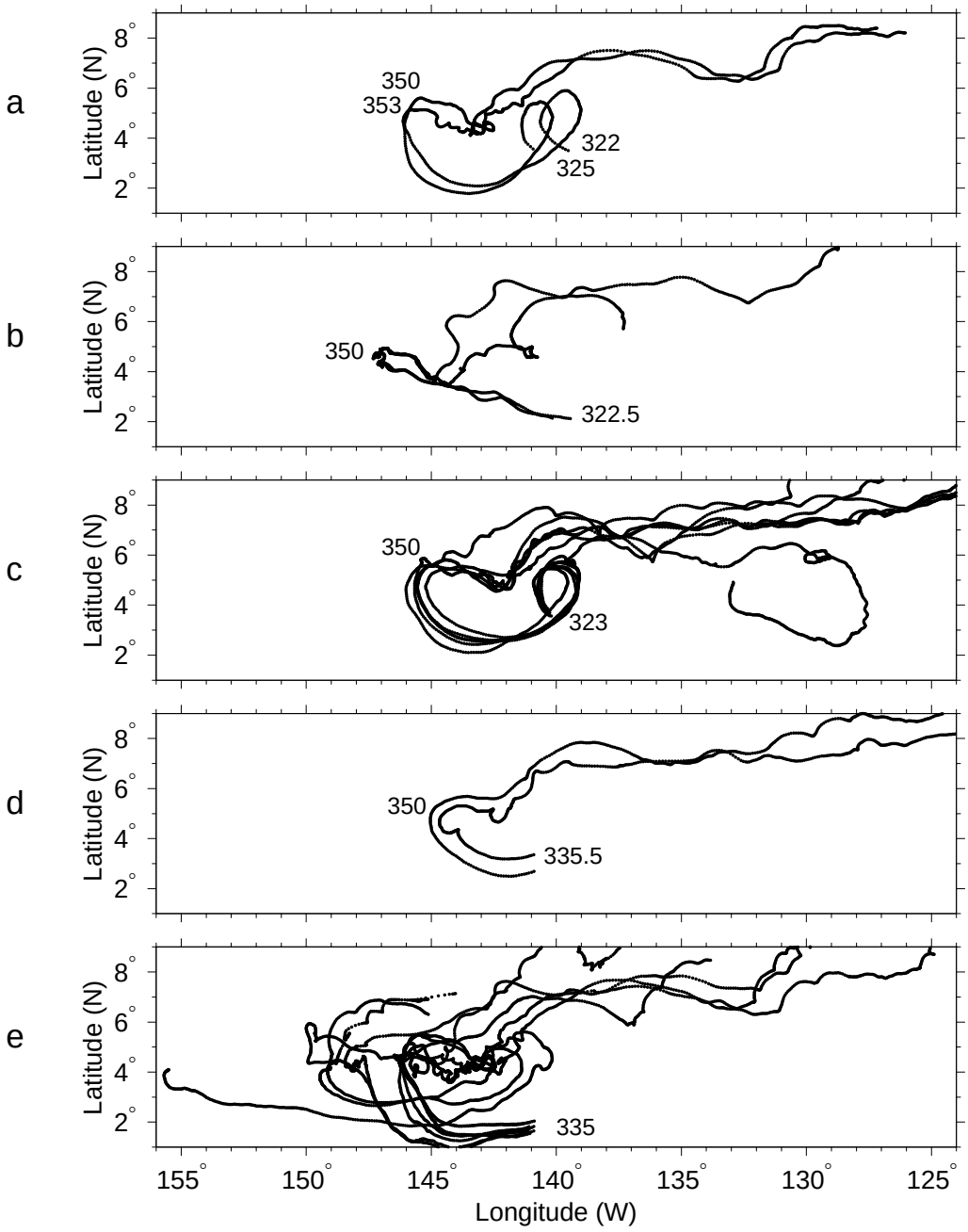

Figure 2.1: Fifteen of the 25 drifter tracks from TIWE-2, grouped by deployment dates and similar patterns. Deployment dates and days that cycloidal motion ceased are marked by Julian day (323 = 19 November 1990).

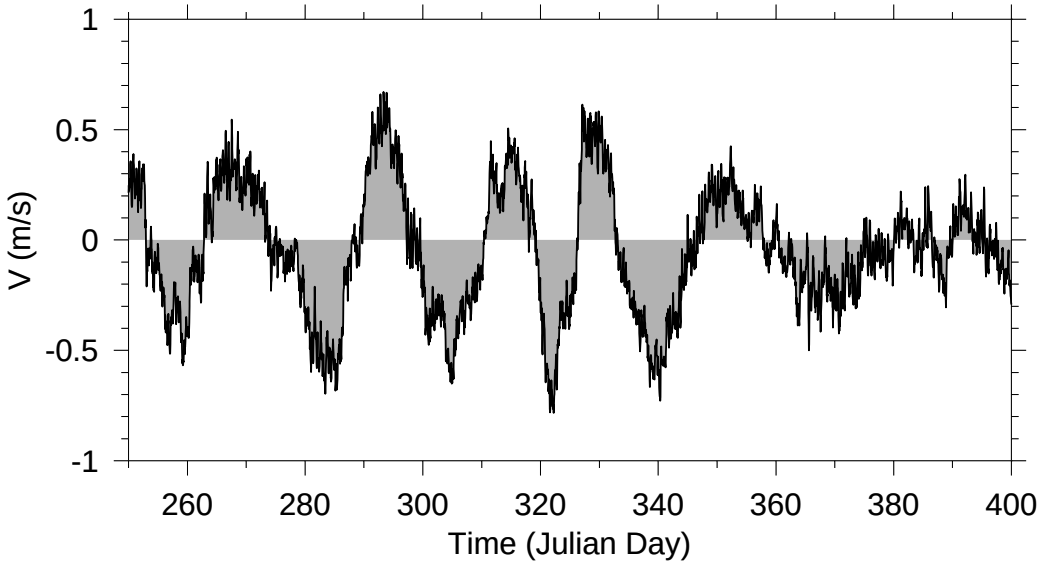

Figure 2.2: Meridional velocity component at 140°W on the equator, between 7 September 1990 - 4 February 1991.

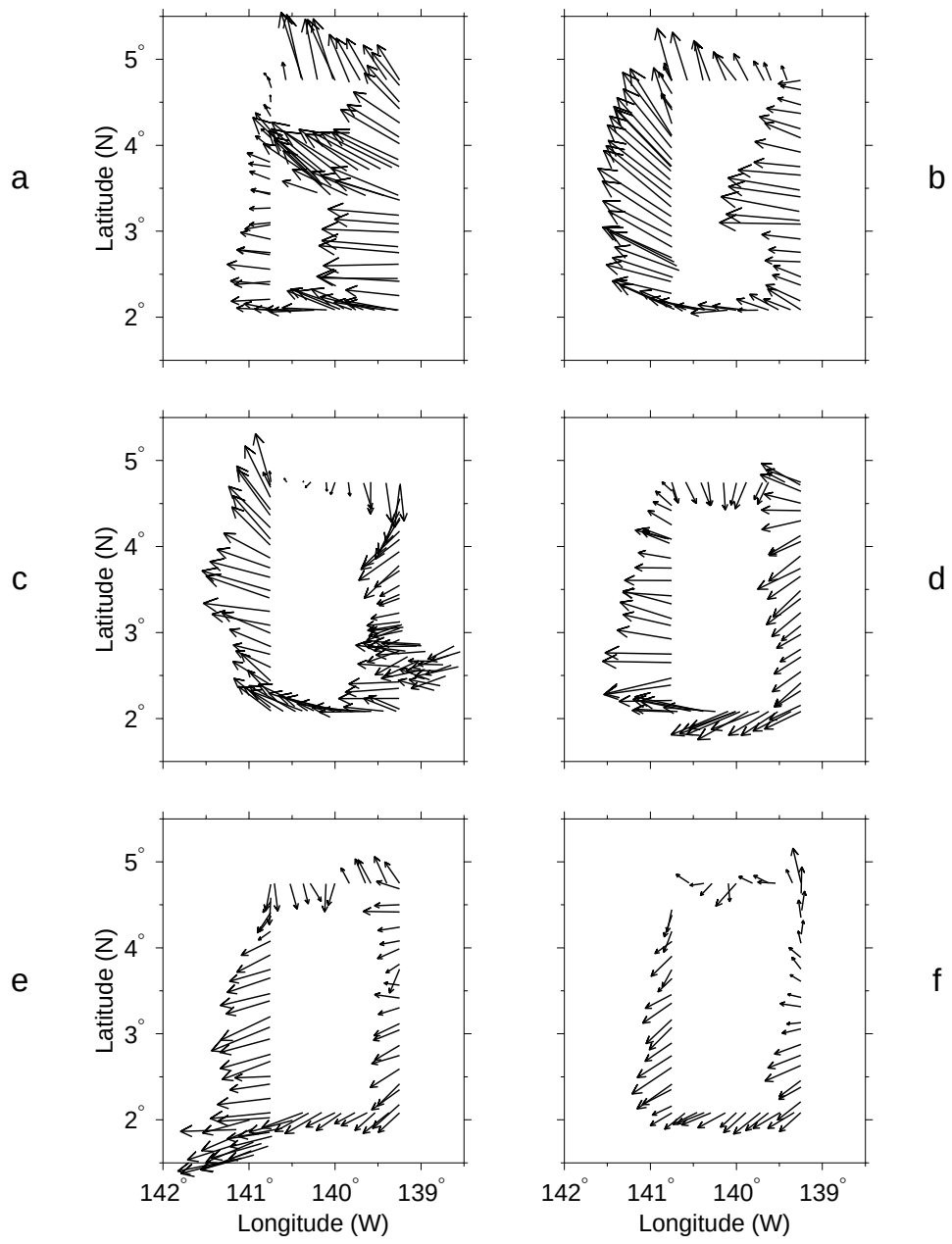

Figure 2.3: Velocity at 22 dbar measured by shipboard ADCP (a) 16-20 Nov, (b) 20-23 Nov, (c) 23-27 Nov, (d) 27-30 Nov, (e) 30 Nov - 3 Dec, and (f) 3-6 Dec 1990. Each survey of the rectangular area proceeds counter clockwise from the top left.

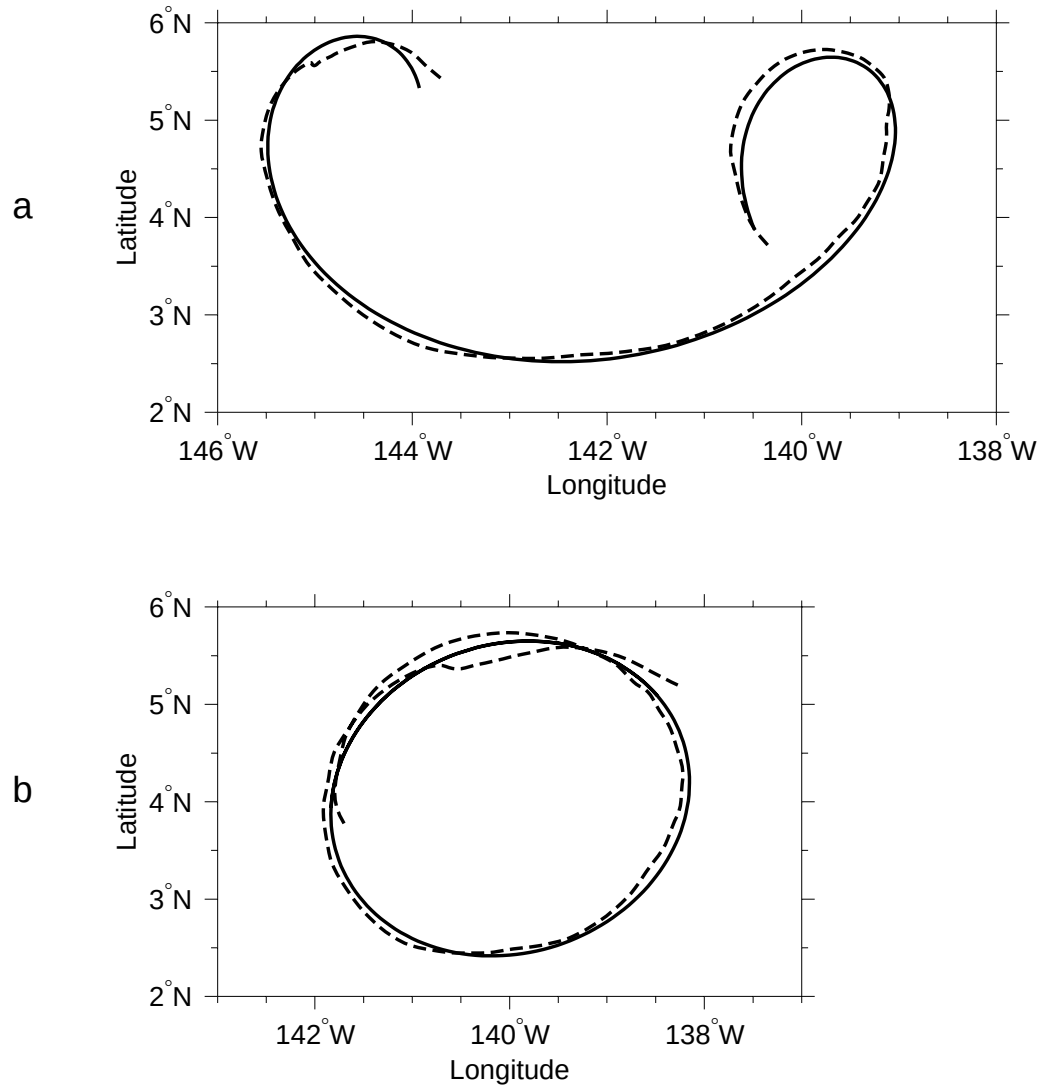

Figure 2.4: Linear regression fit (solid line) of a constant translation speed and harmonic to the trajectory of a drifter (dashed line), (a) in fixed Earth frame and (b) translating reference frame.

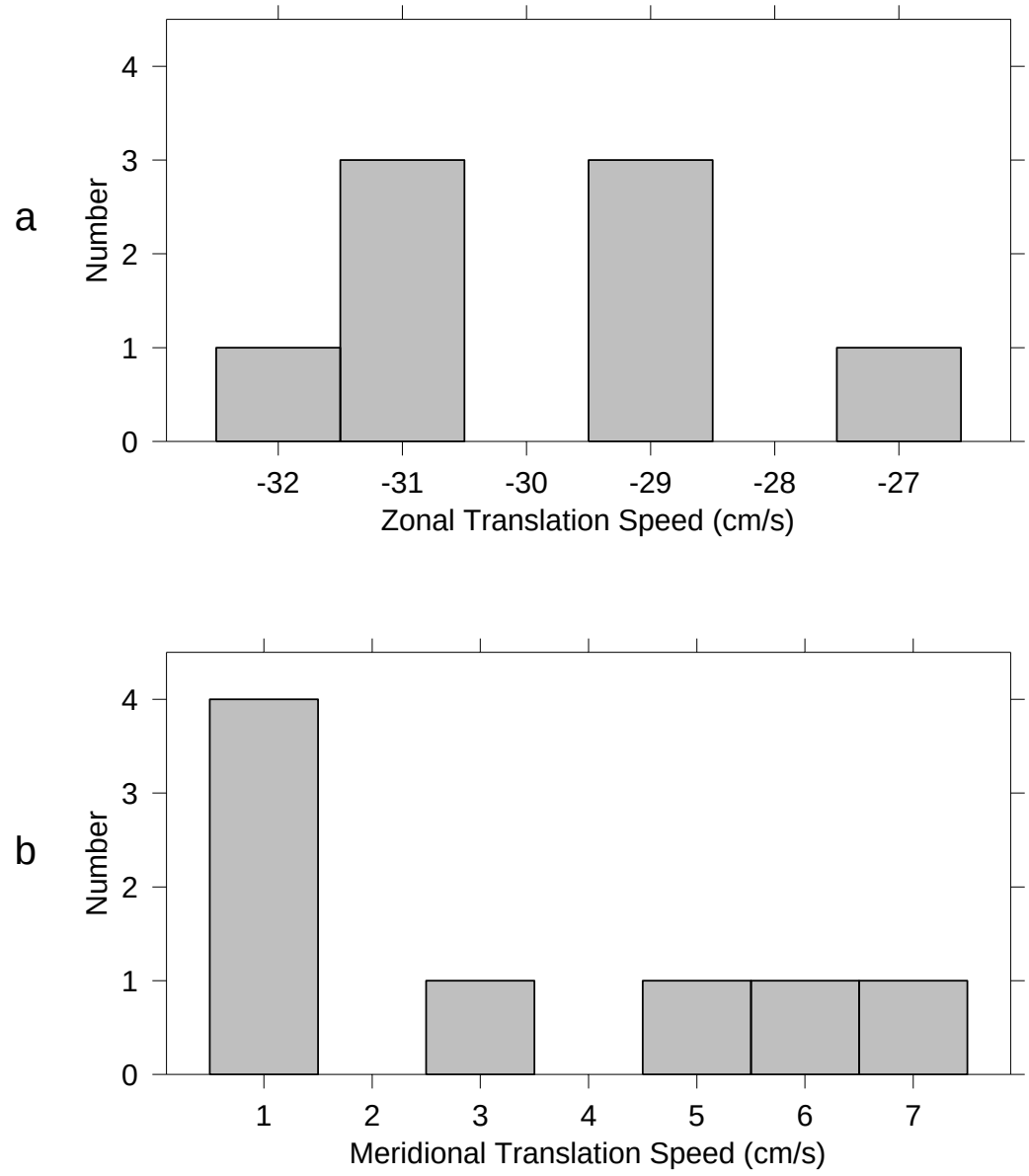

Figure 2.5: Histograms of (a) zonal and (b) meridional translation speeds from linear regression fits to the eight looping drifters.

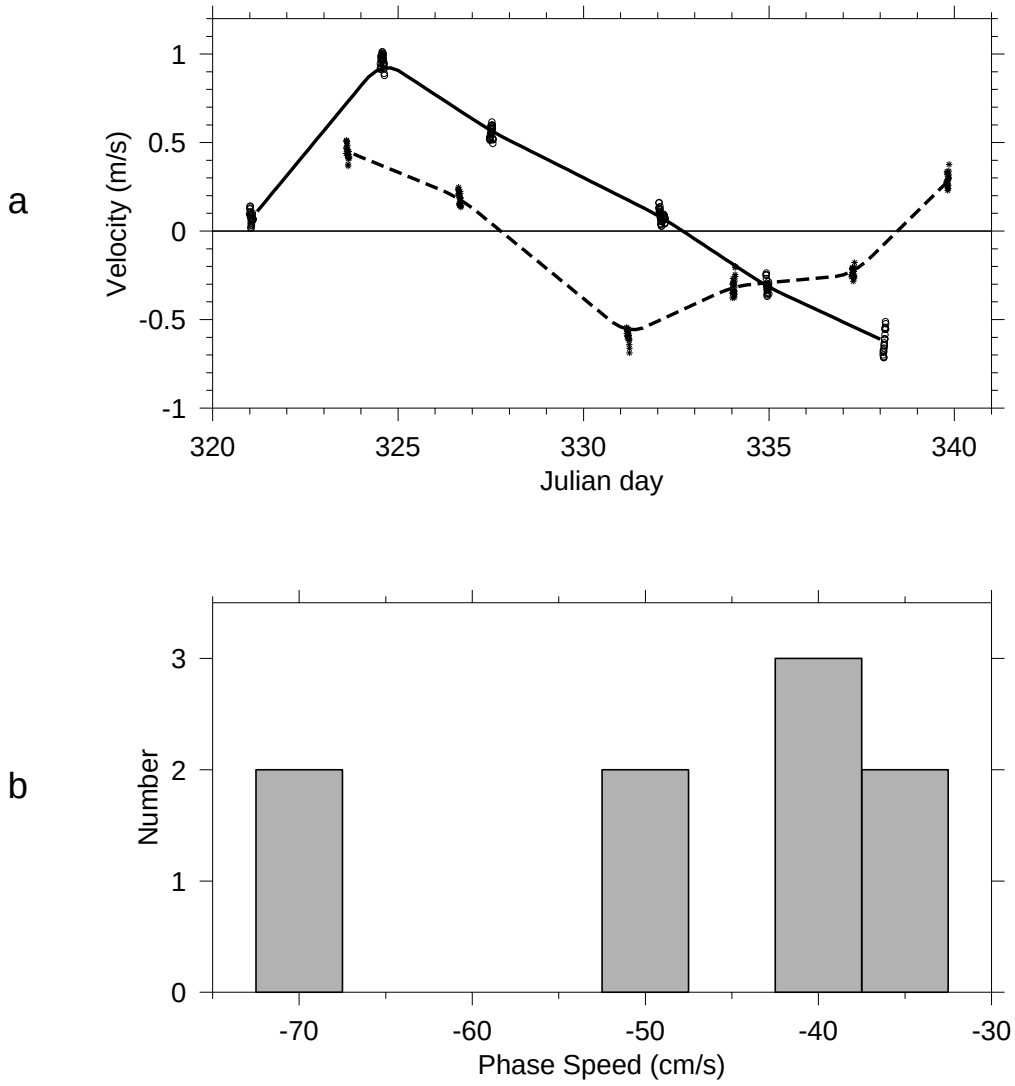

Figure 2.6: (a) ADCP measurements of meridional velocity from 4-4.25°N at 140.75°W (solid line) and 139.25°W (dashed) as time series. (b) A histogram of phase speeds determined from the lags between the time series of v at 140.75°W and 139.25°W (for 11 latitude bands as in (a)).

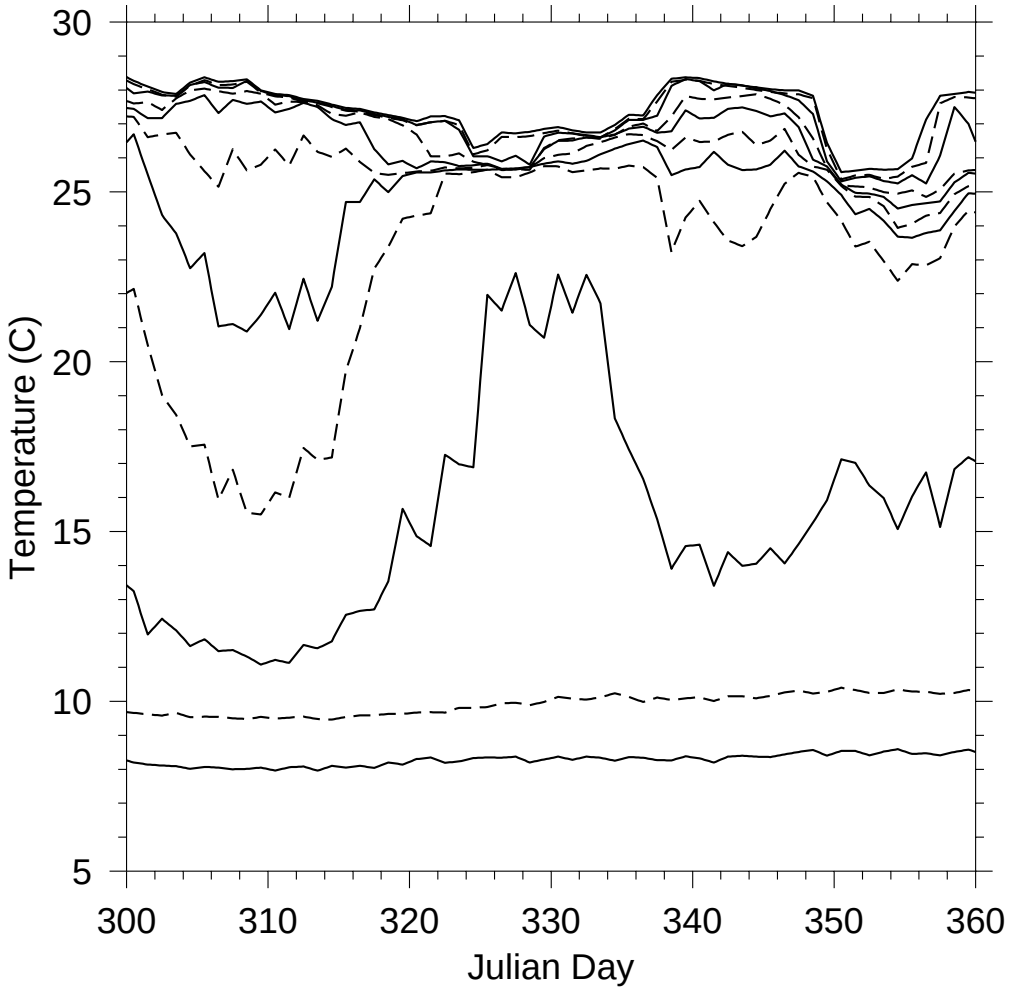

Figure 2.7: Temperature time series during TIWE-2 as measured by thermistor chains on the TAO mooring at 5°N,140°W. Thermistors at 0, 40, 80, 120, 180, and 500 m are solid lines, those at 20, 60, 100, 140, and 300 m are dashed.

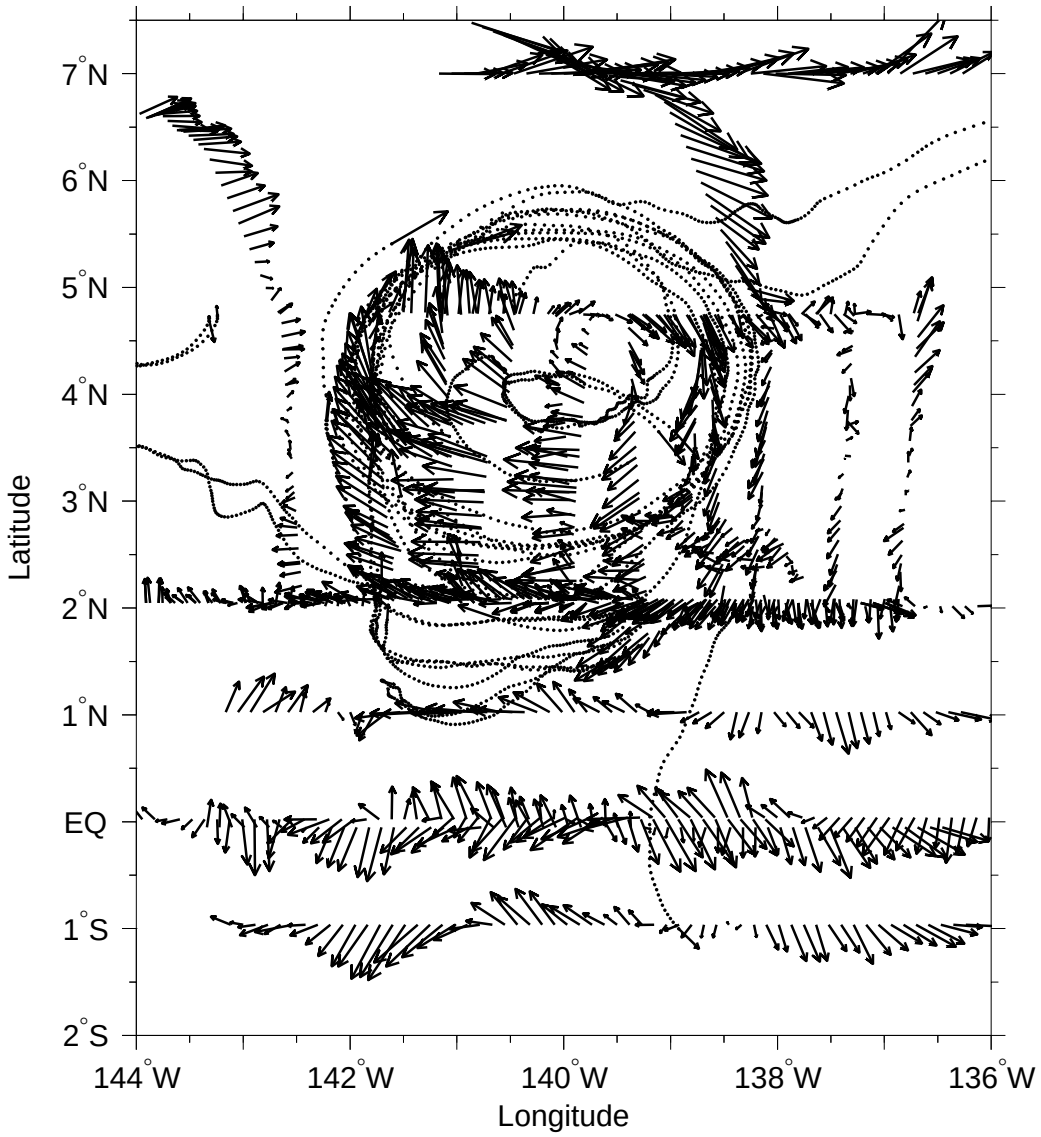

Figure 2.8: Velocity data from shipboard ADCP, drifters, and moored current meters viewed in a reference frame translating with the vortex: westward at 30 cm/s. Longitude corresponds to the position of the features on 25 November 00:00 GMT.

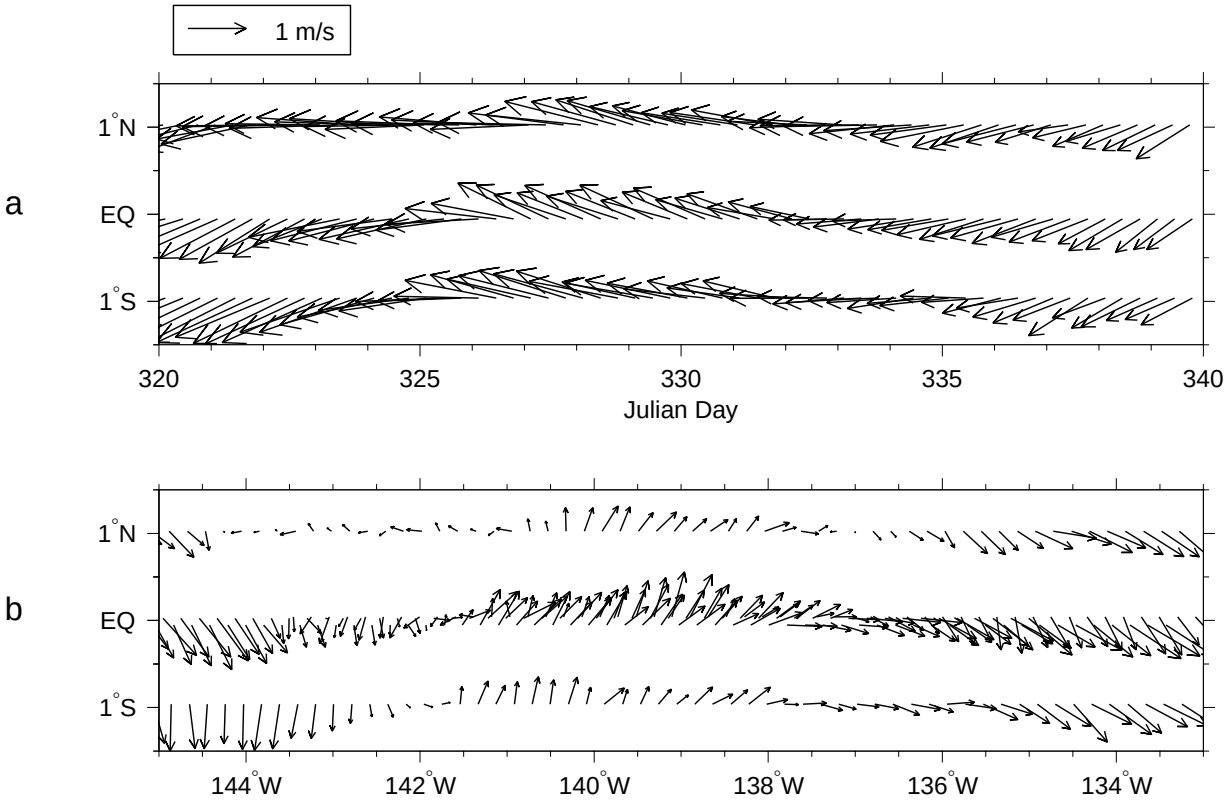

Figure 2.9: Velocity from the equatorial mooring array during 16 November - 6 December: (a) the 3
as a function of time (4 hr. intervals) and (b) all 5 moorings in a reference frame moving at -80
Longitude corresponds to the position of the features on 25 November 00:00 GMT.

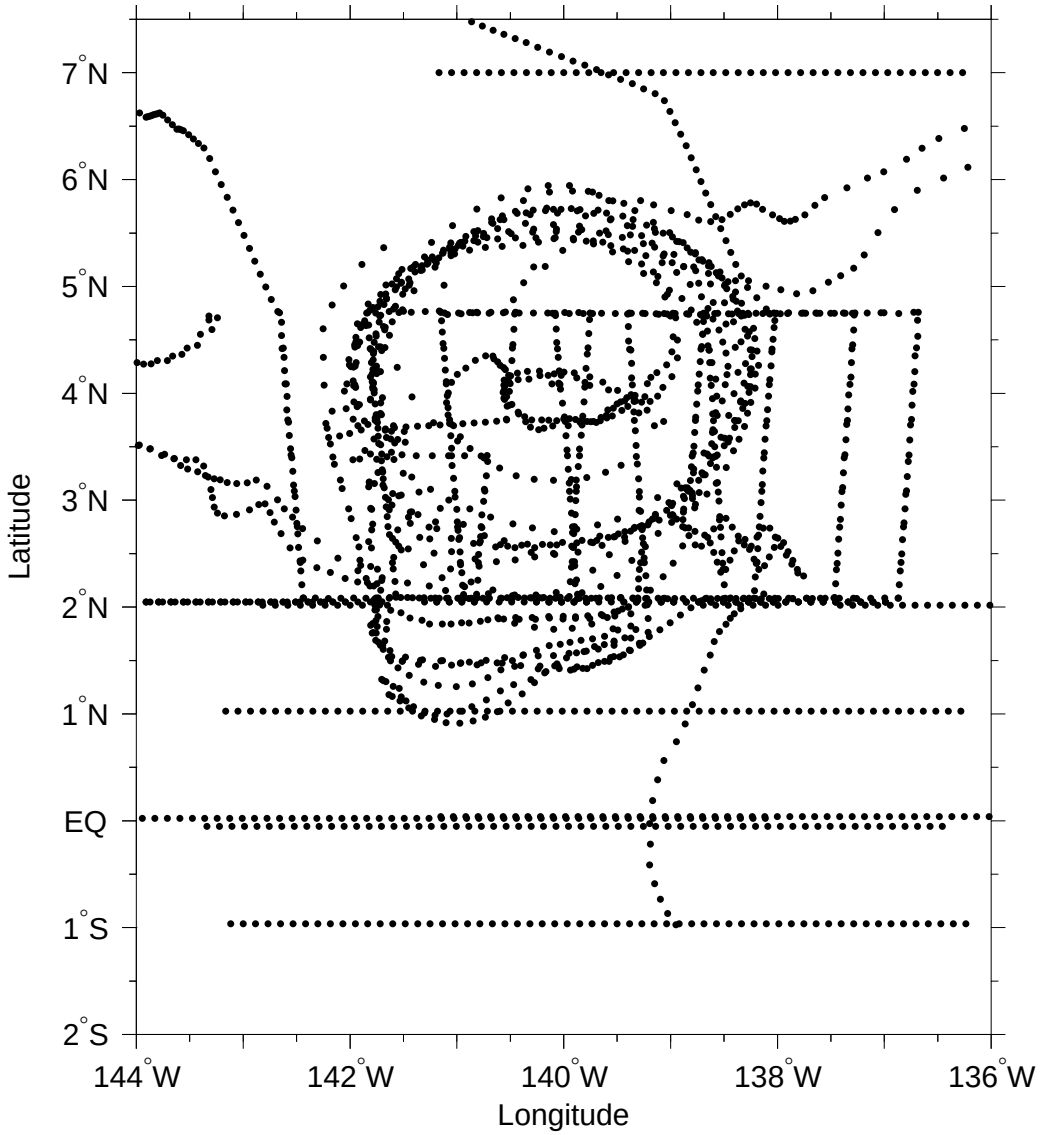

Figure 2.10: The relative spacing of velocity data in the moving reference frame. Each data type is plotted at 1/3 of its resolution to be used in objective mapping (see Table 2.3.2).

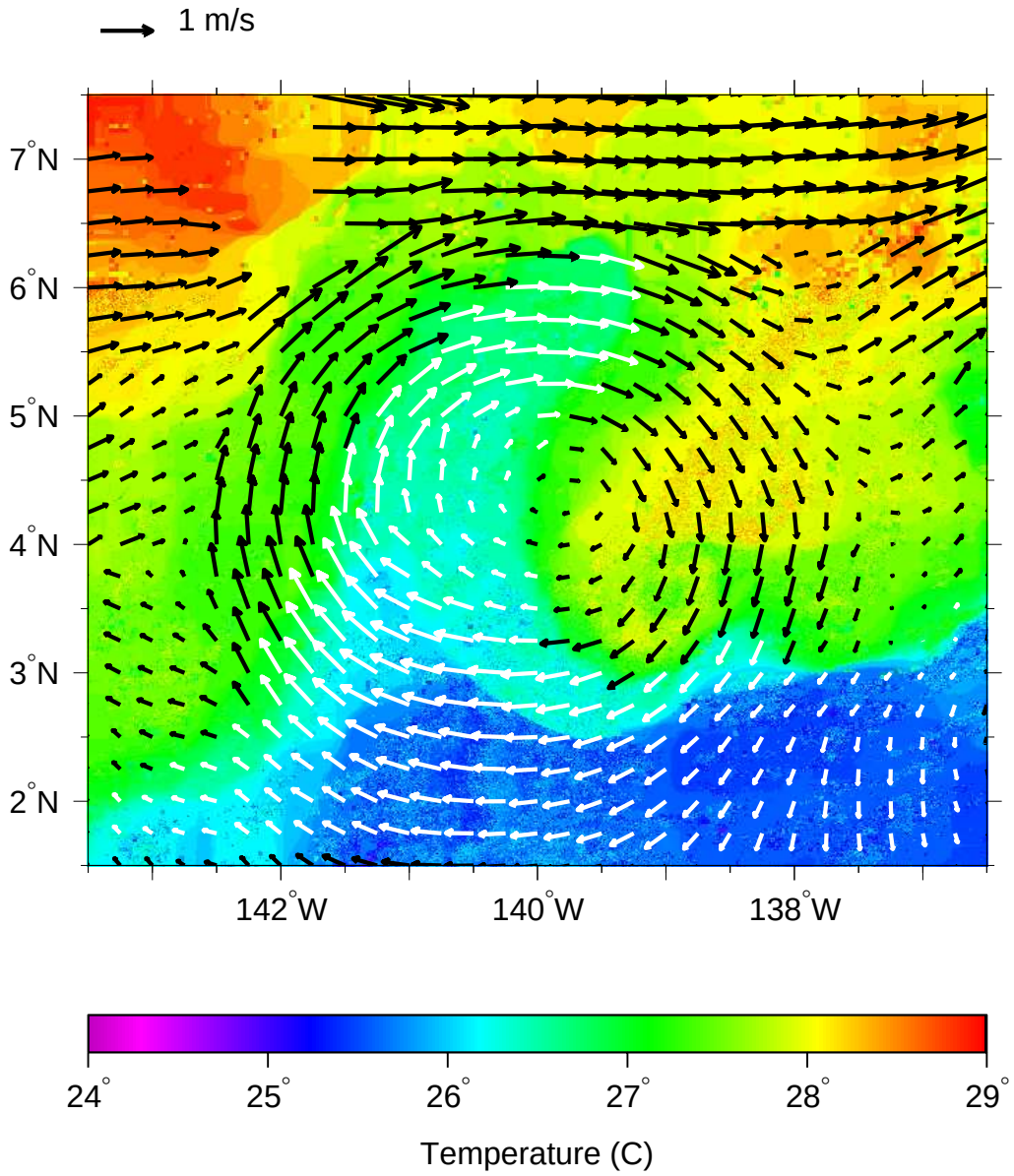

Figure 2.11: Velocity in the moving reference frame gridded to 1/4° resolution. Velocity vectors are superposed on AVHRR SST image from 16 November 1990 (see Figure 1.1).

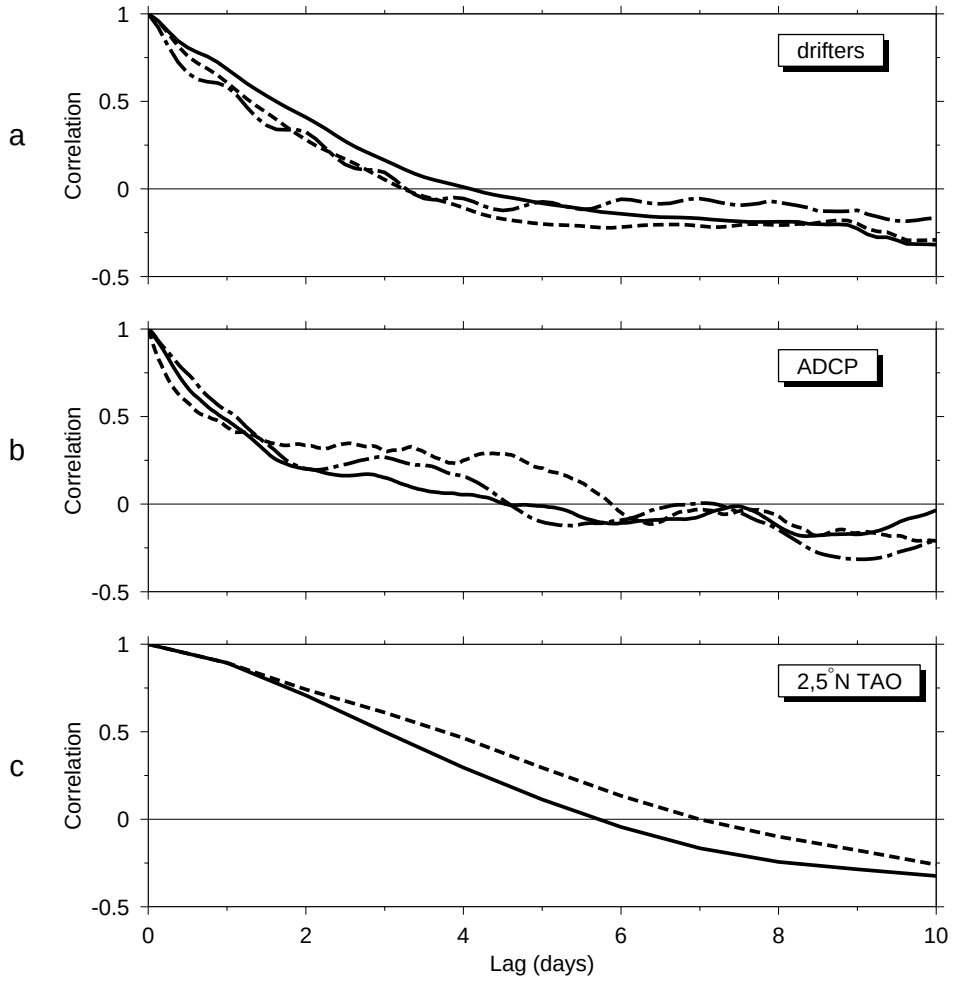

Figure 2.12: Autocorrelation functions for: zonal velocity (solid lines), meridional velocity (dashed), and temperature (dash-dotted) for (a) drifting buoys and (b) shipboard ADCP. (d) Temperature autorcorrelation functions for the 2°N (solid) and 5°N (dashed) moorings. Decorrelation time scales are taken to be the lags at which the autocorrelation becomes negative.

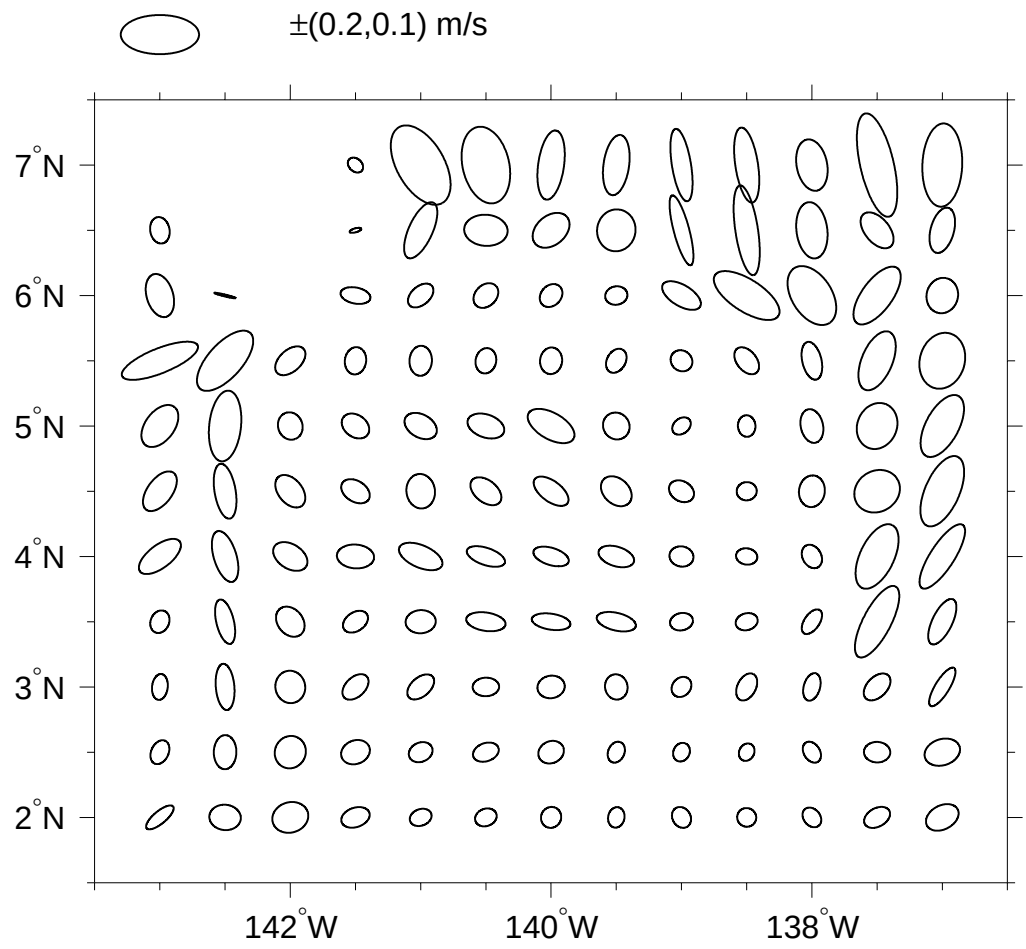

Figure 2.13: Standard error ellipses for the surface velocity map (Figure 2.11).

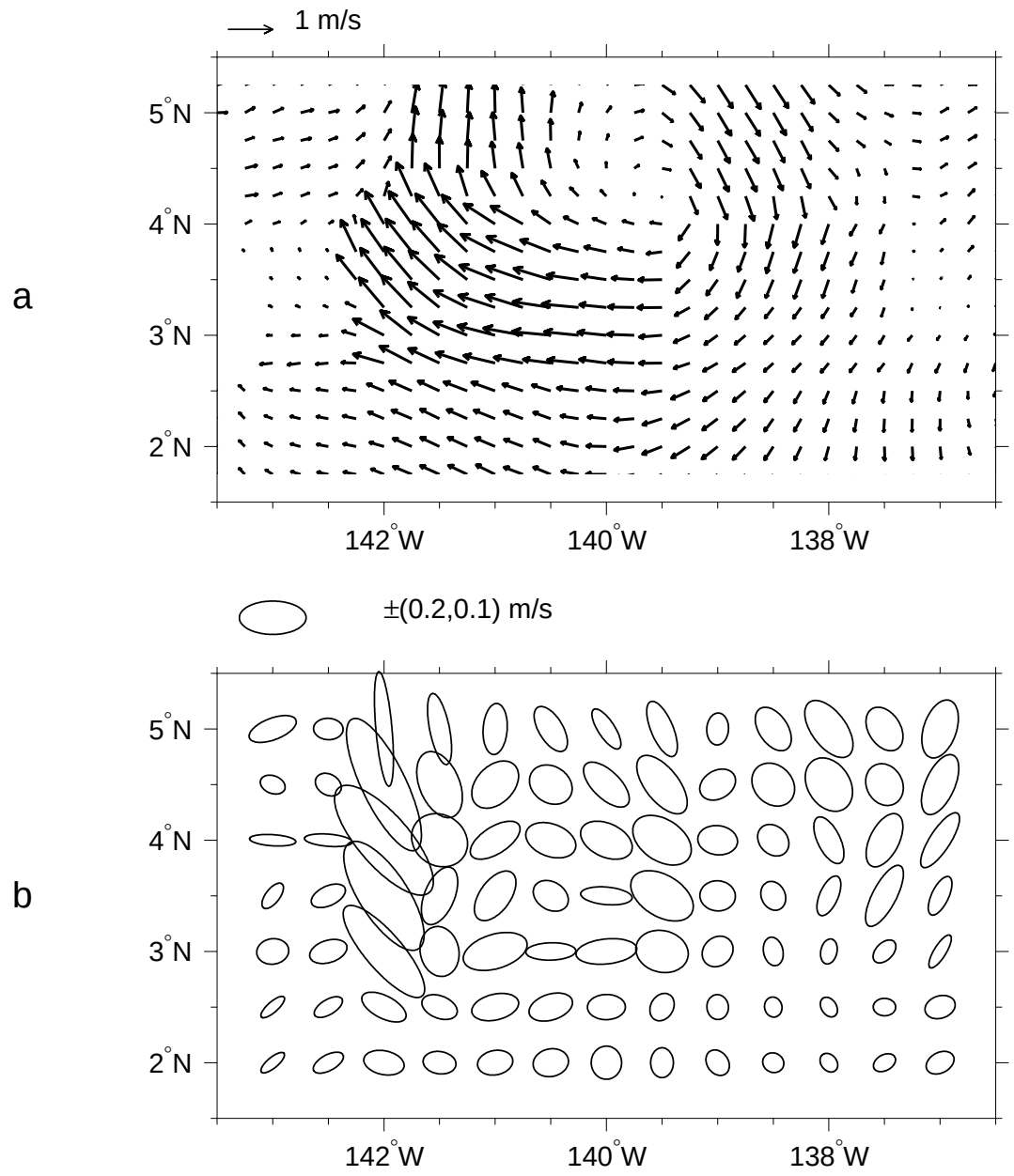

Figure 2.14: (a) Gridded velocity and (b) standard error ellipses for ADCP data between 20-25 m depth.

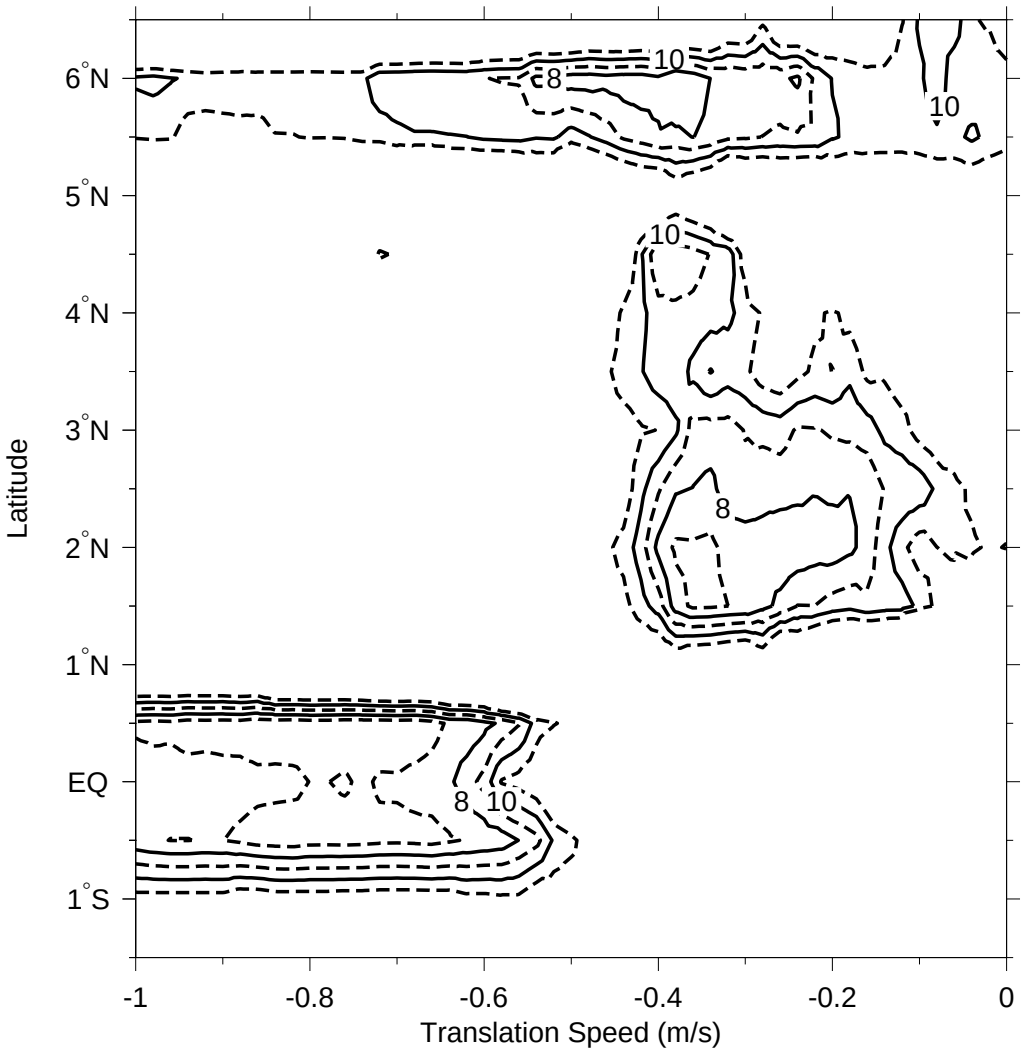

Figure 2.15: The rms error in gridded speed (cm/s) contoured as a function of latitude and longitude. Values greater than 11 cm/s are not contoured. Contour interval is 2 cm/s (solid) with dashed contours indicating 1 cm/s steps.

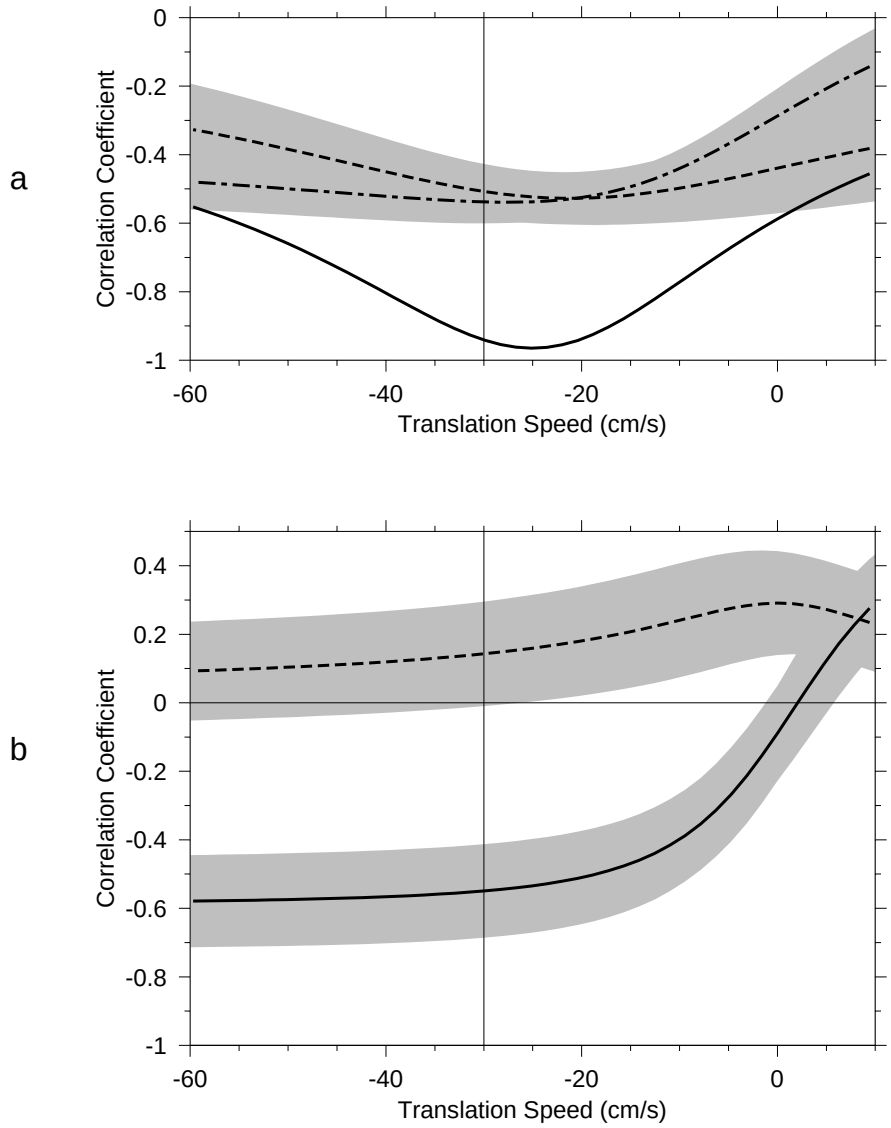

Figure 2.16: The correlation between meridional velocity and longitude as a function of phase speed for (a) looping drifters (solid line), all drifters (dashed), all drifters and ADCP (dash-dotted), and (b) ADCP data above (solid) and below (dashed) the thermocline. Shading indicates confidence intervals of one standard error from bootstrapping.

Chapter 3

The Structure of a Tropical Instability

In which the three-dimensional kinematic and thermohaline structure of a tropical instability is described.

3.1 Convergence and vorticity

Previous observations of the north equatorial front have found that intensified downwelling is associated with the passage of tropical instabilities [Sawyer, 1996; Johnson, 1996], and it has been suggested that this may be responsible for enhanced concentrations of biomass along the front [Yoder *et al.*, 1994]. Let us proceed to analyze the divergence field during TIWE-2.

3.1.1 gridded fields

With the velocity data in the form of a steady, gridded flow field (Figure 2.11), estimation of the horizontal divergence is straightforward. Central differencing is used over the interior:

$$\nabla \cdot \mathbf{u} = \frac{\partial u}{\partial x} + \frac{\partial v}{\partial y} \quad \rightarrow \quad (\nabla \cdot \mathbf{u})^{i,j} = \frac{u^{i,j+1} - u^{i,j-1}}{2\Delta x} + \frac{v^{i+1,j} - v^{i-1,j}}{2\Delta y} \tag{3.1}$$

where the notation follows that introduced in Chapter 2 Section 2.3. $\Delta\, x$ and $\Delta\, y$ are the grid resolutions in the zonal and meridional ($1/4^{\circ}$). To handle the boundaries, first differences are employed:

$$\frac{\partial u}{\partial x}^{i,1} = \frac{u^{i,2} - u^{i,1}}{\Delta x} \quad , \qquad \frac{\partial u}{\partial x}^{i,n} = \frac{u^{i,n} - u^{i,n-1}}{\Delta x}$$

$$\frac{\partial v}{\partial y}^{1,j} = \frac{v^{2,j} - v^{1,j}}{\Delta y} \quad , \qquad \frac{\partial v}{\partial y}^{m,j} = \frac{v^{m,j} - v^{m-1,j}}{\Delta y} \tag{3.2}$$

where m and n indicate the northernmost and easternmost grid points respectively (the number of rows/latitudes and columns/longitudes).

Errors are subsequently estimated using Monte Carlo trial calculations of these finite difference equations: each trial velocity component is sampled from a random distribution, $p(U_q^{i,j})$ and $p(V_q^{i,j})$, where $U_q^{i,j}$ and $V_q^{i,j}$ are Gaussian distributed random variables over the space ranged by q with means given by the grid point estimates ($u^{i,j}$ and $v^{i,j}$]) and standard deviations equivalent to the local standard errors ($\sigma_u^{i,j}$ and $\sigma_v^{i,j}$); ie:

$$p(U_q^{i,j}) = (u^{i,j}\sqrt{2\pi})^{-1} exp\left[-\frac{(U_q^{i,j} - u^{i,j})^2}{2(\sigma_u^{i,j})^2}\right]$$

$$p(V_q^{i,j}) = (v^{i,j}\sqrt{2\pi})^{-1} exp\left[-\frac{(V_q^{i,j} - v^{i,j})^2}{2(\sigma_v^{i,j})^2}\right] \tag{3.3}$$

The standard error of the divergence is then estimated by the standard deviation of the M=1000 Monte Carlo trials:

$$\sigma_{\nabla\cdot\mathbf{u}}^{i,j} = \left(\frac{1}{M-1}\sum_{r=1}^{M}\left[(\nabla\cdot\mathbf{u})_q^{i,j} - \left\langle(\nabla\cdot\mathbf{u})^{i,j}\right\rangle\right]^2\right)^{\frac{1}{2}} \tag{3.4}$$

where

$$\left\langle(\nabla\cdot\mathbf{u})^{i,j}\right\rangle = \frac{1}{M}\sum_{r=1}^{M}(\nabla\cdot\mathbf{u})_q^{i,j} \tag{3.5}$$

Standard propagation of errors formulae give similar results, but in anticipation of the complicated quantities to be calculated in later chapters, we opt for the brute force Monte Carlo approach. These methods are used throughout this study for all calculations based on the basic measured quantities and their standard errors.

Figure 3.1a shows the derived divergence field as contours with shaded regions highlighting values significantly different from zero (based on the Monte Carlo derived standard errors). Convergence above $2.5 \times\ 10^{-6}\ s^{-1}$ appears north of 3.5°N along 142°W. To the east is a stronger region of divergence ($> 5 \times\ 10^{-6}\ s^{-1}$). The remaining, uncontoured field is generally divergent, although not significantly different from zero. Clearly, convergence at the front is intensified along its length which is deformed by the passage of the vortex.

In comparison, when the divergence field is estimated using only gridded ADCP data, the convergence is much stronger, reaching 10^{-5} s^{-1} (approximately the local inertial frequency f), and is more concentrated at 4°N, while the divergence remains relatively unchanged (Figure 3.1b). In each case, the strong convergence and divergence are significant above one standard error from zero; the core of convergence in Figure 3.1b is nearly 3 standard errors from zero.

The difference between the fields obtained with and without drifting buoy data is notable. The imperfect Lagrangian nature of the drifters may be the source of inconsistency between the two maps. As drifting buoys must remain at a fixed depth, upon entering a convergent region, they tend to align along a streamline, so that they quickly become equivalent to only one independent measure. Indeed this happened with the cluster of drifters deployed in the cold water cusp during TIWE-2 (see Figure 2.1c). Divergence tends to keep drifters out of such regions. Consequently, in the absence of

statistically large numbers of independently seeded buoys, drifters will generally undersample and likewise underestimate convergence and divergence.

Figure 3.1 clearly shows stronger convergence when the drifters are not included in the velocity map, while the divergence near the center of the vortex is unchanged because the drifters did not sample the region. Another explanation for the larger convergence when estimated using only ADCP could be the lack of repeated ship sampling in the moving reference frame - temporal gradients will be mapped into spatial ones under the assumption of a steady flow. On the other hand, the estimated convergence is well above one standard error, which should quell fears that the ADCP results are spurious.

The relative vorticity field was also calculated using central differencing and Monte Carlo trials to estimate the error field (Figure 3.2). The vorticity was negative over much of the vortex with a ridge of cyclonic vorticity greater than 5×10^{-6} s^{-1} along 142°W. The anticyclonic vorticity reached the inertial frequency ($f = 10^{-5}$ s^{-1}) at 4°N, 141°W and 139.5°W.

3.1.2 direct measurements

The increase in vorticity and convergence across the front was also measured directly during TIWE-2. A cluster of 7 buoys was deployed with a mean separation of 10 km on the southeast side of the front. The cluster surged northwest with the eddy flow while shrinking in area (Figure 3.3). Restricted to the surface, the drifters collapsed along a line as they converged, continuing to move around the eddy more or less along the same streamline (Figure 1.2). The mean temperature of the cluster as it crossed the front is shown in Figure 3.4a.

To lowest order the flow field may be expressed as varying linearly in the zonal and meridional directions, via a Taylor expansion:

$$u = u_0 + \frac{\partial u}{\partial x}(x - x_0) + \frac{\partial u}{\partial y}(y - y_0) \qquad v = v_0 + \frac{\partial v}{\partial x}(x - x_0) + \frac{\partial v}{\partial y}(y - y_0)$$

where u and v are the velocity components in the x and y directions, and u_0 and v_0 are the velocity components at $[x_0, y_0]$. Since the divergence is $div = \partial u/\partial x + \partial v/\partial y$, and the vorticity is $\zeta = \partial v/\partial x - \partial u/\partial y$, a multiple linear regression of the data to these equations gives the time progression of divergence and vorticity (Figure 3.4b,c). As the cluster crossed the front the convergence grew to a maximum of $5 \pm 2.7 \times 10^{-5}$ s^{-1}, while the vorticity became increasingly positive, reaching about the same magnitude. The error bars (one standard error from a Student-t distribution, which agree with bootstrap estimates) grow as the cluster collapses onto a streamline.

A more direct calculation of the convergence comes from a first difference of the cluster area over time. Cluster area was estimated as elliptical using principal axes fit to the drifter positions. The results, which agree nicely with the regression method, are shown in Figure 3.4d. (Standard errors come from 1000 bootstrap estimations of the areas).

An additional cluster of 8 buoys was deployed near 2°N, 141°W on 31 November 1990 (Figure 2.1e), also at a mean separation of about 10 km. In contrast to the first deployment, this cluster moved westward in the SEC for several days without deforming significantly. Multiple regression and cluster area analyses show that the cluster measured a fairly uniform divergence of approximately 1×10^{-6} s^{-1}, with a standard error of the same value.

The direct measurements of the clusters, then, place the eddy scale gridded field in perspective. The smoothed data agree with the sub-grid scale clusters in the southern region where the field is moderately divergent. Near the deformed equatorial front,

however, the gridded data smooths out velocity gradients and underestimates the largest convergence by a factor of five (see Figure 3.1b). The first cluster gives direct evidence of large gradients in the divergence and vorticity fields near the temperature front.

3.1.3 eddy resolving model

The spatial relationship between cold water cusps, northward flow, and intensified vertical velocities has been predicted by numerical simulations of the equatorial circulation; this includes the magnitude and location of the dipole of intensified convergence and divergence (see Philander *et al.*[1986] Figure 3 and Harrison [1996] Figure 4).

For independent confirmation of the convergence and vorticity patterns observed during TIWE-2 we appeal here to the WOCE Parallel Ocean Climate Model [Semter and Chervin, 1992]. The POCM is an eddy resolving, primitive equation model with latitudinally variable 0.4° spacing. The model has 20 levels in the vertical and is forced with daily ECMWF derived winds. Details of the model are given in Semtner and Chervin [1988] and Semtner and Chervin [1992].

Figure 3.5 shows the velocity and temperature fields of the uppermost level (0-25m) over the region of tropical instability activity (1°S to 9°N, 170-115°W) for Julian day 325, 1990 (21 November), five days after the AVHRR image of the TIWE-2 eddy (Figures 1.1 and 2.11). Five well developed, anticyclonic vortices are positioned at relatively regular intervals of 10° in longitude. Maximum speeds of about 1 m/s occur along the perturbed north equatorial front. Although the minimum temperature of the equatorial cold tongue decreases to the west, the canonical relationship between the anticyclonic eddies and the cusp like disturbances to the equatorial front is confirmed.

The divergence and vorticity fields associated with Figure 3.5 are given in Figures 3.6 and 3.7. Each vortex possesses a dipole of intense convergence and divergence along

its leading (westward) edge, aligned with the northward cold water cusps. As with the TIWE-2 vortex, the maximum values are on the order of $0.5\times\ 10^{-5}\ s^{-1}$. Likewise, the model relative vorticity consistently mimics the observations, with anticyclonic vorticity approaching the inertial frequency and a ridge of large cyclonic vorticity along the front.

The correspondence between the observations and model is striking. While no effort has been made to investigate the persistence of these patterns in the model during a season or as a function of year, cursory examination of the model data has confirmed that over a month or less each vortex seems to hold its form. (Moving with each vortex, the flow is approximately steady on a monthly or shorter time scale). Thus, not only does the POCM agree with previous models, but it confirms the present finding that negative/positive divergence and relative vorticity dipoles aligned with cold water cusps are robust features of tropical instabilities. Consequently, as we examine the single vortex observed during TIWE-2 throughout this manuscript, it is worth keeping in mind that the results are very likely applicable to tropical instabilities as a whole. Of course, confirmation of the universality of this study will require comparisons with several models and observational studies yet to come.

3.2 Vortex flow field

Thus far, observations of currents from myriad sensors during TIWE-2 have been combined, transformed into a moving reference frame, and mapped onto a regular 1/4° spacing grid over the top 25 dbar in the region 143.5-136.5°W, 1.75-5.25°N. This approach is hereby extended over the entire upper layer, defined as the ocean surface down to the thermocline, as well as to the other measured variables (scalars such as temperature and salinity). The result is fully three dimensionally gridded data sets.

All grid manipulations are still as in Equations (3.1)-(2.9), but with the addition of an additional dimension index k.

3.2.1 upper layer

Although hydrographic and ADCP measurements extend to 300 dbar, gridding data in the moving reference frame will be restricted to above the thermocline since available evidence indicates that the translation characteristics were coherent in the upper layer but not below (see Figure 2.16). The vertical resolution is chosen to be 10 dbar beginning with 20-30 dbar, since the ADCP does not measure currents shallower.

In the tropical Pacific the thermocline appears quite sharp, almost as a discontinuity, owing to the intense heating from the sun and quick response of the circulation to wind forcing. In the present case the thermocline was easily identified with the 24.5 σ_θ isentrop. Figure 3.8a shows the depth of this surface mapped in the moving frame; the depth ranges from 120 m to the south and west, to 180 m near the center of the vortex (compare with Figure 2.11).

The geopotential anomaly referenced to 300 dbar shows a similar pattern, with a central high of 10.5 m^2/s^2 falling off towards the edges to 8.5 m^2/s^2 (Figure 3.8b). Tacitly assuming 300 dbar to be a level of no motion, this implies a sea level high associated with the vortex of about 20 cm which compares well with the previous *in situ* IES and satellite altimetry measurements [Miller *et al.*, 1985; Perigaud, 1990] and tropical instability eddies in the POCM. We have already pointed out, however, that moving frame of reference can only be justified above the thermocline. Consequently, possible effects of motions below the thermocline on the geopotential are impossible to assess.

Since the thermocline depth is essentially an integrated measure of the the dynamic height, the similarity with the surface geopotential suggests a degree of coherence of the flow field with depth. This is born out by depth dependent views of the velocity.

3.2.2 velocity

Zonal sections of meridional velocity across three latitudes of the eddy are shown in Figure 3.9. The gridded surface velocity (Figure 2.11) revealed an anticyclonic vortex; here the eddy is seen to extend below the surface to the thermocline. Nevertheless, there is significant vertical structure to the flow. The northward flow of the eddy is most intense at the surface except at 5°N where it has a subsurface maximum greater than 60 cm/s. The depth of penetration increases to the north; speeds of more than 40 cm/s occur only in the top 25 m at 2°N, but extend to the thermocline by 5°N. At 5°N the subsurface flow is centered just below 100 dbar at 142°W, while the peak surface flow has shifted eastward by about 0.5°.

The strongest southward flow is centered near 138°W at about 100 dbar at all three latitudes. In contrast to the surface flow, it appears much broader than the northward branch of the eddy, with speeds over 50 cm/s spanning a degree in longitude and 50 m in depth. The asymmetry between the north and southward branches of the vortex results in the eddy axis shifting to the west by about 1°, or 110 km, over the depth of the upper layer (Figure 3.9a,b).

Meridional sections of zonal velocity are shown in Figure 3.10. The westward propagation of the vortex has been added back into the data (a constant -30 cm/s everywhere) so as to reveal the extent of the SEC. The -30 cm/s contours are marked by a heavy dashed line to denote the zero contour in the moving frame. In all three sections the SEC extends down to the thermocline with maximum speeds of over 40 cm/s. Along

the central axis of the vortex (along 140°W - Figure 3.10b) the SEC approaches 1 m/s below 50 dbar. Although the structure of the flow north of 5.25°N cannot be addressed owing to the lack of ADCP data, current meter moorings at 7°N indicated a swift NECC greater than 50 cm/s eastward down to 100 m.

To lowest order, then, these dissections reveal a strong (>50 cm/s) anticyclonic flow relatively coherent down to the thermocline. To next order, they reveal east-west asymmetry with the core of maximum speed occurring shallower in the northward branch than in the southward one.

3.2.3 divergence

In analyzing the surface flow the salient feature was a dipole of convergence and divergence, with magnitudes approaching the local inertial frequency. This striking pattern is now seen to extend down past about 50 m (Figure 3.11a,b). The vertical velocities implied by the divergence reach 20 m/day below the mixed layer (50 m) and more than 50 m/day at the thermocline.

While model simulations of tropical instabilities have given values an order of magnitude smaller - O(2-5 m/day) [Philander *et al.*, 1986; Harrison, 1996], detailed observational studies of the equatorial front have revealed vertical velocities an order of magnitude larger - O(500 m/day) [Johnson, 1996; Sawyer, 1996]. The scale on which the estimates are made clearly effects the results - our gridded measurements smear out the most intense signals associated with the front. Recall that direct measurements with a cluster of drifters gave a convergence of order 5×10^{-5} s^{-1}, in agreement with Johnson [1996] and Sawyer [1996]. Meanwhile, eddy resolving models do not fully resolve fronts.

Cuts through the eddy flow in the moving frame are shown in Figure 3.12; assuming the flow to be steady, the vectors represent projections of streamlines onto the vertical

planes. As the northward flow reaches 4°N it sinks below the surface. The convergence is connected with the divergence near the center of the vortex via a circulation cell in the zonal-vertical plane. The dynamical mechanisms driving these circulation patterns are the primary focus of the rest of this chapter.

3.3 Thermohaline structure

3.3.1 temperature

In Chapter 2 it was shown that the cold water cusp in remotely sensed SST coincided with the northward flow of the vortex. Although additional AVHRR images during TIWE-2 do not reveal the front as clearly, temperature measured via the drifting buoys, shipboard ADCP transducer, and CTD casts was gridded into the moving frame (Figure 3.13a). The steadiness of the flow in the moving frame is confirmed, as we see the same cold water cusp which appeared in the AVHRR image. Moreover, the temperature increase across the front (2°C) is comparable.

The primary signal in the depth dependent structure of the temperature field is the deepening of the thermocline in the center of the vortex associated with the anticyclonic flow and high geopotential discussed earlier (Figure 3.14). However, there are several additional interesting features evident in the zonal temperature sections. At 3 and 4°N the front is seen to extend below the surface nearly to the thermocline, while at 5°N the same isotherms don't quite reach the surface. Isotherms are seen bowing upwards along 141°W, especially at 4 and 5°N. It seems likely that this deviation from the central high pressure signal (deep isotherms at the center of the eddy) results from the intense divergence which was found to extend past 50 m depth in the region (Figure 3.11).

The structure of the cold water cusp in the northward flow and warmer water moving to the south is manifest by the general downward slope of isotherms to the east (Figure 3.14; compare with Figure 3.9). Especially at 5°N, the southward transport of warm water is evident past 80 m depth.

The gridded surface temperature (Figure 3.13a) shows the front with a width of >50 km, while detailed observations show that a 2°C change actually occurs over less than 5 km [Johnson, 1996; Sawyer, 1996]. In Figure 2.11, the front appears to be order 50 km wide, but this is partly due to smearing in the process of compositing separate images. Close inspection of the front near 140°W, 2.5°N shows a 1°C change over less than 25 km. Radar images (from the Shuttle Radar Laboratory - SRL) also show the front to be extremely narrow (P. Flament and M. Sawyer, personal communication).

Not only is the equatorial front narrow in the presence of instabilities, it also appears relatively straight - both Johnson [1996] and Sawyer [1996] have argued this to be a sign of along front homogeneity. Along cold water cusps, the front is generally straight to within the same order as its width, about 5 km. In the face of the large velocities at the front, how can it be maintained? Clearly the vortex transports cold water northward and warm water to the south, and yet the front remains sharp.

One process which could work to maintain the front is the intense convergence which occurs along its leading edge. As the cold water moves northward it subducts, sinking below the warmer tropical water. Instead of mixing together, which would smear out the front, a vertical circulation is established. Johnson [1996] has suggested that this subduction process at the front releases available potential energy which could be available to the instability; in Chapter 5 this will be investigated further.

Meanwhile, the relative straightness of the perturbed front implies an upper limit on any diffusive parameterizations of the turbulent processes acting in the horizontal. The horizontal turbulent transport of heat by the mean covariance between fluctuating velocity and temperature ($\mathbf{u}'$ and T$'$) is typically parameterized in terms of an eddy diffusivity (K_h) and the larger scale temperature (T) using a Reynold's analogy:

$$\overline{\mathbf{u}' \cdot \nabla T'} = K_h \nabla^2 T \tag{3.6}$$

where the overbar denotes a time averaged mean. The eddy diffusivity thus scales as $K_h \sim lu$ where l is the length scale of disturbances to the front (meaning deviations from straightness) - of order 1-5 km, based on detailed surveys [Johnson, 1996; Sawyer, 1996] and AVHRR and SRL images; and u is the velocity scale of the fluctuations - order $\leq$10 cm/s from the error bars on the velocity field. Consequently, an upper limit on the effects of turbulent diffusion is $K_h \leq 5 \times 10^2$ m^2/s. This is much smaller than the magnitude which would be needed to balance horizontal advection in the absence of convergence at the front, which can be seen by taking typical length and velocity scales for the vortex - $L \sim 10^5$ km and $U \sim$0.5 m/s give $\sim 5 \times 10^4$ m^2/s.

It thus seems that subduction at the equatorial front gives tropical instabilities the common signature of cold water cusps that maintain their form as the vortices translate westward. Still to be explained is why the circulation near the front, and of the vortex as a whole, remains steady. A possible mechanism will be suggested in Chapter 4.

3.3.2 salinity

The observed salinity during TIWE-2 shows an analogous picture to that of temperature (Figure 3.13b). High salinity ($\sim$35) is observed to the southwest in the northward flow,

while very low values (<34.5) are found to the northeast moving southward. This pattern has not been previously observed, but suggests that just as TIWs transport a significant amount of heat [Hansen and Paul, 1984; Baturin and Niiler, 1997], they may also induce a substantial fresh water flux.

The three dimensional view is even more striking - saline water is seen in the northward and southward flow of the eddy below the surface (Figure 3.15). The signal is seen as far north as 5°N, and although lack of CTD casts further north prevents knowing how far it extends, its presence in the return flow along 137.5°W implies that it circuits the entire vortex. This high salinity has also been observed in detailed surveys of the front [Sawyer, 1996] where it was also found subsurface.

Closer inspection reveals that the water in the east at 5°N is more saline and warmer than the waters in the west and to the north (compare Figures 3.15c and 3.14c). To better understand this pattern we look at salinity and velocity in the density range 23.5-24.2 kg/m^3, which encompasses the maximum salinity cores (Figure 3.16). The results confirm the scenario for the northward moving high salinity near 142-143°W. However, the situation in the east is more complicated, with the highest salinity appearing to originate to the east of the mapped region.

If we recall the gridded surface velocity (Figure 2.11), there was some indication that the next vortex was sampled in close proximity to the present one. Indeed the flow at 23.5-24 kg/m^3 hints at this. It seems likely that the northward advection of saline water in the approaching eddy is partly entrained by the one in question. Mixing with the southward moving warm water results in a new water mass, higher in salinity than would be expected for an isolated eddy. Thus, although there is clear indication of

a salinity circulation around the vortex, a contribution through the eastern boundary appears to occur south of 3.5°N.

Beyond indicating significant salt transport, the salinity pattern indicates a possible input of high salinity water into the northern hemisphere from the south. Typically, water of salinity greater than 35 is found in the South Pacific, with most of the water mass exchange believed to occur in the western Pacific [Tsuchiya, 1991; Bingham and Lukas, 1994]. For instance, the climatological maps of Tsuchiya [1968] show the 35 salinity contour right on the equator across most of the Pacific, while it extends northward along the coast of New Guinea. At 160°W the mean Hawaii-Tahiti shuttle data show the 35 contour reaching toward 2°N in the upper layer [Wyrtki and Kilonsky, 1984].

Climatological maps, however, cannot adequately resolve the seasonal signal of tropical instabilities. It may be that equatorial disturbances assist the mean meridional circulation in moving saline water across the equator. Regardless, the present data indicates that a movement even further to the north may be accomplished by the instability vortices. This scenario is supported by one previous synoptic survey where a water mass structure similar to the one described here was observed: Montgomery and Stroup [1962] presented a meridional section of salinity along 150°W that showed water greater than 35 reaching almost to 4°N, with a seemingly detached pocket of high salinity water at 6°N (see their Figure 4). The observations were made from July-August, during the instability wave season, so that the hypothesis of salinity circulating around an instability vortex could explain their observations.

The overall salt fluxes during TIWE-2 are discussed further in Chapter 5.

3.4 Wind forcing

Before proceeding to investigate the dynamics of the vortex flow field, it will help to gain an understanding of the wind forcing during TIWE-2.

3.4.1 observations

Southeasterly trade winds during TIWE-2 were measured using anemometers mounted on a bow tower designed to reduce spurious circulations induced by the ship. Observations were recorded at 1 Hz and later quality controlled and averaged using a median filter onto the same 15 minute time grid as the shipboard ADCP. The resulting wind velocity components during TIWE-2 are shown in Figure 3.17a. Daily averages of winds were also available from the TAO moorings at the equator, 2°N, and 5°N (Figure 3.17b-d). The winds were fairly moderate trades at roughly 5-10 m/s (10-20 kts) except as measured by the ship around 26 November (Julian day 330) when the westward component increased to 15 m/s (30 kts).

The observed winds from the ship and mooring sensors were converted to stresses using a typical bulk parameterization [Gill, 1982; Smith, 1988]:

$$\tau = \rho_{air} C_D |\mathbf{u}_{10}| \mathbf{u}_{10}$$

where $\rho_{air} = 1.2$ kg/m^3 is the air density, $C_D = 1.1 \times 10^{-3}$ is a dimensionless drag coefficient, and U_{10} is the wind velocity measured at 10 m above the sea surface. The calculated stress components are shown as a function of latitude in Figures 3.18a,b; profiles versus latitude (solid lines) were obtained by averaging over all values within 1/4 degree latitude bins.

The average easterly stress of the trade winds decreased gradually to the north, from roughly 0.1-0.02 Pa. However, the 26 November wind event is evident from 2-4°N with stress values much greater than 0.1 Pa. Consequently, the average wind stress curl of about 10^{-7} Pa/m has variations of up to 4 times of either sign (Figure 3.18c).

Wind forcing is usually parameterized as a body force acting over the mixed layer. Here we take the mixed layer depth to be the depth where the density gradient exceeds 0.01 kg/m^{3}dbar. This depth was estimated from individual CTD casts and subsequently gridded into the moving frame as with all other variables. The results are shown in Figure 3.19a: values range from 25-60 m. The zonally averaged mixed layer depth was then calculated for combination with the average wind stress. The method for calculating the zonal average is as in Chapter 5 (see Section 5.1), except that a median estimator was used here since the mixed layer depth has a significant signal directly related to the wind, which is not steady in the moving frame.

The latitudinal profile of mixed layer depth shows a 50% decrease from about 50 m at 2°N to 25 m at 5°N (Figure 3.19b), showing an almost linear relationship to the average zonal wind stress which decreases from about 0.1-0.05 Pa over the same distance. The standard error confidence intervals for the zonal average were obtained as in Chapter 5.

3.4.2 temporal aliasing

Beyond quantifying the mean wind stress and curl during TIWE-2, we are especially concerned with the possible effects of the 26 November wind event on the interpretations of features in the moving reference frame. The rapid increase in wind stress and subsequent decrease as measured from the ship represents temporal variations in the forcing which cannot be adequately separated from spatial features in the moving frame. The

observed wind stress is shown along the ship track in the moving frame in Figure 3.20a. The strong winds map into the region 2-3°N, 140-138°W.

There are several direct effects of wind forcing on the upper layer of the ocean: transient wave responses and the formation of a turbulent boundary layer and the set up of currents balanced by the Coriolis force (Ekman drift).

While no attempt is made here to model transient responses or the expected mixed layer deepening associated with the wind increase, it can be seen that the location of the wind event corresponds well with deepenings of the mixed layer and thermocline (Figures 3.19a and 3.8a). The latter is especially interesting since it represents a significant deviation from azimuthal symmetry of the thermocline depth around the eddy center. Since the mixed layer criterion is somewhat arbitrary and the water column is relatively well mixed above the thermocline, a deepening of the thermocline associated with increasing winds is not unreasonable. The collocation of the wind event and asymmetry in the upper layer thickness (and geopotential anomaly) suggests that this happened as the ship entered this area.

An important result of the thermocline deepening over time would be an apparent geopotential gradient. This gradient would appear spatial in the moving frame, while being truly temporal. We will find in the next chapter that this temporal aliasing is the likely cause of a dynamically unbalanced geopotential gradient in this region of the vortex.

Meanwhile, the Ekman drift induced by the winds can also result in aliased features. The wind driven currents according to Ekman theory $\mathbf{u}_{Ek}$ are:

$$\mathbf{u}_{Ek} = \frac{-\hat{k} \times \tau}{\rho_o f H} \tag{3.7}$$

where $\hat{k}$ is the unit vector in the local vertical, f is the Coriolis parameter, and H is the mixed layer depth. This response might be expected to take place within the time scale given by the inertial frequency, or about 1 day. After gridding the wind stress, the resulting Ekman velocity field is shown in Figure 3.20b. Drift over most of the region is less than 20 cm/s, but approaches 1 m/s near 2-3°N, 139-138°W. However, as already mentioned the effect of the wind probably reaches well below the mixed layer as defined here; therefore, the true Ekman drift could be 1/2 to 1/3 the values shown.

The predicted drift response to the wind indicates a significant ocean velocity divergence pattern in the region of the wind event with the gradients implying convergence at 3°N, 138°W and divergence to the south. Clearly this pattern is not real - the winds, and consequently the Ekman currents, were changing over time, not space. However, if the ocean responded as predicted by Equation (3.7), the ADCP measurements of velocity mapped into this region would reveal a similar pattern because the temporal changes would be mapped into spatial gradients. Indeed, this is seen to be so: the observed, gridded divergence averaged over the top 100 dbar shows an almost identical form along 138°W (Figure 3.21b). When the larger depth of the thermocline in comparison to the mixed layer is taken into account (a factor of 2-3) the correspondence is almost perfect.

Thus, it seems apparent that asymmetry of the vortex central high pressure, and large vertical motions not associated with the divergence/convergence dipole predicted by numerical models are associated with rapidly changing winds during 25-27 November. These temporal changes in the kinematic and thermohaline structure of the eddy were subsequently aliased into spatial gradients in the moving reference frame. However, the sampling of the vortex is such that these effects cannot be separated from the steady flow; nor can a causal relationship be proven.

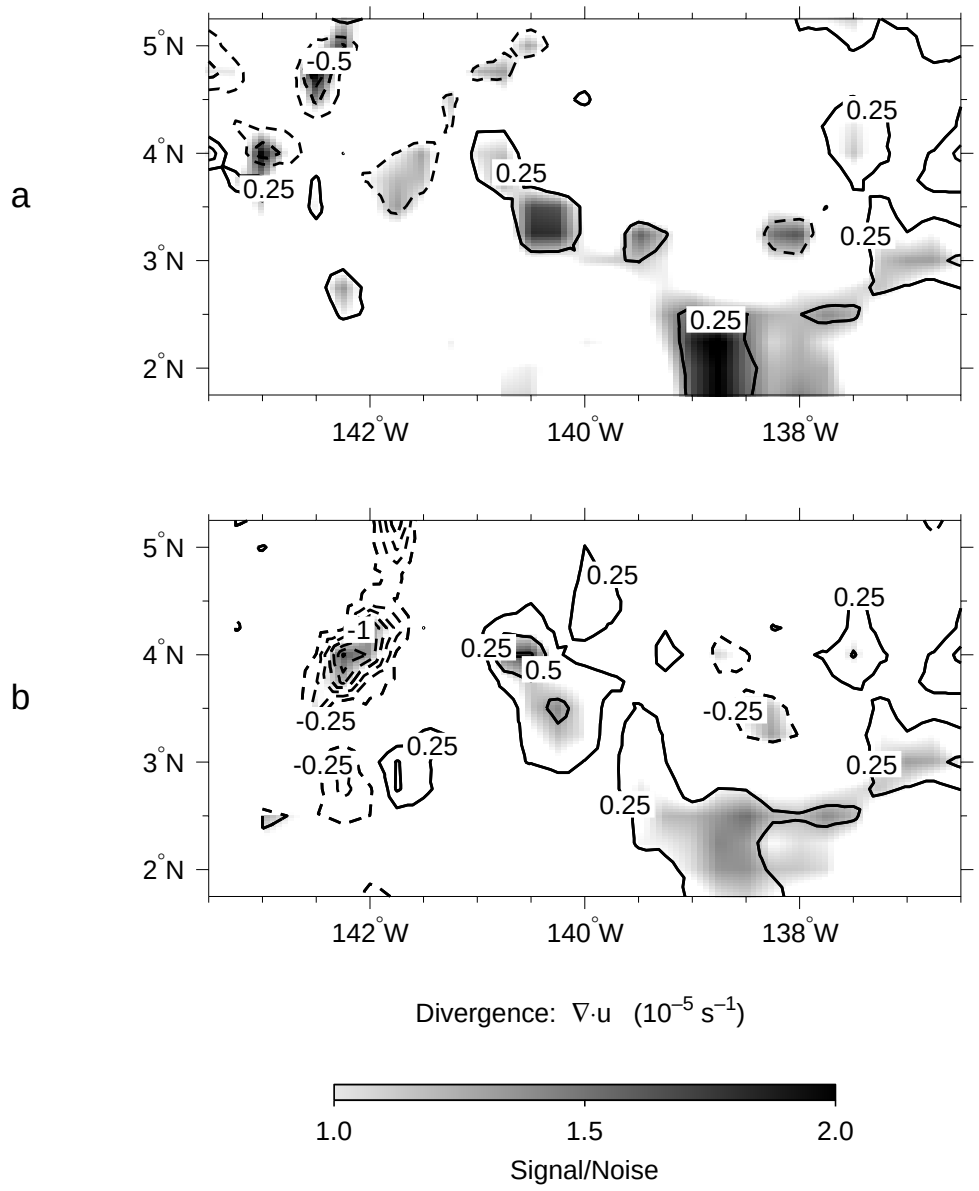

Figure 3.1: Divergence calculated from gridded surface velocity (Figure 2.11) with (a) all data and (b) drifting buoy data excluded. Contour intervals are $0.5\times\ 10^{-5}\ s^{-1}$, with dashed lines for negative values. Thin contours denote $\pm 0.25\ \times\ 10^{-5}\ s^{-1}$. Shading denotes regions with a signal to noise ratio > 1.

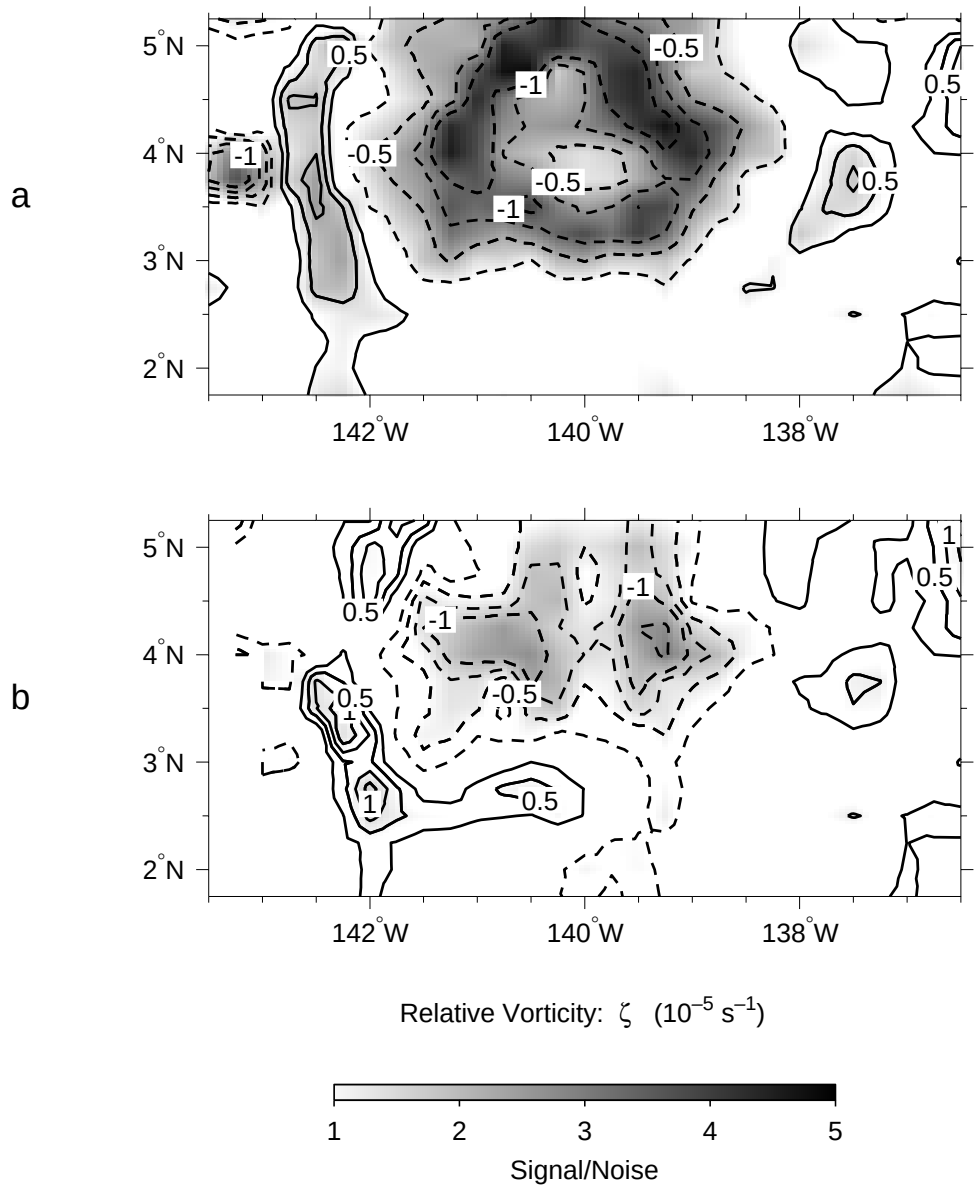

Figure 3.2: Relative vorticity (ζ) calculated from gridded surface velocity (Figure 2.11) with (a) all data and (b) drifting buoy data excluded. Contour intervals are $0.25\times\ 10^{-5}\ s^{-1}$, with dashed lines for negative values. Shading denotes regions with a signal to noise ratio > 1.

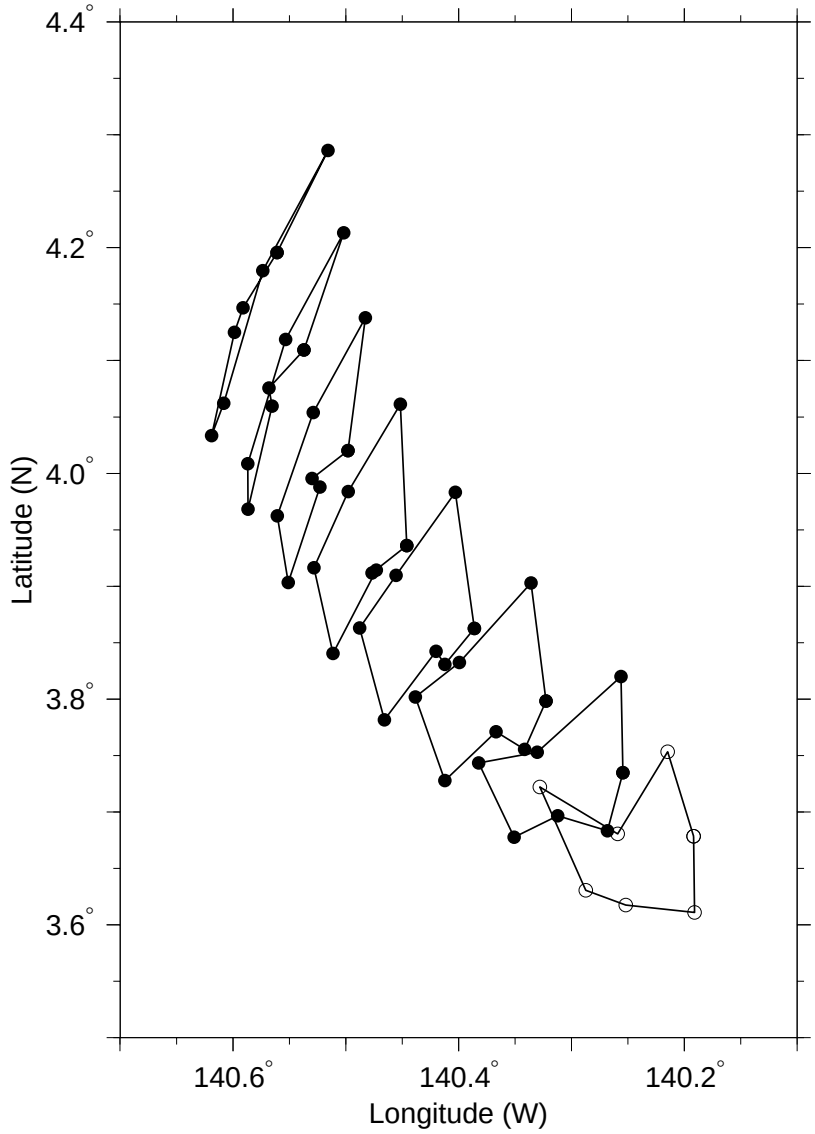

Figure 3.3: Location of buoy cluster (7 drifters) at 4 hour intervals starting at 04:30 GMT, 19 November 1990 (open circles).

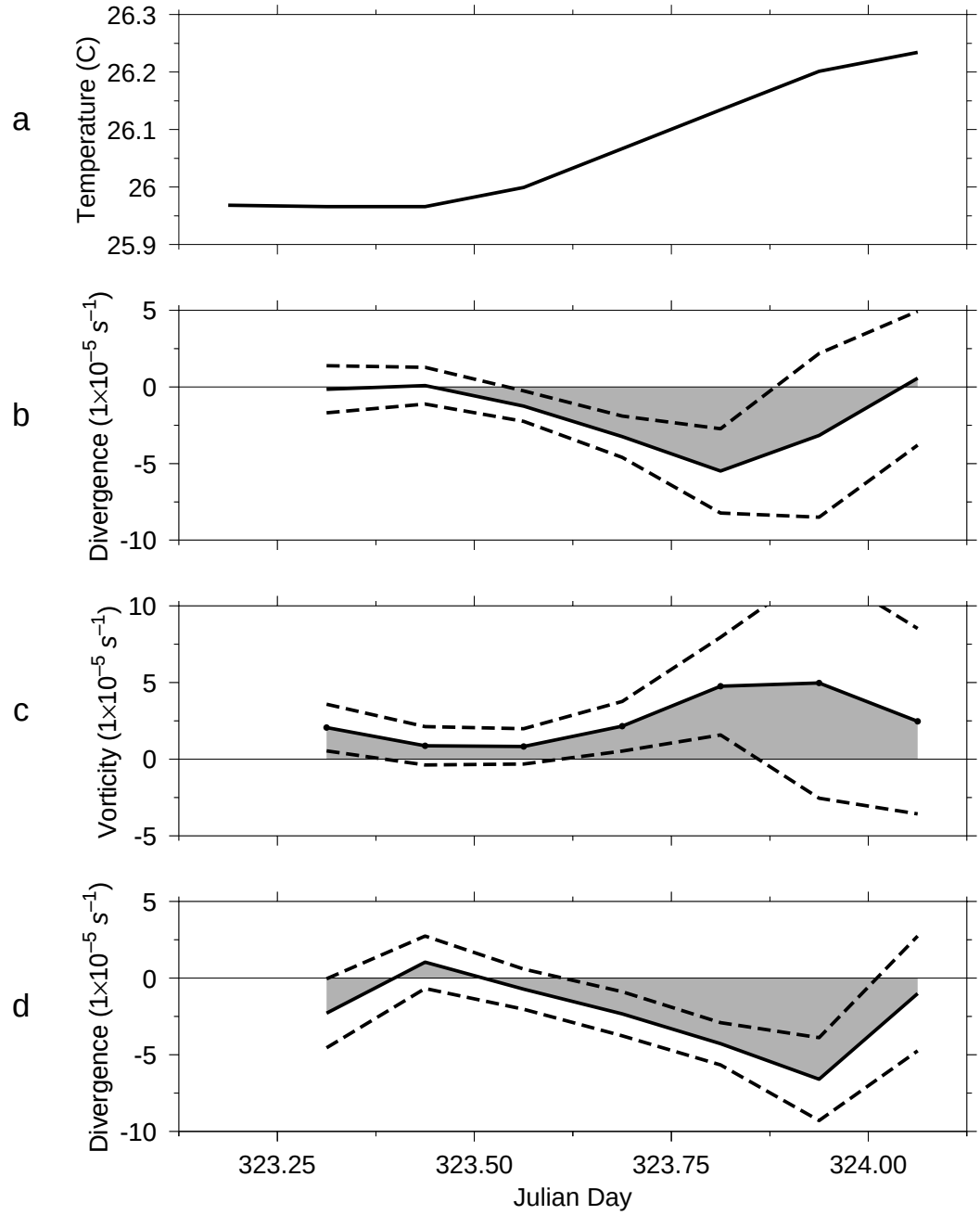

Figure 3.4: Time series following the cluster of Figure 9. (a) Mean temperature measured by buoy thermistors. (b) Divergence and (c) vorticity calculated from buoy velocities as function of positions. (d) Divergence calculated from changes in cluster area.

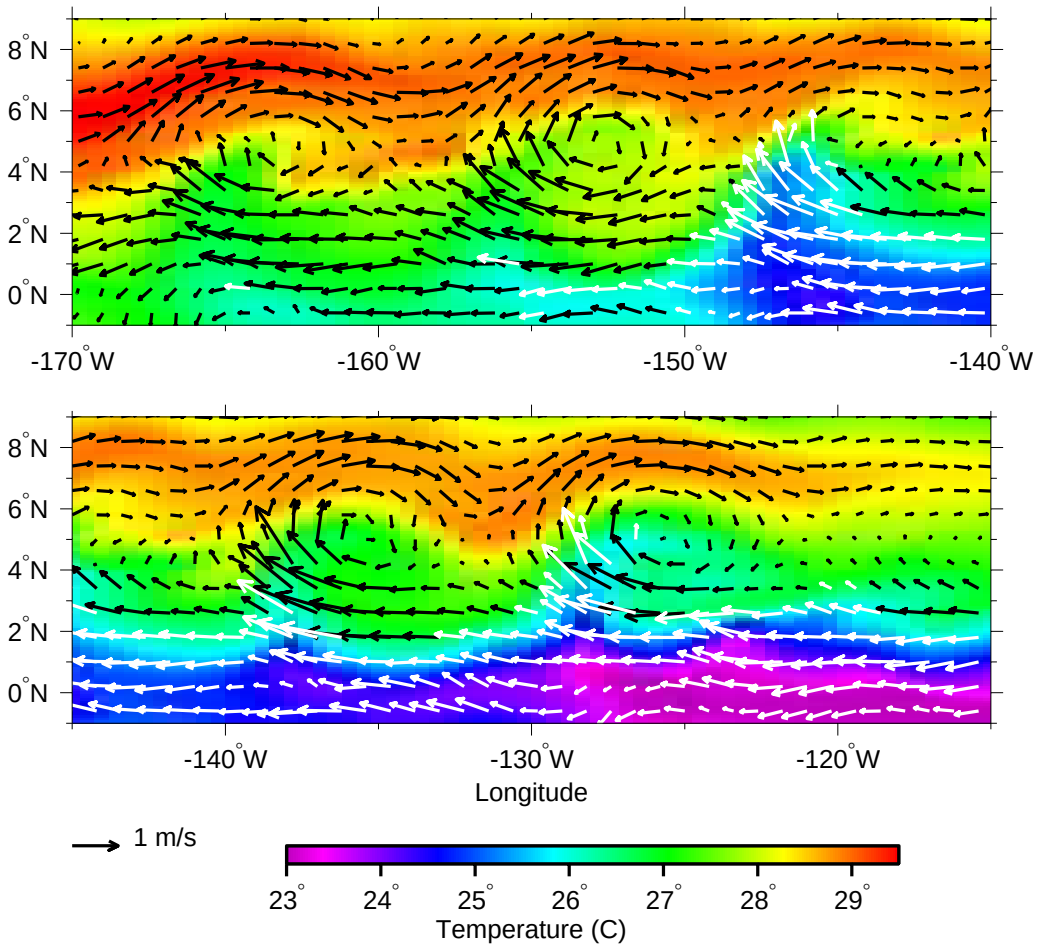

Figure 3.5: Velocity (arrows) and temperature (color shading) over the instability region on 21 N

WOCE POCM.

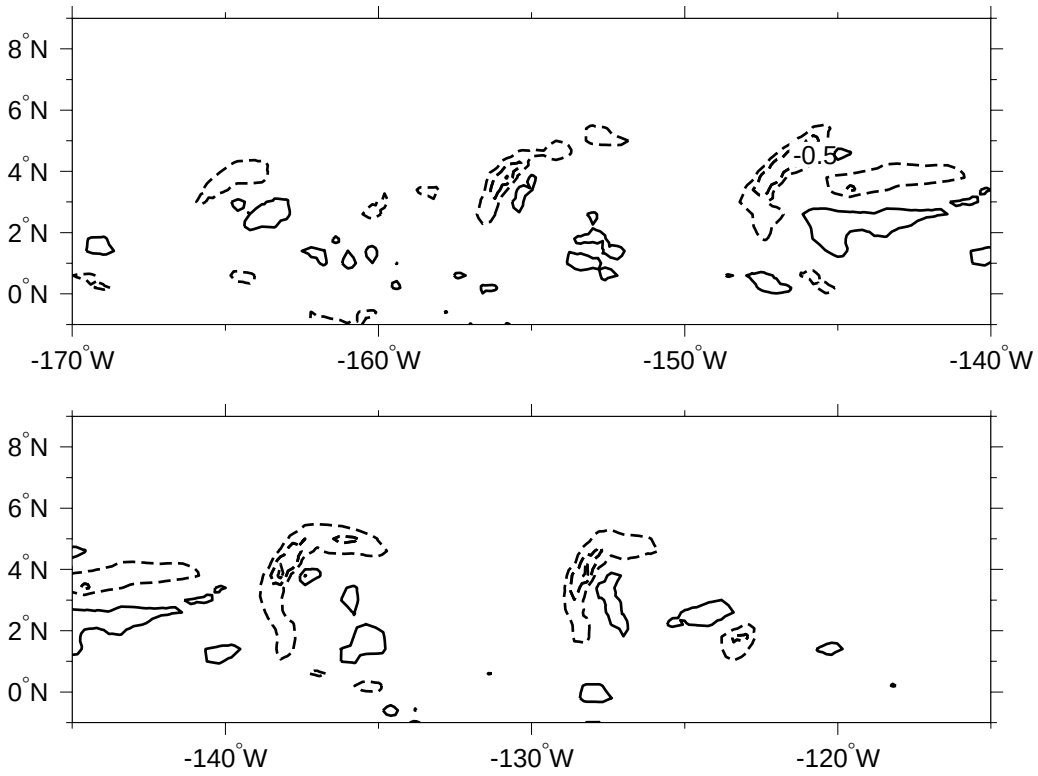

Figure 3.6: Divergence field over the instability region on 21 November 1990 from the WOCE POCM

$0.5\times10^{-5}\mathrm{s}^{-1}$.

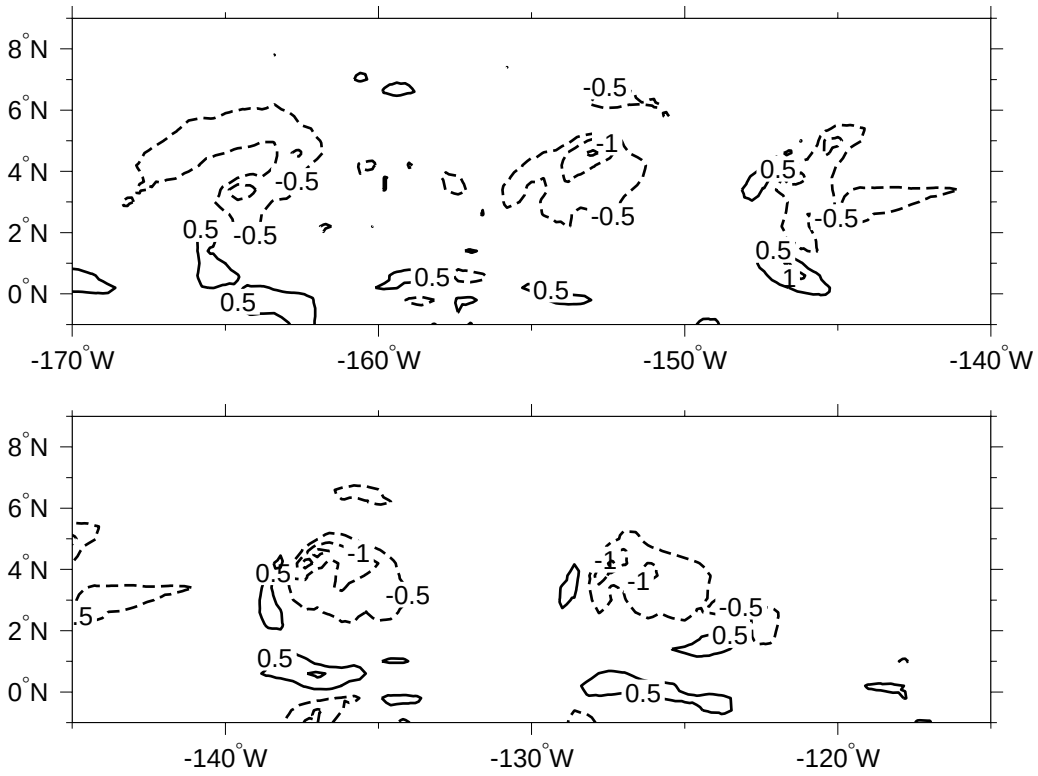

Figure 3.7: Relative vorticity field over the instability region on 21 November 1990 from the WOCE P

are $0.5\times10^{-5}\mathrm{s}^{-1}$.

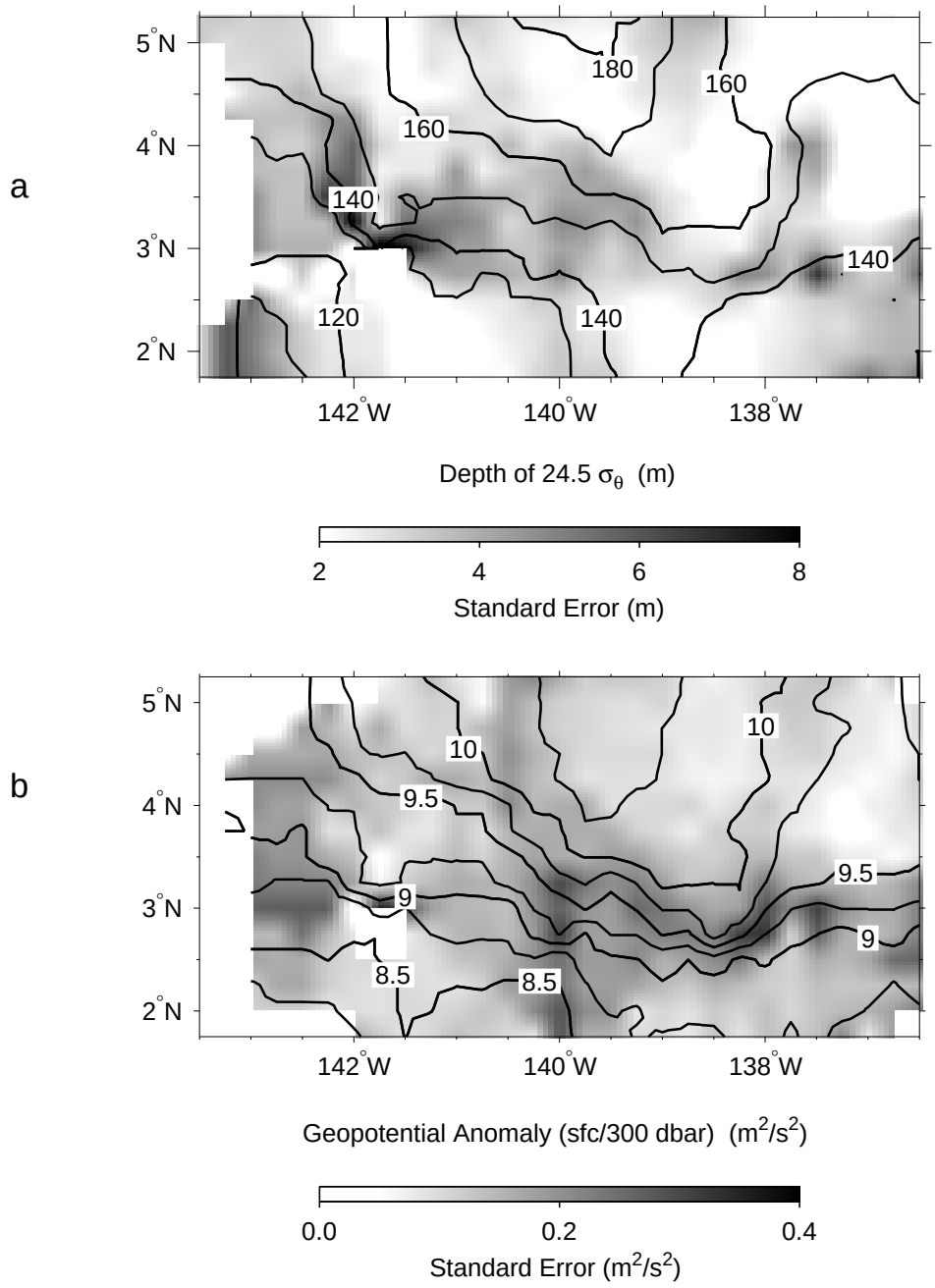

Figure 3.8: (a) Depth (in meters) of the 1024.5 σ_θ isentrop. Contour intervals are 10 m. (b) Geopotential anomaly in the 0-25 dbar range referenced to 300 dbar. Contour intervals are 0.25 m^2/s^2; shading denotes standard errors.

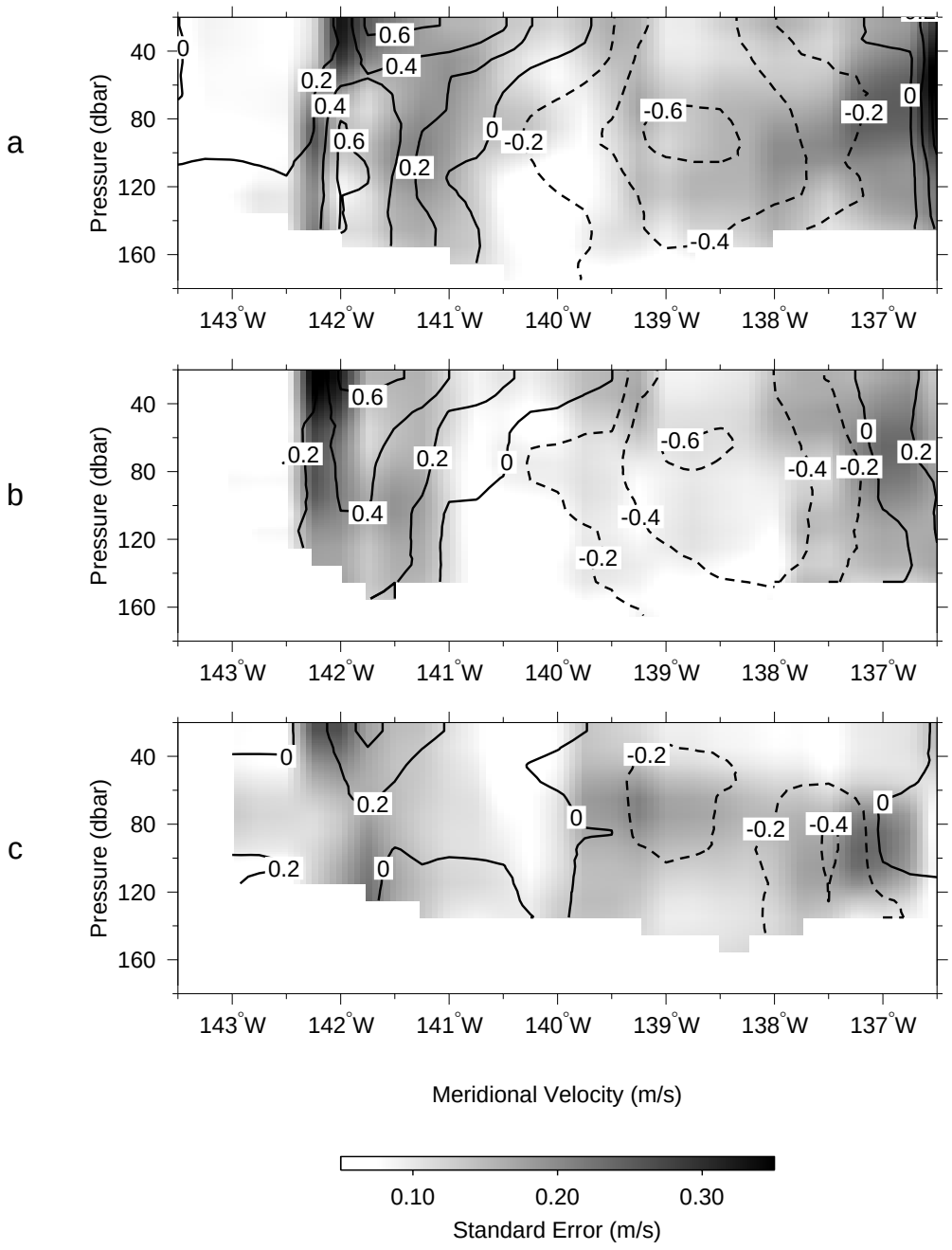

Figure 3.9: Meridional velocity versus pressure along (a) 5°N, (b) 4°N, and (c) 3°N. Contour intervals are 20 cm/s; shading denotes standard errors.

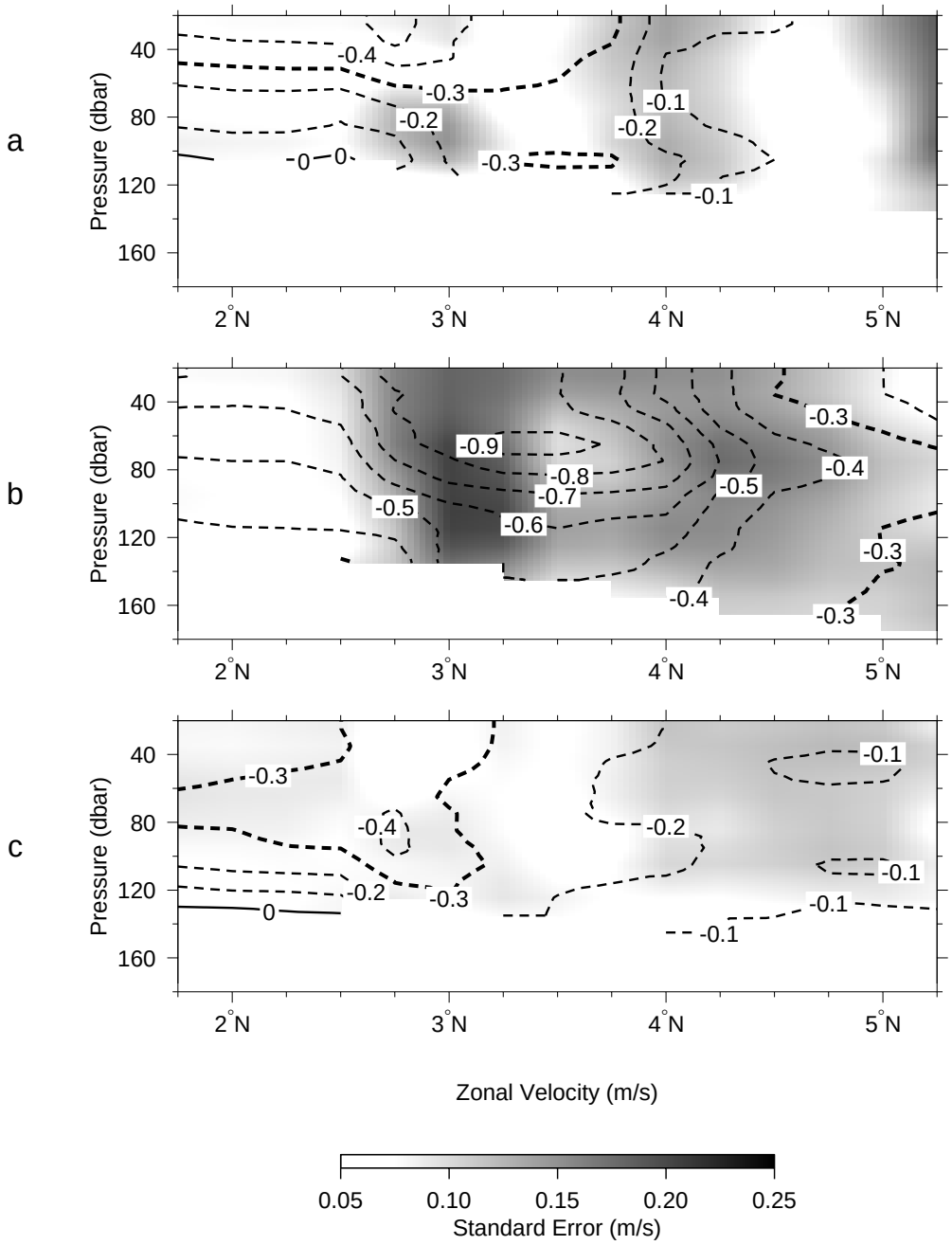

Figure 3.10: Zonal velocity (in the fixed Earth frame) versus pressure along (a) 143°W, (b) 140°W, and (c) 137°W. Contour intervals are 10 cm/s; shading denotes standard errors.

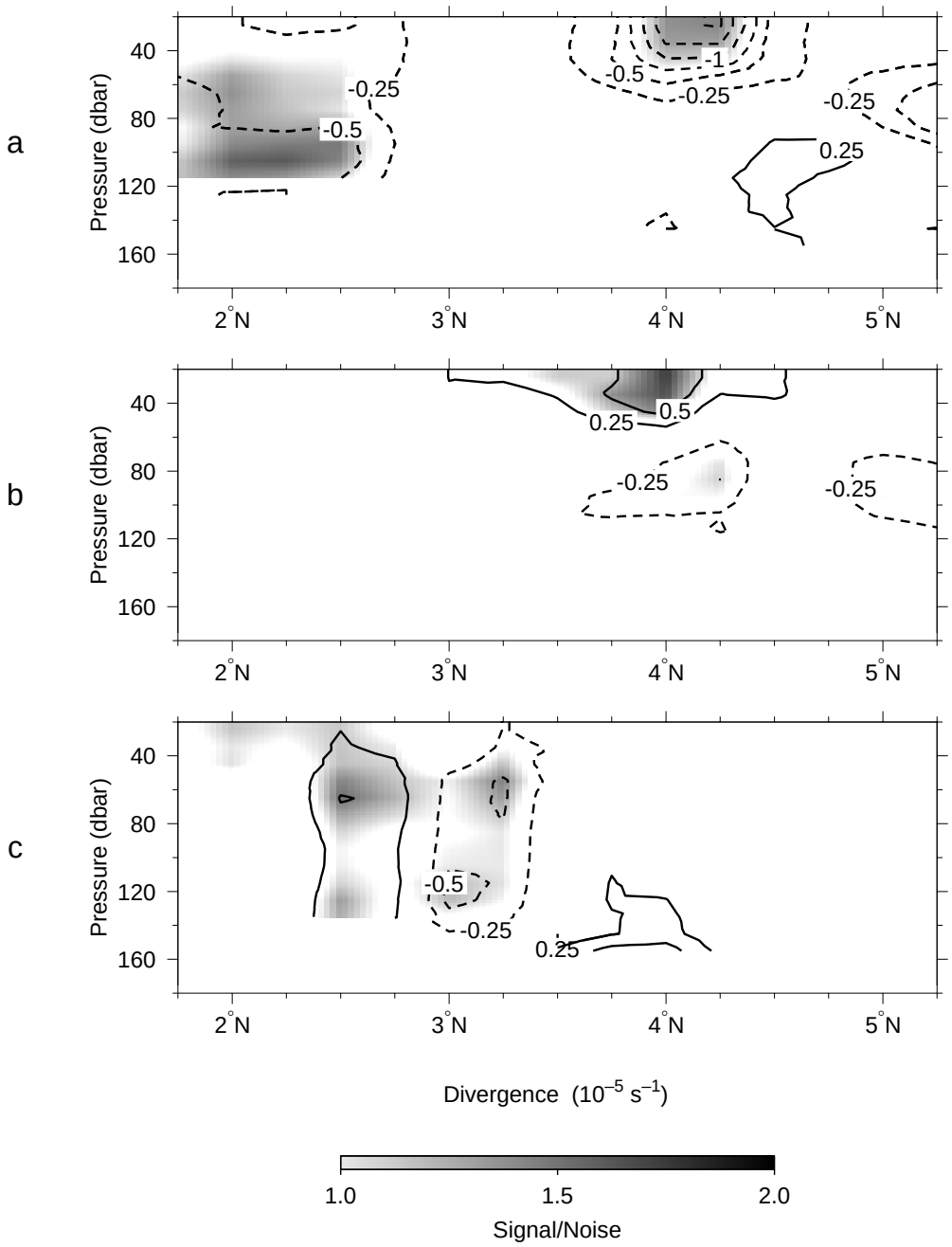

Figure 3.11: Divergence versus pressure along (a) 142°W, (b) 140.5°W, and (c) 138°W. Contour intervals are 0.25× 10^{-5} s^{-1}; shading denotes regions with a signal to noise ratio > 1.

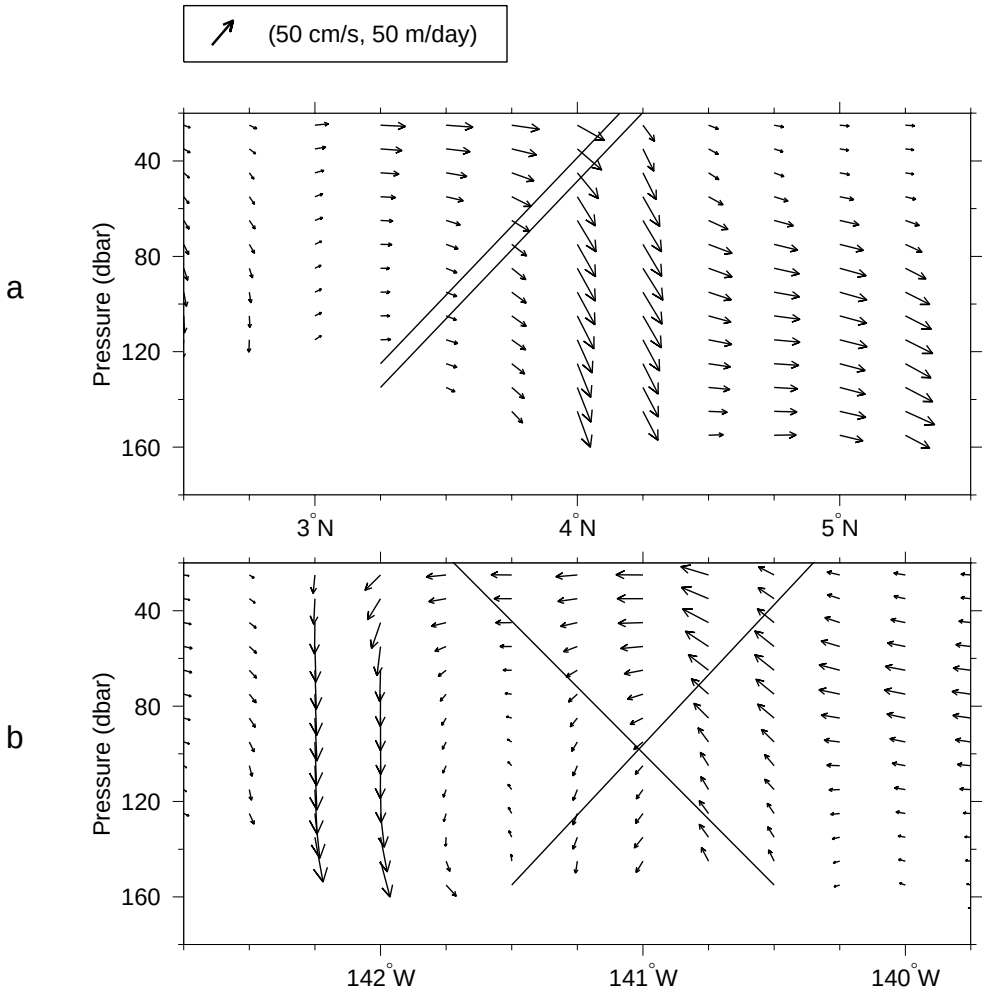

Figure 3.12: Velocity sections through the vortex in the (a) meridional (along 142°W) and (b) zonal (along 4°N) planes

.

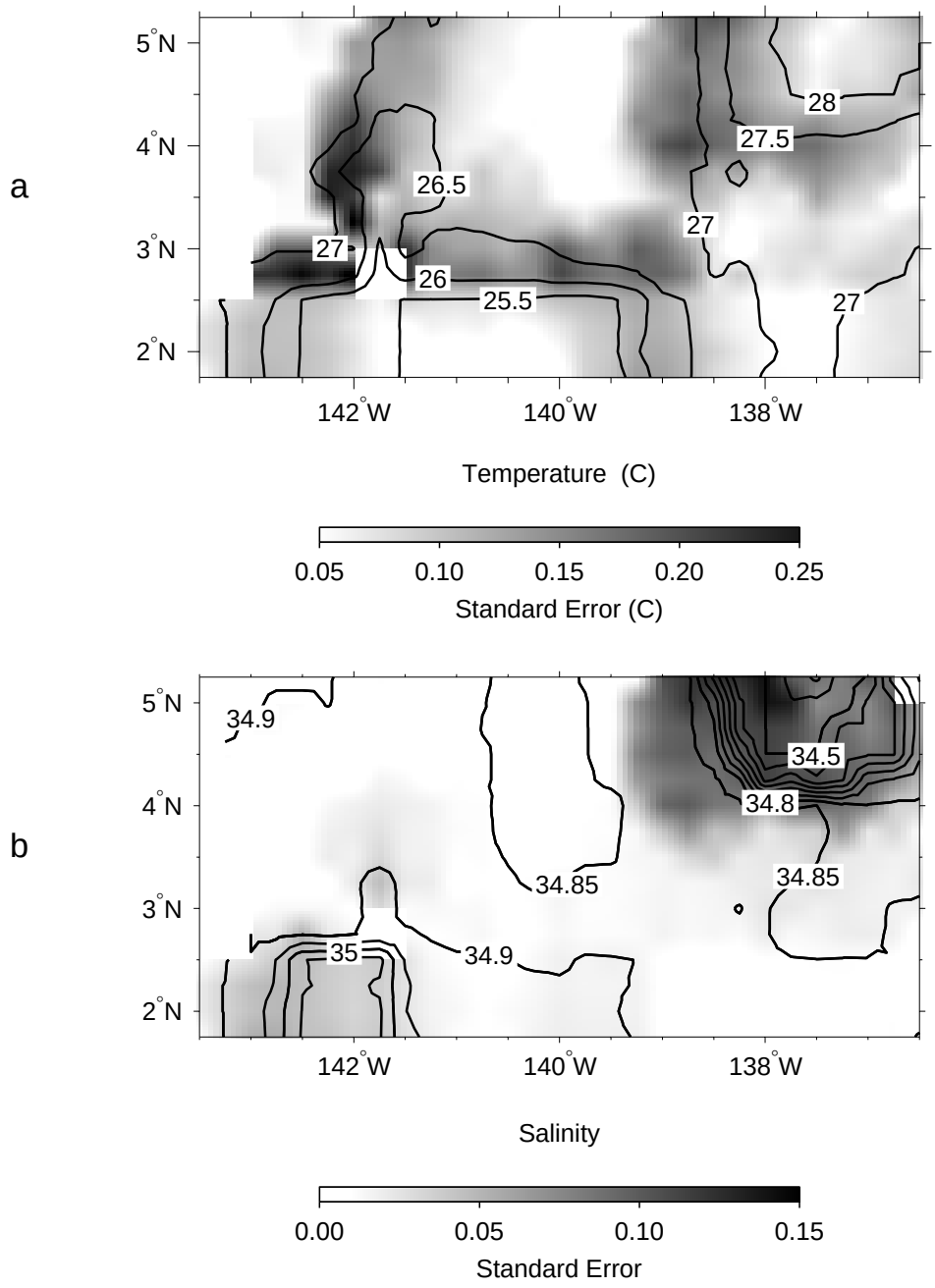

Figure 3.13: (a) Temperature and (b) salinity in the 0-25 dbar range. Contour intervals are 0.5 C and 0.05 respectively; shading denotes standard errors.

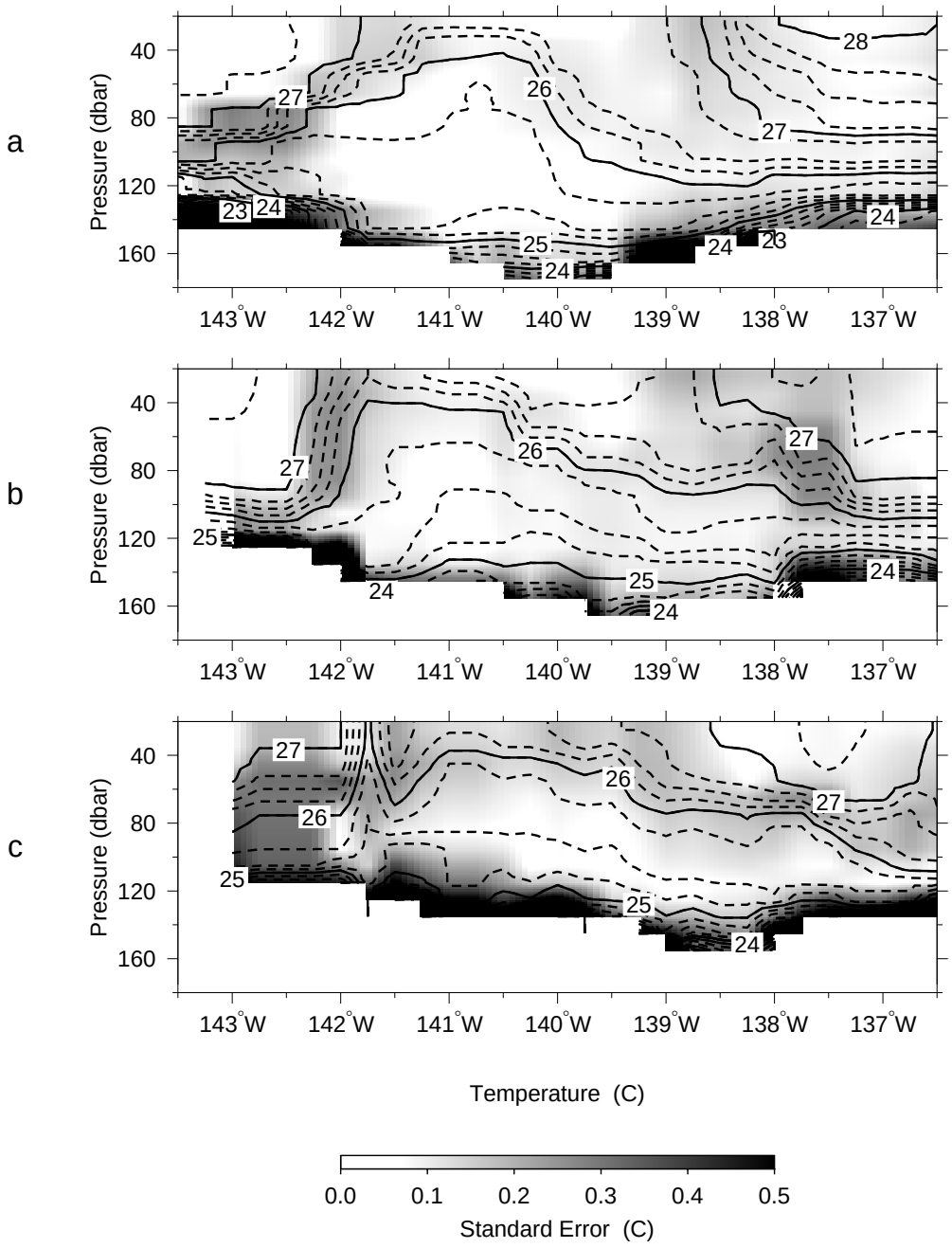

Figure 3.14: Temperature versus pressure along (a) 5°N, (b) 4°N, and (c) 3°N. Contour intervals are 0.25 C; shading denotes standard errors.

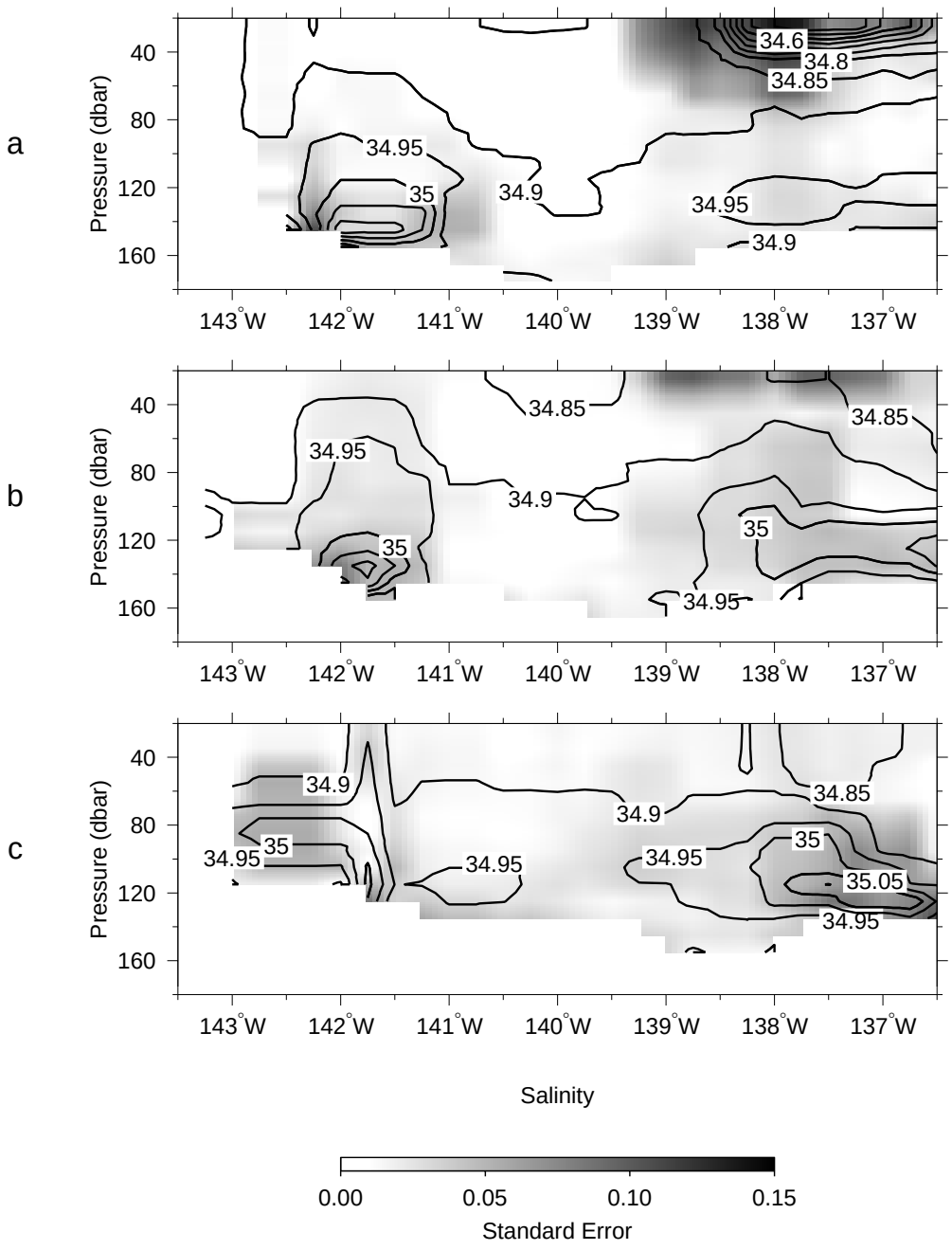

Figure 3.15: Salinity versus pressure along (a) 5°N, (b) 4°N, and (c) 3°N. Contour intervals are 0.05; shading denotes standard errors.

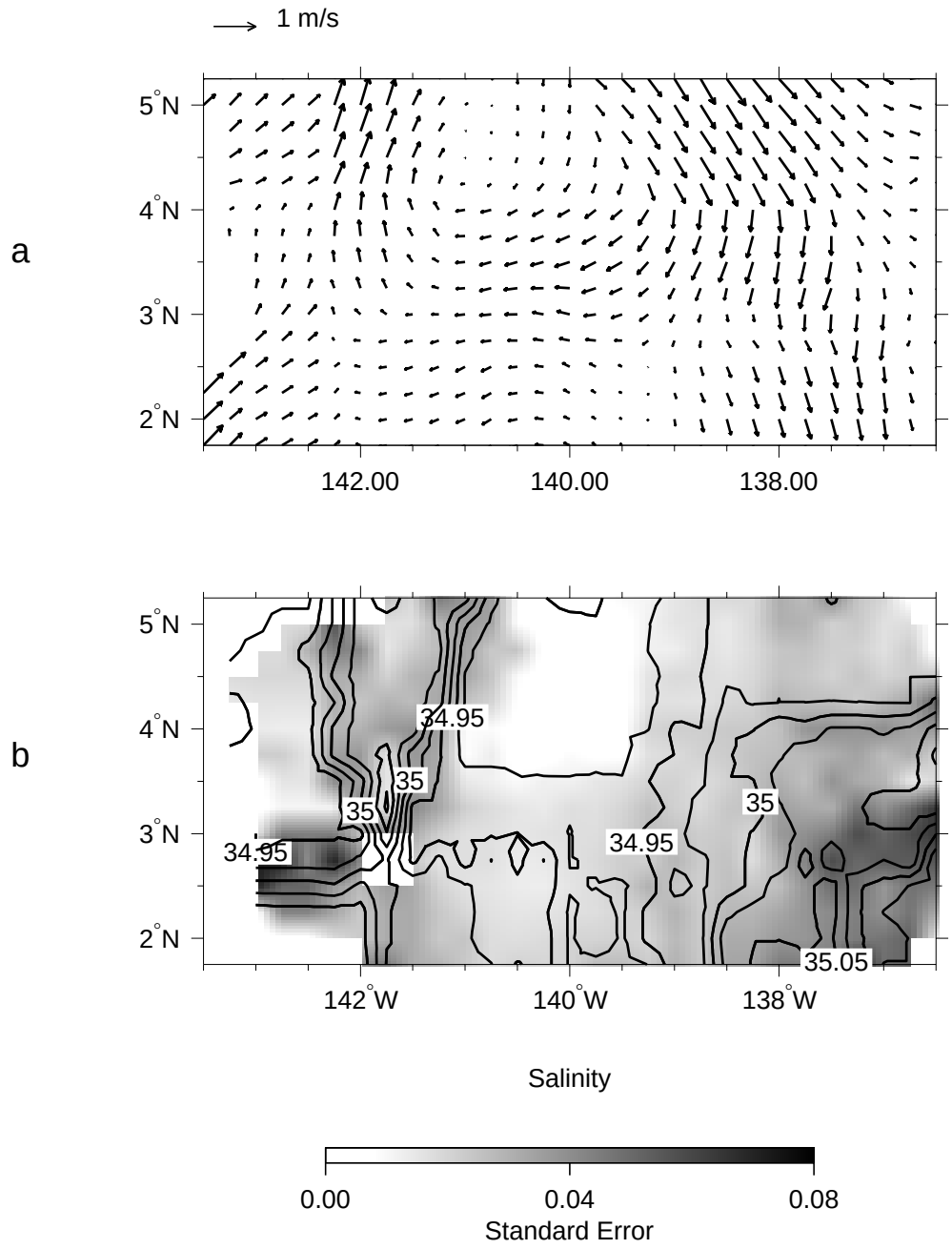

Figure 3.16: Gridded (a) velocity and (b) salinity over the density range 23.5-24 kg/m^3. Contour intervals are 0.025; shading denotes standard errors.

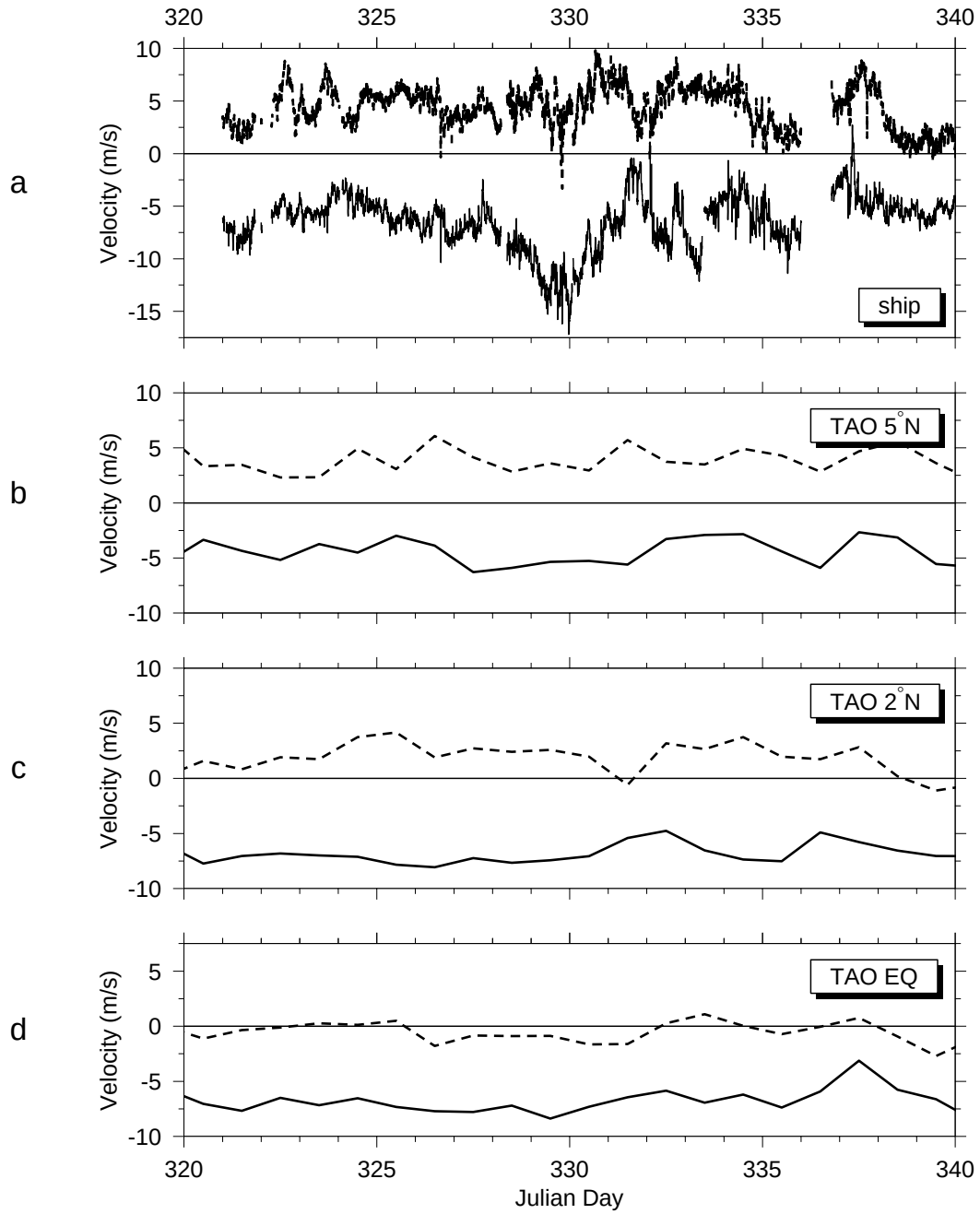

Figure 3.17: Zonal (solid lines) and meridional (dashed) wind velocity during TIWE-2 (11 November to 11 December 1990) as measured by: (a) ship bow mounted tower and TAO moorings along 140°W at (b) 5°N, (c) 2°N, and (d) the equator.

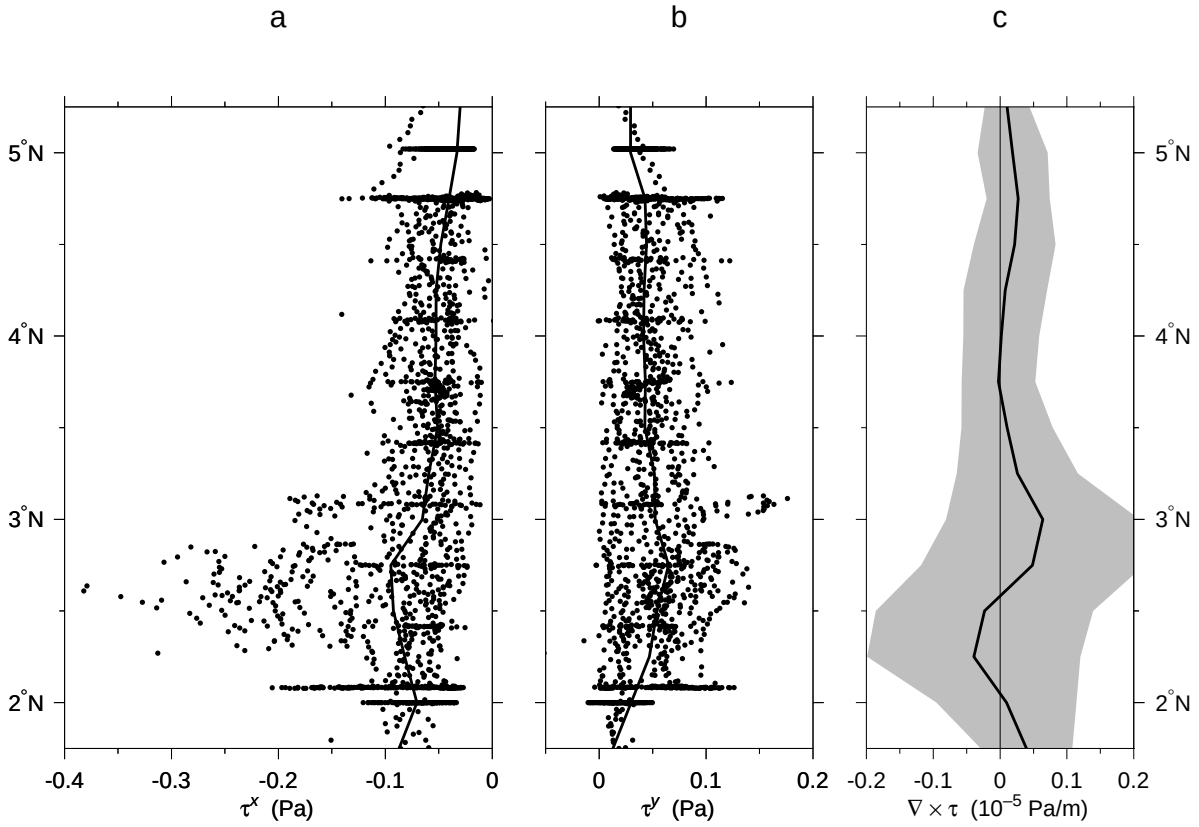

Figure 3.18: (a) Zonal and (b) meridional wind stress from the wind observations in Figure 3.17. I
observations (every 15 minutes for the ship; daily for moorings); solid lines give zonal averages over
Wind stress curl ($\tau^x{}_y$) from the zonally averaged zonal wind stress; shading indicates standard error

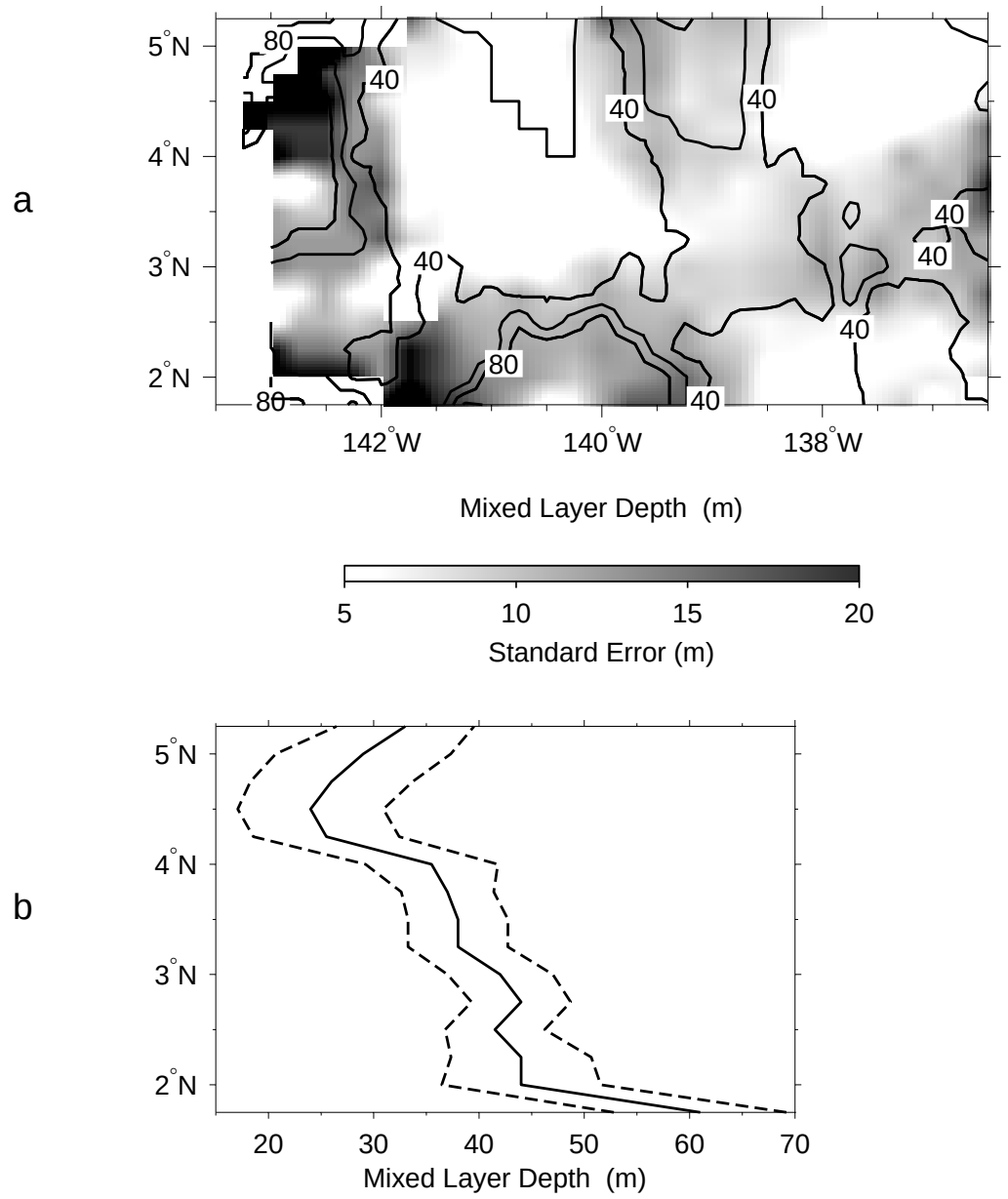

Figure 3.19: (a) Depth (in meters) of the bottom of the mixed layer, defined as the depth where $d\rho/dz > 1$ kg/m^3. Contour intervals are 20 m; shading denotes standard errors > 5 m. (b) Zonally averaged mixed layer depth (solid line) with standard error confidence intervals (dashed lines).

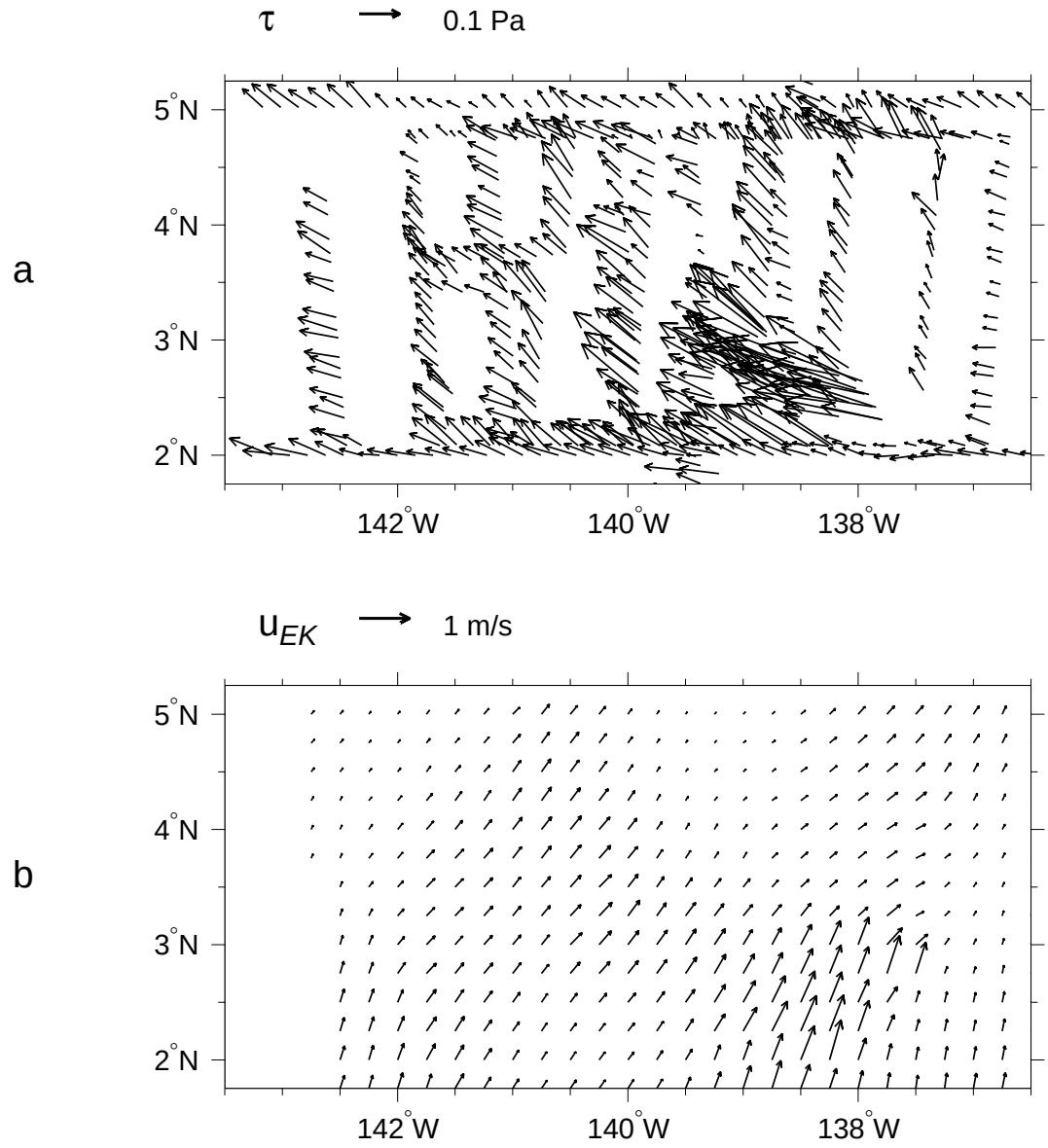

Figure 3.20: (a) Wind stress along the ship track in the moving reference frame. (b) Ekman drift from wind stress in the moving frame.

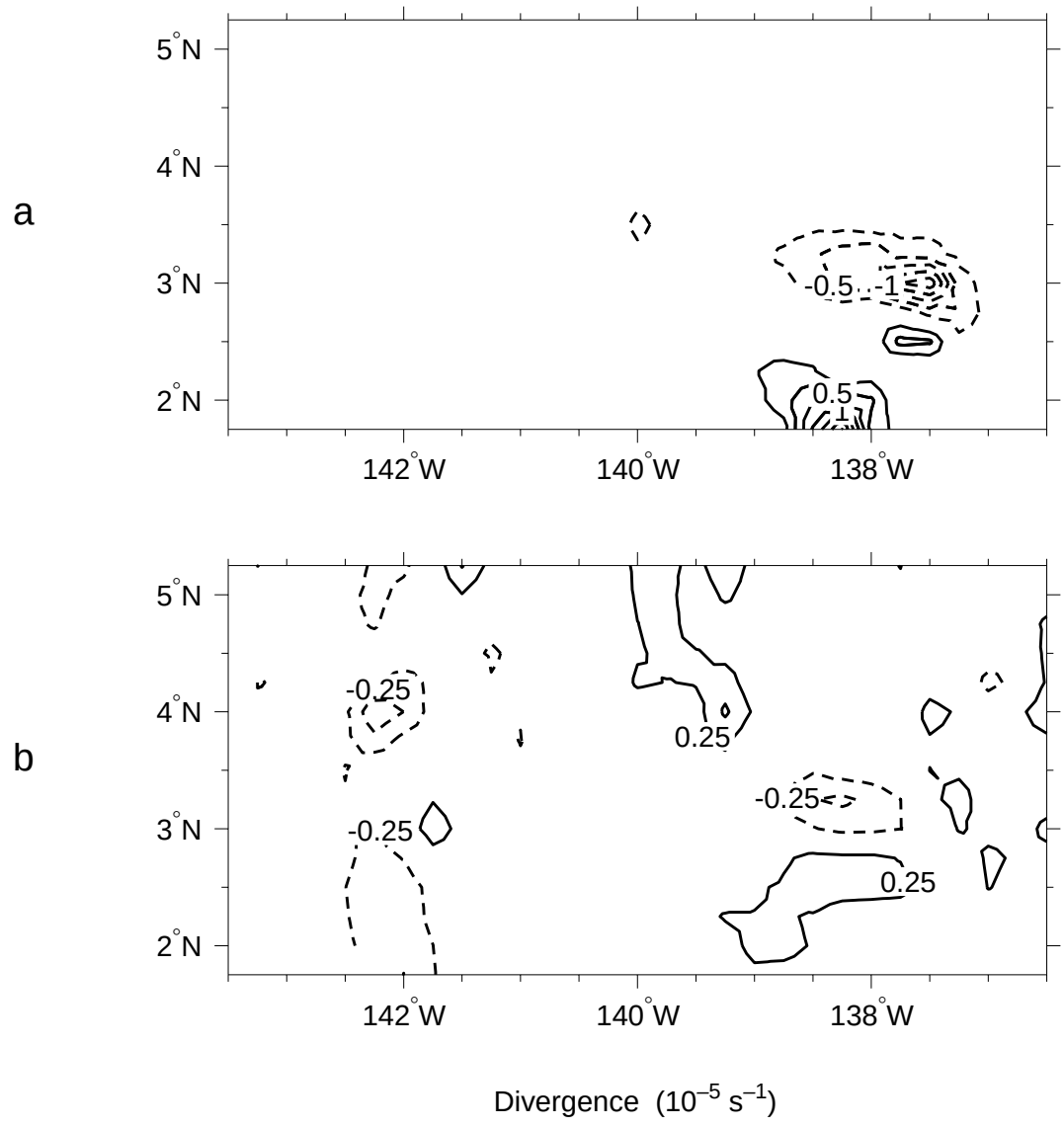

Figure 3.21: (a) Divergence averaged over 20-120 dbar and (b) divergence of the Ekman flow (Figure 3.20). Contour intervals are 0.25×10^{-5} s^{-1}.

Chapter 4

The Dynamics of a Tropical Instability

In which the salient features of a tropical instability are explained in terms of vorticity and momentum dynamics; a mechanism for regulating eddy growth is presented; and biological implications of the vortex circulation are explored.

4.1 Scale analysis

Overall, the anticyclonic flow of the vortex was coherent above the thermocline except at the perturbed equatorial front and near the center of the eddy. In consideration of these phenomena, the dynamical regimes of the vortex will be analyzed using vorticity and momentum balances. Before proceeding, however, the results can be anticipated by a scale analysis using the observations already presented.

4.1.1 momentum

By way of the ship sampling during TIWE-2 and the gridding of the data into a moving reference frame, the smallest time and horizontal length scales that can be resolved are approximately 3 days and 50 km, respectively. Thus, the flow can be assumed hydrostatic, incompressible, and Boussinesq; for simplicity, wind forcing will be expressed as a body force over the mixed layer (as in Equation (3.7)) while turbulent and viscous processes will be parameterized using a Reynold's analogy to molecular viscosity. The resulting simplified momentum equation in isobaric coordinates is, in the moving reference frame (A.1)):

$$\mathbf{u}_t + \mathbf{u} \cdot \nabla \mathbf{u} + \omega \mathbf{u}_p + \mathbf{f} \times (\mathbf{u} + \mathbf{c}) = -\nabla \phi + \frac{\tau}{\rho_o H} + \mathbf{S} \qquad (4.1)$$

where $\mathbf{u} = u\hat{i} + v\hat{j}$ is the horizontal velocity vector, $\nabla = \hat{i}\partial_x + \hat{j}\partial_y$ is the horizontal gradient operator, $\omega = dP/dt$ is the equivalent of vertical velocity in isobaric coordinates, and P subscripts denote partial derivation with respect to pressure. On the right hand side, $\Phi = \int_{ref}^{z} \rho^{-1} dz$ is the geopotential, τ is the wind stress, ρ_o is the density, H is the mixed layer depth, and $\mathbf{S}$ represents unresolved stresses resulting subgrid scale processes and turbulence.

Equation 4.1 differs from the momentum equation in the fixed Earth frame in that the geostrophic balance is unaltered - the translation velocity of the vortex, $\mathbf{c} = \hat{i}c$ appears in the Coriolis term (see Equations (2.4)-(2.6)).

Table 4.1.1 recapitulates each term in the momentum equation with the second row giving the balance in terms of characteristic scale variables, which are: U for horizontal velocity, W for vertical velocity, L for length, and D for depth. The time scale is of order 10 times L/U as the observations show that the flow was steady to within about 10%, except in the case of the 26 November wind event, during which the time scale is $O(L/U)$. Vertical velocity may be scaled using the divergence: $w(z) = \int_{z}^{0} \nabla \cdot \mathbf{u}\, dz$ so that $W \sim \nabla \cdot \mathbf{u}\, D$. It will generally be less than this, however, since we are interested in motion above the thermocline. The unresolved stresses are shown with scales appropriate for a Reynold's analogy parameterization where A_h and A_v are unknown horizontal and vertical eddy viscosity coefficients.

Normalizing by the Coriolis term, we then obtain nondimensional scales for each term in terms of the nondimensional Rossby and bulk Richardson numbers [Philander, 1976]:

Table 4.1: Scaling the momentum equation

$\mathbf{u}_t$	$\mathbf{u}\cdot\nabla\mathbf{u}$	$\omega\mathbf{u}_p$	$\mathbf{f}\times\mathbf{u}$	$\nabla\phi$	$\frac{\tau}{\rho_o H}$	$\mathbf{S}_h$	$\mathbf{S}_v$
$\frac{U}{T}$	$\frac{U^2}{L}$	$\frac{WU}{D}$	fU	$\frac{\Delta\phi}{L}$	$\frac{\tau}{\rho_o H}$	$A_h\frac{U}{L^2}$	$A_v\frac{U}{D^2}$
$\frac{Ro}{10}$	Ro	$<\frac{\nabla\cdot\mathbf{u}}{f}$	1	$Ro Ri\delta$	$\frac{\tau}{fU\rho_o H}$	$\frac{A_h}{fL^2}$	$\frac{A_v}{fD^2}$
$<0.1(\sim 1)$	$(0.5-1)$	$<(0.5-1)$	1	1	0.2	?	$\ll 1$

where

$$Ro = \frac{U}{fL} \qquad and \qquad Ri = \frac{g'd}{U^2} = \frac{\Delta\phi}{U^2\delta}$$

where g' is the reduced gravity and δ is the aspect ratio of thermocline displacements d to the depth scale D. Over the upper layer D is the thermocline depth and $\delta < 1$, whereas at the thermocline the aspect ratio is unity.

The results are shown in the third row of Table 4.1.1. From the observations already presented, typical scales for the vortex are: $L \sim 10^5$ m, $U \sim 0.5$ m/s, $D \sim 150$ m, $\nabla\cdot\mathbf{u} < 0.5$, $\Delta\phi \sim 0.5$ m^2/s^2, and $f \sim 10^{-5}$ s^{-1}. At the front the length scale decreases ($L \sim 50$ km), the velocity scale increases ($U \sim 1$ m/s), and the divergence is nearly f. Thus, the Rossby number ranges from $Ro \sim 0.5$ over most of the region to $Ro \geq 1$ near the disturbed front. These values are used to place magnitudes on the terms in the last row of Table 4.1.1.

The combination of the Rossby and Richardson numbers in the geopotential gradient term has an interesting implication; if we restrict our interest to steady flows in which the pressure gradient is always the dominant term to be balanced (ie: neglect internal

waves, inertial oscillations, etc.), then for quasigeostrophic flows ($Ro \ll 1$) Coriolis must balance the pressure gradient ($1 \sim RoRi\delta$) and the Richardson number must be large ($Ri \gg 1$), while for large Rossby number flows ($Ro \geq 1$) advection must take up the balance ($Ro \sim RoRi$) so that the Richardson number is never less than unity ($Ri = 1$).

To the extent that this bulk Ri behaves like a gradient $Ri_g = N^2/(\partial\ U/\partial\ z)^2$, the critical value of ($Ri_g \leq 1/4$), which is required for unstable stratified shear flow, will not occur. Since vertical eddy diffusion must be related to the stability of the vertical shear, we now have an heuristic argument that it will not play a dominant role in the dynamics. Assuming then that $A_v/(fD^2) < 0.1$, places an upper limit on the vertical eddy viscosity: $A_v < 2 \times 10^{-2}$ m^2/s.

As discussed in the previous chapter, temporal changes in the wind forcing can cause significant deviations from the steady flow assumption - the wind stress exceeded 0.25 Pa (Figure 3.17) during 25-27 November. Yet, the mean wind stress, which is expected to balance with the steady, flow is much weaker at about 0.05 Pa. Taking τ ~0.05 Pa, H ~50 m and ρ_o ~1025 kg/m^3 gives a relative magnitude in Table 4.1.1 of 0.2. In other words, the mean wind driven Ekman currents in the mixed layer are at most 20% of the geostrophic currents, or roughly 10 cm/s. However, for the wind event when the wind stress was much larger we get a relative magnitude of 1! Whereas such large forcing results in local accelerations of the flow this magnitude is best understood as a possible scale for the unsteadiness of the momentum balance; it is indicated in parentheses in Table 4.1.1.

The last row of Table 4.1.1 summarizes the relative magnitudes of all the terms in the the momentum balance. Although significant for inducing aliased unsteady flows, the winds do not play a major role for the steady flow. Meanwhile, vertical advection

is relatively small, and vertical eddy turbulence is believed to be small based on the importance of the geopotential gradient term. Consequently, the most likely dynamical balance for the vortex is a steady, quasigeostrophic one, except near the front where the nonlinear terms will be important and horizontal eddy turbulence, which has not been addressed, may also contribute. Thus:

$$\mathbf{u} \cdot \nabla \mathbf{u} \; + \; \mathbf{f} \times \mathbf{u} \; = \; -\nabla \phi \; + \; [\mathbf{S}] \tag{4.2}$$

4.1.2 vorticity

Let us now consider the vorticity equation, which is obtained by taking the curl of (4.1):

$$\begin{aligned} \zeta_t \; + \; \mathbf{u} \cdot \nabla \zeta \; + \; \omega \zeta_P \; + \; \beta v \; + \; (\zeta + f) \nabla \cdot \mathbf{u} + (u_P \omega_y - v_P \omega_x) \; = \\ \frac{\nabla \times \tau}{\rho_o H} \; + \; T \end{aligned} \tag{4.3}$$

where $\zeta \; = \; v_x - u_y$ is the relative vorticity component in the vertical direction and T represents unresolved torques generated by the subgrid scale and turbulent stresses. The terms describe, in order of appearance: local rate of change, horizontal advection, and vertical advection of relative vorticity; advection of planetary vorticity; vortex stretching; and vortex tilting in the meridional and zonal planes. On the right side are torques exerted on the fluid: vortex stretching via Ekman pumping; and vorticity eddy diffusion in the horizontal and vertical. If the flow is depth independent over the upper layer, of thickness h, and torques are absent, Equation (4.3) may be rewritten as conservation of shallow water potential vorticity:

$$\frac{D}{Dt}\left(\frac{\zeta + f}{h}\right) = 0 \tag{4.4}$$

where $D/Dt = \partial_t + \mathbf{u} \cdot \nabla$ is the material derivative.

For shallow water flow, potential vorticity conservation describes all changes in the relative vorticity of a parcel as caused by meridional movements (changes in planetary vorticity) and changes in layer thickness (vortex stretching). The latter process is related to divergence of the horizontal flow. For this reason we seek to explain the divergence pattern of tropical instabilities as constrained by potential vorticity conservation. However, Equation (4.4) does not lend itself to a budget calculation owing to the occurrence of the vortex stretching term in the denominator and the omission of external torques, so we will focus on estimating the terms in the more general vorticity equation (4.3) instead.

Scaling of the vorticity equation (4.3) proceeds with a substitution of scale variables and normalization by $\zeta\ f$, as shown in Table 4.1.2. Using the same scales as before and taking $\beta \sim 2{\times}10^{-11}$ m^{-1}s^{-1}, $\zeta \sim\ 0.5f{-}f$ (see Figure 4.1), and $\nabla{\times}\tau \sim\ 2.5{\times}10^{-7}$ Pa/m (see Figure 3.17b) we obtain relative dimensionless magnitudes (last row of Table 4.1.2).

The dominant terms are horizontal advection of relative vorticity and vortex stretching. Planetary vorticity advection is significant but cannot account for any significant imbalances. Ekman pumping is negligible. Consequently, the expected vorticity balance is:

$$\mathbf{u} \cdot \nabla\zeta\ +\ (\zeta + f)\nabla \cdot \mathbf{u}\ =\ [T] \tag{4.5}$$

Table 4.2: Scaling the vorticity equation

ζ_t	$\mathbf{u}\cdot\nabla\zeta$	$\omega\zeta_P$	βv	$(\zeta+f)\nabla\cdot\mathbf{u}$	$(u_P\omega_y - v_P\omega_x)$
$\frac{Ro}{10}$	Ro	$< \frac{\nabla\cdot\mathbf{u}}{f}$	$\frac{\beta U}{\zeta f}$	$\frac{\nabla\cdot\mathbf{u}}{f}$	$\frac{Ro\nabla\cdot\mathbf{u}}{\zeta}$
< 0.1	$(0.5-1)$	$< (0.5-1)$	0.2	$(0.5-1)$	$< (0.5-1)$

$\frac{\nabla\times\tau}{\rho_o H}$	T_h	T_v
$\frac{\nabla\times\tau}{\zeta f\rho_o H}$	$\frac{A_h}{fL^2}$	$\frac{A_v}{fD^2}$
0.05	$?$	$\ll 1$

Divergence patterns are likely to be directly related to advection of relative vorticity. Since the advection term is nearly the material derivative in the moving frame (see Equation (2.7)), as parcels enter regions of different relative vorticity they will stretch or shrink to adjust. However, if potential vorticity is not conserved, parcels will also have to adjust to torques from horizontal turbulence. In that case an upper bound may be placed on possible values of the eddy viscosity: $A_h \leq 10^5$ m^2/s.

4.2 Vortex dynamics

In estimating terms in the dynamical balances, gradients are calculated using central differencing in the same way that divergence and vorticity were calculated (see Equations (3.1)-(3.2)). Vertical velocity is taken as a simple vertical integration of the divergence field by assuming a rigid lid at the surface:

$$w^{i,j,k} = \begin{cases} (\nabla \cdot \mathbf{u})^{i,j,1} \, (z_o + \frac{\Delta z}{2}) & \text{k=1,} \\ (\nabla \cdot \mathbf{u})^{i,j,1} \, (z_o + \frac{\Delta z}{2}) \; + \; \sum_{n=2}^{k-1} (\nabla \cdot \mathbf{u})^{i,j,n} \, \Delta z \; + \; (\nabla \cdot \mathbf{u})^{i,j,k} \, \frac{\Delta z}{2} & \text{k>1.} \end{cases} \tag{4.6}$$

where k indicates the kth depth range, z_o is the top 20 dbar unsampled by the ADCP, and $\Delta z = 10$ dbar is the vertical spacing of the gridded data. The factors of 1/2 are added to center the values of w in the range over which the data are gridded.

Standard errors are propagated through all calculations using Monte Carlo experiments; gradients are treated as the divergence was (see Equations (3.3)-(3.4)), while sums, products, and quotients all have appropriate trials.

4.2.1 vorticity dynamics

Figure 4.1 shows the relative and absolute vorticity advection terms (ζ and $\zeta + f$). The contoured fields have been normalized by 10^{-10} s^{-2} (the value of the Coriolis parameter f near 4°N) to allow direct comparison with the nondimensional magnitudes in Table 4.1.2.

As expected from the scale analysis, most of the flow field has values less than 0.5, while reaching 1 in the region 142-141°W, which coincides with the front and associated convergence/divergence dipole (see Figures 2.11, 3.13a, and 3.1). Moreover, these features are significant, with signal to noise ratios greater than one.

A positive band along the front indicates an increase in vorticity following parcels if the flow is steady, since in that case advection is equivalent to the material derivative (see Equation 2.7). On the other hand, if brought to the right hand side of the vorticity equation (4.3), and viewed in the fixed Earth frame (where the flow is unsteady) this

term represents negative vorticity advection, meaning that the vorticity is decreasing locally.

The vorticity advection pattern is directly related to the cyclonic shear of the leading edge of the vortex (Figure 2.11) as opposed to planetary advection of the northward flow, which is much smaller. Relative vorticity dominates the dynamics near the front and even over most of the flow field, owing to the relatively small length scale of the eddy in comparison to variations in the Coriolis parameter.

The other dominant term in the vorticity balance is vortex stretching, shown in Figure 4.2a, which reflects the intense convergence along the front collocated with large cyclonic vorticity. However, the sum with vorticity advection clearly shows that the vortex stretching is not a simple result of advection, as the imbalance has both positive and negative values of magnitude one (Figure 4.2b).

Since the wind stress curl is far too small to account for the imbalance (we saw in Chapter 2 Section 3.4 that the winds were significant only near 138°W) it must represent either unresolved temporal changes in the flow field or torques from eddy turbulence. To help sort out the situation a similar analysis was performed on a tropical instability vortex from the POCM on its day 325 near 140-135°W. The vortex stretching and net balance are each plotted as with the observations from TIWE-2 in Figure 4.3.

Without going into much detail, the correspondence between the POCM and TIWE-2 fields is more striking - the vortex stretching is nearly identical while the net balance shows in each case a negative-positive-negative tripole of order ≥ 0.5.

4.2.2 turbulence at the front

Since the vortices in the model are quite regular and steady over periods of order a month, the implication is that the net vorticity imbalance near the front represents the unestimated subgrid scale and turbulent torques.

Therefore, we conclude that the vorticity balance of Equation (4.5) holds at the front with unresolved eddy torques playing a significant role. As a parcel approaches the front in the northward flow it experiences an increase in positive vorticity by entering the cyclonic shear of the leading edge. At the same time, equally large eddy vorticity diffusion provides torques on the parcel as it enters the region. Specifically, roughly east of 142°W the eddy torque induces cyclonic vorticity while to the west it creates anticyclonic vorticity. In the former case, this is nearly balanced by the vorticity advection, while in the latter the two reinforce each other to induce large vortex stretching.

Hence, the intense convergence which is typically found along the north equatorial front in the presence of TIWs, appears to result from relative vorticity advection and turbulent stress torques. As was discussed in Chapter 3 Section 3.3, the subduction associated with the frontal convergence is probably responsible for maintaining the shape of the cold water cusps, and therefore the front itself. However, if the turbulent stresses which induce the subduction are too large they will simultaneously smear out the front. Based on this reasoning an upper limit for the eddy temperature diffusion coefficient was estimated to be $K_h \leq 5 \times 10^2$ m^2/s. On the other hand, the eddy viscosity must be much larger to give the observed torques: $A_h \sim 10^4 - 10^5$ m^2/s, giving a horizontal turbulent Prandtl number of:

$$Pr_h = \frac{A_h}{K_h} \sim 100 - 1000 \tag{4.7}$$

which would imply that the turbulence at the front transfers momentum more efficiently than heat.

However, the scales which were used to infer the diffusivity coefficient are unresolved by our objective mapping. The smallest resolved scales are 25-75 km, not 1-10 km. This brings the Prandtl number down to only 10-100. Furthermore, there is no reason to believe that the unresolved dynamics at the front are adequately parameterized by a Reynold's analogy. While convenient, it belies the anisotropic nature of the circulation at the NEF.

Thus, we must conclude that subgrid scale advection of temperature, momentum, and vorticity are crucial to modeling the frontal dynamics and thermodynamics. Still, it is unclear how this effects eddy resolving global circulation model simulations of oceanic phenomena which involve frontal dynamics. We will find evidence in Chapter 5 that the front is intensified by vortex flow and is not the progenitor (as hypothesized by McCreary and Yu [1992]). Thus, our use of the POCM in analyzing TIVs seems justified.

4.2.3 polar coordinates

Since we are investigating the dynamics of a vortex, our analysis of the vector momentum will be simplified by working in polar coordinates centered on the axis of the eddy, with r the radial distance positive outward and θ the azimuthal angle positive counter clockwise:

$$r = \sqrt{x^2 + y^2} \quad , \qquad \theta = \arctan\left(\frac{y}{x}\right) \tag{4.8}$$

The radial and azimuthal velocity components are:

$$\begin{pmatrix} U \\ V \end{pmatrix} = \begin{pmatrix} \cos(\theta) & \sin(\theta) \\ -\sin(\theta) & \cos(\theta) \end{pmatrix} \begin{pmatrix} u \\ v \end{pmatrix} \tag{4.9}$$

which also applies to all other vector components such as geopotential gradient, wind stress, *etc.* The material derivative of velocity, which involves changes in coordinate directions following the motion, transforms as:

$$\begin{pmatrix} \frac{DU}{Dt} \\ \frac{DV}{Dt} \end{pmatrix} = \begin{pmatrix} \cos(\theta) & \sin(\theta) \\ -\sin(\theta) & \cos(\theta) \end{pmatrix} \begin{pmatrix} \frac{Du}{Dt} \\ \frac{Dv}{Dt} \end{pmatrix} + \begin{pmatrix} -\frac{V^2}{r} \\ \frac{UV}{r} \end{pmatrix} \tag{4.10}$$

Hence, the momentum component equations in polar coordinates become [Batchelor, 1967; Kundu, 1990]:

$$U_t + \mathbf{u} \cdot \nabla U - \frac{V^2}{r} - f(V + c^\theta) = -\frac{\partial \phi}{\partial r} + \frac{\tau^r}{\rho_o H} + S^r \tag{4.11}$$

$$V_t + \mathbf{u} \cdot \nabla V + \frac{UV}{r} + f(U + c^r) = -\frac{1}{r}\frac{\partial \phi}{\partial \theta} + \frac{\tau^\theta}{\rho_o H} + S^\theta \tag{4.12}$$

where r and θ superscripts denote the radial and azimuthal components of a vector, $\mathbf{c} = c^r\ \hat{r} + c^\theta\ \hat{\theta}$ is the vortex translation velocity, and $\mathbf{S} = S^r\ \hat{r} + S^\theta\ \hat{\theta}$ represents turbulent stresses. Aside from the simplification of following motion around the vortex, Equation (4.12) differs from Equation (4.1) in the addition of two terms, the centripetal acceleration ($-V^2/r$) and a Coriolis-like term (UV/r). Flows in which these terms play a dominant role are called cyclostrophic.

Each of the terms in Equation (4.12) were calculated directly from the gridded fields using the transformations given by Equations (4.8)-(4.10). In the following discussion, the terms "force" and "acceleration" will be used specifically to refer to terms which appear on the right and left hand sides respectively of Equation (4.12). By "force," the more cumbersome "force per unit mass" will be understood.

4.2.4 forcing terms

Before including the geopotential gradient in the momentum balance, corrections were made for the mean zonal currents and high frequency fluctuations of the thermocline depth.

Underlying the thermocline depth signal of the vortex is a meridional slope associated with the thermal wind balance of the mean zonal currents. The tropical ridge, or deepest point of the thermocline, occurs ideally where the mean zonal velocity is zero. However, the SEC is not always restricted to the thermocline, so that dynamic height calculations in the region cannot safely assume a level of no motion [Chiswell *et al.*, 1995]. To compensate for this problem, the ADCP measurements at 300 dbar were averaged over 1/4° bins and used to infer a geopotential gradient correction assuming geostrophic balance Therefore, the true geopotential gradient is estimated as:

$$\frac{\partial \phi}{\partial y}\Big|_z = \frac{\partial \phi}{\partial y}\Big|_{z/300} - f\overline{u}_{300} \tag{4.13}$$

where the subscripts indicate geopotential relative to 300 dbar and velocity at 300 dbar.

The velocity error was taken as a simple standard deviation, with the geopotential gradient error equal to f times this. The mean zonal velocities at 300 dbar are as high

as 20 cm/s, giving a correction of about -0.15 to 0.15×10^{-5} m/s^2 (Figure 4.4). No attempt was made to correct for the mean meridional currents.

The resulting geopotential gradient components are shown in Figure 4.5. The field shows some azimuthal symmetry, to be expected from the central high pressure, but is overwhelmed by large spikes on a relatively small scale (<75 km). Unlike the velocity field, the geopotential and thermocline depth are sensitive to high frequency motions such as internal waves. These temporal changes in the thermal structure, which are not indicative of the vortex structure, are aliased into the moving frame by the hydrographic sampling.

Consequently, an attempt has been made to remove this noise through a further smoothing of the geopotential gradient, beyond the initial objective mapping of the observations. A simple linear boxcar filter of half width 1/2° was applied separately in the direction of each gradient component. In this way, changes from one CTD cast to the next which were not associated with the larger scale thermal structure of the vortex are hopefully removed.

The final geopotential gradient for use in the momentum balance is shown in Figure 4.6. In the radial component, the force is everywhere positive, owing to the central high pressure of the vortex. The largest values occur near 140°W from 2.5-4°N, and eastward from 2.5-3°N. The azimuthal component shows clockwise forcing in the eastern half of the vortex and counterclockwise to the west.

The other forcing term we can estimate is the mean wind stress, which is quite small compared to the geopotential (Figure 3.17). The southeast trades transform into polar coordinates as positive and negative radial forcing in the northwest and

southeast, respectively, and azimuthal forcing which approximately partially cancels the geopotential gradient in the southwest and northest of the region.

4.2.5 acceleration terms

As expected from the scaling in Section 4.1, a good portion of the geopotential gradient forcing is accounted for by a geostrophic balance (Figure 4.7). The Coriolis term shows an overall pattern of positive radial acceleration and the separation between azimuthal accelerations and decelerations in the eastern and western halves of the vortex, although the magnitudes do not match with the geopotential in several places.

The remaining significant terms are the centripetal and advective accelerations, given in Figures 4.8 and 4.9. As with the wind, the centripetal terms are generally less than half the geopotential, with parcels accelerating radially outward as they circulate around the vortex, and slowing down in their anticyclonic motion near 3.5°N, 140.5°W (Figure 4.8). Consequently, the large Rossby number character of the flow, especially near the front, cannot be explained as an artifact of the eddy circulation.

The bulk of the contribution to large Ro is directly related to parcels entering varying flow regimes. The advective terms are particularly interesting since for steady flow they represent the accelerations following the flow (see Equation (2.7)). Parcels encountering the front slow down, as evidenced by the radially inward and counterclockwise accelerations along 142°W. Near3°N, 140°W parcels are accelerated radially outward. These patterns are again largely confirmed by the POCM - parcels along the front slow down, while those to the southeast of the front accelerate outward from the vortex center (Figure 4.10).

This last feature corresponds closely to the large divergence which was discussed earlier, but left unexplained by the vorticity balance (compare with Figures 3.1 and

3.6). In the next section we will explore the possibility that this net forcing on parcels results from inertial instability.

With all the terms calculated the momentum balance is summarized in Figure 4.11. The largest net imbalance in both the radial and azimuthal components occurs along the front, most likely indicating the presence of turbulent eddy stresses. For the flow to be steady along the front would require radially inward and counterclockwise forcing from the stresses, which is consistent with a frictional type force opposing the vortex flow in that region.

The turbulent stresses were found in the vorticity balance to probably only be important near the front; yet, a significant imbalance appears between 140 and 138°W. The only other term which cannot be directly estimated is the local time rate of change, or the unsteadiness of the flow. However, strong evidence was found in Chapter 3 Section 3.4 that a period of strong winds during 25-27 November could have caused a thermocline deepening and temporally varying Ekman currents which would violate the steady flow assumption of the moving reference frame. Asymmetry in the geopotential field and unreasonable divergence patterns near 2-3.5°N, 138°W provided strong support for this hypothesis.

Hence, it seems likely that the failure to close the momentum balance from 140-138°W is associated with the aliasing of temporal changes in the geopotential field into spatial gradients: the deepening of the thermocline at 138°W is consistent with the apparent net clockwise acceleration to the west. It is important to realize that this aliasing of temporal gradients is a sampling problem of the experiment and not an indication of unsteady vortex flow.

Keeping in mind these caveats then, the momentum balance may then be summarized as predominantly quasi-geostrophic over most of the eddy, with large turbulent stresses at the front.

$$\mathbf{u} \cdot \nabla \mathbf{u} \; + \; \mathbf{f} \times (\mathbf{u} + \mathbf{c}) \; = \; -\nabla \phi \; + \; [\mathbf{S}] \tag{4.14}$$

4.3 An inertially limited vortex

Although the intense dipole of convergence and divergence observed during TIWE-2 is predicted by numerical simulations of tropical instabilities ([Philander *et al.*, 1986; Harrison, 1996] (and see Figure 3.6), the origin and significance of the pattern has remained unknown.

We have shown that the convergence along the leading edge of the front can be explained as a vortex stretching response to advection of relative vorticity, and torques from turbulent stresses encountered by parcels as they cross the front in the northward flow of the vortex. However, vorticity dynamics did not lend any insight into the upwelling feature because the strongest divergence occurs simultaneously with absolute vorticity near zero, in which case vortex stretching is a free parameter (see Figures 3.1,3.2 and 3.6,3.7 and Equation (4.3)).

Vertical circulation patterns not unlike the one in Figure 3.12 are also found in models of inertial instability in the atmosphere [Dunkerton, 1981; Dunkerton, 1983] and in laboratory experiments of centrifugal instability [Kundu, 1990], so that a consideration of the relevant dynamics may give insight into our observations. In this section we apply the concept of vortex instability to the TIWE-2 eddy to explain the pattern of upwelling and near zero absolute vorticity near the vortex center.

4.3.1 vortex instability

Rayleigh [1916] first described a necessary and sufficient condition for centrifugal instability of an axisymmetric flow between concentric cylinders in terms of energy release during the exchange of rings in the radial-vertical plane. The same condition can also be obtained via an analysis of the forces on a parcel which is perturbed from the initial flow state:

$$\frac{d}{dr}(Vr)^2 < 0 \tag{4.15}$$

which states that an azimuthal velocity distribution is unstable if the square of the circulation decreases with radius anywhere [Kloosterziel and van Heijst, 1991].

Meanwhile, a sufficient condition for the instability of zonally symmetric parallel shear flow on an f-plane is:

$$f(f + \zeta) < 0 \tag{4.16}$$

which means that if the absolute vorticity is anywhere anticyclonic the flow is unstable [Dunkerton, 1981; Holton, 1979].

When a zonal shear flow satisfies this latter condition (Equation (4.15)) it is said to be inertially unstable, while a vortex which meets the former condition (Equation (4.16)) is centrifugally unstable. Both are parcel instabilities, of which another example is gravitational instability, or convection. Parcel instabilities involve the direct acceleration of mass away from some initial position, and are simply modeled by second order differential equations of the form:

$$\frac{d^2x}{dt^2} = -\sigma^2 x \tag{4.17}$$

For instance, in the case of gravitational stability, if σ is real ($\sigma^2 > 0$) it gives the buoyancy frequency, while an imaginary value represents the growth rate for convection. Likewise, similar coefficients can be derived for centrifugal and inertial shear flows.

The relevant coefficient for the motion of a displaced parcel in a vortex on an f-plane has been derived by Kloosterziel [1990]:

$$\sigma^2 = 2\left(\frac{V}{r} + \frac{f}{2}\right)(f + \zeta) \tag{4.18}$$

so that the condition for instability for such a flow is:

$$\left(\frac{V}{r} + \frac{f}{2}\right)(f + \zeta) < 0 \tag{4.19}$$

The conditions for centrifugal and inertial instability (Equations (4.15) and (4.16)) can each be regained by letting $f \to 0$ and $r \to \infty$ respectively. To avoid confusion with these more restrictive flows then, we will refer to this more general case as "vortex instability," since it applies to any axisymmetric vortex on an f-plane.

To understand the implications of this criterion, it helps to first nondimensionalize Equation (4.18) by the Coriolis parameter f:

$$\frac{\sigma^2}{f^2} = \left(\frac{\omega}{f} + \frac{1}{2}\right)(1 + Ro) \tag{4.20}$$

highlighting the different roles played by the vortex rotation rate $\omega = V/r$ and the rotating reference frame. Figure 4.14 shows σ/f over the parameter space defined by ω/f and Ro. When $\omega/f > 0$ the vortex is cyclonic and vice versa, while $Ro > 0$ represents anticyclonic relative vorticity. The vertical axis ($\omega/f = 0$) represents the situation for zonally symmetric shear flow - pure inertial instability occurs when $Ro < -1$. It is apparent that with the exception of very strong anticyclonic vortices ($\omega/f < -1$), negative absolute vorticity ($\zeta + f < 0$, or $Ro < -1$) is required for instability. Consequently, anticyclonic vortices are more likely to be unstable than cyclonic ones [Kloosterziel and van Heijst, 1991].

4.3.2 stability of the TIWE-2 vortex

Although conditions for parcel instability are not strictly applicable in the absence of flow symmetries, they are conceptually easy to understand. They are associated with force imbalances on fluid parcels, and can result in secondary circulation patterns which are required by symmetry to conserve mass. For this reason, vortex instability is an intriguing candidate for the upwelling feature of the TIWE-2 eddy.

The coefficient for vortex flow (Equation (4.18)) was calculated from the gridded data, revealing some isolated regions where the flow could be unstable (Figure 4.15). As should be expected, the surface layer shows regions with $\sigma^2 < 0$ that coincide well with anticyclonic absolute vorticity (see Figure 3.2). A similar correspondence is found in the depth dependence (compare Figure 4.15b with Figure 4.13a). Although most of the growth rates are not significantly different from zero, they are nearly so, and the values are large, ranging from 0.1-0.4 s^{-1} (e-folding time scales of 3-12 days).

A drawback of the stability condition (4.19) (as well as the Rayleigh and inertial conditions (4.15) and (4.16)) is that it applies only to axisymmetric vortices - zonally

symmetric for inertial instability. Separable differential equations which describe the acceleration of a parcel cannot be established for asymmetric flows, in which case numerical methods are needed [Ripa, 1989]. Thus, the applicability of this theory to the observations is difficult to assess. Likely, the absence of strong upwelling in the southward flow of the eddy is related to asymmetry of the flow, such as the intense front along the leading edge. If the distance from the vortex center r is reinterpreted as the radius of curvature of the flow, then asymmetric effects may be partially accounted for, but an analytical solution such as Equation (4.18) is not currently known [Kloosterziel, personal communication].

The above theory also does not include turbulence or friction. However, these have been shown to effect mainly vertical length scales of the secondary circulation patterns induced by centrifugal instability in the laboratory and inertial instability in the atmosphere [Kundu, 1990; Dunkerton, 1981; Dunkerton, 1983].

Therefore, the collocation of the upwelling patch with a portion of the region showing vortex instability provides strong evidence that the region around 4°N, 140.5°W was indeed unstable. Moreover, the vertical circulation cell (Figure 3.12 and radial outward acceleration of parcels in this region (Figures 4.9a and 4.13b) is exactly what would be expected in an unstable situation - in a parcel instability, the acceleration of mass away from an initial position requires, via mass conservation, the establishment of a secondary circulation pattern.

The inertial-like character of the vortex instability is important because it implies the existence of an absolute limit on the vorticity amplitude that the TIWE-2 vortex, and most likely all other TIWs, can attain: $\zeta + f = 0$. It thus provides a possible explanation for the regular, wave-like appearance of tropical instabilities over space and

time. Instead of growing to a point where they break up via turbulent stresses, or having finite amplitudes dependent on the particular current structure - which depends on space and time - the TIWs have a definite maximum vorticity and associated flow structure to be attained. Hence, the most paradoxical feature of TIWs - their wave-like appearance - may result from inertial-centrifugal instability of the shear instabilities themselves.

4.4 Biological implications

Some recent studies have discussed the possibility that tropical instabilities may be responsible for increases in primary production in the central Pacific [Yoder *et al.*, 1994; Bidigare and Ondrusek, 1996; Foley *et al.*, 1997]. Suggested mechanisms have included intensified equatorial and local upwelling and convergence of flotsam at the equatorial front. We attempt to address this issue here.

4.4.1 a proxy for zooplankton abundance

The shipboard ADCP yields ocean currents by measuring the Doppler shift of suspended particles, which are generally zooplankton grazers. Thus, a proxy for zooplankton concentrations is the backscatter intensity measured by the shipboard ADCP [Flagg and Smith, 1989]:

$$backscatter(db) = 10log_{10}(I_r/I_e) \tag{4.21}$$

where the backscatter is given in decibels of the ratio between the reflected and emitted acoustic intensities. This return has a strong decay with depth because of the signal spreading with distance from the transmitter, and along the return path. In the present

case we present the raw automatic gain control (AGC) count, which can be roughly equated to the decibel level by a constant factor (about 0.43; E. Firing, personal communication).

After removing the mean depth dependence signals associated with relative zooplankton concentrations become evident. Figure 4.16a shows the relative backscatter (cruise depth dependent mean removed) over the top 100 m as a function of time of day. The strongest signal is from the diurnal migrations of the zooplankton which move into the euphotic zone during dusk (16:48-20:24 local time, 01:48-05:24 UTC) and retreat during dawn (03:36-08:24 local, 12:36-17:24 UTC).

Therefore, to investigate other patterns which may be present over the study region, the data set is divided into two time periods: night (05:24-12:36 UTC) and day (17:24-01:48 UTC). The raw backscatter for day and night, before removing a mean, clearly shows the strong depth dependence on depth and the enhanced zooplankton abundance during night (Figure 4.16b). The data to be analyzed then, consists of these two separate data sets with their respective mean depth profiles removed.

4.4.2 backscatter in the moving frame

We wish to investigate possible relationships between zooplankton abundance and the vortex flow. However, the concentrations of grazers can be expected to depend strongly on several processes, including primary production, advection, and mixing, not to mention possible many other factors effecting the marine ecosystem. Therefore, before gridding the data, some main features can be seen in the moving frame by viewing the backscatter as observed along the ship track;

Figure 4.17 shows the relative backscatter averaged over 4 hour time intervals and the top 100 m for both day and night. Although the signal is noisy, some dominant features

may be distinguished. Higher backscatter tends to occur in the southwest of the study region, with lower return to the northwest. A strong signal, deviating from the overall pattern, appears near 2.5°N, 138°W, especially during the day. As previously discussed, this region of the moving frame is contaminated in various ways by the strong winds during 25-27 November. Most likely, these winds induced a thermocline deepening (see Chapter 3 Section 3.4) which could be responsible for local, episodic input of nutrients into the euphotic zone and an associated increase in primary production and subsequent zooplankton abundance.

The overall pattern seems to be a correlation between high zooplankton abundance and the cold water advection of the eddy (compare with Figures 2.11 and 3.13). This is easily understood in terms of the high productivity which is generally found in the relatively cold upwelling water, and a subsequent advection by the eddy.

To obtain views of the depth structure, the backscatter data were subsequently gridded in the moving frame as with all other measured variables. Zonal sections through the vortex are shown in Figures 4.18 and 4.19 (compare with Figures 3.9 and 3.15). Again the primary pattern is relatively high backscatter in the northward flow relative to the eastern half of the vortex.

Nevertheless, there is an interesting exception to this from 139-138°W at 5°N during the day and 4°N at night, where unusually high zooplankton abundance is indicated. Even though this pattern does not appear in all the sections, the correspondence with the high salinity in the strong southward flow is interesting. If this signal is directly related to advection of zooplankton by the steady flow, it implies that like salinity, grazers entrained by the vortex complete a circuit around its center.

4.4.3 instabilities and zooplankton abundance

A rich source for zooplankton is the nutrient rich, upwelled equatorial water to the south of the TIWE-2 study region. Recent studies have indicated that the marine ecosystem in the region are iron limited [Coale *et al.*, 1996b], while iron concentrations increase dramatically below the thermocline which is closer to the surface equatorward [Coale *et al.*, 1996a]. Thus, during the instability season, iron input into the euphotic zone could be accomplished at the equator via the large upwelling there. This idea is supported by the detection of enhanced pigment concentrations in the presence of TIWs [Bidigare and Ondrusek, 1996]. Since these pigments indicate primary production, they are likely to also be associated with larger than normal zooplankton abundance.

Meanwhile, direct input of iron or other nutrients near the equatorial front would result in enhanced primary production there. Observations from ship and space have indicated high concentrations of biomass at the north equatorial front in the presence of TIWs [Yoder *et al.*, 1994; Bidigare and Ondrusek, 1996]. However, while the three dimensional circulation documented here (Chapter 3) indicates strong vertical motions, there is no direct evidence of mixing across the thermocline by the circulation at the front (recall the steadiness of the thermocline depth). It should be noted, therefore, that the observations could be explained by plankton entrained in the vortex converging at the front faster than other processes, such as sinking or predation, remove them.

Consequently, we conjecture that the abundance of biomass in the presence of instabilities is an advective phenomenon north of about 2°N, and not a result of local input of nutrients into the upper layer through upwelling or turbulent mixing. While the primary production on the equator is probably enhanced during the instability season by the direct input of nutrients via upwelling [Harrison, 1996; Bidigare and Ondrusek,

1996], the subsequent entrainment by eddies to the north could transport the thriving ecosystem poleward. While detailed measurements of biological parameters during TIWE-2 are lacking, the apparent scenario is consistent with the flow structure of the TIWE-2 vortex and the observation that it entrains saline water from the south.

Thus, in the same way that tropical instabilities induce large meridional heat and fresh water fluxes [Hansen and Paul, 1984; Flament *et al.*, 1996; Baturin and Niiler, 1997] (and Chapter 5), they may be responsible for a significant flux of nutrients and plankton poleward into the North Pacific. The appearance of biomass at the front may be more an indication of a large scale meridional transport of biomass than local growth via vertical inputs through the thermocline and mixed layer. If this is the case, models of the tropical marine ecosystem will need to be coupled with fully three dimensional physical models for the response to seasonal forcing to be fully quantified.

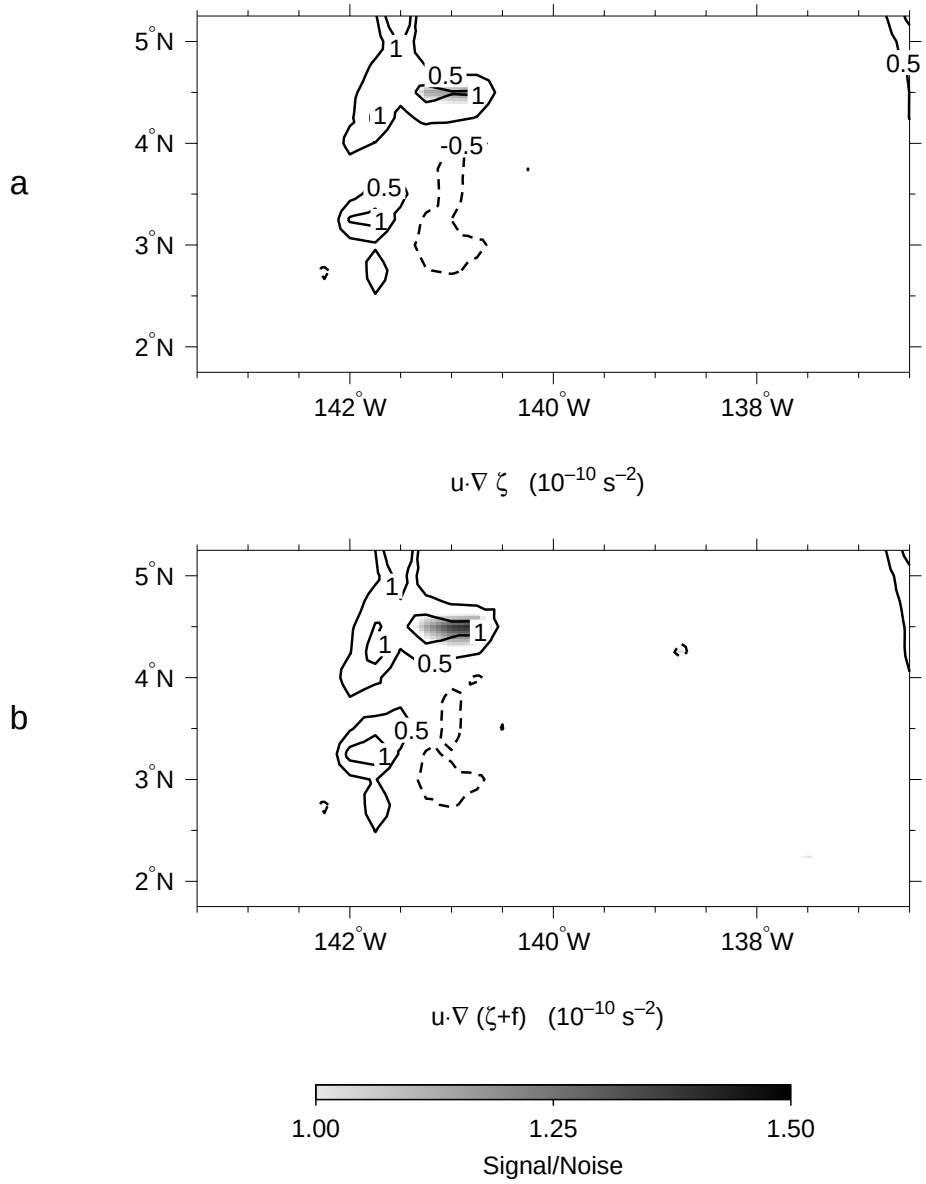

Figure 4.1: Advection of (a) relative (ζ) and (b) total ($\zeta + f$) vorticity. Contour intervals are 0.25×10^{-10} s^{-2}; shading denotes regions with a signal to noise ratio > 1.

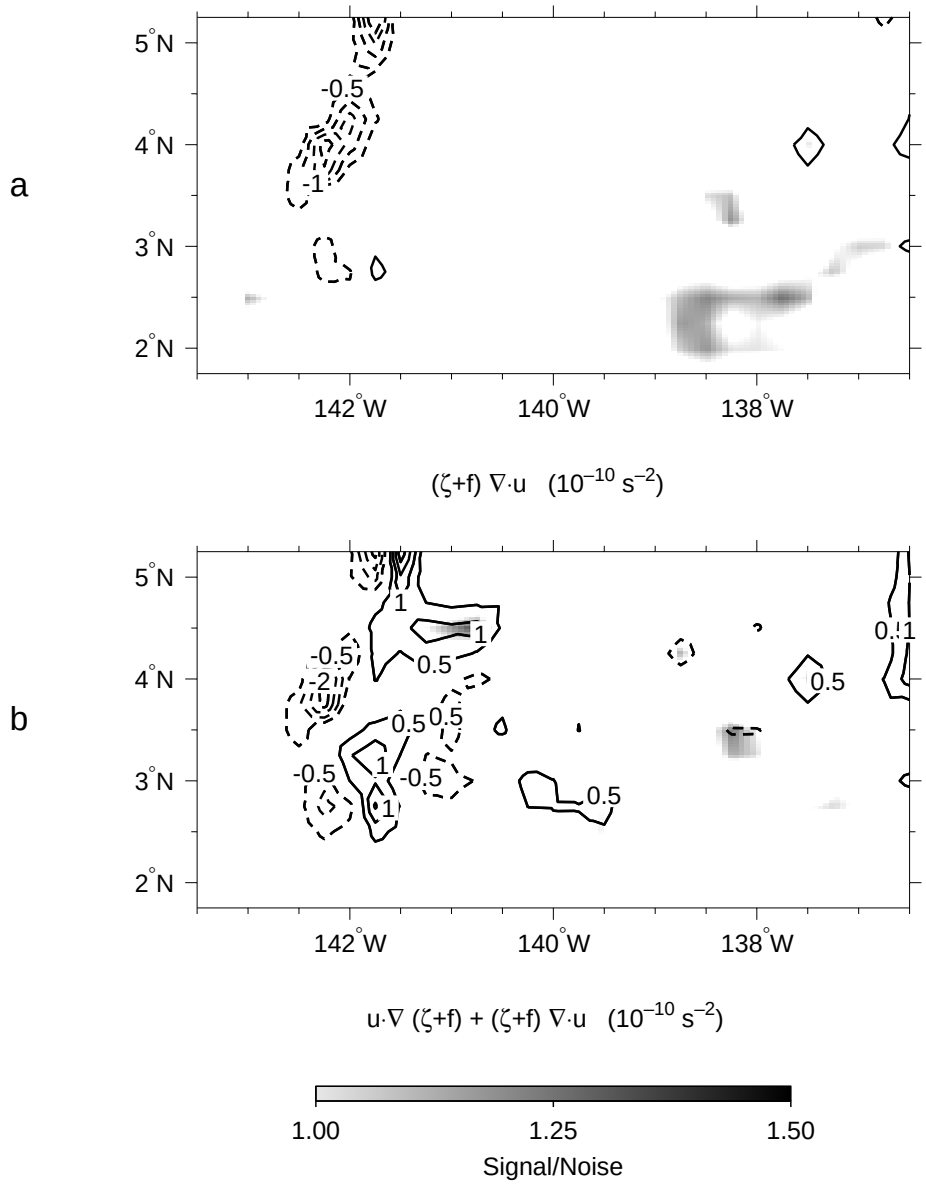

Figure 4.2: Observed (a) Vortex stretching (-(ζ+f)∇·u) and (b) the net vorticity balance - the sum of vortex stretching with total vorticity advection (Figure 4.1). Contour intervals are 0.25×10^{-10} s^{-2}; shading denotes regions with a signal to noise ratio > 1.

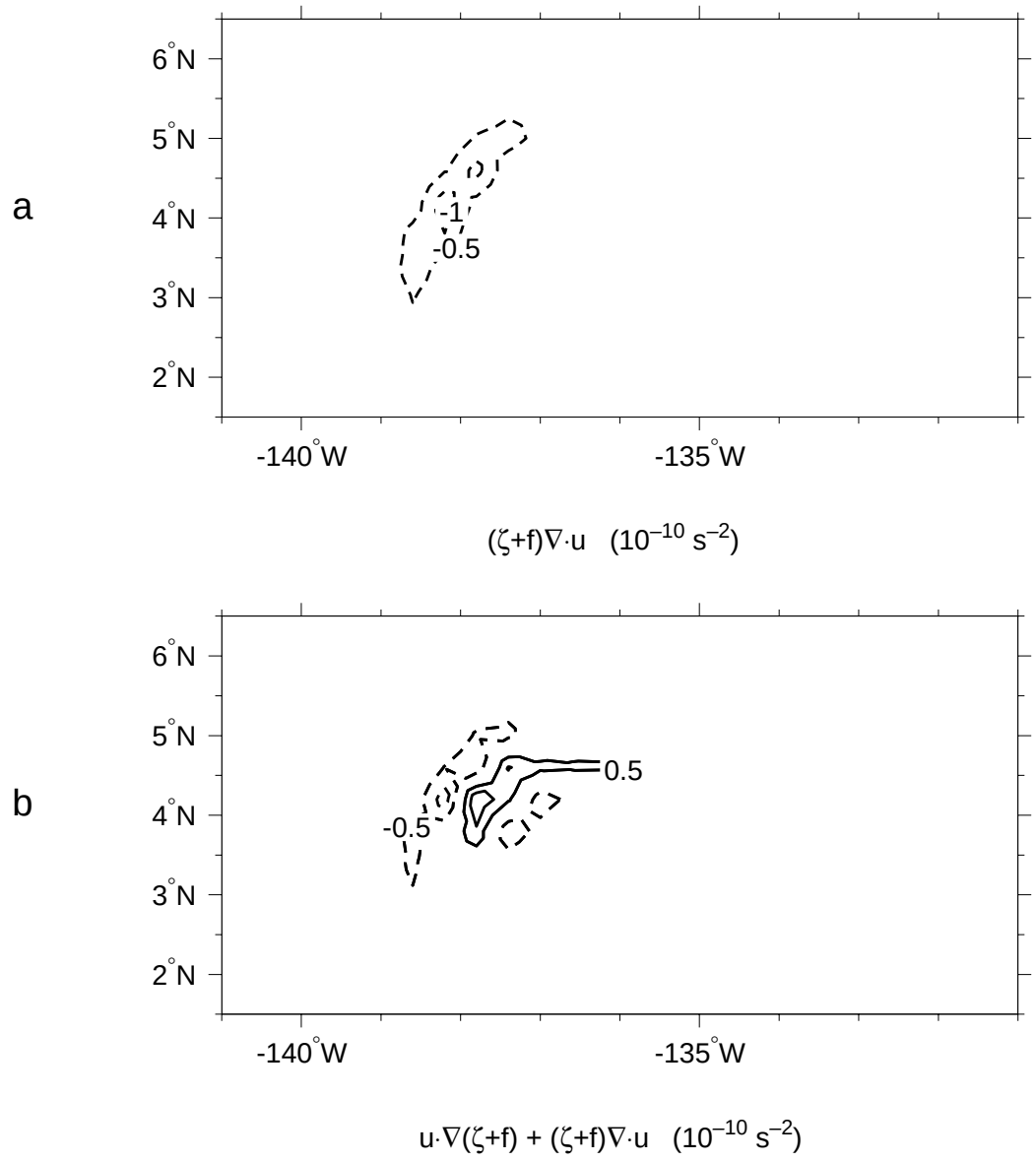

Figure 4.3: Model (a) vortex stretching (-$(\zeta + f)\nabla$·u) and (b) the net vorticity balance - the sum of vortex stretching with total vorticity advection. Contour intervals are 0.25×10^{-10} s^{-2}; shading denotes regions with a signal to noise ratio > 1.

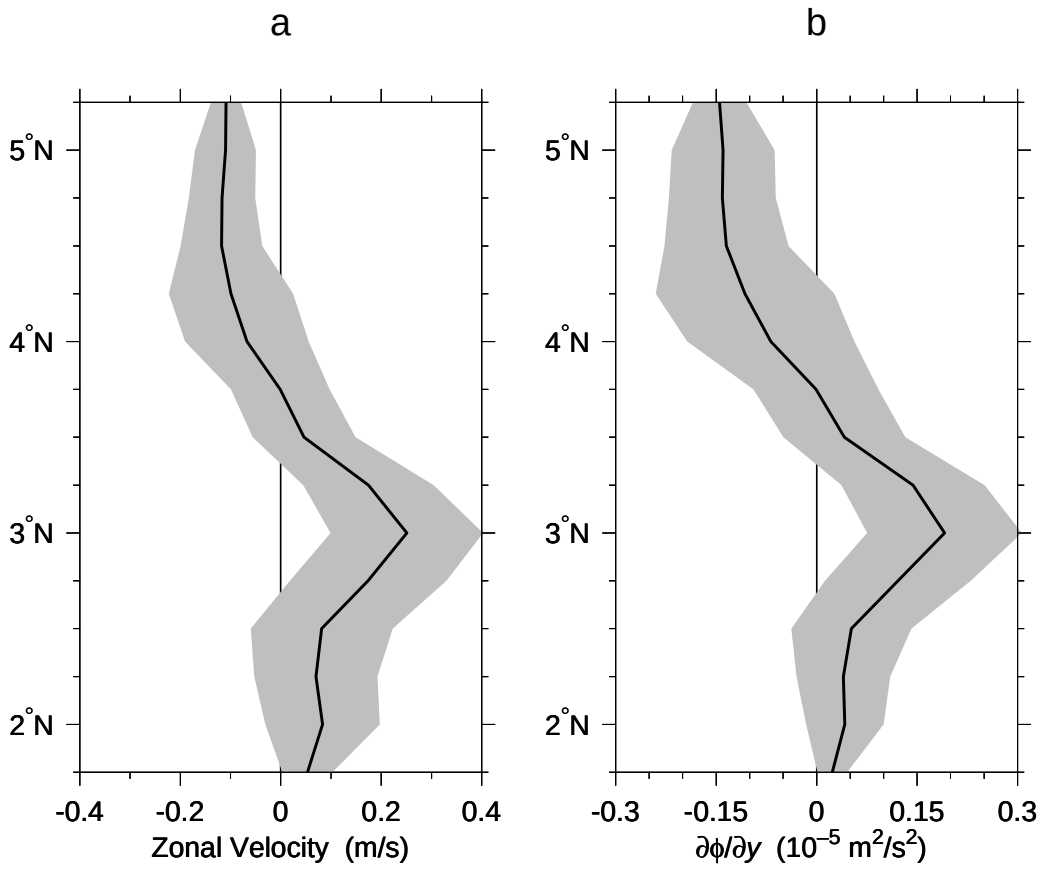

Figure 4.4: Geopotential gradient at 300 dbar inferred from ADCP velocity: (a) mean zonal velocity at 300 dbar and (b) the inferred meridional geopotential gradient at 300 dbar. Shading denotes standard errors.

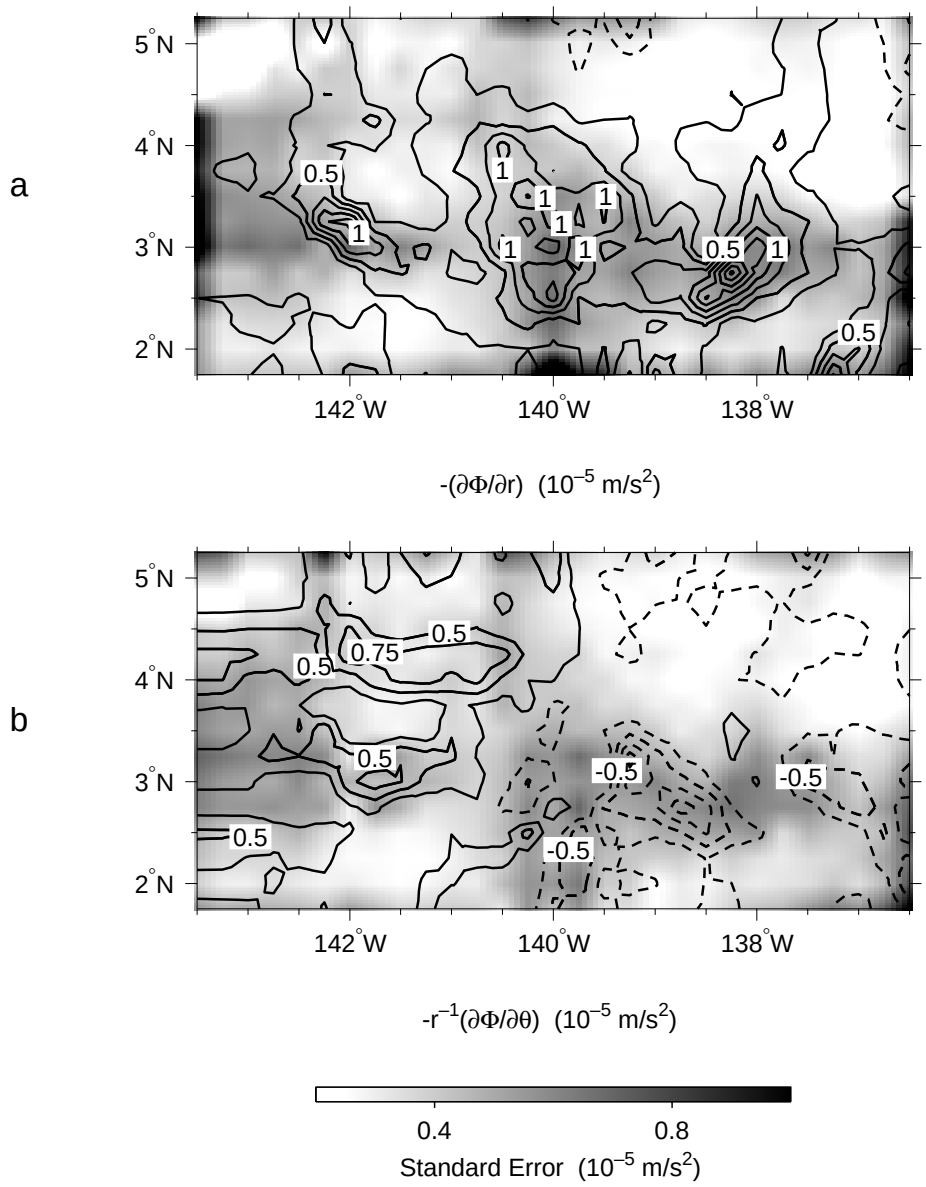

Figure 4.5: Geopotential gradient force (corrected for motion at 300 dbar) in the (a) radial and (b) azimuthal directions. Contour intervals are 0.25×10^{-5} m/s^2; shading denotes standard errors.

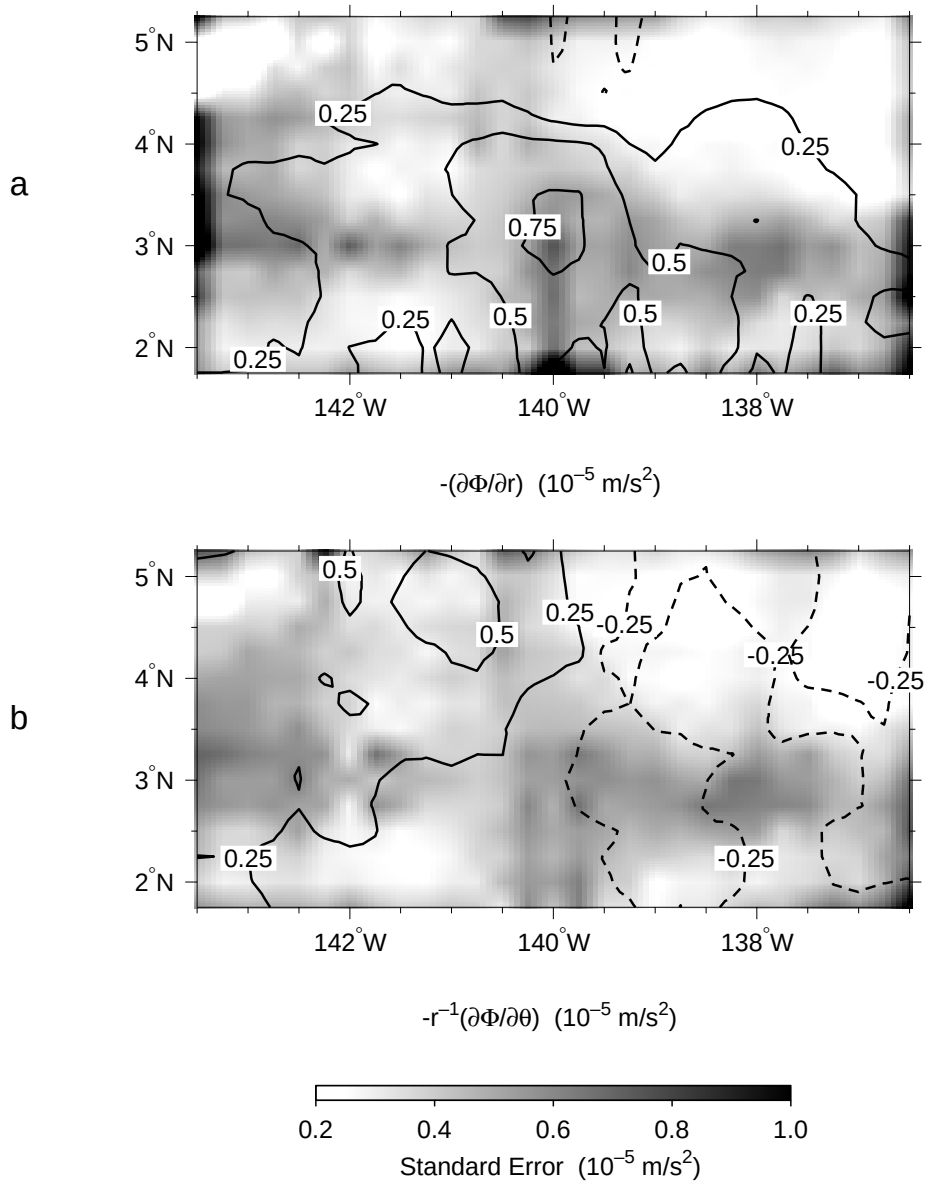

Figure 4.6: Geopotential gradient force (Figure 4.5) smoothed with a 1/2° half width boxcar filter in the (a) radial and (b) azimuthal directions. Contour intervals are 0.25×10^{-5} m/s^2; shading denotes standard errors.

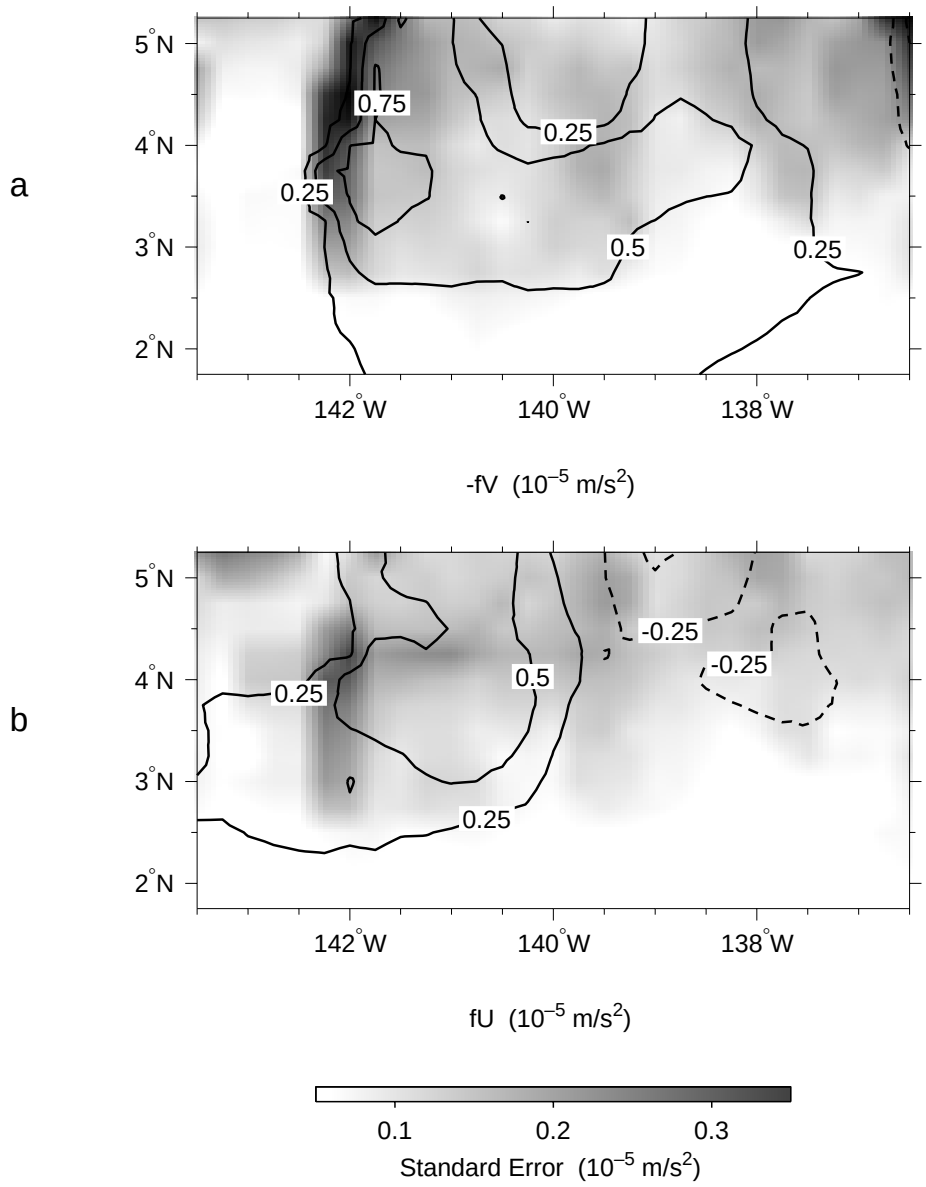

Figure 4.7: Observed Coriolis acceleration in the (a) radial and (b) azimuthal directions. Contour intervals are 0.25×10^{-5} m/s^2; shading denotes standard errors.

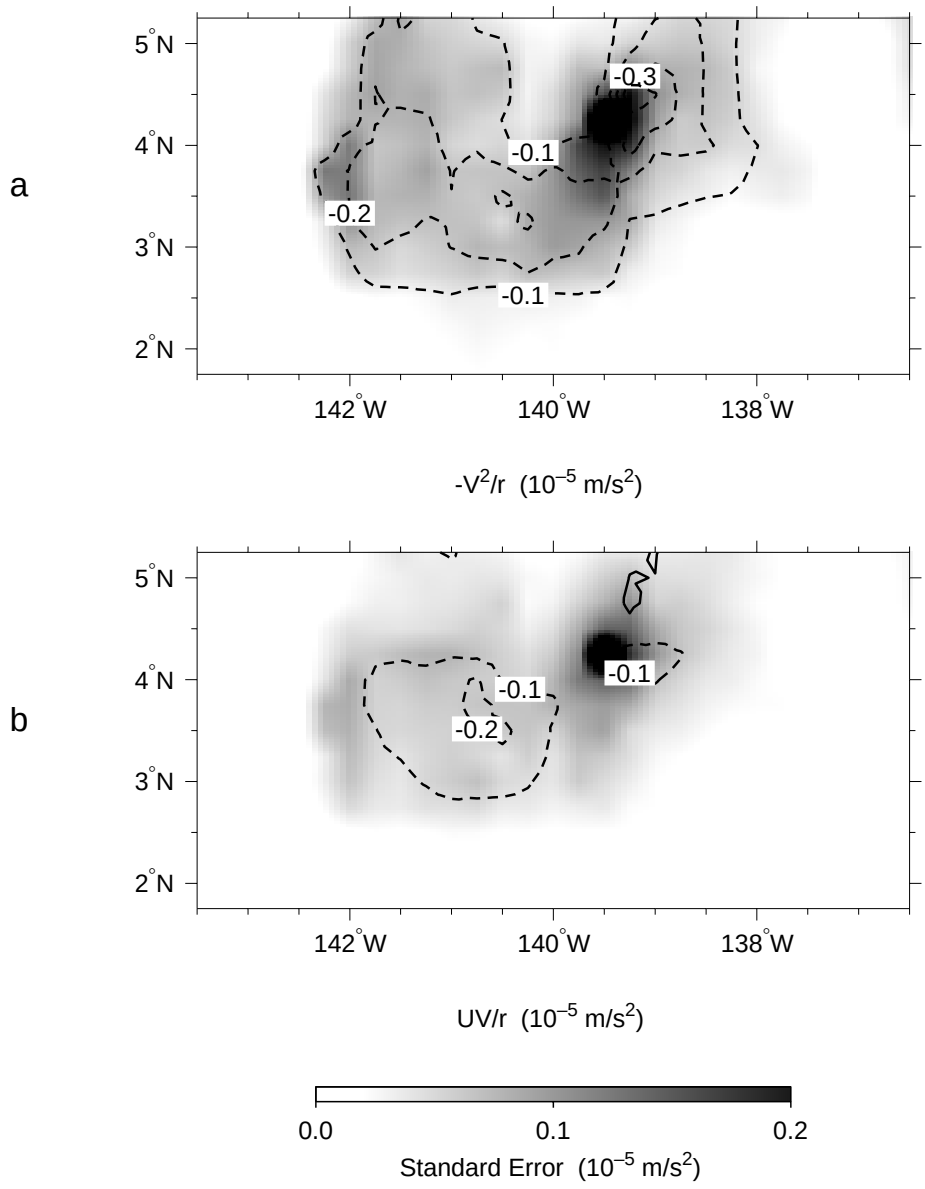

Figure 4.8: Observed Centrifugal acceleration in the (a) radial and (b) azimuthal directions. Contour intervals are 0.25×10^{-5} m/s^2; shading denotes standard errors.

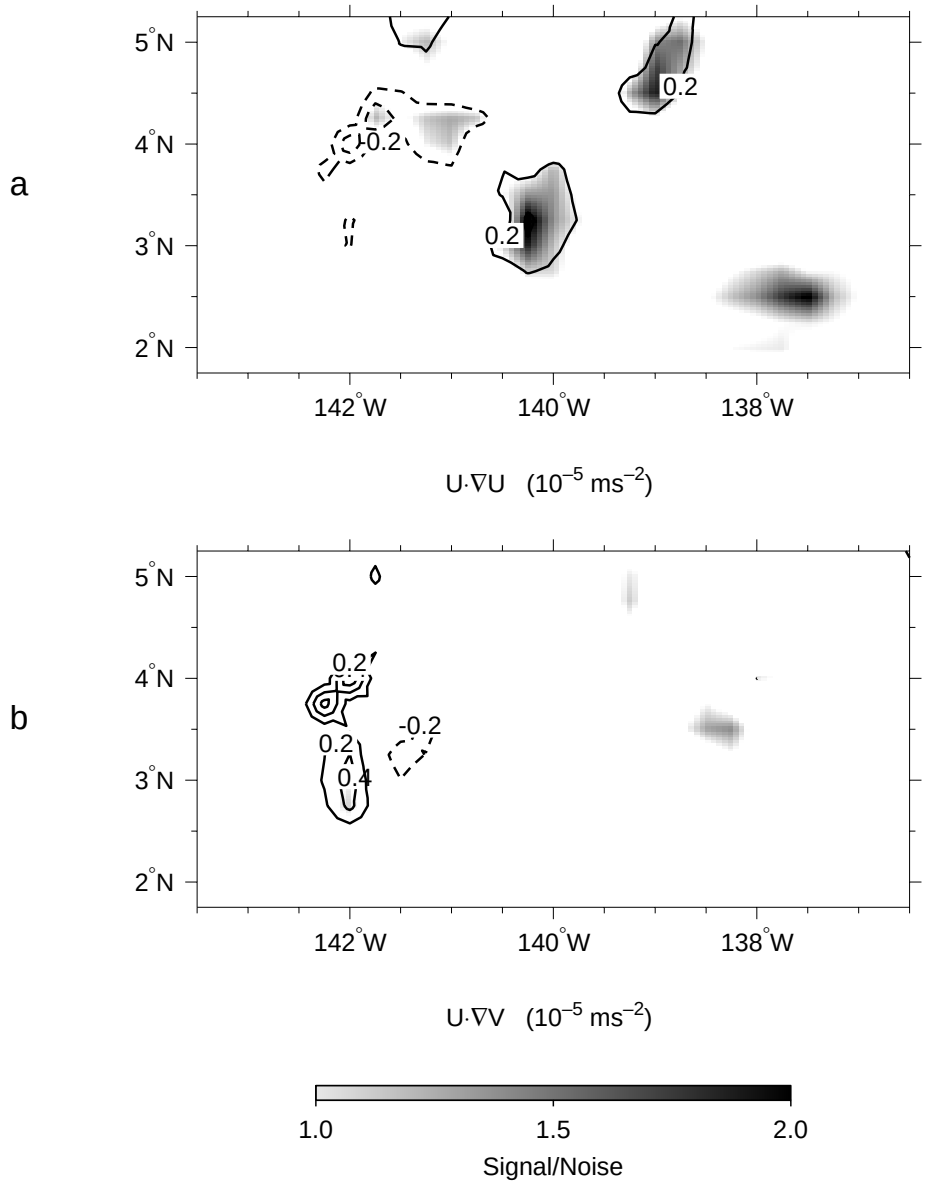

Figure 4.9: Observed momentum advection (parcel accelerations, or material derivatives for steady flow) in the (a) radial and (b) azimuthal directions. Contour intervals are 0.25×10^{-5} m/s^2; shading denotes regions with a signal to noise ratio > 1.

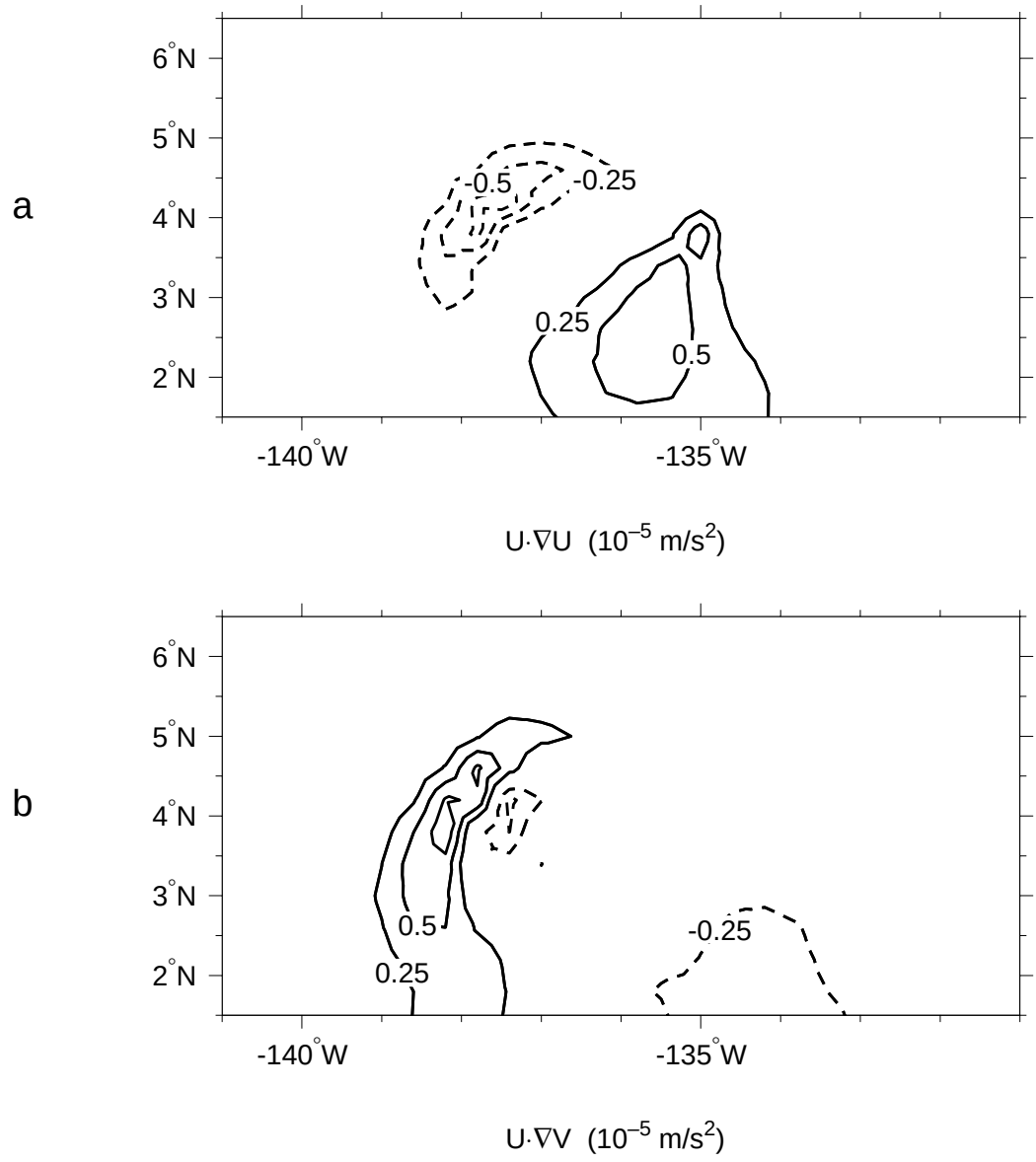

Figure 4.10: Model momentum advection (parcel accelerations, or material derivatives for steady flow) in the (a) radial and (b) azimuthal directions. Contour intervals are 0.25×10^{-5} m/s^2; shading denotes regions with a signal to noise ratio > 1.

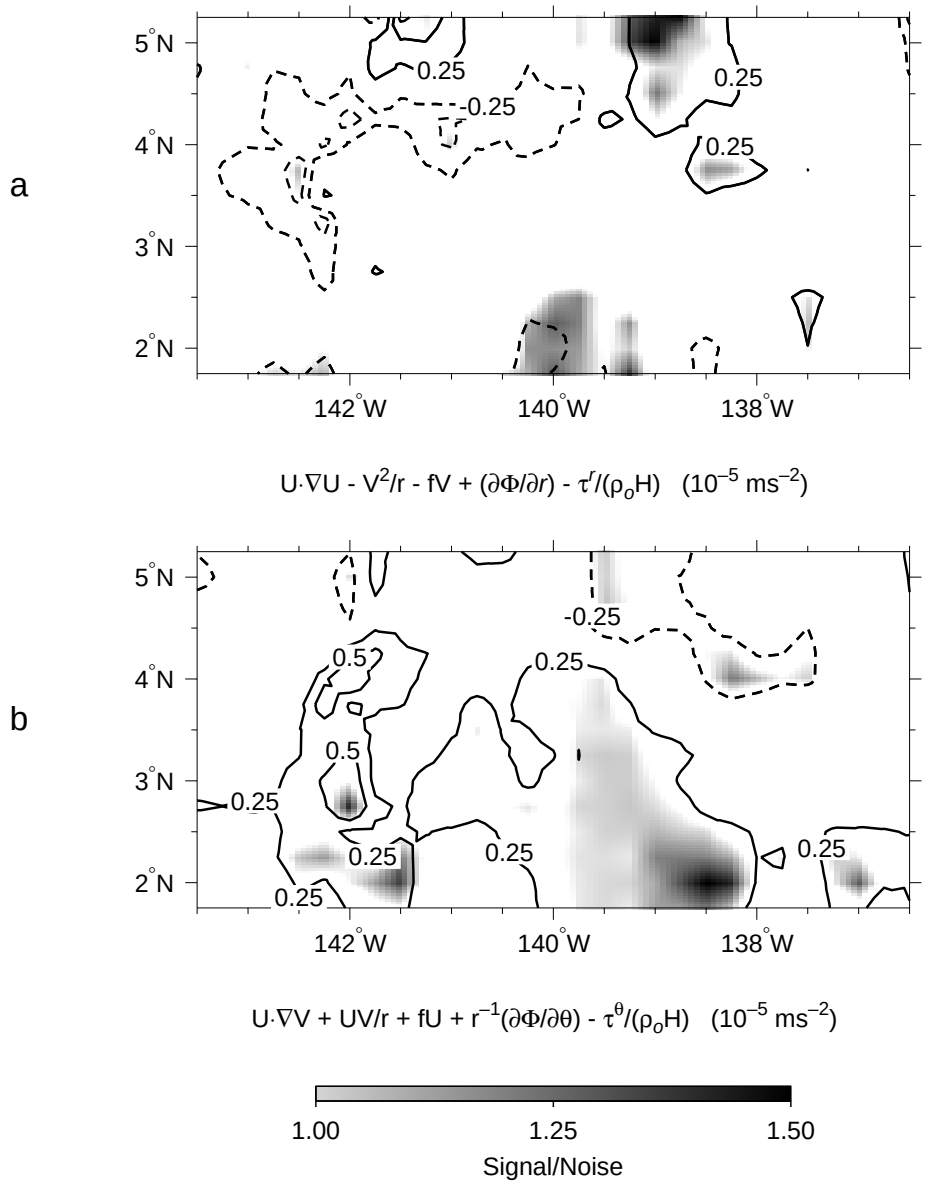

Figure 4.11: Observed net momentum balance for the (a) radial and (b) azimuthal components. Contour intervals are 0.25×10^{-5} m/s^2; shading denotes regions with a signal to noise ratio > 1.

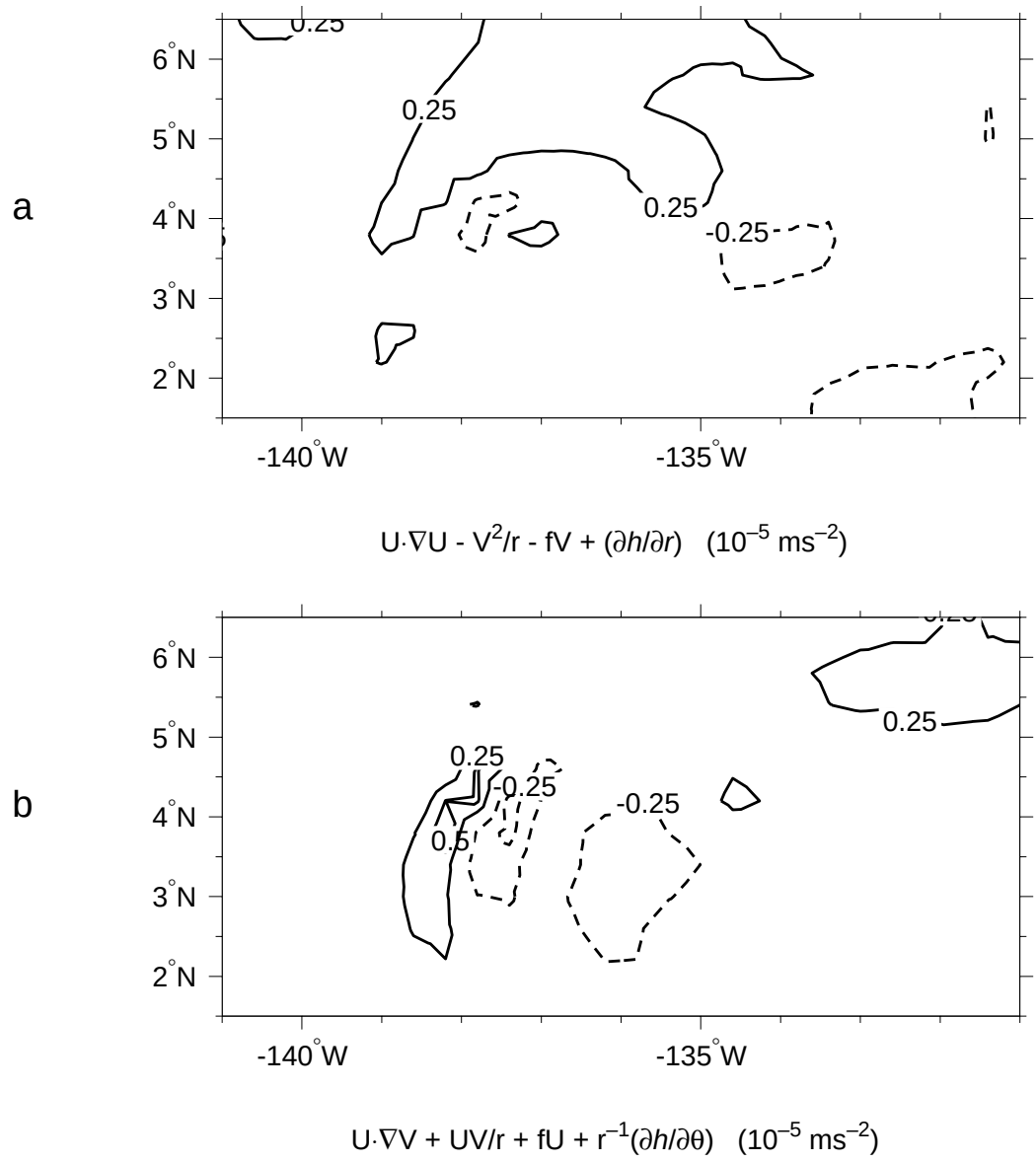

Figure 4.12: Model net momentum balance for the (a) radial and (b) azimuthal components. Contour intervals are 0.25×10^{-5} m/s^2; shading denotes regions with a signal to noise ratio > 1.

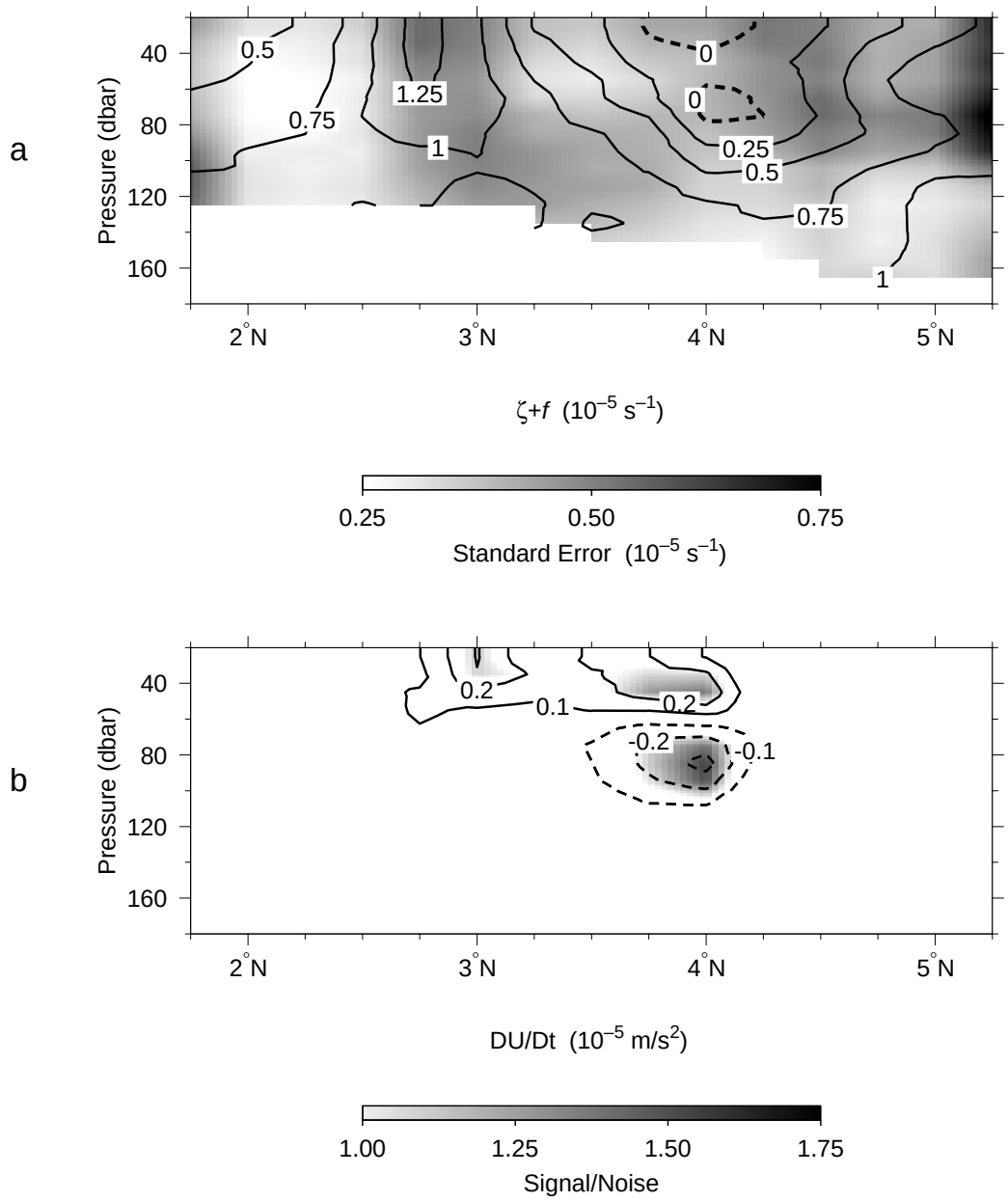

Figure 4.13: (a) Absolute vorticity ($\zeta + f$) and (b) radial momentum advection as a function of pressure along 140.5°W. Contour intervals are 0.25×10^{-5} s^{-1} and 0.1×10^{-5} m/s^2, respectively. Shading denotes standard errors in (a) and regions with a signal to noise ratio > 1 in (b).

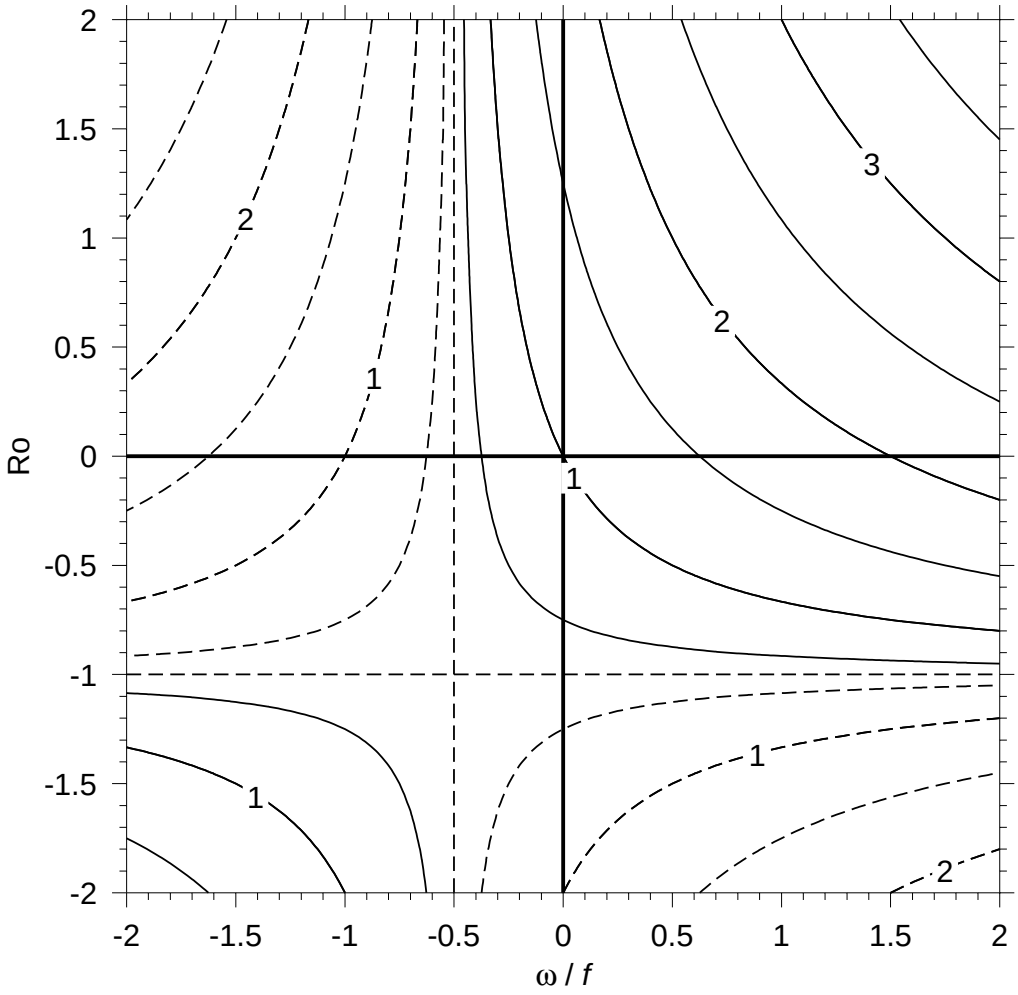

Figure 4.14: The real (solid lines) and imaginary (dashed) values of natural parcel frequency in vortex flow on an f-plane as a function of Rossby number Ro and vortex strength ω/f (where ω is the angular rotation velocity of a vortex); ie: The function σ, where $\sigma^2 = (Ro, \omega/f) = (\omega/f + f/2)(Ro + 1)$. Dashed contours correspond to growth rates. All values can be dimensionalized by f.

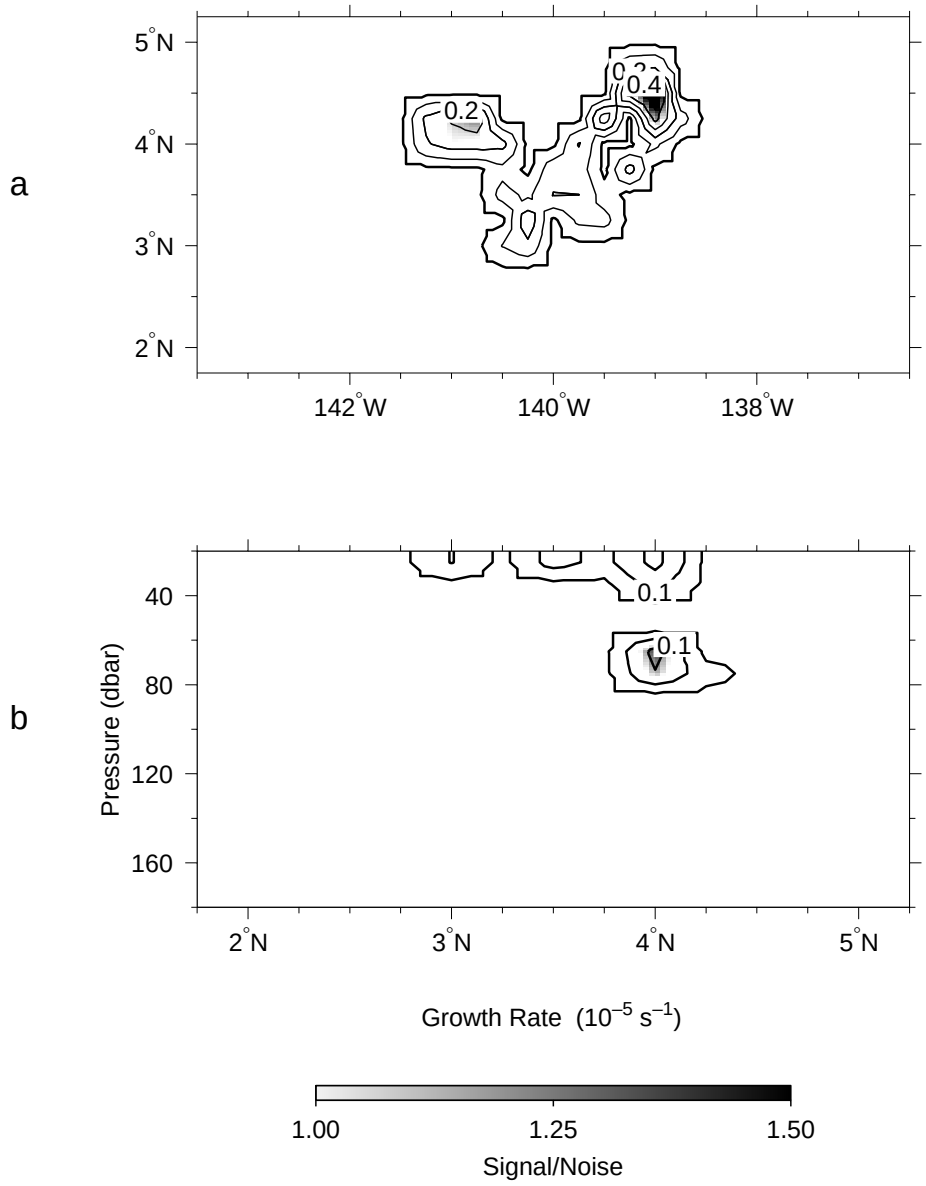

Figure 4.15: The inertial instability growth rate (a) at the surface and (b) along 140.5°W. Contour intervals are 0.1×10^{-5} s^{-1}, or approximately 1.25 per pendulum day (14.5 days); shading indicates regions with a signal to noise ratio > 1.

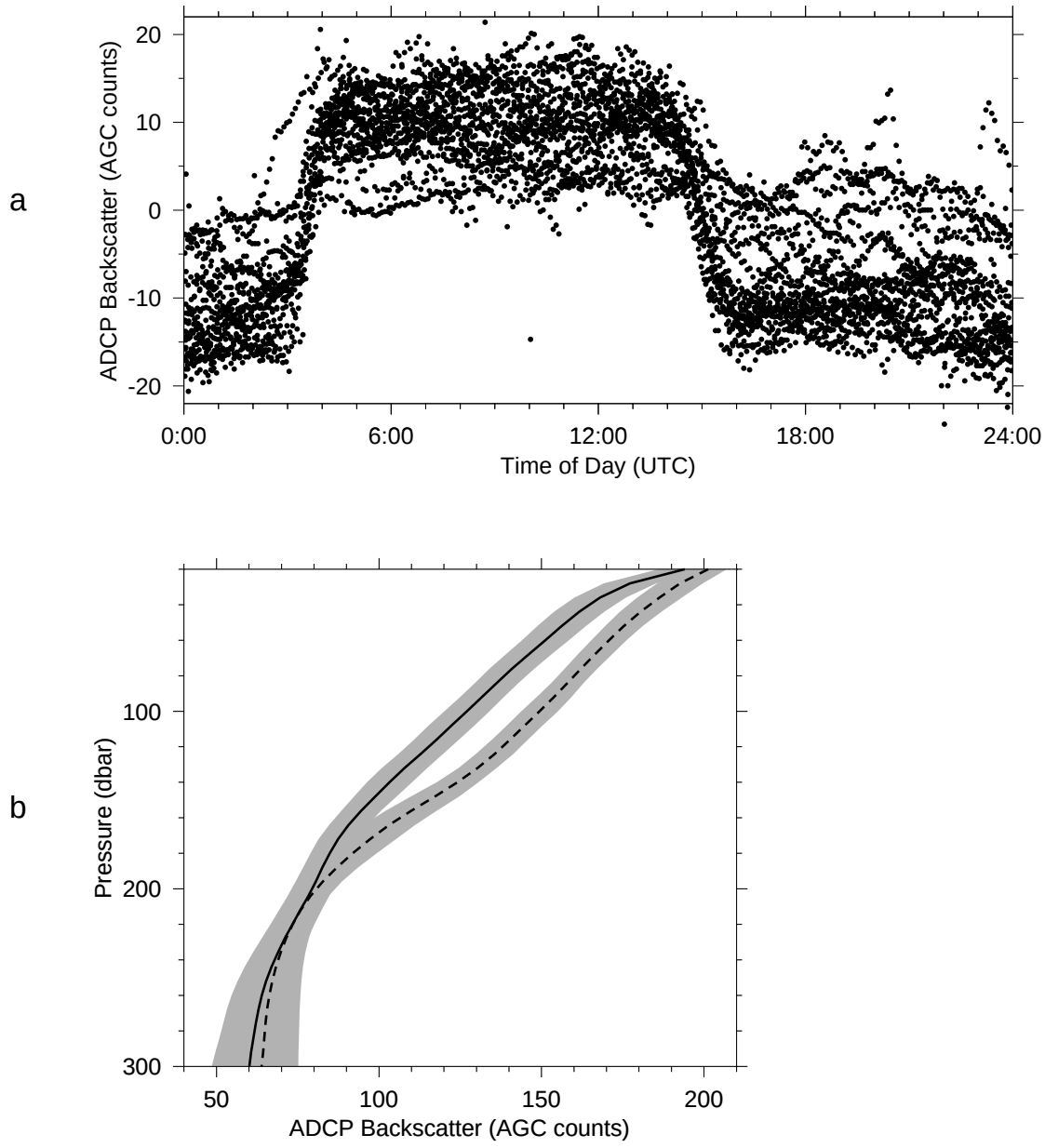

Figure 4.16: Diurnal migrations of zooplankton scatterers: (a) 15 minute averages of ADCP backscatter (with cruise depth average removed) versus time of day; (b) mean backscatter profiles for daytime (17:24-01:48 UTC) (solid line) and nighttime (05:24-12:36 UTC) (dashed). Shading denotes standard deviation intervals.

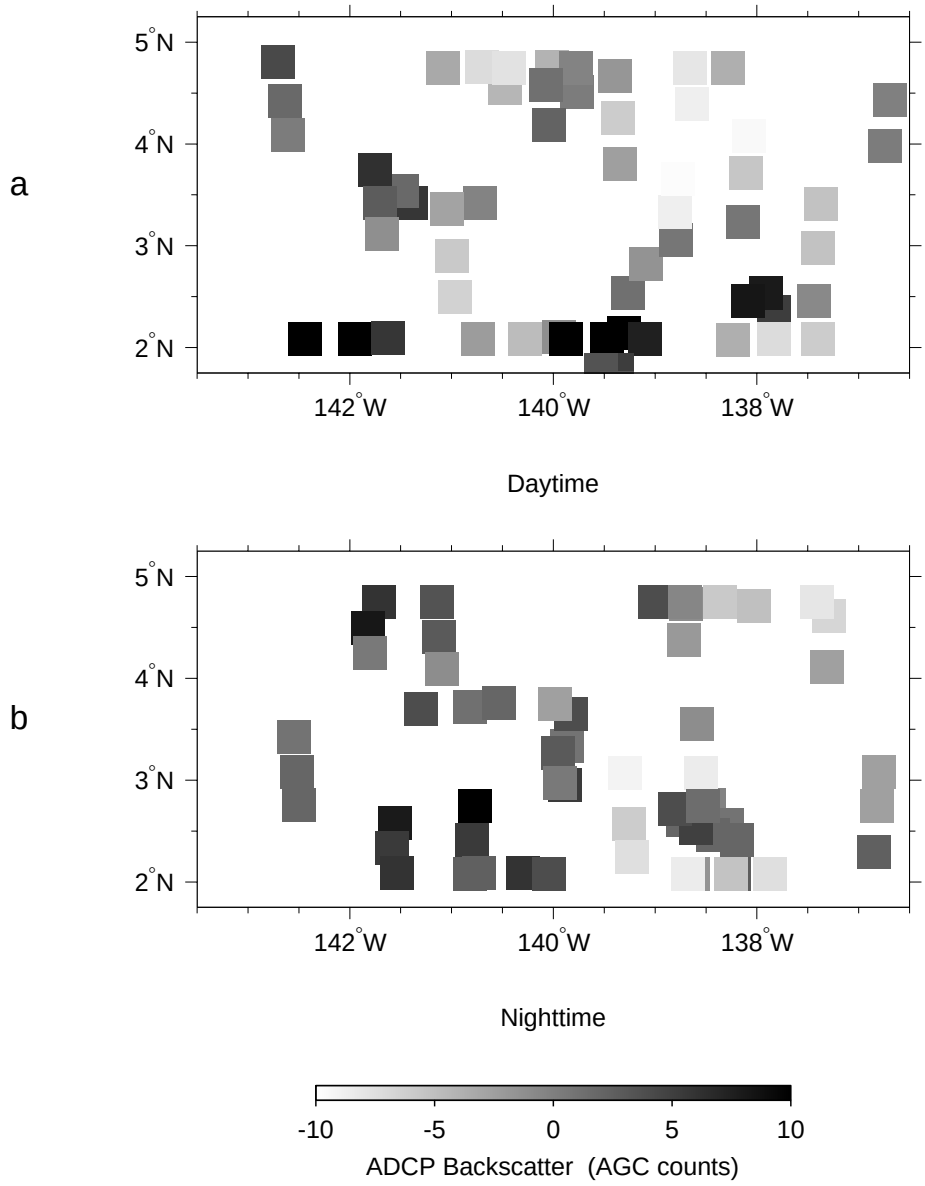

Figure 4.17: Relative ADCP backscatter averaged over 4 hour intervals and the top 100 m along the ship track in the moving reference frame: (a) daytime (17:24-01:48 UTC) and (b) nighttime (05:24-12:36 UTC).

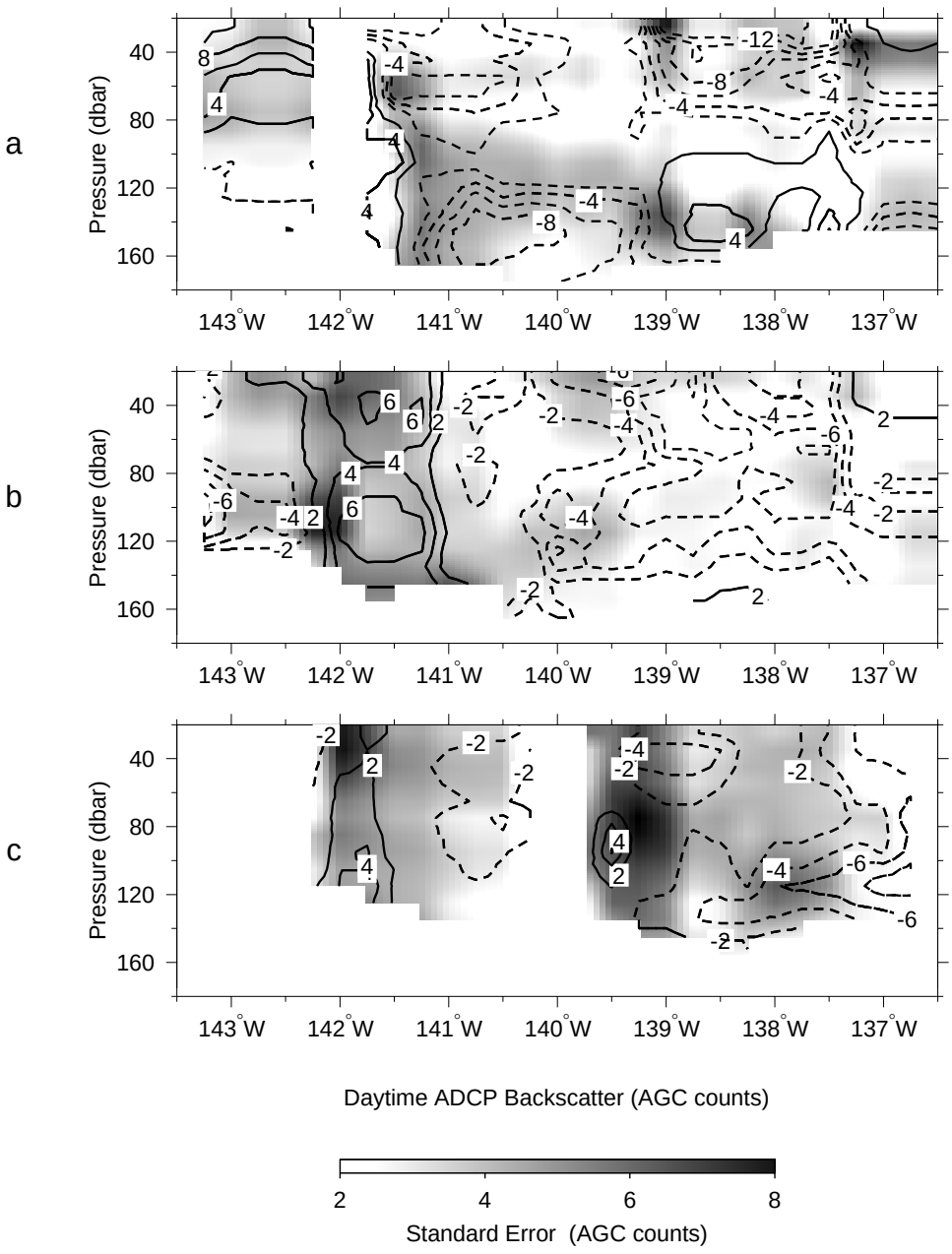

Figure 4.18: Gridded relative daytime ADCP backscatter intensity versus pressure along (a) 5°N, (b) 4°N, and (c) 3°N. Contour intervals are 2 AGC counts; shading denotes standard errors > 2 AGC counts.

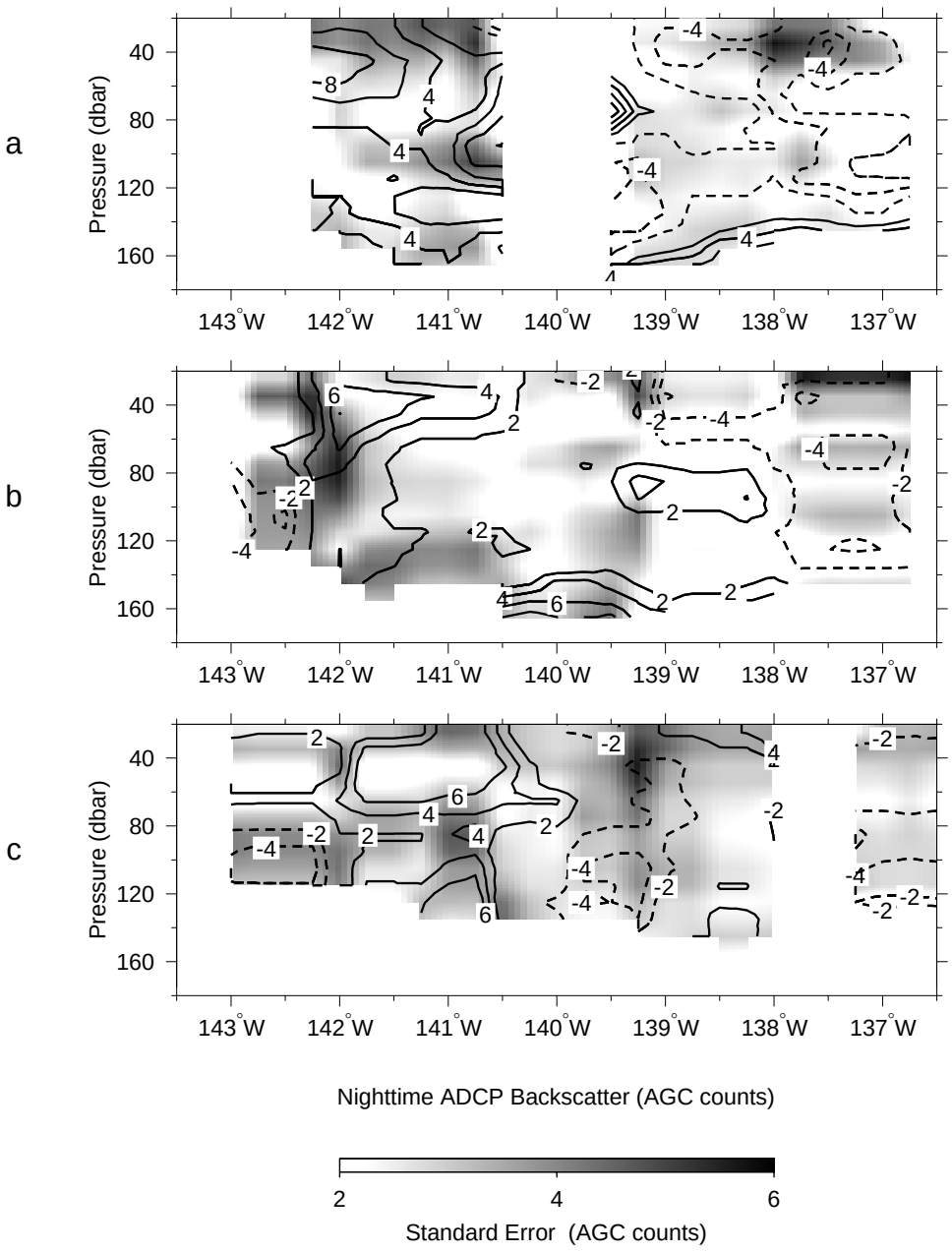

Figure 4.19: Gridded relative nighttime ADCP backscatter intensity versus pressure along (a) 5°N, (b) 4°N, and (c) 3°N. Contour intervals are 2 AGC counts; shading denotes standard errors > 2 AGC counts.

Chapter 5

The Fluxes Induced by a Tropical Instability

In which we examine the fluxes of heat, salt, and energy induced by the vortex. Barotropic shear instability is found to be the most likely source of energy.

5.1 Mean quantities

We now turn to matters concerning TIWs which have received considerable attention in the literature: the relationship of the instabilities to the mean circulation. We begin by describing the averaging process and then proceed in turn to estimate the fluxes of heat, salt, and energy induced by the TIWE-2 vortex. The POCM is used to address the problem of defining a mean state, and the chapter is concluded with an application of wave overreflection theory to the observations.

As previously discussed (see Chapter 2, the data viewed in a reference frame moving with the vortex indicate a steady flow to lowest order. Under this assumption, time variations in the flow at a point in the fixed frame become zonal variations in the steady frame. Then to study the effects of variations induced by the vortex, the variables associated with the flow can be separated into mean and a fluctuating parts, where the mean is defined by a zonal average. For example:

$$\mathbf{u} = \bar{\mathbf{u}} + \mathbf{u}' \qquad\qquad T = \bar{T} + T' \tag{5.1}$$

where primes denote the fluctuating fields and an overbar denotes the mean. This separation of the flow properties, the Reynolds decomposition, is generally conceived

using a time average [Tennekes and Lumley, 1972]:

$$\overline{\mathbf{u}} = \lim_{T\to\infty} \frac{1}{T} \int_{t_o}^{t_o+T} \mathbf{u} dt \tag{5.2}$$

where mean is independent of t_o (the flow properties are steady) and the averaging time T is long enough to ensure that spatial gradients commute with the averaging integral. Consequently,

$$\frac{\partial \overline{\mathbf{u}}}{\partial t} = 0 \quad , \qquad \overline{\mathbf{u}'} = 0 \quad , \qquad \overline{\frac{\partial \mathbf{u}}{\partial x}} = \frac{\partial \overline{\mathbf{u}}}{\partial x} \quad , \qquad \overline{\frac{\partial \mathbf{u}'}{\partial x}} = \frac{\partial \overline{\mathbf{u}'}}{\partial x} = 0 \tag{5.3}$$

When wave-mean flow interactions in the atmosphere are considered, a zonal average is used and the conditions (5.3) are satisfied by a periodic boundary condition. In our present situation, however, the zonal average extends over only one vortex width:

$$\overline{\mathbf{u}}_{i,k} = \frac{1}{n} \sum_{j=1}^{n} \mathbf{u}_{i,j,k} \tag{5.4}$$

where, as in Chapter 2, n is the number of grid points in the zonal direction (indices are now subscripts to avoid confusion with the primes). With our steady flow assumption, and a little algebra applied to the finite differencing (equations (3.1) and (3.2)) the conditions (5.3) become:

$$\frac{\partial \overline{\mathbf{u}}}{\partial t} = 0 \quad , \qquad \overline{\mathbf{u}'}_{i,k} = \frac{1}{n} \sum_{j=1}^{n} \mathbf{u}'_{i,j,k} = 0 \quad , \qquad \frac{\partial \overline{\mathbf{u}}_{i,k}}{\partial x} = 0$$

$$\overline{\frac{\partial \mathbf{u}}{\partial x}}_{i,k} = \overline{\frac{\partial \mathbf{u}'}{\partial x}}_{i,k} = \frac{1}{2n\Delta x} \Big[\big(\mathbf{u}_{i,2,k} - \mathbf{u}_{i,n-1,k}\big) + 3\big(\mathbf{u}_{i,n,k} - \mathbf{u}_{i,1,k}\big) \Big] \tag{5.5}$$

The last line states that the fluctuations have a mean slope, which involves the overall slope of the flow properties and errors in determining the proper averaging distance. With respect to energy, terms with this form appear only in the energy of the mean flow (see Appendix A), but they are relevant in equations for the mean heat and salt flux.

Zonal averages as described by Equation (5.4) of all the primary dynamic and thermohaline fields are presented in Figures 5.1-5.4. As in previous meridional sections versus pressure, the mean quantities are only valid down to the thermocline depth, since the applicability of the moving frame below is unknown. Standard errors for the mean quantities were calculated as the root mean square of the grid point errors divided by the square root of the degrees of freedom. Here, the DOF is defined to be 4 in analogy with the number of length scales occurring in one wavelength.

The zonal velocity has been plotted in the fixed Earth frame frame, so that comparisons with previous estimates of the mean zonal currents can be made without confusion; the zero line in the moving frame (-30 cm/s in the plot) is marked by a heavy dashed line for easy reference to the critical surface, to be made later in this chapter. The SEC reaches almost 70 cm/s near 3°N and extends northward out of the region sampled by the ship (past 5.25°N) (Figure 5.1a). Further to the east and west the SEC has been observed to extend only to 4°N [Wyrtki and Kilonsky, 1984; Hansen and Paul, 1984; Luther and Johnson, 1990; Chiswell *et al.*, 1995], but recently Baturin and Niiler [1997] also find the SEC to reach 5°N at 140°W from 14 years of drifter data. Thus, the present sampling seems representative.

The mean meridional flow is mostly to the south at 5-10 cm/s except at in the mixed layer north of 3°N, where it is northward at about 5 cm/s (Figure 5.1b). The

surface flow is the wind driven Ekman flow, while the southward flow is the return flow of the mean meridional circulation cell [Wyrtki and Kilonsky, 1984]. Temperature is dominated by the thermal wind through the thermocline, with the front smoothed out in the mean owing to its changes in latitude over the width of the vortex.

Salinity on the other hand, traces several interesting features. As described in Chapter 3, fresh water influenced by rain in the ITCZ is entrained by the eddy at the surface, while saline water from the South Pacific enters from the south near 100 dbar. Below the thermocline the gradient with fresh North Pacific water is evident (Figure 5.3b). Yet, as can be seen in Figures 5.4a,b, the effect of these large salinity gradients is minimal on the geopotential and density anomaly fields, which reflect again the larger scale thermal wind balance of the SEC; geopotential is lower to the south, with positive density anomalies reflecting the raised thermocline there.

The mean flow is divergent over most of the region with a pocket of convergence below the mixed layer near 3°N, which is related to the wind event discussed in Chapter 3 Section 3.4. The frontal convergence and upwelling near the center of the eddy largely cancel each other in the zonal average. The associated mean vertical velocity is also shown (Figure 5.2b).

These means are subtracted from the total fields to obtain fluctuations for calculating eddy fluxes of heat, salt, and energy. If the estimates of the mean flow are wrong, then of course the eddy fluxes will be misleading. However, experimenting with the averaging distance in the POCM has revealed that the fluxes are relatively insensitive errors in estimating the vortex width, so that the results appear to be robust. For the purpose of determining eddy fluxes this is all that matters. Care should be taken not to confuse the importance of determining the mean flow in a linear stability analysis with the present

calculations. In performing stability analyses the mean is a conceptual device on which perturbations grow - it cannot be properly estimated in the presence of instabilities. In determining eddy fluxes, on the other hand, the mean is the non fluctuating part of a flow in the presence of finite amplitude disturbances.

The mean variances of the velocity components and temperature and salinity are shown in Figures 5.5 and 5.6. The zonal velocity variance peaks near 0.07 m^2/s^2 in the westward flow of the vortex near 3°N while the meridional variance reaches 0.12 m^2/s^2 just north of the vortex center. Both Hansen and Paul [1984] and Baturin and Niiler [1997] find the same pattern, but with larger magnitudes - 0.15-0.2 m^2/s^2. In temperature the prominent feature is a variance minimum from 3-4°N with the largest values to the north and south around 0.3 C^2. The same minimum in temperature variance was also observed by Hansen and Paul, although again their values were larger (almost 1 C^2) [1984]. The salinity variance is order 0.001 over most of the region with an order of magnitude increase north of 4°N in the mixed layer, where the fresh ITCZ water is moving southward with the vortex.

5.2 Heat and salt fluxes

5.2.1 eddy flux equations

As evidenced in the sections of temperature and salt presented in Chapter 3 (Figures 3.13,3.15), the vortex entrained warm, relatively fresh water from the north and colder, saline water from the south. The convergence of the fluxes of these quantities can be estimated from the observations. Equations for the conservation of heat and salt (S) are:

$$\rho_o C_p \Big(T_t + \mathbf{u} \cdot \nabla T + \omega T_P - \alpha T \omega \Big) = D^H + Q^H \tag{5.6}$$

$$S_t + \mathbf{u} \cdot \nabla S + \omega S_P = D^S + Q^S \tag{5.7}$$

where C_p is the specific heat at constant pressure, *alpha* is the where C_P is the specific heat at constant pressure, α is the coefficient of thermal expansion, D^H and D^S represent subgrid scale, including turbulent, transfers of heat and salt, and Q^H and Q^S are sources or sinks of heat and salt. The equations are written in isobaric coordinates.

Applying the mean flow decomposition (Equation (5.1)) to (5.6) and (5.7) gives:

$$\rho_o C_p \overline{T}_t = -\rho_o C_p \Big(\overline{v}\overline{T}_x + \overline{\omega}\overline{T}_p + \overline{u}\overline{T'_x} + \overline{u'T'_x} + \overline{v'T'_y} + + \overline{\omega'T'_p} \Big) \tag{5.8}$$

$$\overline{S}_t = -\overline{v}\overline{S}_y - \overline{\omega}\overline{S}_P - \overline{u}\overline{S'_x} - \overline{u'S'_x} - \overline{v'S'_y} - \overline{\omega'S'_P} \tag{5.9}$$

where the vector products have been expanded into their components and turbulent diffusion and sources and sinks are not written. The compressibility effects have been dropped since they are insignificant for the TIWE-2 data, which are restricted to the upper 300 m of the ocean.

In Appendix A eddy energy equations are derived using the Reynolds decomposition described above. In that case we can assume that the local time derivatives $\frac{\partial}{\partial t}$ are zero because the moving frame was chosen in Chapter 2 to have a steady flow field. However, there is no reason for the scalar fields, such as temperature and salinity, to have zero local rates of change in the moving frame; in other words, the vortex may gain or lose heat or temperature during its life cycle.

The equations, (5.8) and (5.9) give the separate effects of mean and eddy advection on the local changes in heat and salt. The advection terms in these equations may be understood when rewritten, using continuity, as divergences of fluxes, ie: $\mathbf{u} \cdot \nabla S = \nabla \cdot (S\mathbf{u})$. However, transforming the terms in this manner runs the risk of introducing large errors [Luther and Johnson, 1990], especially in regards to the mean quantities. Estimating $\frac{\partial}{\partial y}(\overline{S}\overline{v}) + \frac{\partial}{\partial P}(S\overline{\omega})$ for instance, involves the difference between two very large numbers compared to estimating $\overline{v}\overline{S}_y + \overline{\omega}\overline{S}_P$. Thus, all flux convergences are left in their advective forms.

5.2.2 heat flux

The mean eddy zonal and meridional heat fluxes are shown in Figure 5.7. The eddy transports heat eastward and to the south over most of the region with some northward transport at 80-100 m south of 4°N. The results at the surface agree well with previous results and even reflect a minimum in the magnitude of $\overline{v'T'}$ near 3-4°N which was also observed by Hansen and Paul [1984].

The overall pattern reinforces the mean circulation, in which the SEC transports cold water to the west and the meridional cell brings cold water northward in the mixed layer and warm water equatorward below. However, it is not known whether this enhanced circulation results in net heat losses or gains in the tropical region relative to the annual mean. Hansen and Paul [1984] argued that the TIWs deposit heat in the equatorial region, making up for an imbalance between the surface heating and upwelling of cool water. Although our observations do not address the equator, a net heating in the presence of the vortex is indicated (Figures 5.8 and 5.9). This is accomplished primarily through a convergence of the mean eddy meridional heat flux, on the order of 5 W/m^3.

The flux of heat into the ocean at the air-sea interface in the region is approximately 30 W/m^2 [Weare *et al.*, 1981], which over a 50 m mixed layer corresponds to a heat storage rate of 0.6 W/m^3, an order of magnitude smaller than the vortex induced heating. We make no attempt to close the heat budget here, but it is also noteworthy that the net heating by the vortex is as large as the effect of the mean circulation (Figure 5.9a). Consequently, TIWs represent a significant source of seasonal fluctuations to the tropical heat budget, which makes understanding their dynamics essential to the eventual coupling of oceanic and atmospheric climate models.

5.2.3 salt flux

The mean eddy salt flux is eastward and northward over the region, which again reinforces the mean circulation. The ultimate source of the saline water is the South Pacific; the saline water is partially transported across the equator by the upwelling at the equator and eastward from the western Pacific where waters are exchanged by the western boundary currents. The largest signal is clearly the southward transport of the fresh ITCZ water, restricted to the mixed layer.

Fresh water fluxes have not been previously reported for instability waves, but these imply that they are comparable to the annual mean inputs via evaporation and precipitation. Rainfall in the ITCZ and evaporation to the south range from 1-5 m/yr or about 0.6-3.0 μg/m^{3}s [Gill, 1982; Peixoto and Oort, 1992]. While it has been known that the mean circulation brings saline water northward in the mixed layer, the southward fresh water flux induced by TIWs is an important addition to the overall flux.

The overall effect appears to be a net freshening of the SEC-NECC shear region, although the results are not statistically significant relative to the standard errors (Figures 5.11 and 5.12). The freshening is associated in the mixed layer with the southward

entrainment of warm fresh water and near the thermocline in the south with the northward movement of saline equatorial water.

In summary, we find the eddy heat fluxes induced by the TIWE-2 vortex in the mixed layer to be consistent with previous findings, and present evidence that the net heating is even stronger than previously thought below the surface. While these results show that TIWs probably have as large a role in the annual heat budget as the mean circulation, their contribution to the fresh water balance may be even more important. The freshening of the mixed layer by the vortex far exceeds that by the mean circulation and has the same magnitude as the annual local evaporation and rainfall in the ITCZ rates. Without data for the northern half of the vortex we can only speculate that the mixed layer north of 5° (under the ITCZ) gains salt during the TIW season.

5.3 Eddy energy production

Previous observational studies of tropical instabilities have focused on eddy energetics as a method for deducing the underlying dynamics [Hansen and Paul, 1984; Weisberg and Weingartner, 1988; Luther and Johnson, 1990; Qiao and Weisberg, 1997]. The results have shown significant conversions of mean to eddy energy, consistent with the hypothesis that the currents are unstable, with eddying motions feeding off of the mean flow. Recently, Proehl [1996] has showed the utility of applying wave overreflection concepts to the same flows, demonstrating a correspondence between the results implied by energy budgets and critical layer geometries.

In this section we calculate a traditional eddy energy budget, finding, in agreement with some previous studies, that the TIW vortex obtains its energy from the mean KE

of the SEC-NECC shear region. This result will also be supported through an application of critical layer geometries to the observed mean state.

The eddy energy budget is calculated using the same procedures as in the preceding section. In keeping with the Boussinesq approximation, the mean vertical gradients of density and geopotential were subtracted from the data before calculating mean and eddy quantities (see Figures 5.4a,b).

5.3.1 instability dynamics

The eddy energy equations appropriate for hydrostatic flow with zonal averaging are derived in Appendix A and are given by Equations (A.16)-(A.18). These equations are useful for studying unstable flow because they describe the pathways that energy takes in moving between the mean and eddy flows. For instance, the term:

$$-\overline{u'v'}\overline{u}_y \tag{5.10}$$

from Equation (A.16) indicates conversion of KE of the mean to eddy KE when positive. It is traditionally associated with barotropic instability because it depends only on the meridional shear of the mean flow, and can occur in an unstratified fluid. A necessary but insufficient condition for instability of such a flow is that the absolute vorticity gradient $(\beta - \overline{u}_{yy})$ change sign somewhere in the flow [Holton, 1979]. This term has been found to account for most of the eddy energy production on the equator in the Pacific and Atlantic oceans [Weisberg and Weingartner, 1988; Qiao and Weisberg, 1997], and has also been found to dominate eddy energy production in some models of the tropical Pacific [Philander *et al.*, 1986; Cox, 1980; Donohue, 1995]; it is therefore of primary interest.

Another term which is typically used to indicate instability is:

$$-\overline{\rho' v'}\overline{\rho}_y \tag{5.11}$$

which accounts for conversion of APE of the mean flow to the eddy APE. This term is often used to probe for baroclinic instability because it is closely related to the eddy heat fluxes which occur in that situation. Hansen and Paul [1984] found this term to be as large as the barotropic conversion near 3-5°N, while Luther and Johnson [1990] found it to be significant in the mixed layer from December-March and further north in the thermocline from April-June. Various models have also found baroclinic conversions in the SEC-NECC shear to be important [Semter and Holland, 1980; Cox, 1980].

The classic example of baroclinic instability occurs in a vertically sheared zonal flow with no meridional potential vorticity gradient. Although the mean flow is in thermal wind balance, the absence of an absolute vorticity gradient isolates baroclinic effects from barotropic instability. However, it has also been suggested that the density gradient associated with the North Equatorial Front can play a dominant role in generating instabilities [McCreary and Yu, 1992; Yu *et al.*, 1995].

These terms (Equations (5.10) and (5.11)) are directly related to eddy advection of eddy energy across a mean gradient: $-\overline{u' v'}\overline{u}_y$ represents meridional eddy advection of eddy zonal momentum across the mean meridional gradient of zonal momentum, while $-\overline{\rho' v'}\overline{\rho}_y$ is the meridional eddy advection of eddy density across the mean density slope.

The remaining conversion terms in (A.18) ($-\overline{u'\omega'}\overline{u}_P, -\overline{v'\omega'}\overline{v}_P, -\overline{\rho'\omega'}\overline{\rho}_P$) have similar interpretations as advective processes, except for the term:

$$-\overline{v'v'}\overline{v}_y \tag{5.12}$$

which represents convergence of eddy KE by the mean flow. Because $\overline{v'v'}$ is positive definite, a convergent mean flow will always convert mean flow KE to the eddy field. Another way to view this is by examining the vorticity equation (4.3), where convergence indicates vortex stretching, and always increases the magnitude of the relative vorticity (unless the absolute vorticity is negative, in which case inertial instability dominates the dynamics, and these considerations are moot). Consequently, this term is directly tied to the growth of vorticity in the flow.

5.3.2 mean to eddy kinetic energy

Figure 5.13a shows the estimates of the barotropic conversion terms (Equation (5.10)). The eddy is gaining energy from the mean flow in a region trapped to the mixed layer from 3.5-4.5°N via the term $-\rho_o\overline{u'v'}\overline{u}_y$. This is the term traditionally associated with barotropic shear instability. The peak values of more than 0.15 mW/m^3 are about three times smaller than the values previously obtained by Hansen and Paul [1984], but agree well with Baturin and Niiler [1997] and are on the same order as estimates for the equator [Luther and Johnson, 1990; Qiao and Weisberg, 1997].

To the south and below the mixed layer, the eddy flow gains energy at a lower rate via the term $-\rho_o\overline{v'v'}\overline{v}_y$ (Figure 5.13b). This region corresponds to the largest mean convergence (Figure 5.2). The sum with $-\rho_o\overline{u'v'}\overline{u}_y$ is shown in Figure 5.13c. The remaining advective conversions terms for eddy KE ($-\rho_o\overline{u'\omega'}\overline{u}_P, -\rho_o\overline{v'\omega'}\overline{v}_P$) are shown

in Figure 5.14, with their sum in the lower panel. Their net effect is to convert eddy energy to the mean flow in the region of frontal convergence. The sum of all four mean to eddy KE conversion terms is shown in the top panel of Figure 5.16.

To understand the mean to eddy kinetic energy conversion, the unaveraged values $(-\rho_o u'v'\overline{u}_y)$ are contoured in Figure 5.15a over the vortex region for the observations and in Figure 5.15b for the POCM. Both reveal that the barotropic conversion arises in the center of the convergence/divergence dipole of the vortex flow (compare with Figure 3.1). The model values are about twice as large as the observations, but in both cases the sign of the conversion represents a mean to eddy exchange.

This pattern suggests a relationship between the dipole and the mean to eddy exchange. We speculate that the mean to eddy exchange of the shear instability is directly responsible for accelerating the flow to the south (see the discussion on wave overreflection) which then causes the front, as per the vorticity dynamics discussed in Chapter 4, while the divergence is limiting the vortex growth (recall the discussion of vortex instability).

5.3.3 mean to eddy available potential energy

The baroclinic conversion (5.11) reveals a small gain in eddy energy south of 3°N in the mixed layer. The values are positive, corresponding to the northward eddy transport of cold water. The unaveraged quantity $(-C\rho'v'\overline{\rho}_y)$ for both observations and the POCM is given in Figure 5.17, which shows that mean to eddy available potential energy conversion is associated with the northward flow of cold water in the vortex cusp.

The total sum of eddy energy conversions appears in Figure 5.16c. The most prominent feature is the eddy energy gain at 4°N from the barotropic conversion at the front.

Because of the restriction of the moving reference frame to above the thermocline, the findings of Luther and Johnson [1990] that baroclinic conversion occurs in the thermocline cannot be addressed here.

5.3.4 eddy energy advection

The eddy growth is reflected in the pattern of EKE and EAPE advection (Figures 5.18 and 5.19). For both, eddy advection dominates eddy energy advection by the mean flow. With the steady flow assumption, the advection terms can be viewed as changes following parcels. Both EKE and EAPE advection show a gain south of 4°N in the mixed layer which then reaches below the surface to the north. The unaveraged eddy advection of EKE ($\mathbf{u}' \cdot \nabla EKE$) shows that this occurs at the front as the northward moving water crosses the front - both in the observations and POCM (Figure 5.20). Parcels gain EKE just east of 142°W from 3-4°N and lose to the northwest, associated with the frontal convergence.

5.3.5 eddy work

We found in calculating a momentum budget for the vortex that the geopotential field was susceptible to violations of our steady flow field assumption. In the case of investigating the energy production via work this problem is magnified because work is only achieved by the ageostrophic flow. Figure 5.21 shows the eddy work estimated from the observations and for the model. They are not in agreement; according to the model, the parcels do work as they cross the front, and the magnitudes are on the same order as the EKE advection. Yet, the observations indicate working rates up to 3 times the EKE advection, and over a larger region.

While the model cannot be proven to accurately model TIWs, it seems to be a reasonable check on our results. As with the momentum budget, we feel that such strong disagreement between the observations and model indicates a failure of the steady flow assumption when applied to the geopotential field. Consequently, no attempt is made to estimate any of the mean working terms.

5.3.6 summary

The results from Figures 5.16-5.20 demonstrate that the mean to eddy conversion of energy for the vortex is mainly kinetic and occurs at the leading edge of the perturbed North Equatorial Front. This result confirms the findings of Hansen and Paul [1984] and Baturin and Niiler [1997]. However, we do not find significant baroclinic conversion as they did. At the same time, our values for the baroclinic term agree with Luther and Johnson [1990] but we find larger barotropic conversion.

An interesting aspect of our findings is the concentration of mean to eddy energy conversion at the leading edge of the deformed North Equatorial Front (Figure 5.15). McCreary and Yu [1992] have modeled the unstable modes in a 2-1/2 layer model with variable layer temperature. They concluded that one of their unstable modes obtained eddy energy from the mean APE of the equatorial front [McCreary and Yu, 1992; Yu *et al.*, 1995]. Our results, however, show the baroclinic term to be weak (Figure 5.17), apparently invalidating the hypothesis of frontal instability. Rather, it seems that the instability is a barotropic process localized at, and perhaps intensifying the front.

5.4 Wave overreflection

A necessary condition for barotropic shear instability of a quasigeostrophic flow is that the meridional gradient of the mean potential vorticity (PVG) change sign somewhere [Kuo, 1973; McPhaden and Ripa, 1990]:

$$\overline{q}_y = \beta - \overline{u}_{yy} = 0 \tag{5.13}$$

where β is the planetary vorticity gradient. A surface where this occurs is a turning, or reflecting, latitude for the planetary wave modes of the system [Lindzen and Tung, 1978]. Lukas [1987] has shown that the barotropic PVG changes sign at 2°N and 2°S, but did not have data to address the SEC-NECC shear region.

Unfortunately, fulfillment of the condition (Equation (5.13)) does not guarantee instability. According to wave overreflection theory this is because shear instability also requires the existence of a critical surface, where the unstable mode propagation and mean flow velocities are equal, and a specific geometric arrangement of the critical and reflecting surfaces such that the wave modes of the system will "overreflect." It has been demonstrated that Kelvin-Helmholtz, barotropic, and baroclinic shear instabilities can be adequately modeled using these concepts [Lindzen and Tung, 1978; Lindzen *et al.*, 1980; Lindzen, 1980].

The advantage of wave overreflection concepts is the identification of an instability process with specific propagation characteristics of a vorticity wave mode. A conjunction of oscillatory and exponential wave behavior regions creates a situation where wave energy can continually interact with a critical surface to extract energy from the mean flow. The critical surface is a singularity of the eddy potential vorticity equation which

can totally absorb and freely emit waves. It has often been heuristically argued that only when unstable modes are locally stationary relative to the mean flow can they extracted energy from the mean. Thus, the critical surface should be the region where mean to eddy energy conversion occurs [Lindzen, 1988; Proehl, 1996].

The character of wave propagation for barotropic flow can be understood from the perturbation potential vorticity equation:

$$\Psi_{yy} + \left(\frac{\overline{q}_y}{\overline{u} - c_o} - k^2 \right) \Psi = 0 \tag{5.14}$$

where $\Psi \sim exp[ik(x - ct)]$ is the perturbation stream function under quasigeostrophic scaling [Lindzen, 1988]. The nature of the solutions depends on the sign of the coefficient in brackets:

$$\left(\frac{\overline{q}_y}{\overline{u} - c_o} - k^2 \right) \quad \begin{cases} > 0 & \text{free waves} \\ < 0 & \text{evanescent} \\ = 0 & \text{reflection} \\ \to \infty & \text{total absorption} \quad (\overline{u} - c_o = 0) \end{cases} \tag{5.15}$$

The geometry of these regions required for overreflection is depicted in Figure 5.22a. The critical surface (solid line) must be separated, by an evanescent region (the critical layer; bounded by the critical surface and a reflecting surface), from a region bounded by reflecting surfaces (dashed). The bounded reflecting layer is needed to continually return reflected waves towards the critical layer. The evanescent critical layer is needed to allow partial transmissions through the reflecting surface to approach the critical surface in a

finite time. As perturbation energy at the critical surface is continually increasing, the reflecting surface bordering the evanescent critical layer will emit a greater amount of wave energy than it partially transmits, thus giving the overreflection [Lindzen, 1988; Proehl, 1996].

The overreflection geometry has been applied to the TIWE-2 data by calculating the location of the critical surface and the zero lines of the PVG for two cases: barotropic, and baroclinic (Figures 5.22b,c). In each case the critical surface ($\overline{u} - c_o = 0$) is marked with a solid contour, the turning latitudes ($\overline{q}_y = 0$) are given by dashed lines, and the reflecting layer is shaded. (The critical surface is the line of zero mean zonal velocity in the moving frame and the -30 cm/s contour in the fixed Earth frame). The barotropic case is given by Equations (5.13) and (5.14) while the baroclinic is:

$$\Psi_{zz} + \left(\frac{\overline{q}_y}{\overline{u} - c_o} - m^2 \right) \Psi = 0$$

$$\overline{q}_y = \beta - \frac{f^2}{N^2} \overline{u}_{zz} \tag{5.16}$$

where $\Psi \sim exp[im(x - ct)]$, after Lindzen [1988].

It is clear from Figures 5.22b,c that in the baroclinic case the critical layer lacks an evanescent region of significant vertical extent with a bounded free region on the other side, whereas in the barotropic situation the appropriate geometry is found. Consequently, barotropic instability should be preferred.

In order for wave overreflection to occur it is also necessary for the meridional wavenumber to be quantized in the bounded region, which is the overreflection theory analogy to the eigenvalue problem for normal modes analyses. Since Rossby waves experience a -$\pi/2$ phase change upon reflecting at a turning latitude, the appropriate

quantization condition is an odd multiple of $\pi/2$, or one quarter wavelength [Proehl, 1996]. The width of the shaded reflecting region in Figure 5.22b ($\sim 1.25°$) is nearly 1/4 the meridional extent of the vortex, which extends from 2-7°N, so that all the conditions for barotropic instability appear to be satisfied.

A comparison with Figures 5.16 and 5.18 shows that the reflecting layer corresponds with the region in which the surface flow is accelerating, while the critical layer is collocated with the mean to eddy KE conversion. It thus seems that that overreflection is capable of explaining the physical separation between barotropic conversion at the front and flow acceleration to the south. We suspect that if the working terms could be estimated with confidence the energy pathways connecting these regions could be investigated.

One could argue that the finite amplitude nature of the observed flow violates the assumptions of the potential vorticity equations from which the wave characteristics are deduced. Nevertheless, planetary wave overreflection is a convenient paradigm for understanding shear instability, and is easily applied to the present observations.

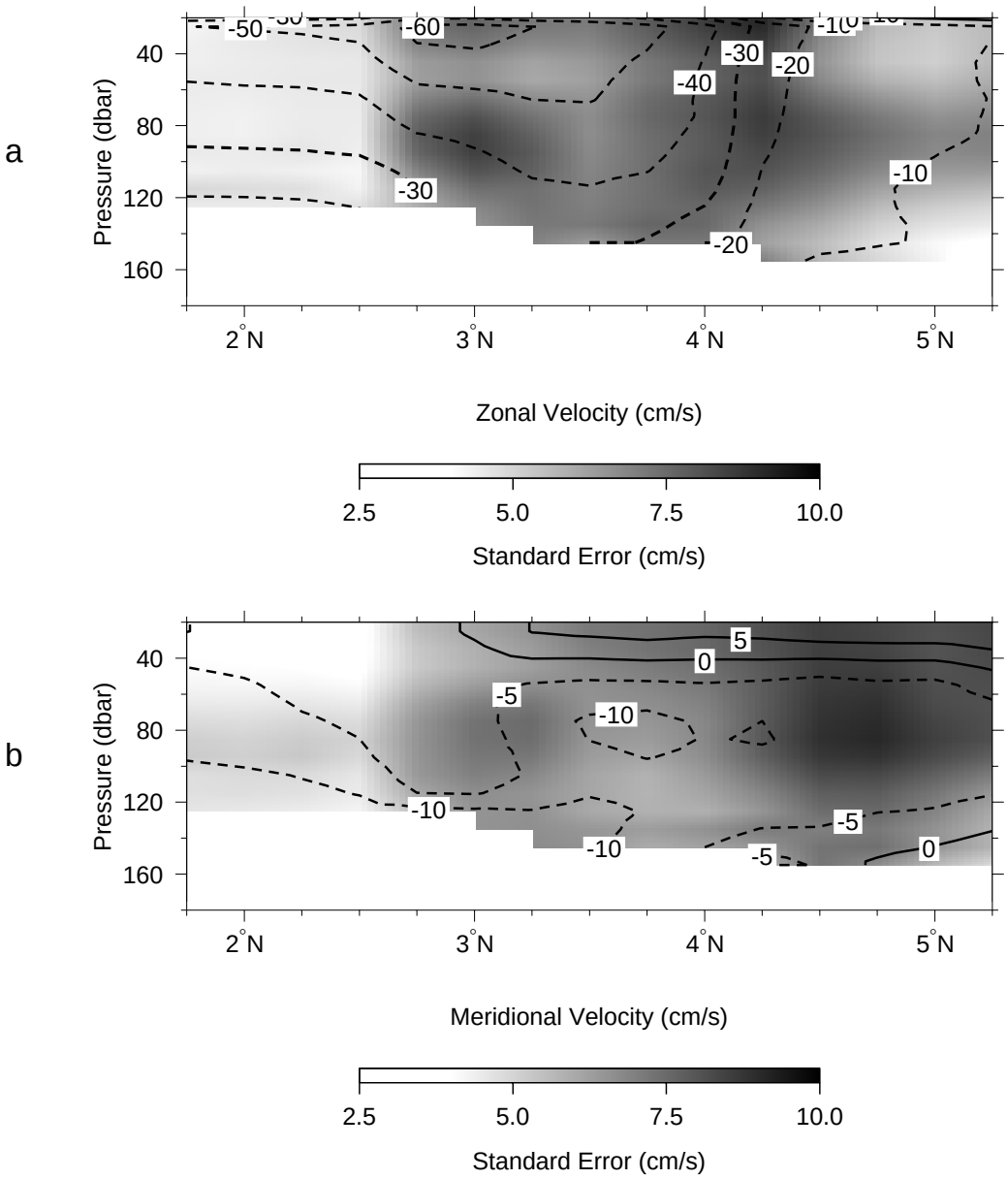

Figure 5.1: Mean (a) zonal and (b) meridional velocity. Contour intervals are 10 and 5 cm/s respectively; shading denotes standard errors.

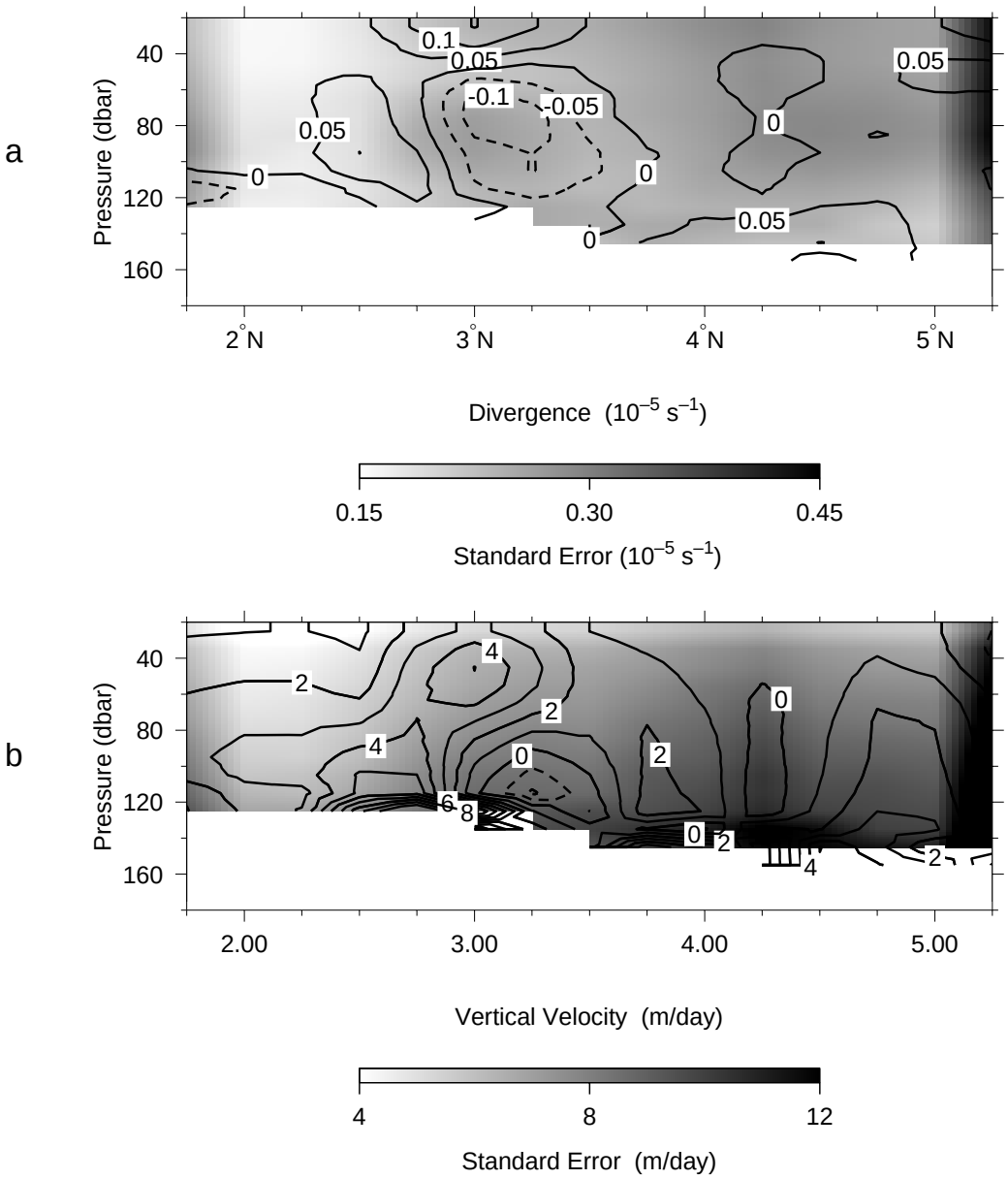

Figure 5.2: Mean (a) divergence and (b) vertical velocity. Contour intervals are 0.05×10^{-5} s^{-1} and 1 m/day respectively; shading denotes standard errors.

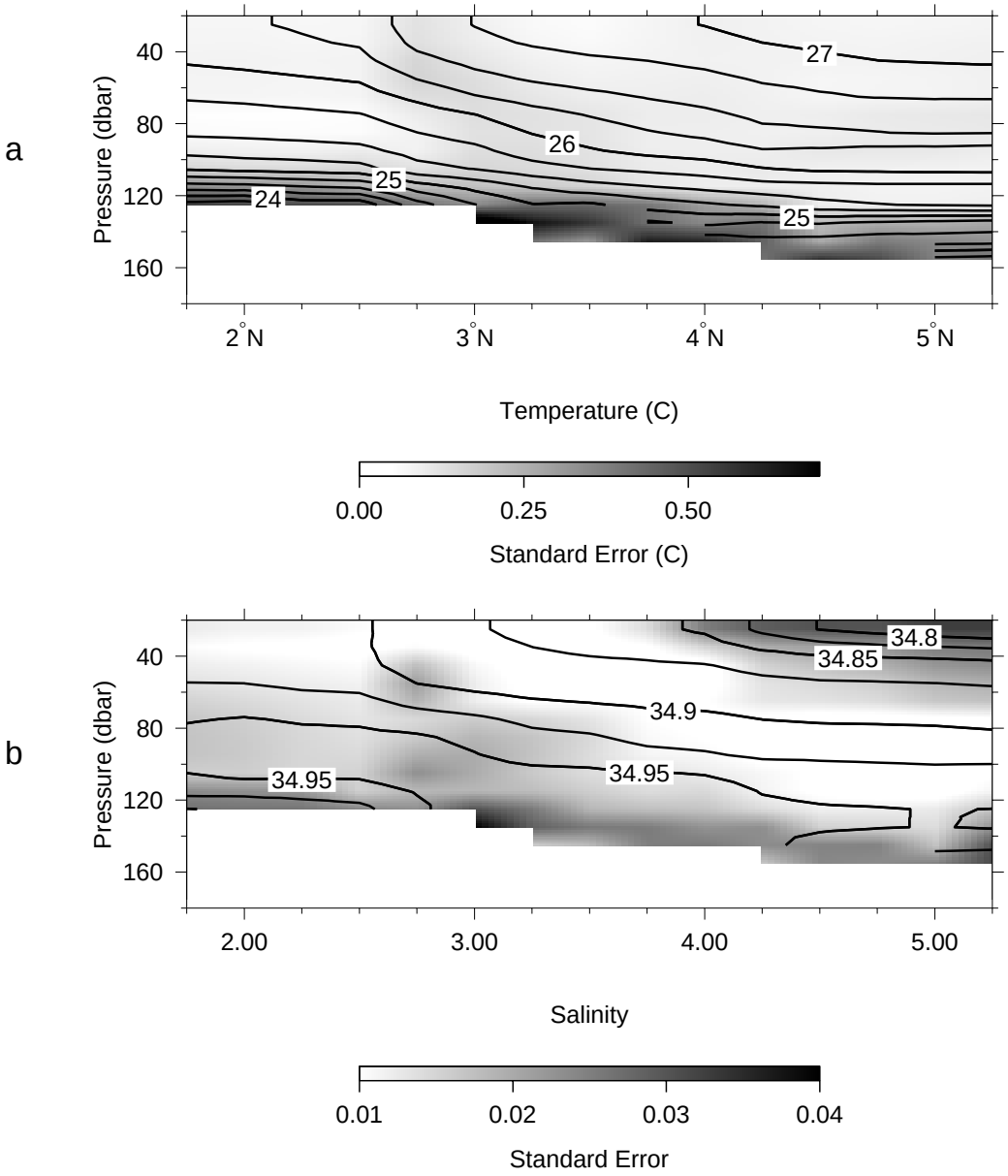

Figure 5.3: Mean (a) temperature and (b) salinity. Contour intervals are 0.25 C and 0.05 respectively; shading denotes standard errors.

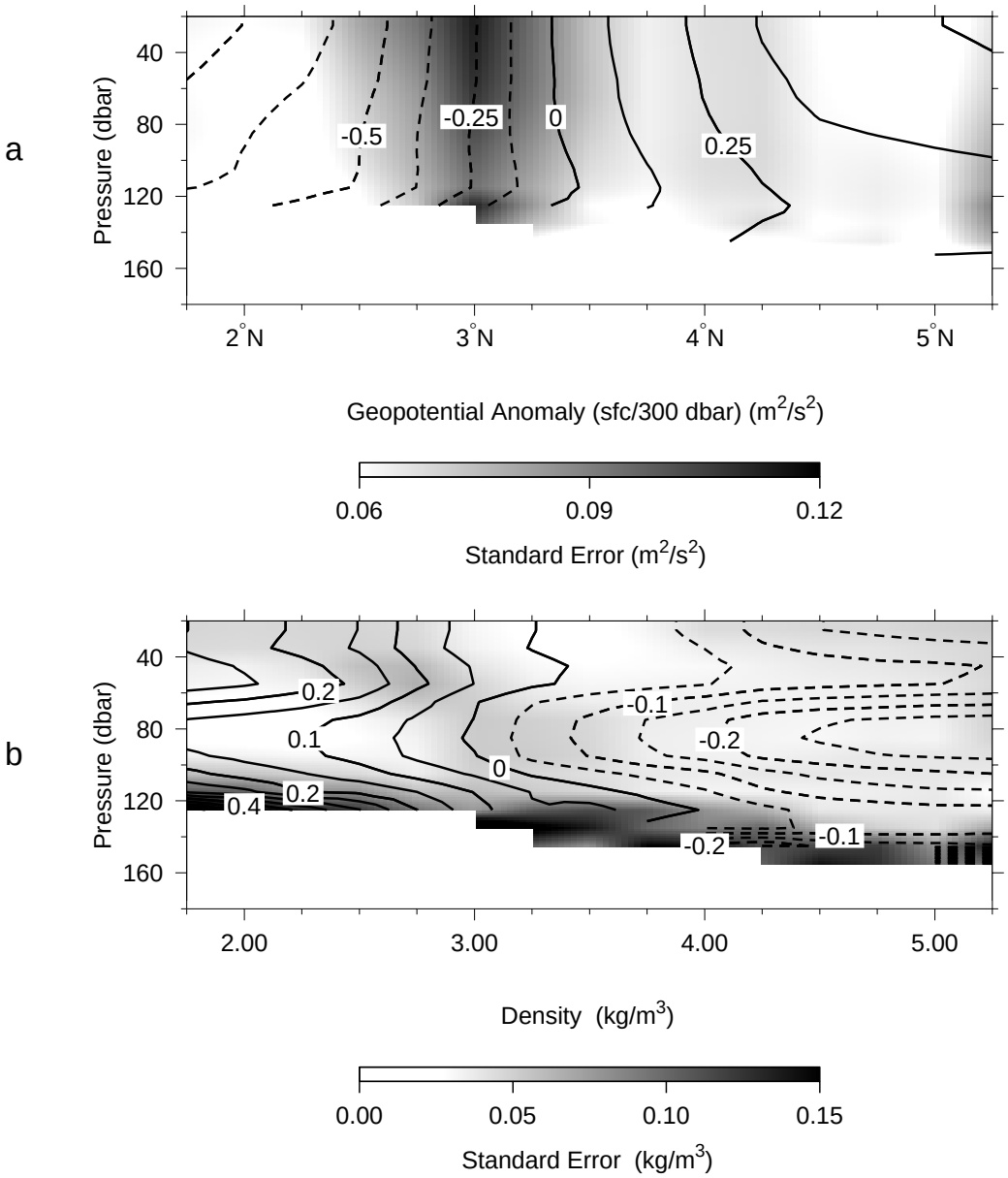

Figure 5.4: Mean (a) geopotential and (b) density anomalies relative to the overall depth dependent mean (the Boussinesq part). Contour intervals are 0.125 m^2/s^2 and 0.05 kg/m^3 respectively; Shading denotes standard errors.

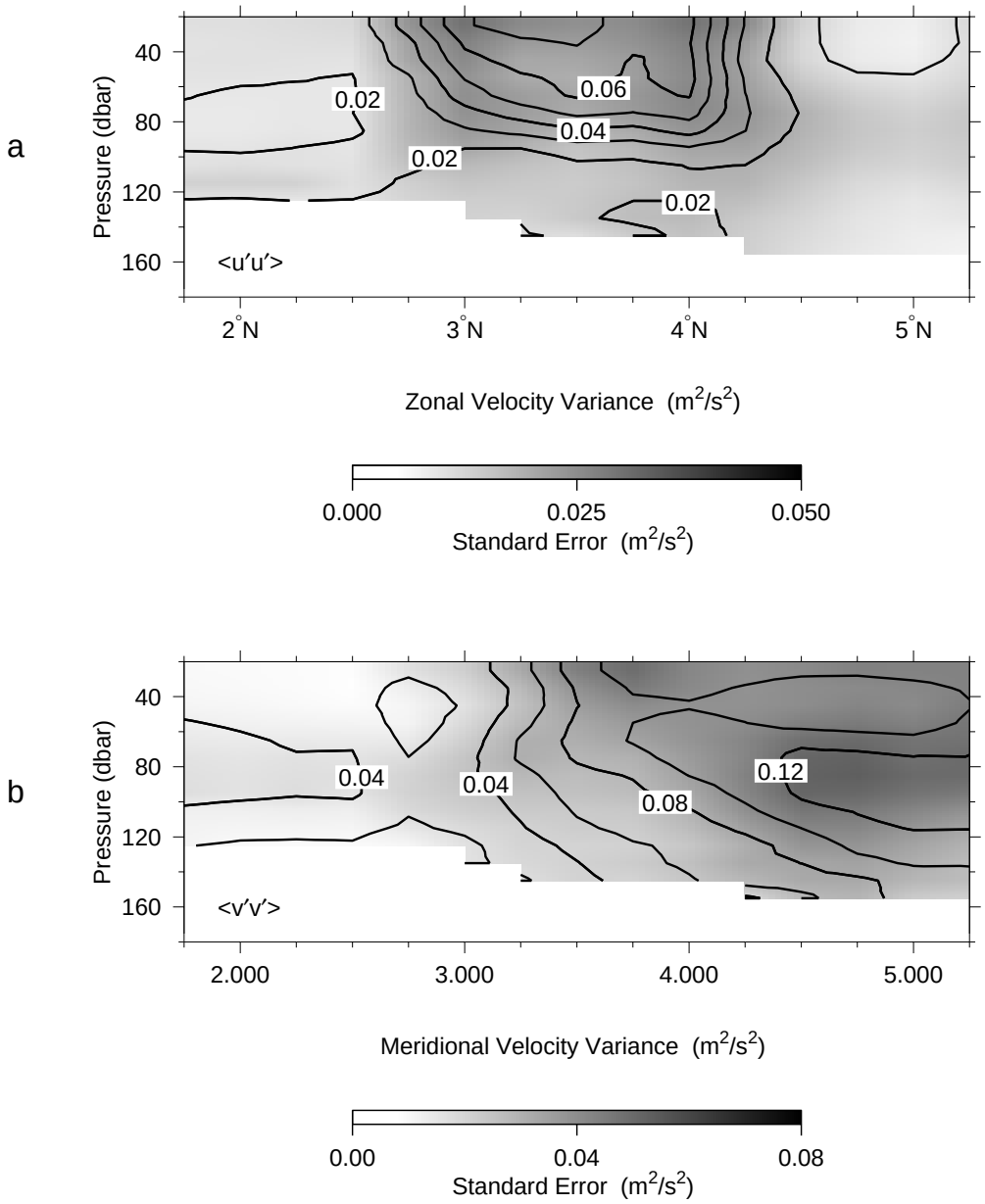

Figure 5.5: Mean variance of (a) zonal velocity $\overline{u'u'}$ and (b) meridional velocity $\overline{v'v'}$. Contour intervals are 0.01 and 0.02 $\mathrm{m}^2/\mathrm{s}^2$ respectively; shading denotes standard errors.

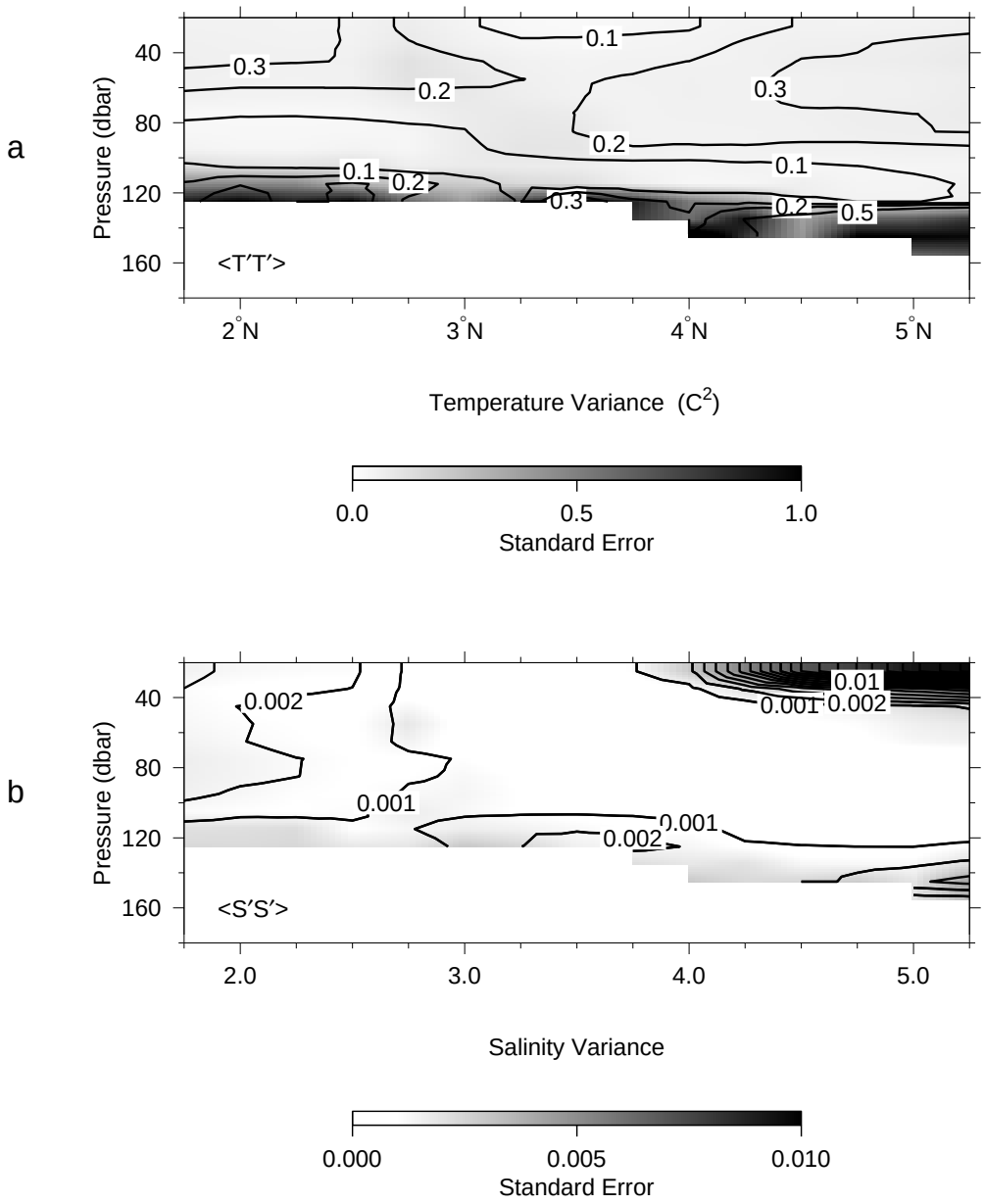

Figure 5.6: Mean variance of (a) temperature $\overline{T'T'}$ and (b) salinity $\overline{S'S'}$. Contour intervals are 0.1 C^2 and 0.001 respectively; shading denotes standard errors.

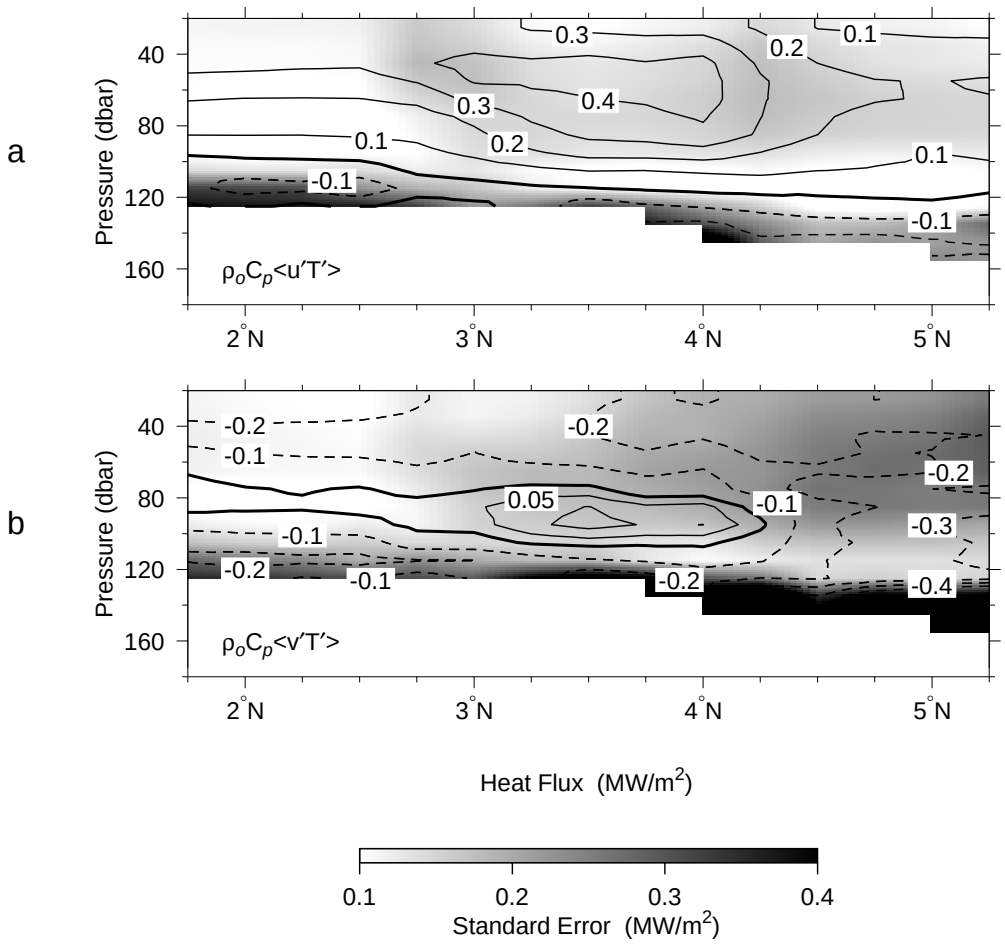

Figure 5.7: Mean eddy fluxes of heat in the (a) zonal $\rho_o\ C_P\overline{u'T'}$ and (b) meridional directions $\rho_o\ C_P\overline{v'T'}$. Contour intervals are 0.5 MW/m^2; shading denotes standard errors.

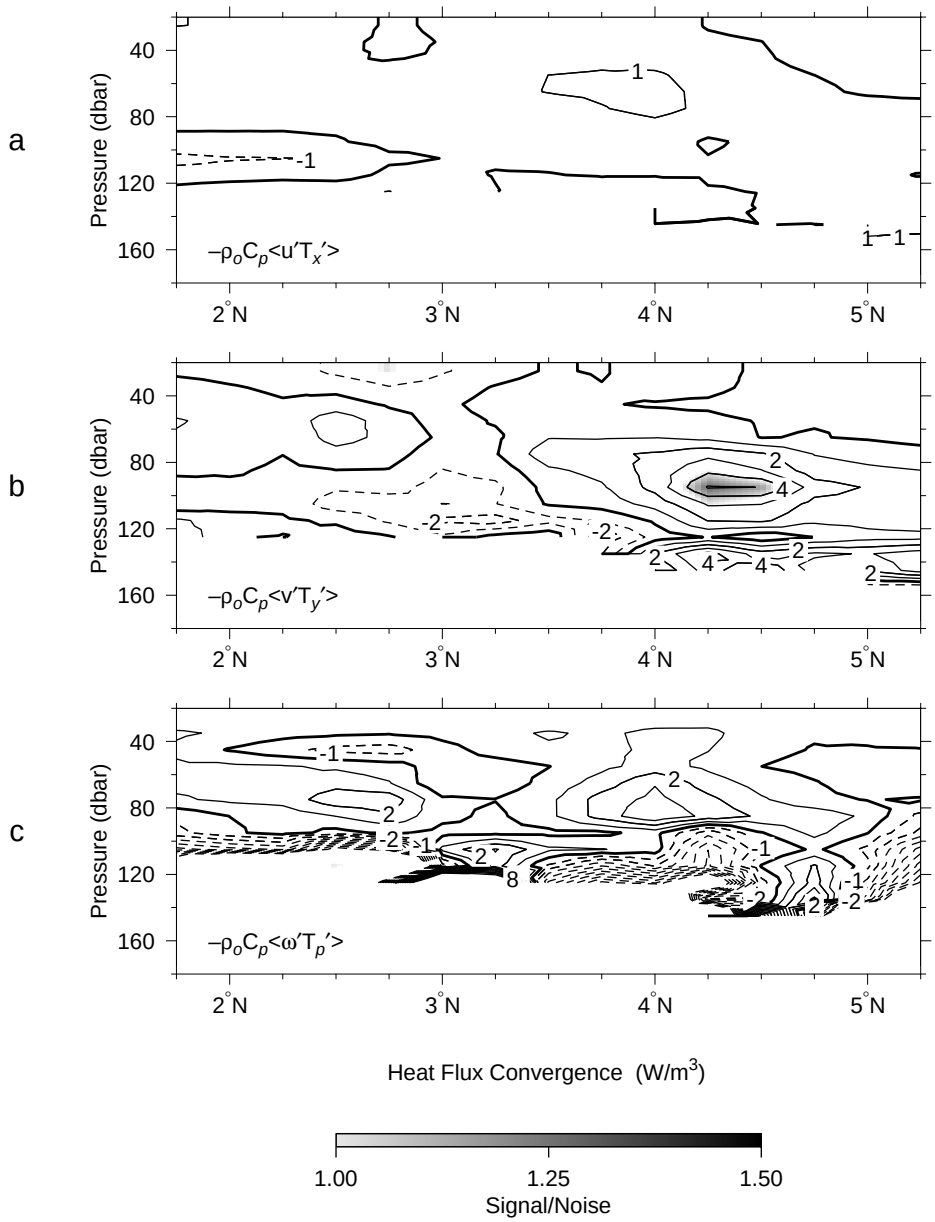

Figure 5.8: Mean eddy heat flux convergence contributions in the: (a) zonal ($-\rho_o\ C_P\overline{u'T'_x}$), (b) meridional ($-\rho_o\ C_P\overline{v'T'_y}$), and (c) vertical ($-\rho_o\ C_P\overline{w'T'_z}$) directions. Contour intervals are 1 W/m^3; shading denotes regions with a signal to noise ratio $> 1/2$.

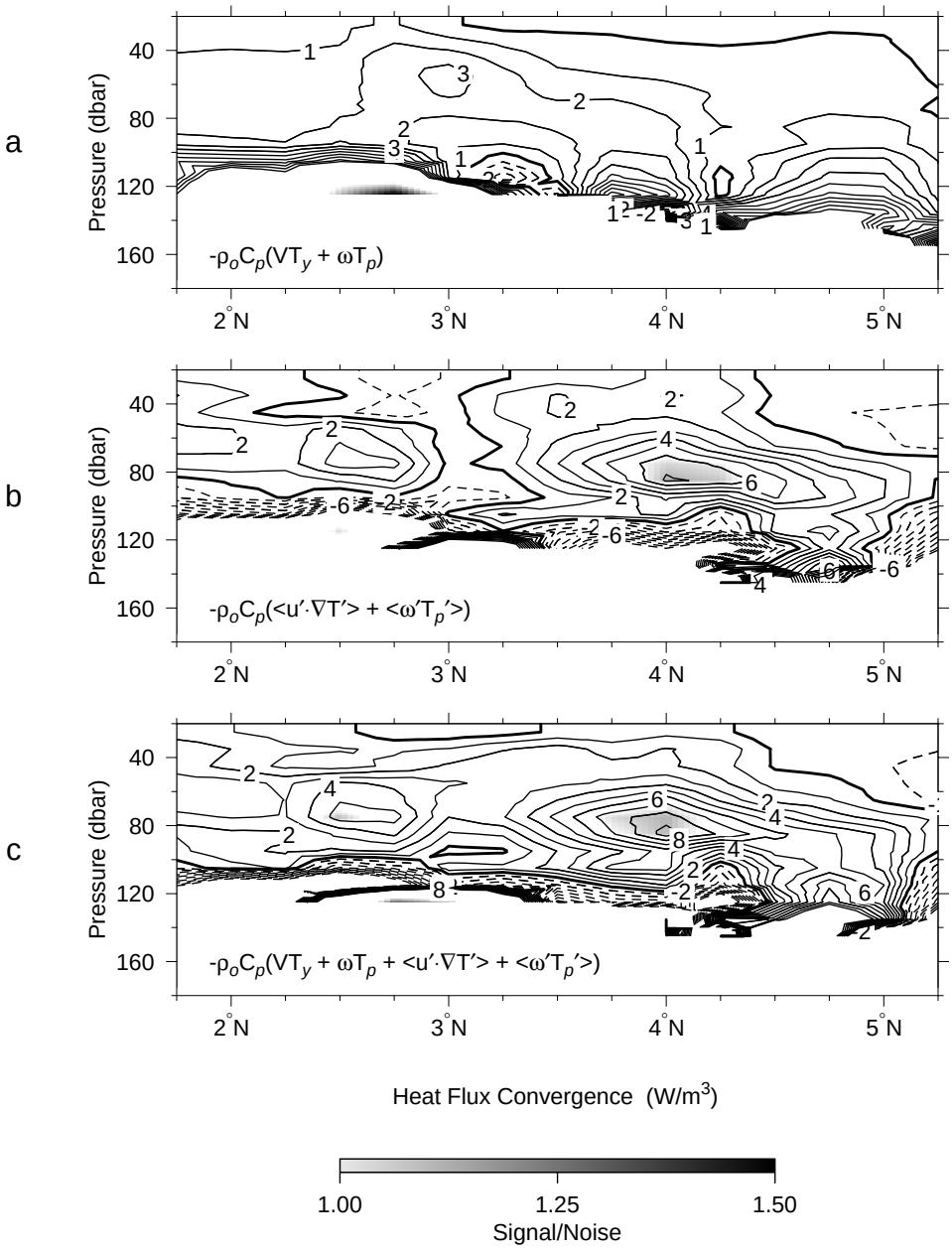

Figure 5.9: Mean heat flux convergence by the: (a) mean flow ($-\rho_o C_P(\overline{v}\partial_y\overline{T}+\overline{w}\partial_z\overline{T})$), (b) eddy flow ($-\rho_o\ C_P(\overline{u'\partial_x\ T'}\ +\ \overline{v'\partial_y\ T'}\ +\ \overline{w'\partial_z\ T'})$), and (c) the total. Contour intervals are 1 W/m^3; shading denotes regions with a signal to noise ratio $> 1/2$.

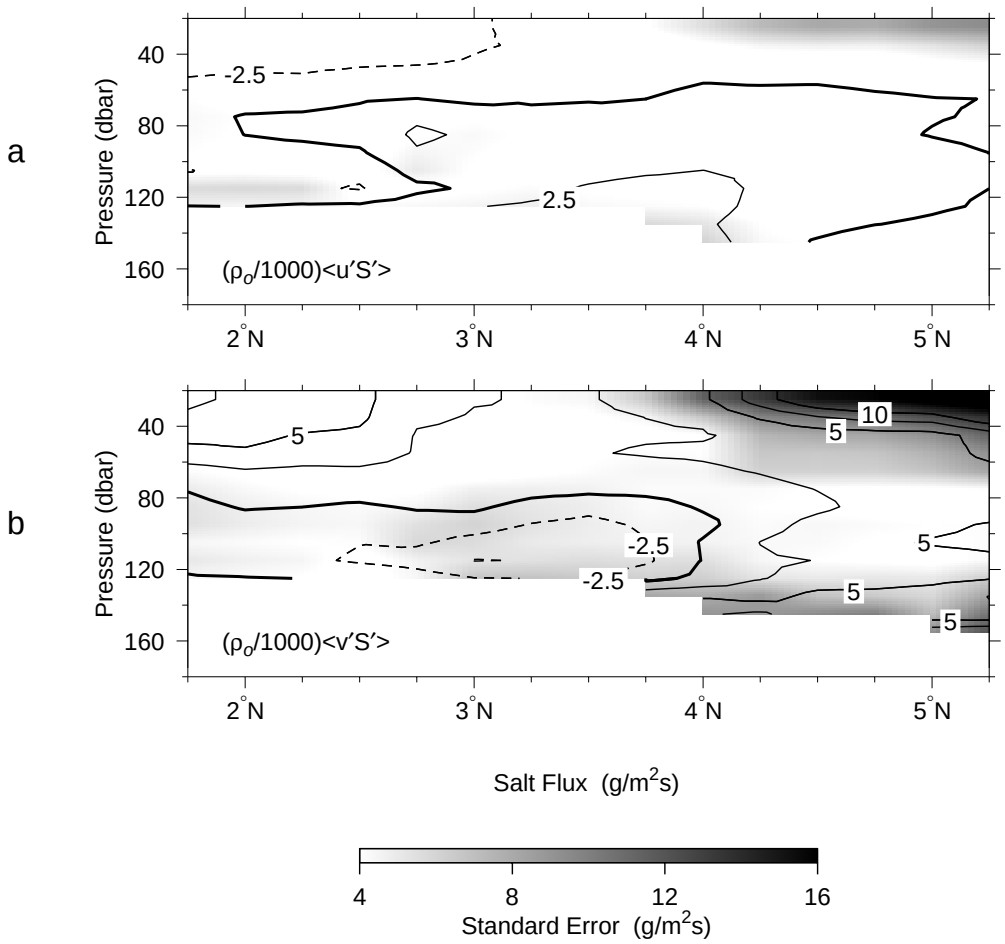

Figure 5.10: Mean eddy fluxes of salt in the (a) zonal $(\rho_o/1000)\overline{u'S'}$ and (b) meridional directions $(\rho_o/1000)\overline{v'S'}$. Contour intervals are 1.25 g/m^{2}s; shading denotes standard errors.

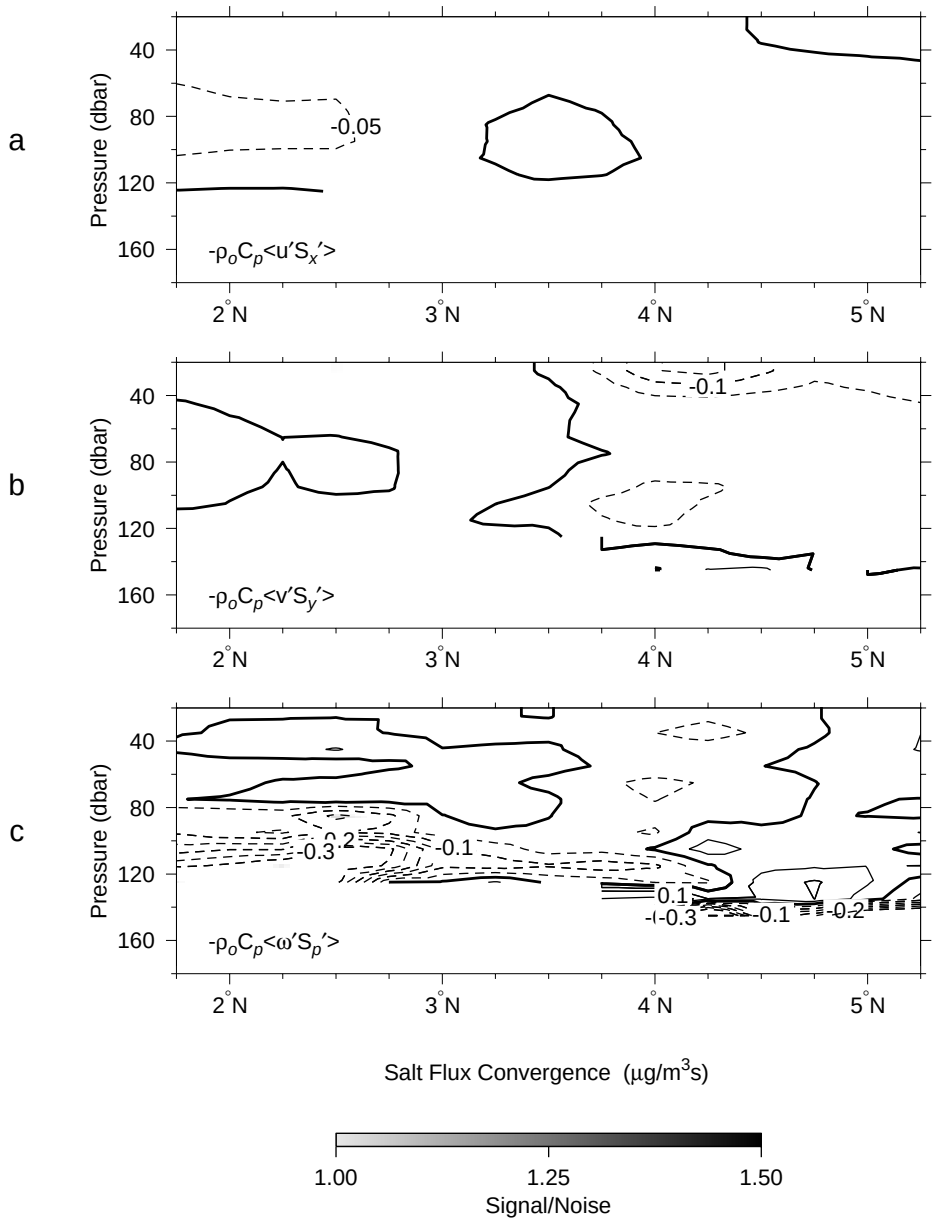

Figure 5.11: Mean eddy salt flux convergence in the: (a) zonal ($-(\rho_o/1000)\overline{u'S'_x}$), (b) meridional ($-(\rho_o/1000)\overline{v'S'_y}$), and (c) vertical ($-(\rho_o/1000)\overline{w'S'_z}$) directions. Contour intervals are 0.05 mg/m^3; shading denotes regions with a signal to noise ratio $> 1/2$.

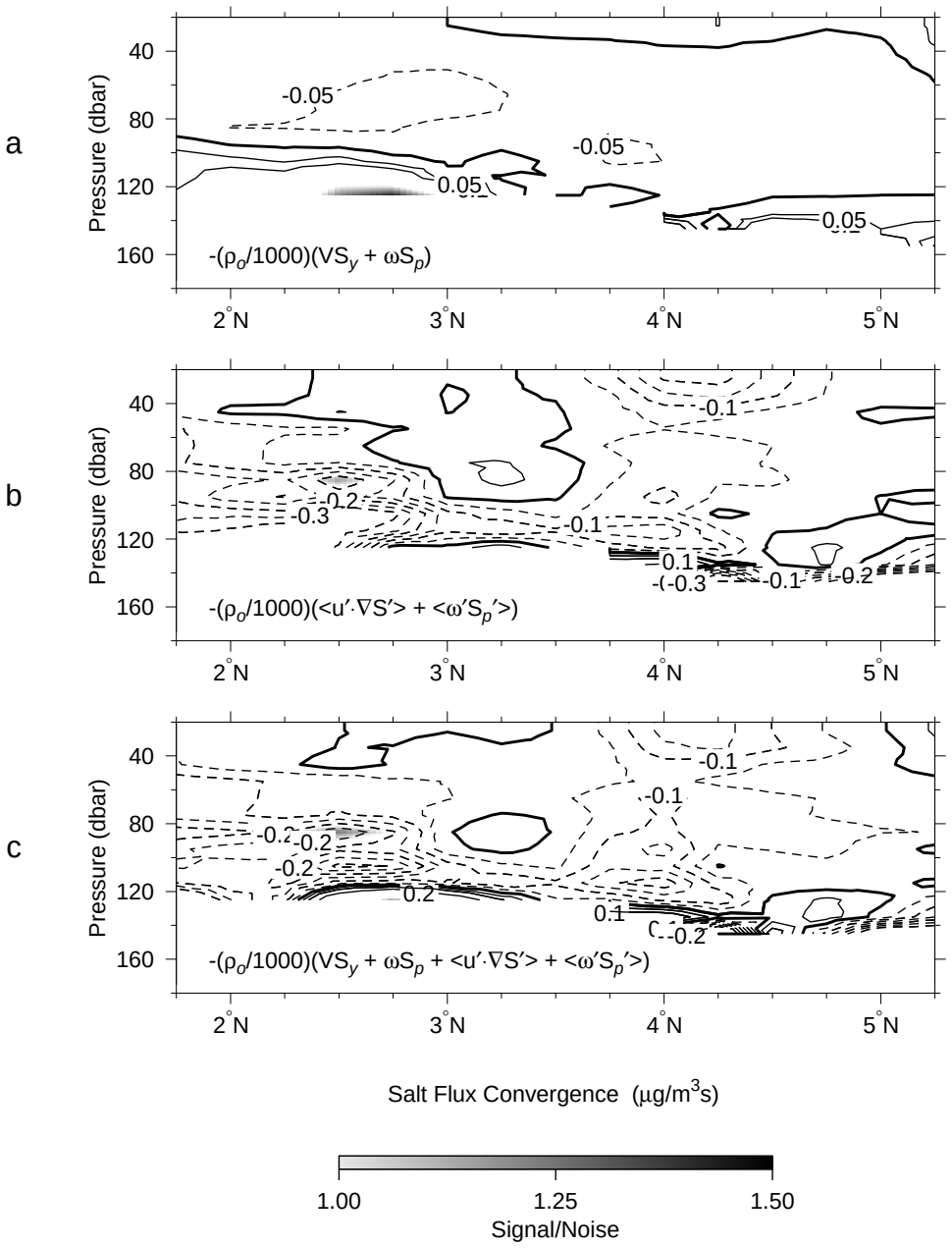

Figure 5.12: Mean salt flux convergence by the: (a) mean flow ($-\rho_o\ (\overline{v}\partial_y\overline{S}\ +\ \overline{w}\partial_z\overline{S})$), (b) eddy flow ($-\rho_o\ (\overline{u'\partial_x\ S'}\ +\ \overline{v'\partial_y\ S'}\ +\ \overline{w'\partial_z S'})$), and (c) the total. Contour intervals are 0.05 mg/m^3; shading denotes regions with a signal to noise ratio $> 1/2$.

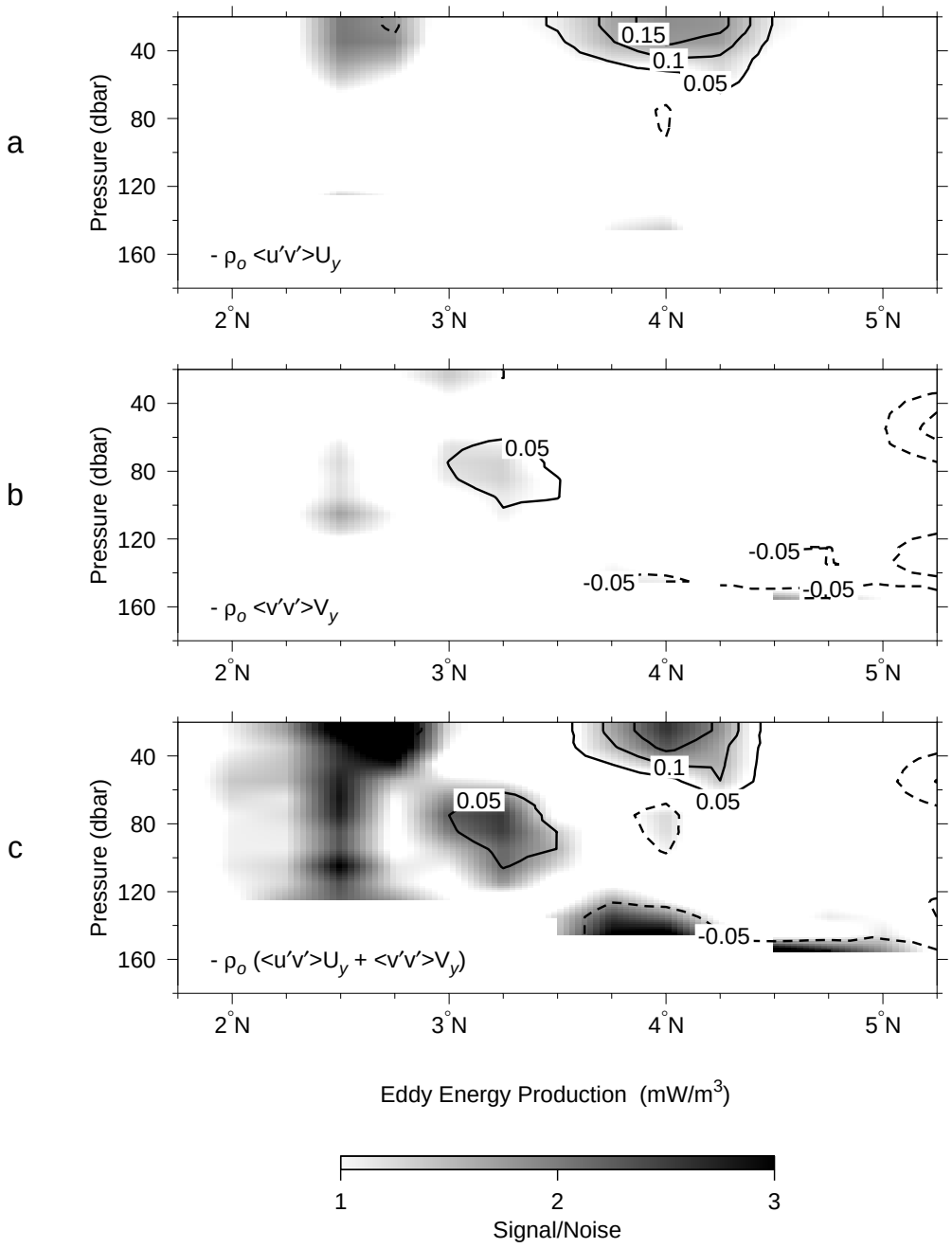

Figure 5.13: Horizontal barotropic mean to eddy kinetic energy conversions: (a) $-\rho_o \overline{u'v'}\overline{u}_y$, (b) $-\rho_o \overline{v'v'}\overline{v}_y$, and (c) the sum $-\rho_o \overline{v'\mathbf{u}}\cdot\overline{\mathbf{u}}_y$. Contour intervals are 0.05 mW/m^3; shading denotes regions with a signal to noise ratio > 1.

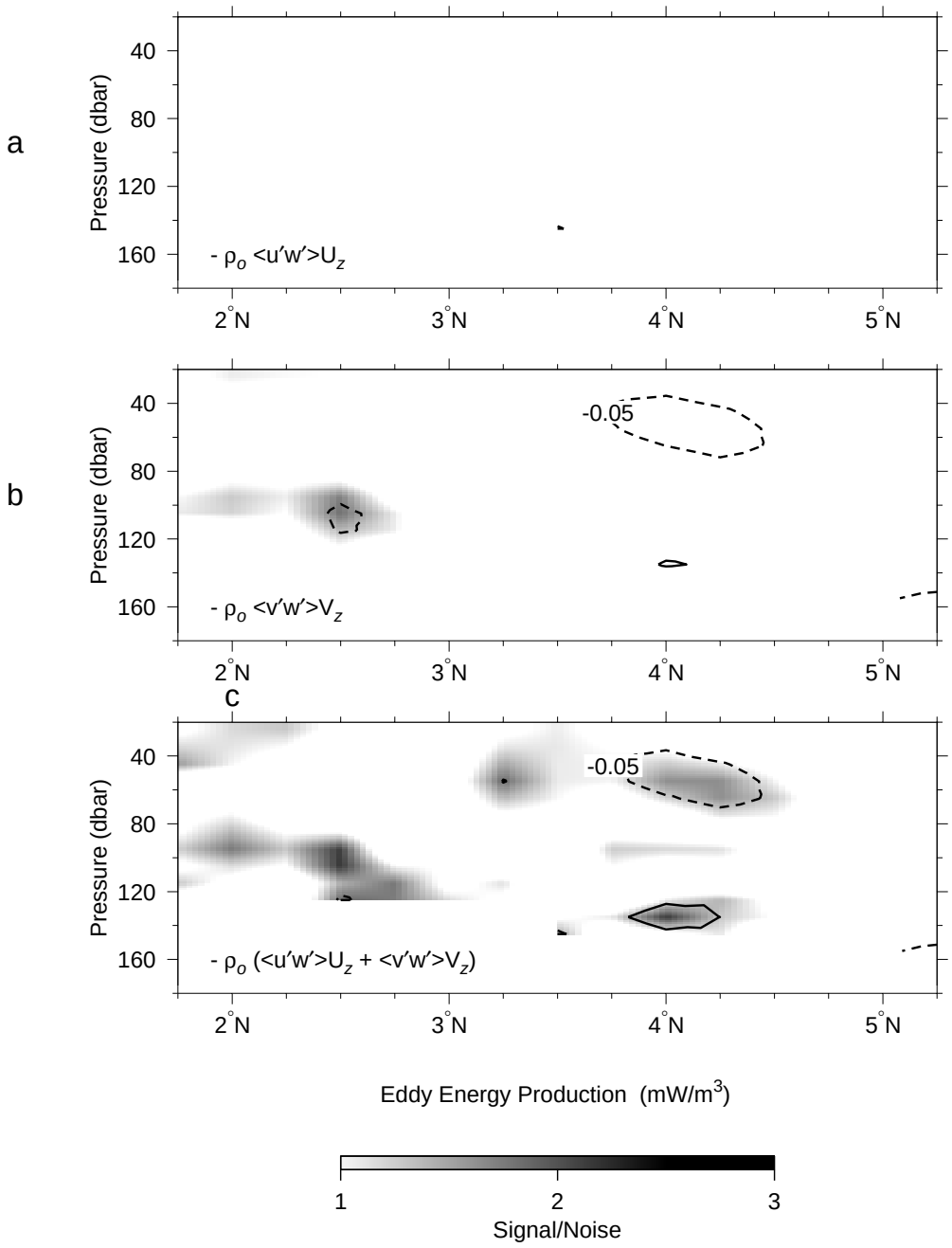

Figure 5.14: Vertical barotropic mean to eddy kinetic energy conversions: (a) $-\rho_o \overline{u'w'}\overline{u}_z$, (b) $-\rho_o \overline{v'w'}\overline{v}_z$, and (c) the sum $-\rho_o \overline{w'\mathbf{u}'} \cdot \overline{\mathbf{u}}_z$. Contour intervals are 0.05 mW/m^3; shading denotes regions with a signal to noise ratio > 1.

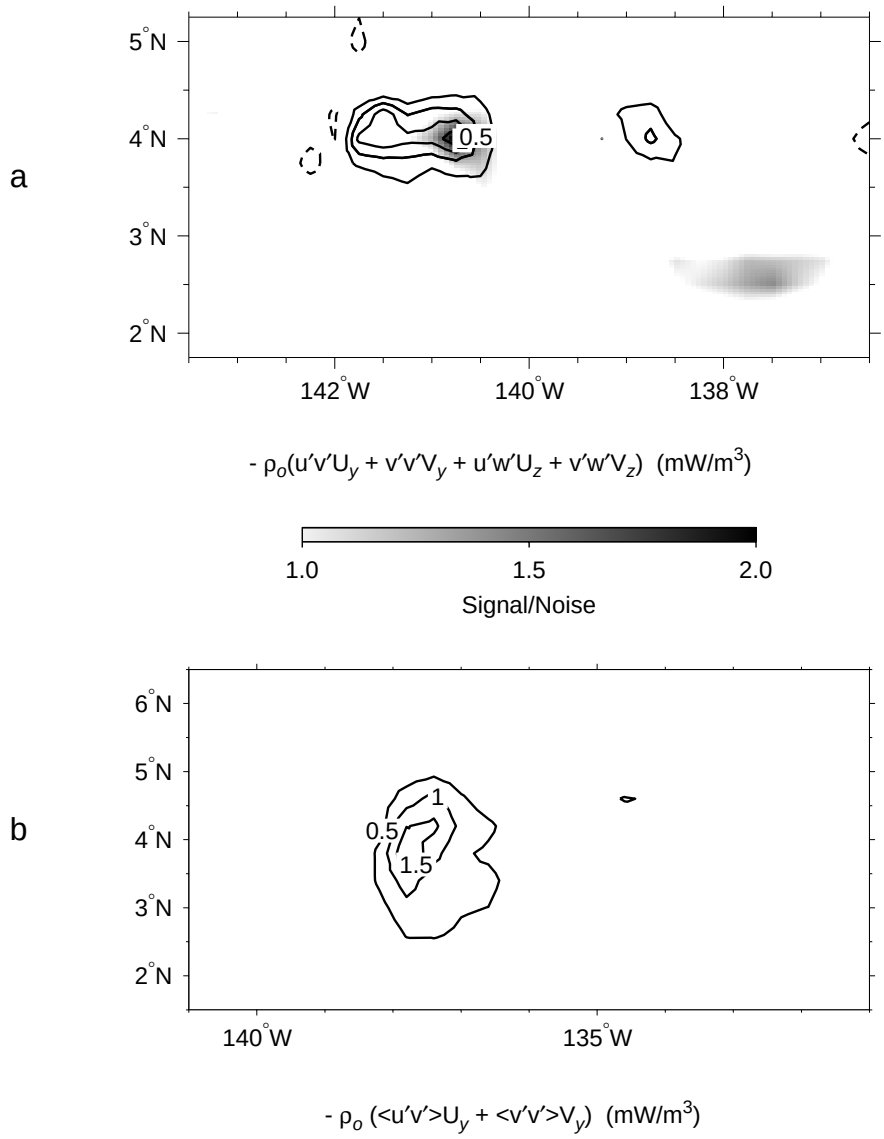

Figure 5.15: Barotropic mean to eddy kinetic energy conversion ($-\rho_o \overline{\mathbf{u}' \cdot (\mathbf{u}' \cdot \nabla \overline{\mathbf{u}}_y)}$) from the (a) observations and (b) POCM. Contour intervals are 0.25 and 0.5 mW/m^3 respectively; shading in (a) denotes regions with a signal to noise ratio > 1.

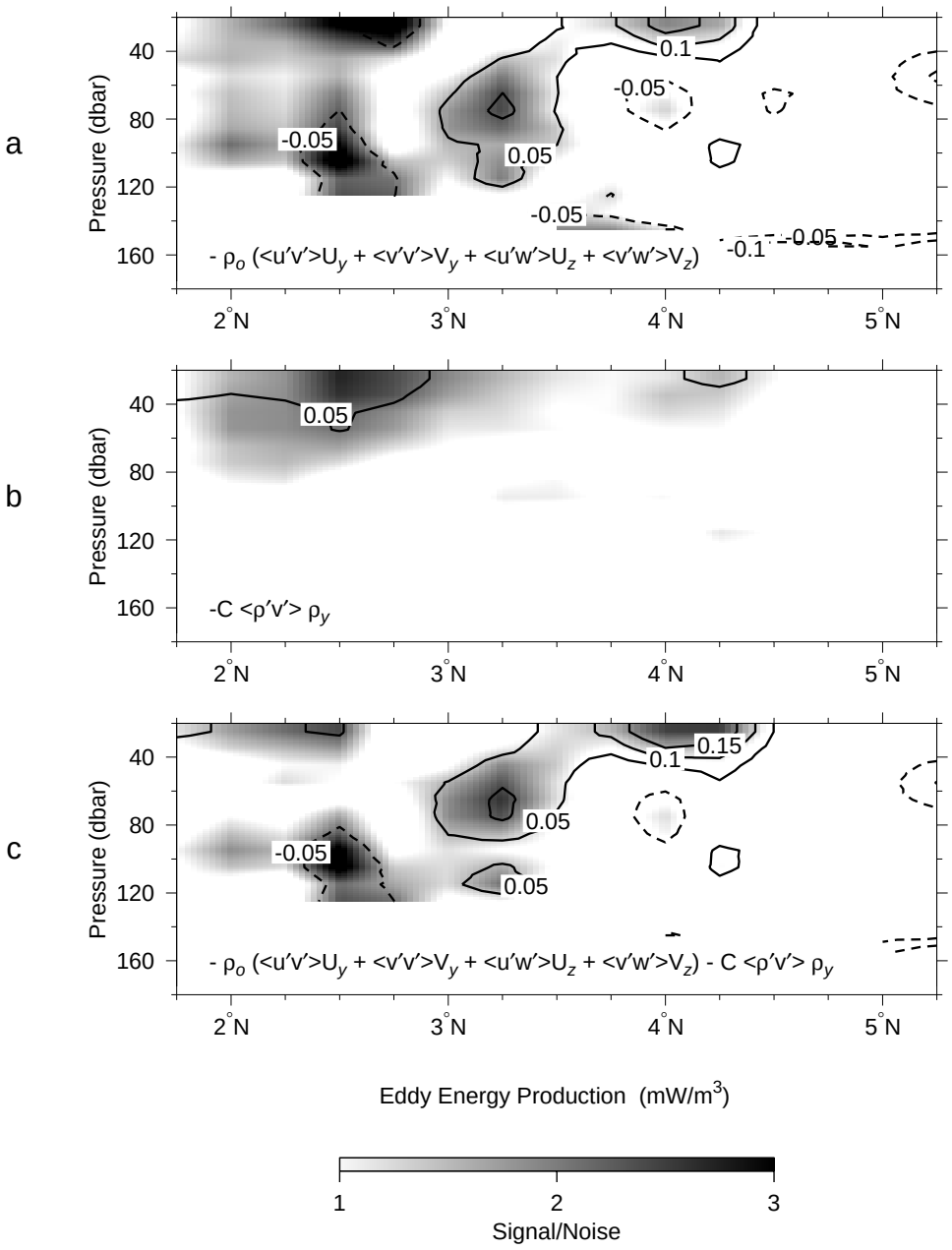

Figure 5.16: Mean to eddy energy conversions: (a) total barotropic ($-\rho_o \overline{\mathbf{u}' \cdot (\mathbf{u}' \cdot \nabla \overline{\mathbf{u}})}$), (b) baroclinic $-C\overline{\rho' v'}\overline{\rho}_y$, and (c) the sum $(-\rho_o \overline{\mathbf{u}' \cdot (\mathbf{u}' \cdot \nabla \overline{\mathbf{u}})} - C\overline{\rho' v'}\overline{\rho}_y$. Contour intervals are 0.05 mW/m^3; shading denotes regions with a signal to noise ratio > 1.

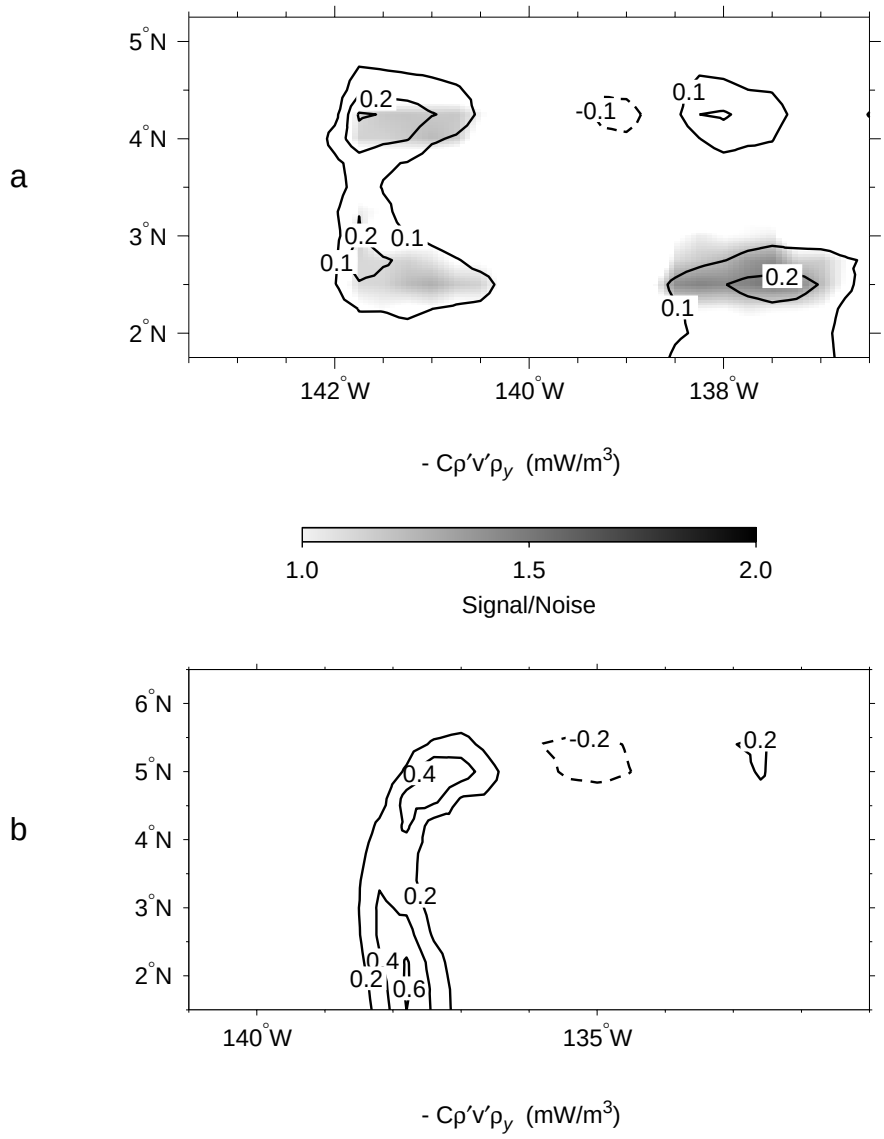

Figure 5.17: Baroclinic mean to eddy available potential energy conversion ($-C\rho' v' \overline{\rho}_y$) from the (a) observations and (b) POCM. Contour intervals are 0.1 and 0.2 mW/m^3 respectively; shading in (a) denotes regions with a signal to noise ratio > 1.

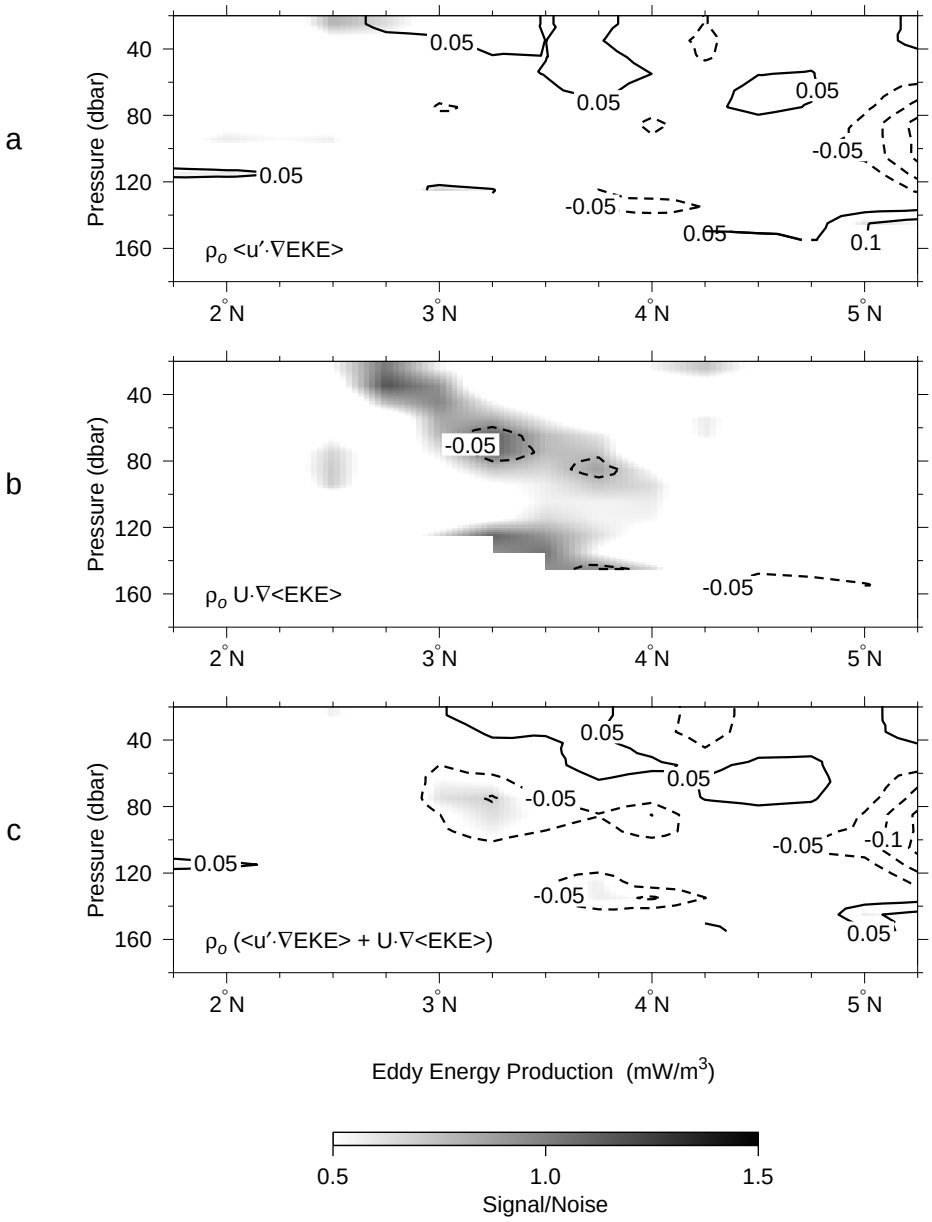

Figure 5.18: Mean advection of eddy kinetic energy via the (a) mean flow $\overline{\mathbf{u}} \cdot \nabla \overline{EKE}$, and (b) the eddy flow $\overline{\mathbf{u}' \cdot \nabla \ EKE}$. (c) The sum of the two - total EKE advection $\overline{\overline{u} \ + \ \mathbf{u}') \cdot \nabla \ EKE}$. Contour intervals are 0.05 mW/m^3; shading denotes regions with a signal to noise ratio > 1.

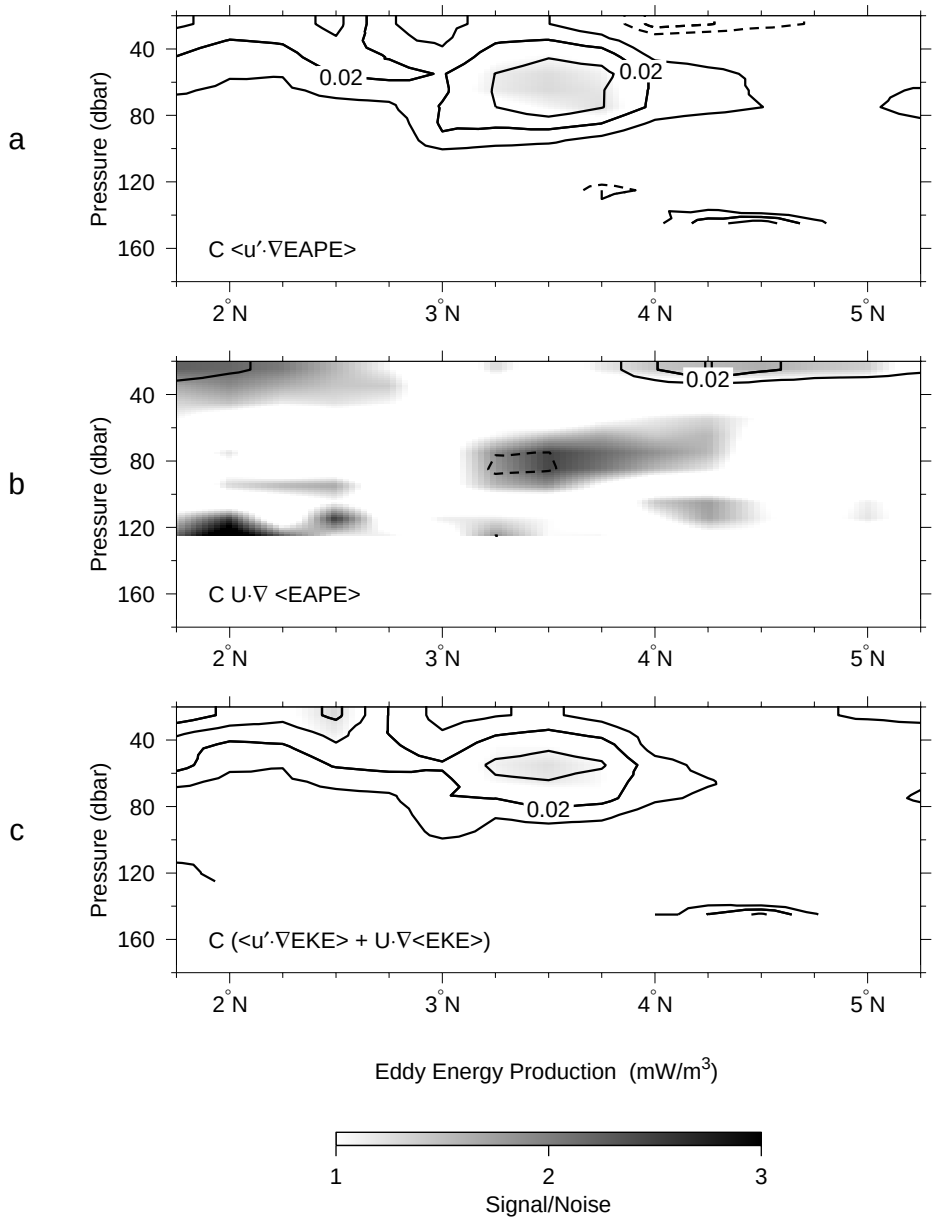

Figure 5.19: Mean advection of eddy available potential energy via the (a) mean flow $\overline{\mathbf{u}} \cdot \nabla \overline{EAPE}$, and (b) the eddy flow $\overline{\mathbf{u}' \cdot \nabla \ EAPE}$. (c) The sum of the two - total EAPE advection $\overline{\overline{u} \ + \ \mathbf{u}') \cdot \nabla \ EAPE}$. Contour intervals are 0.01 mW/m^3; shading denotes regions with a signal to noise ratio > 1.

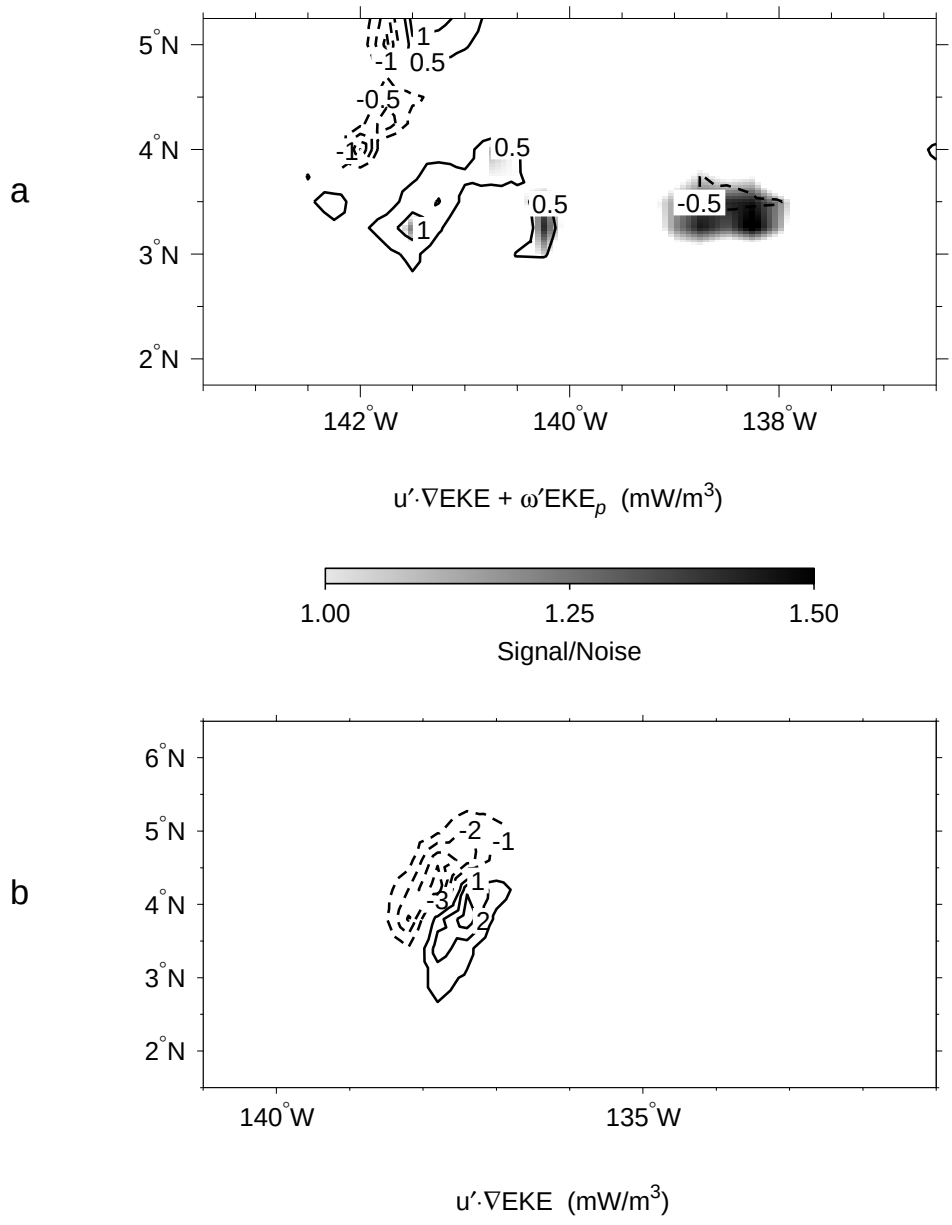

Figure 5.20: Eddy advection of eddy kinetic energy ($\mathbf{u}' \cdot \nabla\ EKE$) from the (a) observations and (b) POCM. Contour intervals are 0.5 and 1 mW/m^3 respectively; shading in (a) denotes regions with a signal to noise ratio > 1.

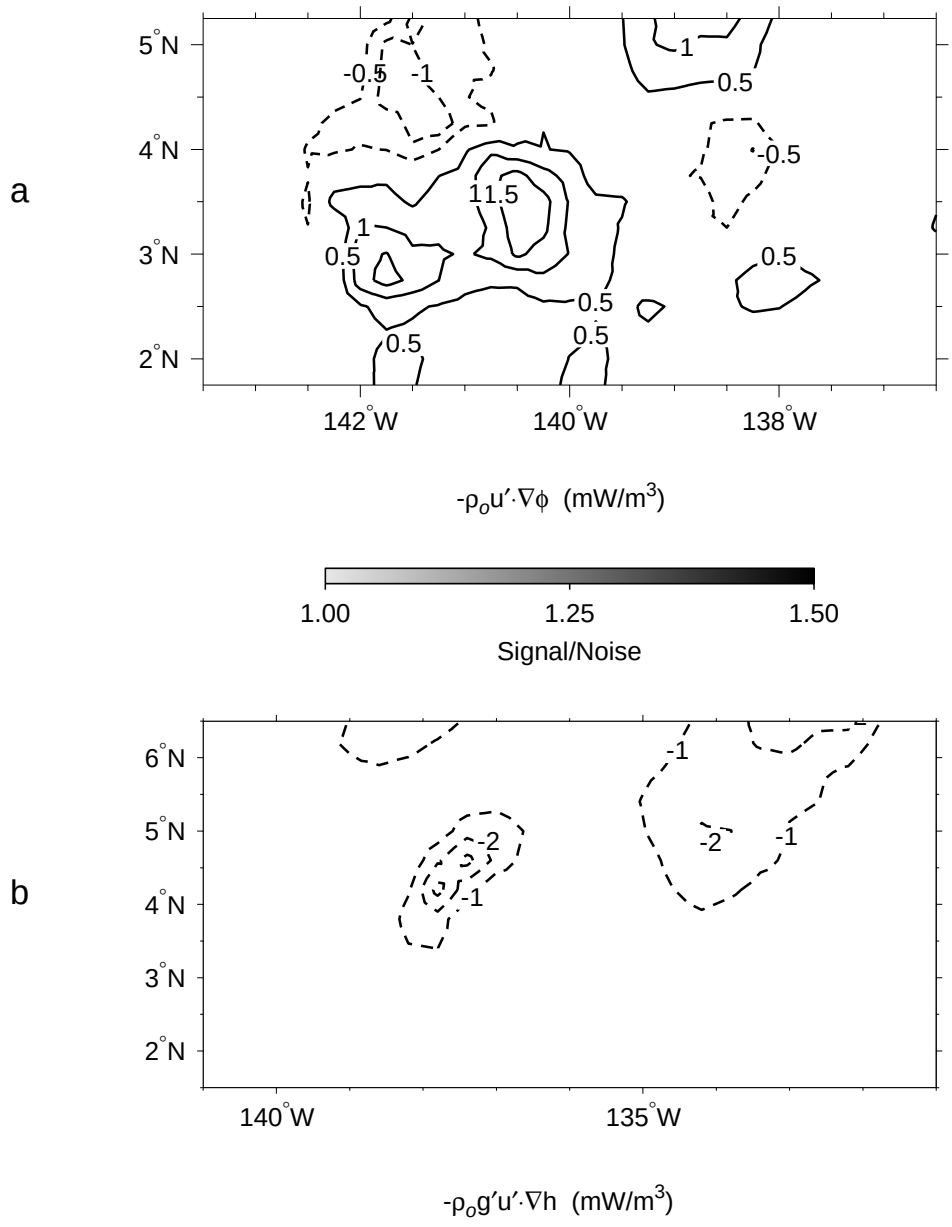

Figure 5.21: Eddy geopotential work from the (a) observations ($-\rho_o \mathbf{u}' \cdot \nabla \phi'$) and (b) POCM ($-\rho_o\ g\mathbf{u}' \cdot \nabla\ h'$). Contour intervals are 0.5 and 1 mW/m^3 respectively; shading in (a) denotes regions with a signal to noise ratio > 1.

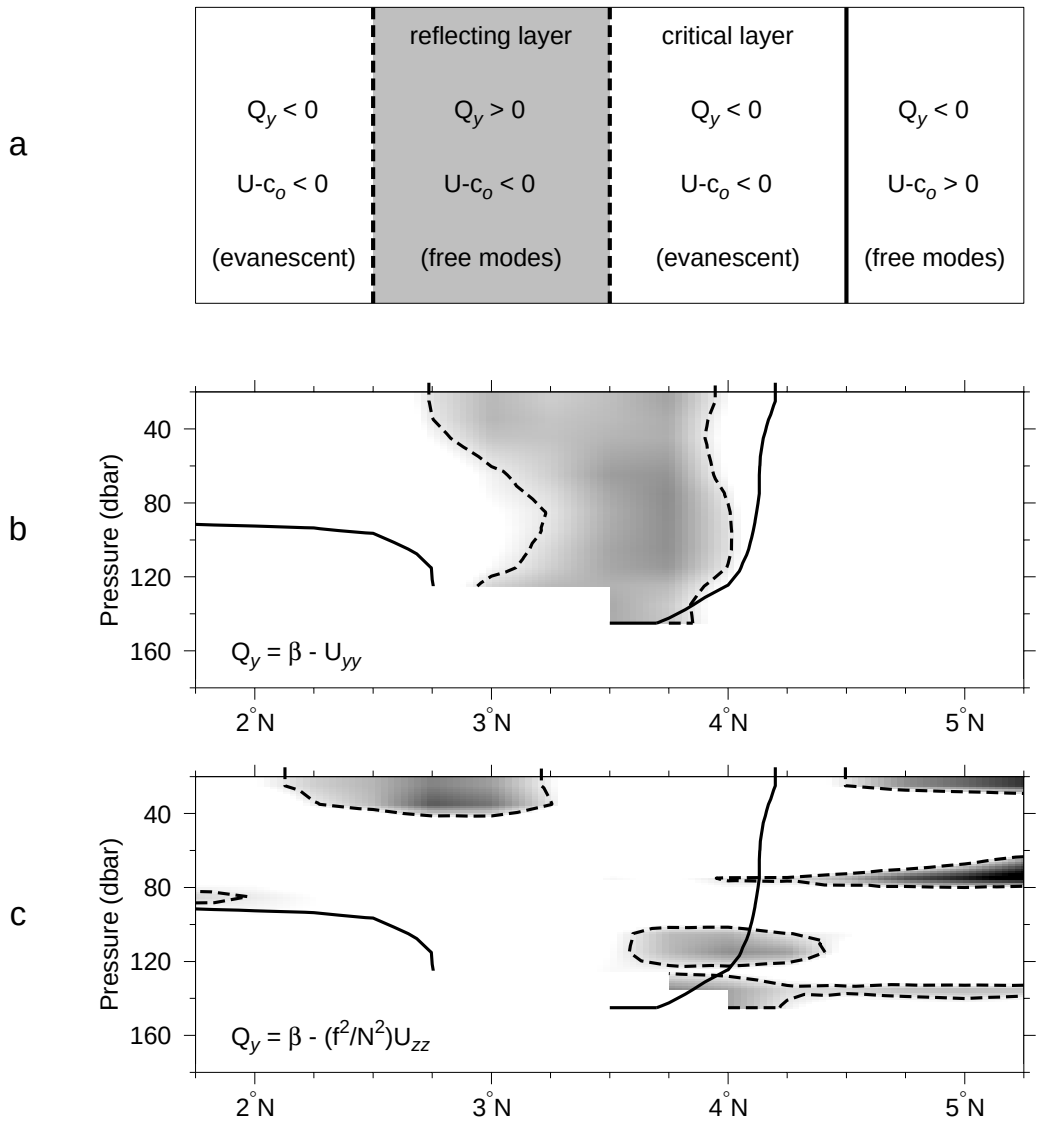

Figure 5.22: (a) Conceptualized geometry for wave overreflection after Lindzen [1988]. The solid line marks the critical surface ($\overline{u} - c_0 = 0$) and the dashed lines indicate zero lines of the potential vorticity gradient ($Q_y = 0$). (a) Barotropic case ($Q_y = \beta - \overline{u}_{yy}$) and (b) baroclinic case ($Q_y = \beta - (f^2/N^2)\overline{u}_{zz}$) from the observations.

Chapter 6

Summary

We have described the kinematics, structure, dynamics, and eddy fluxes of a tropical instability vortex using observations made during the Tropical Instability Wave Experiment from November to December 1990. The results have been confirmed, and generalized to other tropical instability vortices, using the Parallel Ocean Climate Model.

6.1 Kinematics

Six drifting buoys moved westward in the SEC-NECC shear region in a cycloidal motion. Moored thermistors were used to determine the local time of passage of a high pressure as 30-35 days, in agreement with previous long term observations [McPhaden, 1996]. In combination with ADCP measurements, this information was used to show that the drifter motion was induced by the passage of a vortex translating at -30 cm/s, or 0.24 °/day. The translation speed of the vortex was found to be applicable over the upper layer (above the thermocline) north of about 1.5-2°N.

At the same time, meridional oscillations of the EUC and SEC between 1°S and 1°N translated westward at about 80 cm/s - more than twice as fast. We thus have evidence that Tropical Instability Waves may manifest themselves simultaneously as more than one phenomenon. Consequently, we have chosen the terms SEC-NECC shear vortices, or tropical instability vortices (TIVs) to describe the perturbations in the anticyclonic SEC-NECC shear region, and reserved the traditional term equatorial long waves for the oscillations at the equator. While this study cannot address the dynamics at the equator, the shear vortices have been found here to be directly associated with a

barotropic instability. The equatorial disturbances appear to be consistent with a finite amplitude wave process capable of inducing significant heat and energy fluxes [Halpern *et al.*, 1988; Qiao and Weisberg, 1997].

6.2 Structure

The flow and thermohaline structure of the observed vortex were objectively mapped in three dimensions by first transforming all observations into a reference frame moving with the vortex. In this reference frame, the flow was nearly steady, apart from a 3 day wind event which aliased temporal changes into spatial gradients over the southeastern part of the study region. Strong divergence and geopotential gradients in that area were shown to correspond closely to aliased wind driven currents and thermocline deepening.

This study concludes that TIVs are the cause of sea level highs and cold water cusps that propagate across the central tropical Pacific with wavelengths of 500-1500 km and periods of 25-35 days. The vortex flow was directly related to a central high pressure, similar to sea level highs previously observed with IES arrays and from satellite altimeters [Miller *et al.*, 1985; Perigaud, 1990; Busalacchi *et al.*, 1994], and a northward cusp of cold water, resembling the typical meridional deformations to the North Equatorial Front visible in AVHRR images [Legeckis, 1977; Legeckis, 1986a; Pullen *et al.*, 1987]. Comparisons with shear vortices in the POCM confirm this relationship throughout the TIW season.

Observations of relative zooplankton abundance, inferred from ADCP backscatter, imply that the relatively cold and saline water entrained from the south was also biomass-rich. We suggest that the high concentrations of biomass found at the NEF do

not originate through local inputs of nutrients into the euphotic zone, but instead result from the intense advective processes found in the vortex flow.

6.3 Dynamics

The vortex flow was found to be of Rossby number ≥ 1, with the nonlinear (advection) terms largest in the vicinity of the North Equatorial Front; the nonlinear role was not an artifact of a cyclostrophic balance.

Intense convergence, on the order of the local inertial frequency (10^{-5} s^{-1}), was found at the northwestward leading edge of the front (cold cusp), both in an objectively mapped velocity field and in direct observations of the deformation of a drifting buoy cluster. A vorticity balance revealed that the frontal convergence constituted a vortex stretching response to relative vorticity advection at the westward edge of the vortex, where the shear of the leading edge creates locally large positive vorticity. Similar results for the POCM vortex lead to the conclusion that subgrid scale and turbulent processes play a significant role in the balance.

Intense divergence, also comparable to f, was measured just off center (about 0.5-1° west) in the vortex, in a dipole pattern with the frontal convergence. Analysis of the momentum equations in polar coordinates revealed that parcels in the region were accelerating radially outward. The upwelling, however, had little effect on the vorticity budget because of near zero local absolute vorticity, suggesting that inertial instability could be relevant. This idea was supported by application of a stability criterion for vortices on an f-plane, which showed that the central region of the vortex should be unstable and limited to a near zero absolute vorticity.

The evidence that the vortex was unstable and inertially limited is supported by instability vortices in the POCM which consistently exhibit the convergence/divergence dipole pattern with anticyclonic vorticity near the center not exceeding f in magnitude. Such an instability process could explain the relatively regular amplitude of TIWs which has lead to the common use of the term equatorial long waves. The growth of SEC-NECC shear vortices is due to the shear instability of the zonal currents, as established by previous observations and this study. The existence of an absolute constraint on vorticity growth, imposed by the rotation of the Earth, guarantees that the shear instability will consistently create nearly identical vortices.

6.4 Eddy fluxes

The vortex entrained cold, saline water from the south and warmer, fresher water from the north, inducing equatorward fluxes of heat and fresh water (order 0.2 MW/m^2 and 5 g/(m^{2}s). The heat flux observations are in agreement with previous observations and modeling studies [Hansen and Paul, 1984; Baturin and Niiler, 1997; Bryden and Brady, 1989], while the salt fluxes, strongest in the mixed layer, represent the first such observations. The flux divergences between 2 and 5° imply net heating and freshening on the order of 2-5 W/m^3 and 0.1 μg/(m^{3}s).

Eddy energetics reveal that the vortex obtained kinetic energy from the mean flow via barotropic instability of the mean zonal shear ($-\overline{u'v'}\overline{u}_y$) at the rate of 0.15 mW/m^3, in agreement with the observations of Baturin and Niiler [1997] (also Hansen and Paul [1984], although not in magnitude). Baroclinic instability ($-\overline{\rho'v'}\overline{\rho}_y$) played a secondary role with mean to eddy APE conversions of 0.05 mW/m^3. The mean to eddy kinetic

energy conversion was localized in the dipole of convergence and divergence, suggesting that the instability mechanism is responsible for intensifying the front.

An application of wave overreflection geometry to the observations gives sufficient conditions for barotropic instability: the proper arrangement of reflecting and critical layers, and quantization of meridional wavenumber in the reflecting layer. The increase in eddy KE following the parcels follows the path of water subducting at the front, and appears to coincide with the reflecting layer, where overreflection manifests itself. The critical layer is collocated with the region of mean to eddy KE conversion.

Appendix A

Eddy Energy Equations

A.1 Isobaric coordinates

The basic equations in isobaric coordinates are [Kasahara, 1974]:

$$\mathbf{u}_t + \mathbf{u} \cdot \nabla \mathbf{u} + \omega \mathbf{u}_p + \mathbf{f} \times \mathbf{u} = -\nabla \phi \tag{A.1}$$

$$\nabla \cdot \mathbf{u} + \omega_p = 0 \tag{A.2}$$

$$\rho_t + \mathbf{u} \cdot \nabla \rho + \omega(\rho_o + \rho)_p \tag{A.3}$$

where $\phi = \int_{ref}^{p} \rho^{-1} dp$ is the geopotential, $\omega = dp/dt$ is the equivalent of vertical velocity in isobaric coordinates, and p subscripts denote partial derivation with respect to pressure. The Boussinesq approximation has been made after separating the total density and geopotential fields into depth dependent and fluctuating parts:

$$\begin{aligned} \rho^*(x,y,z,t) &= \rho_o(z) + \rho(x,y,z,t) \\ \phi^*(x,y,z,t) &= \phi_o(z) + \phi(x,y,z,t) \end{aligned} \tag{A.4}$$

so that the total hydrostatic balance in isobaric coordinates has the form:

$$\frac{\partial \phi^*}{\partial P} = \frac{-1}{\rho^*} = \frac{-1}{\rho_o + \rho} \approx \frac{-1}{\rho_o} + \frac{\rho}{\rho_o^2}$$

where the last step involves a Taylor expansion.

Since the balance for the rest state is $\phi_{op} = -\rho_o^{-1}$, the hydrostatic flow obeys:

$$\frac{\partial \phi}{\partial P} = \frac{\rho}{\rho_o^2} \tag{A.5}$$

A.2 Energy equations

The kinetic energy equation ($\rho_o \mathbf{u}\cdot$ (A.1)) is:

$$\frac{D}{Dt}(KE) + \omega KE_p = -\nabla \cdot (\phi \mathbf{u}) + \rho_o \phi \nabla \cdot \mathbf{u} \tag{A.6}$$

where the material derivative includes horizontal advection only. The work terms on the right hand side have been expressed in terms of the total work and horizontal deformation work instead of the net work to highlight the role of divergence in converting APE to KE. (The equations can be written in the conventional form by adding the hydrostatic relation times the vertical velocity).

We can derive the APE equation in isobaric coordinates by multiplying (A.3) by $C\rho$:

$$\frac{D}{Dt}(APE) - \frac{\rho^2}{2}\frac{DC}{Dt} = -\rho_o(\phi\omega)_p - \rho_o \phi \nabla \cdot \mathbf{u} \tag{A.7}$$

where $C = -(\rho_o \rho_p^*)$ is the $C = -g/\rho_z^*$ of Luther and Johnson [1990] expressed in pressure coordinates. With this definition APE does not advect conservatively, thus the second term on the left hands side involving the rate of change of C following the motion.

A.3 Eddy kinetic energy

Using the decomposition given by (5.1) and (5.2), the total mean kinetic energy is:

$$\begin{aligned}(\overline{KE}+\overline{EKE})_t+\overline{u}\overline{EKE_x}+\overline{v}(\overline{KE}+\overline{EKE})_y+\overline{\omega}(\overline{KE}+\overline{EKE})_p=\\ -\overline{\mathbf{u'}\cdot\nabla(\rho_o\overline{\mathbf{u}}\cdot\mathbf{u'}+EKE)}-\overline{\omega'(\rho_o\overline{\mathbf{u}}\cdot\mathbf{u'}+EKE)_p}\\ -\rho_o\nabla\cdot(\overline{\phi}\overline{\mathbf{u}}+\overline{\phi'\mathbf{u'}})+\rho_o\overline{\phi}\nabla\cdot\overline{\mathbf{u}}+\rho_o\overline{\phi'\nabla\cdot\mathbf{u'}}\end{aligned} \tag{A.8}$$

where $\overline{KE}=\rho_o|\overline{\mathbf{u}}|^2/2$ is the kinetic energy of the mean flow, and $\overline{EKE}=\rho_o\overline{|\mathbf{u'}|^2}/2$ is the mean eddy kinetic energy. The third term on the right hand side arises from the mean zonal gradients and errors caused by the finite averaging width (see Chapter 5 Section 5.1).

The mean momentum is:

$$\overline{\mathbf{u}}_t+\overline{u\mathbf{u}_x}+\overline{v}\,\overline{\mathbf{u}}_y+\overline{\omega}\mathbf{u}_p+\overline{\mathbf{u'}\cdot\nabla\mathbf{u'}}+\overline{\omega'\mathbf{u}_p{}'}+\mathbf{f}\times\overline{\mathbf{u}}=-\nabla\overline{\phi} \tag{A.9}$$

which shows that the mean momentum depends on the eddies through eddy advection of eddy momentum. Again, the mean zonal gradients are not zero so the second term remians.

An equation for the evolution of the KE of the mean flow is formed by taking $\overline{\mathbf{u}}\cdot$(A.9), giving:

$$\overline{KE}_t + \overline{u}\overline{EKE}_x + \overline{v}\overline{KE}_y + \overline{\omega}\overline{KE}_p + \rho_o\overline{\mathbf{u'}\cdot\nabla(\overline{\mathbf{u}}\cdot\mathbf{u'})} + \rho_o\overline{\omega'(\overline{\mathbf{u}}\cdot\mathbf{u'})_p} =$$
$$\rho_o\overline{\mathbf{u'}\cdot(\mathbf{u'}\cdot\nabla\overline{\mathbf{u}})} + \rho_o\overline{\omega'\mathbf{u'}}\cdot\overline{\mathbf{u}}_p - \rho_o\nabla\cdot(\overline{\phi}\overline{\mathbf{u}}) + \rho_o\overline{\phi}\nabla\cdot\overline{\mathbf{u}} \tag{A.10}$$

The first two terms on the right are deformation work by the mean Reynolds stresses; they are pathways to the mean eddy KE, which can be seen by subtracting (A.10) from (A.8):

$$\overline{EKE}_t + \overline{v}\overline{EKE}_y + \overline{\omega}\overline{EKE}_p + \overline{\mathbf{u'}\cdot\nabla EKE} + \overline{\omega' EKE_p} =$$
$$-\rho_o\overline{\mathbf{u'}\cdot(\mathbf{u'}\cdot\nabla\overline{\mathbf{u}})} - \rho_o\overline{\omega'\mathbf{u'}}\cdot\overline{\mathbf{u}}_p - \rho_o\nabla\cdot(\overline{\phi'\mathbf{u'}}) + \rho_o\overline{\phi'\nabla\cdot\mathbf{u'}} \tag{A.11}$$

The local rate of change of mean eddy KE is governed by divergence of the mean eddy KE and pressure work fluxes, mean eddy pressure deformation work, and conversion from KE of the mean flow, or mean eddy Reynolds stress deformation work. Over a region without boundary sources, the divergent energy fluxes integrate to zero, leaving only the conversions with $\overline{KE}$ and deformation work conversion with the mean eddy APE to change the mean EKE.

A.4 Eddy available potential energy

Using Equations (5.1) and (5.2) on (A.7), the total mean APE evolution is given by:

$$(\overline{APE} + \overline{EAPE})_t + \overline{u}\overline{EAPE}_x + \overline{v}(\overline{APE} + \overline{EAPE})_y$$
$$+ \overline{\mathbf{u'}\cdot\nabla(EAPE + C\rho'\,\overline{\rho})} =$$
$$-\rho_o(\overline{\phi}\overline{\omega} + \overline{\phi'\omega'})_p - \rho_o\overline{\phi}\nabla\cdot\overline{\mathbf{u}} - \rho_o\overline{\phi'\nabla\cdot\mathbf{u'}} \tag{A.12}$$

where $\overline{APE} = C\overline{\rho}^2/2$ is the APE of the mean flow, and $\overline{EAPE} = C\overline{\rho'^2}/2$ is the mean eddy APE. Variations in C have been ignored; for the TIWE-2 data they are negligible.

The mean continuity equation is:

$$\overline{\rho}_t + \overline{u\rho_x} + \overline{v}\,\overline{\rho}_y + \overline{\mathbf{u}' \cdot \nabla\rho'} + \overline{\omega}(\rho_o + \overline{\rho})_p + \overline{\omega'\rho'_p} = 0 \tag{A.13}$$

which shows that the eddies can change the mean density. The equation for APE of the mean flow is obtained by multiplying (A.13) by $C\overline{\rho}$:

$$\begin{aligned} \overline{APE}_t + \overline{u}\overline{EAPE}_x + \overline{v}\overline{APE}_y + \overline{\mathbf{u}' \cdot \nabla(C\rho'\overline{\rho})} = \\ C\overline{\rho'\mathbf{u}'} \cdot \nabla\overline{\rho} - \rho_o(\overline{\phi}\overline{\omega})_p - \rho_o\overline{\phi}\nabla \cdot \overline{\mathbf{u}} \end{aligned} \tag{A.14}$$

while the mean eddy APE equation results from subtracting (A.14) from (A.12):

$$\overline{EAPE}_t + \overline{v}\overline{EAPE}_y + \overline{\mathbf{u}' \cdot \nabla EAPE} = C\overline{\rho'\mathbf{u}'} \cdot \nabla\overline{\rho} - \rho_o(\overline{\phi'\omega'})_p - \rho_o\overline{\phi'\nabla \cdot \mathbf{u}'} \tag{A.15}$$

The common term in equations (A.14) and (A.15) has opposite signs; it represents conversion of APE of the mean to mean eddy APE, and is traditionally used as a probe for baroclinic instability. APE associated with the sloping isopycnals of the mean flow can be released to the eddy flow. If the equations are integrated over a horizontal region with no-source boundaries, the only other source terms are vertical pressure work and deformation conversion with $\overline{KE}$ and $\overline{EKE}$.

A.5 Summary eddy energy equations

$$\begin{aligned}\overline{EKE}_t = &- \overline{v}\overline{EKE}_y - \overline{\omega}\overline{EKE}_p - \overline{u'EKE_x} - \overline{v'EKE_y} - \overline{\omega'EKE_p} \\ &- \rho_o\overline{u'v'}\overline{u}_y - \rho_o\overline{v'v'}\overline{v}_y - \rho_o\overline{u'\omega'}\overline{u}_p - \rho_o\overline{v'\omega'}\overline{v}_p \\ &- \rho_o(\overline{\phi'v'})_y + \rho_o\overline{\phi'\nabla\cdot\mathbf{u}'}\end{aligned} \tag{A.16}$$

$$\begin{aligned}\overline{EAPE}_t = &- \overline{v}\overline{EAPE}_y - \overline{u'EAPE_x} - \overline{v'EAPE_y} \\ &- C\overline{\rho'v'}\overline{\rho}_y \\ &- \rho_o(\overline{\phi'\omega'})_p - \rho_o\overline{\phi'\nabla\cdot\mathbf{u}'}\end{aligned} \tag{A.17}$$

$$\begin{aligned}(\overline{EKE}+\overline{EAPE})_t = &- \overline{v}\overline{EKE}_y - \overline{\omega}\overline{EKE}_p - \overline{u'EKE_x} - \overline{v'EKE_y} - \overline{\omega'EKE_p} \\ &- \overline{v}\overline{EAPE}_y - \overline{u'EAPE_x} - \overline{v'EAPE_y} \\ &- \rho_o\overline{u'v'}\overline{u}_y - \rho_o\overline{v'v'}\overline{v}_y - \rho_o\overline{u'\omega'}\overline{u}_P - \rho_o\overline{v'\omega'}\overline{v}_P \\ &- C\overline{\rho'v'}\overline{\rho}_y \\ &- \rho_o(\overline{\phi'v'})_y - \rho_o(\overline{\phi'\omega'})_p\end{aligned} \tag{A.18}$$

References

Batchelor, G. K., (1967). *An Introduction to Fluid Dynamics*. Cambridge Univ. Press.

Baturin, N. G. and Niiler, P. P., (1997). Effects of instability waves in the mixed layer of the equatorial Pacific. *J. Geophys. Res.*, **to be submitted**, .

Bidigare, R. R. and Ondrusek, M. E., (1996). Spatial and temporal variability of phytoplankton pigment distributions in the central equtorial Pacific Ocean. *Deep-Sea Res.*, **43**, 809–833.

Bingham, F. M. and Lukas, R., (1994). The southward intrusion of North Pacific Intermediate Water along the Mindanao coast. *J. Phys. Oceanogr.*, **24**, 141–154.

Bryden, H. L. and Brady, E. C., (1989). Eddy momentum and heat fluxes and their effects on the circulation of the equatorial Pacific Ocean. *J. Marine Res.*, **47**, 55–79.

Busalacchi, A. J., McPhaden, M. J., and Picaut, J., (1994). Variability in equatorial Pacific sea surface topography during verification phase of the TOPEX/POSEIDON mission. *J. Geophys. Res.*, **99**, 24,725–24,738.

Chew, F. and Bushnell, M. H., (1990). The half-intertial flow in the eastern equatorial Pacific: a case study. *J. Phys. Oceanogr.*, **20**, 1124–1133.

Chiswell, S. M., Donohue, K. A., and Wimbush, M., (1995). Variability in the central equatorial Pacific, 1985-1989. *J. Geophys. Res.*, **100**, 15,849–15,863.

Coale, K. H., Fitzwater, S. E., Gordon, R. M., Johnson, K. S., and Barber, R. T., (1996). Control of community growth and export production by upwelled iron in the equatorial Pacific Ocean. *Nature*, **379**, 621–624.

Coale, K. H., Johnson, K. S., Fitzwater, S. E., Gordon, R. M., Tanner, S., Chavez, F. P., Ferioli, L., Sakamoto, C., Rogers, P., Millero, F., Steinberg, P., Nightingale, P., Cooper, D., Cochlan, W. P., Landry, M. R., Constantinou, J., Rollwagen, G., Trasvina, A., and Kudela, R., (1996). A massive phytoplankton bloom induced by an ecosystem-scale iron fertilization experiment in the equatorial Pacific Ocean. *Nature*, **383**, 495–501.

Cox, M. D., (1980). Generation and propagation of 30-day waves in a numerical model of the Pacific. *J. Phys. Oceanogr.*, **10**, 1168–1186.

Donohue, K. A., (1995). *Wave propagation in the central equatorial Pacific ocean.* PhD dissertation, University of Rhode Island.

Düing, W., Hisard, P., Katz, E., Meincke, J., Miller, L., Moroshkin, K. V., Philander, G., Ribnikov, A. A., Voigt, K., and Weisberg, R., (1975). Meanders and long waves in the Equatorial Atlantic. *Nature*, **257**, 280–284.

Dunkerton, T. J., (1981). On the inertial stability of the equatorial middle atmosphere. *J. Atmos. Sci*, **38**, 2354–2364.

Dunkerton, T. J., (1983). A nonsymmetric equatorial inertial instability. *J. Atmos. Sci*, **40**, 807–813.

Firing, J., Firing, E., Flament, P., and Knox, R., (1994). Acoustic doppler current profiler data from R/V Moana Wave cruises MW9010 and MW9012. Technical Report 93-05, School of Ocean and Earth Science and Technology, University of Hawaii at Manoa.

Flagg, C. N. and Smith, S. L., (1989). On the use of acoustic Doppler current profiler to measure zooplankton abundance. *Deep-Sea Res.*, **36**, 455–474.

Flament, P., Kennan, S. C., Knox, R., Niiler, P., and Bernstein, R., (1996). The three-dimensional structure of an upper ocean vortex in the tropical Pacific. *Nature*, **382**, 610–613.

Flierl, G. R., (1981). Particle motions in large-amplitude wave fields. *Geophys. Astrophys. Fluid Dynamics*, **18**, 39–74.

Foley, D. G., Dickey, T. D., Bidigare, R. R., Ondrusek, M., Barber, R. T., Lindley, S., McPhaden, M. J., and Trees, C., (1997). Intra-seasonal variations of primary productivity in the central equatorial Pacific Ocean. *Geophys. Res. Letters*, **submitted**, .

Gill, A. E., (1982). *Atmosphere-Ocean Dynamics*, volume 30 of *International Geophysics Series.* Academic Press.

Halpern, D., Knox, R., and Luther, D., (1988). Observation of 20-day period meridional current oscillations in the upper ocean along the pacific equator. *J. Phys. Oceanogr.*, **18**, 1514–1534.

Hansen, D. V. and Herman, A., (1989). Temporal sampling requirements for surface drifting buoys in the tropical Pacific. *J. Atmos. Oceanogr. Tech.*, **6**, 599–607.

Hansen, D. V. and Paul, C. A., (1984). Genesis and effects of long waves in the equatorial Pacific. *J. Geophys. Res.*, **89**, 10431–10440.

Harrison, D. E., (1996). Vertical velocity in the central tropical Pacific: a circulation model perspective for JGOFS. *Deep-Sea Res.*, **43**, 687–705.

Holton, J. R., (1979). *An Introduction to Dynamic Meteorology*, volume 23 of *International Geophysics Series*. Academic Press, second edition.

Johnson, E. S., (1996). A convergent instability wave front in the central tropical Pacific. *Deep-Sea Res.*, **43**, 753–778.

Kasahara, A., (1974). Various vertical coordinate systems used for numerical weather prediction. *Month. Weath. Rev.*, **102**, 509–522.

Kloosterziel, R. C. and Heijst, G. J. F.v., (1991). An experimental study of unstable barotropic vortices in a rotating fluid. *J. Fluid Mech.*, **223**, 1–24.

Kloosterziel, R. C., (1990). *Barotropic vortices in a rotating fluid*. PhD dissertation, Univ. of Utrecht, The Netherlands.

Kundu, P. K., (1990). *Fluid Mechanics*. Academic Press, Inc.

Kuo, H. L., (1973). Dynamics of quasigeostrophic flows and instability theory. *Advances in Applied Mechanics*, **13**, 247–330.

Leetmaa, A. and Molinari, R. L., (1984). Two cross-equatorial sections at 110°w. *J. Phys. Oceanogr.*, **14**, 255–263.

Legeckis, R., Pichel, W., and Nesterczuk, G., (1983). Equatorial long waves in geostationarry satellite observations and in a multi-channel sea-surface temperature analysis. *Bulletin of the American Meteorological Society*, **64**, 133–139.

Legeckis, R., (1977). Long waves in the eastern equatorial Pacific Ocean: A view from a geostationary satellite. *Science*, **197**, 1179–1181.

Legeckis, R., (1986). Long waves in the equatorial Pacific and Atlantic Oceans during 1983. *Ocean-Air Interactions*, **1**, 1–10.

Legeckis, R., (1986). A satellite time-series of sea surface temperature in the eastern equatorial Pacific Ocean. *J. Geophys. Res.*, **90**, 12879–12886.

Lindzen, R. S. and Tung, K. K., (1978). Wave overreflection and shear instability. *J. Atmos. Sci*, **35**, 1626–1632.

Lindzen, R. S., Farrell, B., and Tung, K.-K., (1980). The concept of wave overreflection and its application to baroclinic instability. *J. Atmos. Sci*, **37**, 44–63.

Lindzen, R. S., (1980). Instabilities in a stratified fluid having one critical level. part III: Kelvin-Helmholtz instabilities as overreflected waves. *J. Atmos. Sci*, **40**, 530–542.

Lindzen, R. S., (1988). Instability of plane parallel shear flow (toward a mechanistic picuture of how it works. *Pure Appl. Geophys.*, **126**, 103–121.

Lukas, R., (1987). Horizontal reynolds stresses in the central equatorial Pacific. *J. Geophys. Res.*, **92**, 9453–9463.

Luther, D. S. and Johnson, E. S., (1990). Eddy energetics in the upper equatorial Pacific during Hawaii–to–Tahiti Shuttle Experiment. *J. Phys. Oceanogr.*, **7**, 913–944.

McCreary, J. P. and Yu, Z., (1992). Equatorial dynamics in a 2-1/2-layer model. *Prog. Oceanogr.*, **29**, 61–132.

McPhaden, M. J. and Ripa, P., (1990). Wave-mean flow interactions in the equatorial ocean. *Ann. Rev. Fluid Mech.*, **22**, 167–205.

McPhaden, M. J., (1996). Monthly period oscillations in the Pacific North Equatorial Countercurrent. *J. Geophys. Res.*, **101**, 6337–6359.

Miller, L., Watts, D. R., and Wimbush, M., (1985). Oscillations of dynamic topography in the eastern equatorial Pacific. *J. Phys. Oceanogr.*, **15**, 1759–1770.

Montgomery, R. B. and Stroup, E. D., (1962). Equatorial waters and currents at 150°w in july – august 1952. Technical Report 1, The John Hopkins University.

Niiler, P. P., Davis, R. E., and White, H. J., (1987). Water-following characteristics of a mixed-layer drifter. *Deep-Sea Res.*, **34**, 1867–1882.

Peixoto, J. P. and Oort, A. H., (1992). *Physics of Climte*. American Inst. Physics.

Perigaud, C., (1990). Sea level oscillations observed with Geosat along the two shear fronts of the Pacific North Equatorial Countercurrent. *J. Geophys. Res.*, **95**, 7239–7248.

Philander, S. G. H., Hurlin, W. J., and Pacanowski, R. C., (1986). Properties of long equatorial eaves in models of the seasonal cycle in the tropical Atlantic and Pacific Oceans. *J. Geophys. Res.*, **91**, 14207–14211.

Philander, S. G. H., Hurlin, W. J., and Seigel, A. D., (1987). Simulation of the seasonal cycle of the Tropical Pacific Ocean. *J. Phys. Oceanogr.*, **17**, 1986–2002.

Philander, S. G. H., (1976). Instabilities of zonal equatorial currents. *J. Geophys. Res.*, **81**, 3725–3734.

Philander, S. G. H., (1978). Instabilities of zonal equatorial currents, 2. *J. Geophys. Res.*, **83**, 3679–3682.

Proehl, J. A., (1996). Linear stability of equatorial zonal flows. *J. Phys. Oceanogr.*, **26**, 602–621.

Pullen, P. E., Bernstein, R., and Halpern, D., (1987). Equatorial long-wave characteristics determined from satellite sea surface temperature and in situ data. *J. Geophys. Res.*, **92**, 742–748.

Qiao, L. and Weisberg, R. H., (1995). Tropical instability wave kinematics: observations from the Tropical Instability Wave Experiment. *J. Geophys. Res.*, **100**, 8677–8693.

Qiao, L. and Weisberg, R. H., (1997). Tropical instability wave energetics: observations from the Tropical Instability Wave Experiment. *J. Phys. Oceanogr.*, **submitted**, .

Rayleigh, L., (1916). On the dynamics of revolving fluids. *Proc. Royal Soc. London A*, **93**, 148–154.

Ripa, P., (1989). On the stability of ocean vortices. In Nihoul, J. C. J. and Jamart, B. M., editors, *Mesoscale/Synoptic Coherent Structures in Geophysical Turbulence*, pages 167–179. Elsevier.

Sawyer, M., Flament, P., and Knox, R., (1994). Hydrographic seasoar data from the R/V Moana Wave cruises mw9010 and mw9012. Technical Report 94-04, University of Hawaii SOEST.

Sawyer, M., (1996). Convergence and subduction at the North Equatorial Front. Master's thesis, School of Ocean and Earth sci and Technology, University of Hawaii at Manoa.

Semter, A. J. and Chervin, B. M., (1988). A simulation of the global ocean circulation with resolved eddies. *J. Geophys. Res.*, **93**, 15,502–15,522;15,767–15,775.

Semter, A. J. and Chervin, B. M., (1992). Ocean general circulation from a global eddy-resolving model. *J. Geophys. Res.*, **97**, 5493–5550.

Semter, A. J. and Holland, W. R., (1980). Numerical simulation of equatorial circulation. part I: A basic case in turbulent equilibrium. *J. Phys. Oceanogr.*, **10**, 667–693.

Smith, S., (1988). Coefficients for sea surface wind stress, heat flux and wind profile as a function of wind speed and temperature. *J. Geophys. Res.*, **93**, 15467–15472.

Tennekes, H. and Lumley, J. L., (1972). *A First Course in Turbulence*. MIT Press.

Trefois, C., Flament, P., Knox, R., and Firing, J., (1993). Hydrographic data from R/V Moana Wave cruises MW9010 and MW9012. Technical Report 93-01, School of Ocean and Earth sci and Technology, University of Hawaii at Manoa.

Tsuchiya, M., (1968). Upper waters of the intertropical pacific ocean. Technical Report 4, The John Hopkins University.

Tsuchiya, M., (1991). Flow path of the Antarctic Intermediate Water in the western equatorial South Pacific Ocean. *Deep-Sea Res.*, **38**, S273–279.

Weare, B. C., Strub, P. T., and Samuel, M. D., (1981). Annual mean surface heat fluxes in the Tropical Pacific Ocean. *jpo*, **11**, 705–717.

Weisberg, R. H. and Weingartner, T. J., (1988). Instability waves in Equatorial Atlantic Ocean. *J. Phys. Oceanogr.*, **18**, 1641–1657.

Weisberg, R. H., Donovan, J. C., and Cole, R. D., (1991). The Tropical Instability Wave Experiment (TIWE) equatorial array: a report on data collected using subsruface moored acoustic Doppler current profilers, May 1990 - June 1991. Technical report, University of South Florida.

Weisberg, R. H., (1984). Instability waves observed on the equator in the Atlantic Ocean during 1983. *Geophysical Research Letters*, **11**, 753–756.

Wilson, D. and Leetmaa, A., (1988). Acoustic Doppler Current Profiling in the equatorial Pacific in 1984. *J. Phys. Oceanogr.*, **18**, 1641–1657.

Wyrtki, K. and Kilonsky, B., (1984). Mean water and current structure during the Hawaii–Tahiti Shuttle Experiment. *J. Phys. Oceanogr.*, **14**, 242–254.

Yoder, J. A., Ackleson, S. G., Barber, R. T., Flament, P., and Balch, W. M., (1994). A line in the sea. *Nature*, **371**, 689–692.

Yu, Z., Julian P. McCreary, J., and Proehl, J. A., (1995). Meridional asymmetry and energetics of tropical instability waves. *J. Phys. Oceanogr.*, **25**, 2997–3007.